Structural mechanics of echinoid skeletons as candidate systems for biomimetic research

Dissertation

der Mathematisch-Naturwissenschaftlichen Fakultät

der Eberhard Karls Universität Tübingen

zur Erlangung des Grades eines

Doktors der Naturwissenschaften

(Dr. rer. nat.)

vorgelegt von

MSc. Tobias B. Grun

aus Stuttgart

Tübingen

2018

Gedruckt mit Genehmigung der Mathematisch-Naturwissenschaftlichen Fakultät der Eberhard Karls Universität Tübingen.

Tag der mündlichen Qualifikation:	26.07.2018
Dekan:	Prof. Dr. Wolfgang Rosenstiel
1. Berichterstatter:	Prof. Dr. James H. Nebelsick
2. Berichterstatter:	Prof. Dr. Oliver Betz
3. Berichterstatter:	Prof. Dr. William I. Ausich

Gerace Research Center transportation vehicle “Truck S”,
our solid partner during field work in San Salvador, Bahamas

Institute for Marine Biology in Campese, Giglio, Italy

Acknowledgments

I greatly acknowledge the support of my supervisors James Nebelsick and Oliver Betz for accompanying me the long way from the Bachelor and Master theses throughout this PhD graduation. Their technical confidence and broad though detailed knowledge in the fields of biology and paleontology have very advantageous throughout the studies in which I've learned a great deal from them. I am also in great gratitude to many of my colleagues, who supported me throughout this work, especially Wilfried Konrad, who's passionate analytical comprehension influenced my scientific understanding. I furthermore highly appreciate the support and effort of Hartmut Schulz, who introduced me to the SEM and taught me his knowledge until I was able to self-sufficiently work with the equipment. I also thank Raouf Jemmali for μCT scanning of the many echinoid tests.

I gratefully thank the Gerace Research Center for hosting me twice during the research and providing me with infrastructure and the excellent knowledge of the local research-sites. This thank especially deserves to Tom Rothfuss, Troy Dexter and Michał Kowalewski. I also thank all fellows at the GRC for the great assistance I've received during this time. I also thank the Institute for Marine Biology in Giglio, Italy, especially Claus Valentin, Jenny Tuček and Reiner Krumbach for their support, lodging and arranging field trips.

I must take this opportunity to express my deepest gratitude to my family: my mother, father and sisters, who kindly supported me under all possible circumstances during the last years. They have been, and still are, the most important backing during such challenging times, especially when time becomes a rare good. Thanks! I also highly acknowledge the many delightful support of my friends.

This work was funded by the Deutsche Forschungsgemeinschaft (German Research Foundation) within the Collaborative Research Center SFB-TRR 141: Biological Design and Integrative Structures – Analysis, Simulation and Implication in Architecture. The SFB-TRR 141 provided a framework for interdisciplinary collaboration between biology, paleontology, engineering sciences and architecture. The aim of this SFB-TRR is the identification of evolutionary optimized building principles, which can be implemented in engineered structures and architectural design with simultaneously increasing the understanding of natural systems. This biomimetic approach can be beneficial for biologists, paleontologists, engineers and architects.

Table of contents

Abbreviations

The abbreviations used in the main body of this thesis are defined below. In the published articles, these abbreviations may vary in punctuation or capitalization depending on the journals corporative design

3d – three dimensional
abbr – abbreviation
ant – antonym
CT – x-ray computed tomography
deg – degree
e.g. – exempli gratia (lat); for example (eng)
eng – English term
et al. – et alii (lat); and colleagues (eng)
FEA – Finite Element Analysis
FEM – Finite Element Method
i.e. – id est (lat); in other words (eng)
ITA – inter-trabecular angle
lat – Latin term
mad – median absolute deviation
max – maximum
min – minimum
N – sample size
pl – plural
sd – standard deviation
SEM – scanning electron microscopy
syn – synonym
µCT – micro x-ray computed tomography

Symbols

The symbols used in the main body of this thesis are defined below, but may have alternative or additional meanings in other disciplines. For geometrical purposes are usually Greek minuscule employed

° – degree
p – p-Value of a significance test
τ – see tau
tau – coefficient of tortuosity
θ – see theta
theta – angle, see glossary
Φ – see phi
phi – angle, see glossary

Glossary

This glossary provides a brief overview of terms with a specific meaning used in this thesis. Terminologies used in the published papers usually follow these definitions but may follow a narrower or expanded definition. The key-word "usually" indicates that a term is used herein with a specific meaning but can also be used differently in another context.

aboral side – top of the echinoid

accessory pore – unpaired pore which can occur in both the ambulacral- and interambulacral fields; part of the water-vascular system

ambitus – widest lateral extent of the echinoid's test

ambulacral pore – paired pores within the ambulacral fields; part of the water-vascular system

anterior – front of the echinoid; particularly applicable for irregular echinoids that show an overprinted bilateral symmetry

apical disc – aboral ring of plates enclosing the periproct including genital pores and the madreporite; usually used for regular echinoids

apical system – usually used in irregular echinoids, where the apical disc is fused with the madreporite and the genital pores

bilateral symmetry – for echinoids often used in the sense of "overprinted bilateral symmetry" or "secondary bilateral symmetry"

biocalcite – biomineralized calcite, contains organic matters

biogenic calcite – see biocalcite (syn)

biomimetic – coinage from bio (= biology) and mimetic, meaning: "learning from nature"

biomineralization – mineralization process of organisms

buttress – internal support bridging the oral- and aboral side of the test. It is attached to the test over its entire length

candidate mechanism – a mechanism, or structural principle, that possesses the potential as a role model in technical applications

collagenous fibers – collagen; biochemically similar, but not identical to collagen of the vertebrates

dorsal – see aboral side; incorrect usage for echinoids

dorsoventrally flattened – flattened at the oral and aboral side

dynamic – state that may change over time; compare to static (ant)

echinoid – sea urchin (syn)

element – building unit; used for both biological and technical structures

galleried stereom – stereom type where trabeculae are aligned, forming a gallery-like architecture

genital pore – pore in the apical system releasing gametes from the test cavity to the environment

glassy tubercle – knob-like structure on the echinoid's test surface, made-up from an imperforat, dense stereom; often glassy appearance

hydropore – connection between the water-vascular system and the sea water

in extenso – (lat) in detail

in situ – (lat) under natural conditions

inter-trabecular angle – ITA (abbr). Angle formed by two trabecula meeting in one common node

irregular echinoid – mostly flattened test; periproct migrated posteriorly, sometimes closely to the peristome. Compare regular echinoids

Irregularia – see irregular echinoid

jaw apparatus – chewing mouth parts, follow pentamerous symmetry

labyrinthic stereom – stereom type where trabeculae direction is unordered

lantern – also known as Aristotle's lantern (syn)

macro-canal – lacuna system within the test, formed by a tight mesh-like support system; hosting the water-vascular system

masking – behavior in which the echinoid covers itself by available materials using its sticky tube-feet

member – unit of a structure; used in a technical context

mesh-like support – complex system of small and narrow walls bridging the oral- and aboral side of the test

micro-canal – lacuna system within plates, formed and filled by the water-vascular system

node – intersection point of trabeculae

ocular pore – pore closely attached to the apical system; hosting ocular cells for light perception

oral side – bottom side of the echinoid

organic matrix – unspecified assemblage of mesodermal, endodermal, or ectodermal tissues or any possible combination of these three tissues; usually used when collagenous fibers are involved

pentamerous symmetry – five-fold symmetry

periproct – anal opening in the echinoid test

peristome – mouth opening in the echinoid test

petal – a single element of the pentamerous flower-like petalodium; see petalodium

petalodium – ambulacral area in which the paired ambulacral pores are located. Usually used for irregular echinoids, where it is restricted to the aboral side, forming a pentamerous flower-like structure

peticellaria – claw-like appendage of the echinoid skeleton, employed for the removal of foreign objects or as predator defense; may be venomous

phi – descriptor of the trabecular orientation in relation to the plate's horizontal plane

pillar – internal support bridging the oral- and aboral side; fairly fixed to the oral- and aboral side of the test. Individual pillars can cross and fuse

posterior – rear of the echinoid; particularly meaningful for irregular echinoids that show an overprinted bilateral symmetry

regular echinoid – globular in shape; periproct centrally on the aboral side. Compare irregular echinoids.

"Regularia" – see regular echinoid. Quotation marks indicate that this term represents a paraphyletic group

sea urchin – echinoid (syn)

stereom – lattice-like meshwork of calcite struts forming single skeletal members; resemble a micro-beam system

stiffness – ability of a structure returning to its original form after load application

strength – ability to resist mechanical stress until permanent deformation or failure

strain – deformation of a structure

stress – force per unit area of a structure

suture – interface between adjoining plates

taphonomy – processes of fossilization

technical biology – analyzing biological structures by using engineering techniques

test – skeleton of the echinoid that is entirely denuded with no appendages attached

theta – descriptor of the trabecular orientation in relation to the axis perpendicular to the plate's surface – Also used for the angle between two intersecting trabeculae

toughness – ability to absorb energy and plastically deform without fracturing

trabecula – trabeculae (pl). Single strut or rod of the stereom

tube-foot – tube-feet (pl). Evagination of the water-vascular system; penetrating the test via ambulacral pores and accessory pores. Often sticky for locomotion and masking, also respiratory organ

tubercle – knob-like structure on the echinoid's test surface; structures on which the spines are mounted

unipore – see accessory pore (syn)

ventral – see oral side; incorrect usage for echinoids

water-vascular system – hydrostatic vessel system for locomotion and respiration

Thesis

Zusammenfassung

Echinidenskelette bestehen aus vielen Einzelteilen, wozu die Platten der Schale, Stacheln, Kieferapparat, Skelettscheiben der Ambulakralfüßchen, und die Skelettelemente der Pedicellarien zählen. Diese Elemente sind aus einem kalzitischen Leichtbau Gitternetzwerk, dem Stereom, aufgebaut. Die Schale der Echiniden umgibt die inneren Organe sowie Gewebe und dient als Stützapparat für z.B. die Stacheln. Außerdem fungiert diese Schale als Schutz gegen äußere biotische, sowie abiotische Faktoren. Besonders die Schalen der Clypeasteriden, einer Gruppe irregulärer Echiniden, welche häufig im Sediment eingegraben leben, weisen eine erstaunliche Stabilität auf. Diese Stabilität äußert sich in dem sehr häufigen Auftreten der Clypeasteriden Schalen in rezenten Lebensräumen, als auch im Fossilbeleg. Die Gründe für die besondere Stabilität der Schalen wird in deren strukturellem Aufbau vermutet. Die Schalen der Clypeasteriden, vor allem von *Clypeaster rosaceus* und *Echinocyamus pusillus*, werden *in extenso* untersucht, um die zugrunde liegenden strukturellen Skeletteigenschaften aufzudecken, welche für die Stabilität der Schalen verantwortlich sind.

Die Schalen der beiden oben genannten Echiniden Arten wurden mittels Elektronenmikroskopie und Mikro-Computertomographie auf ihre Architektur untersucht. Durch die Anwendung von computerbasierten Methoden für räumliche- und volumetrische Untersuchungen werden neuartige Einblicke in die Mikrostruktur der Schalen,sowie deren strukturelle Einbindung ermöglicht. Ergebnisse zeigen, dass die Schlen der beiden Untersuchungsobjekte meherere Verstärkungsmechanismen auf verschiedenen hierarchischen Ebenen aufweisen, deren Wirkung aber durch biologisch notwendige Strukturen reduziert werden kann. Eine Stabilisierungsstrategie ist das Einbinden der Platten in ein Mosaik, welches von zusätzlichen skeletalen Verbindungen zwischen den Platten sowie Verdickungen an deren Grenzen verstärkt wird. Dieses Plattenarrangement verleiht der Schale eine monolithische Struktur. Auch die Anwesenheit interner Stützelemente hat gezeigt, dass diese sowohl Druck-, als auch Zugspannungen in der Schale verringern. Die Untersuchung der Stereomarchitektur und deren Topologie ergab, dass das Stereom eine gut ausgebildete Lastenträgereigenschaft hat.

Summary

The skeletons of echinoids are multi-element and light-weight constructions which are formed by a lattice-like meshwork, the stereom. The echinoids' skeletons include various calcareous components, such as the plates that form the test, spines, jaw-apparatus, skeletal discs of the tube feet and skeletal elements of the pedicellariae. The tests enclose the internal organs and tissues of the echinoid thus functioning as a shell construction, supportive for the attachment of e.g. spines and as a protection against biotic and abiotic environmental factors. Especially the tests of clypeasteroid echinoids, a group of irregular sea urchins which commonly live infaunally, feature notable strong tests, which is indicated by the abundant occurrence in both recent environments and the fossil sedimentary record. Reasons for the stable nature of the clypeasteroids' tests are assumed to be found in their structural skeletal design. Tests of clypeasteroid echinoids, particularly of the sea biscuit *Clypeaster rosaceus* and the pea-urchin *Echinocyamus pusillus*, are analyzed in-depth to discover skeletal strengthening mechanisms which are responsible for their high test integrity.

The tests of *Clypeaster rosaceus* and *Echinocyamus pusillus* have been analyzed using Scanning Electron Microscopy and x-ray micro-computed tomography for the analyses of their skeletal architecture. The employment of computational techniques for spatial and volumetric analysis allowed for a novel insight into both the micro-structural design of the tests and its structural integrity within the system. Results show that the clypeasteroids' tests are characterized by various strengthening mechanisms on different hierarchical levels, which, however, might be reduced by the presence of biologically necessary infrastructures. The arrangement of plates into a mosaic provides a first plate interlocking mechanism. Additional skeletal bridges between the plates and sutural thickening intensify the plate interlocking, leading to a shell construction which behaves monolithic. The presence of internal buttressing has been shown to reduce compressive and tensile forces in the shell system. A detailed analysis of the stereom architecture and topology revealed that the stereom is a well-constructed load-bearing system.

List of publications

The following manuscripts are the basis of this thesis. Accepted and submitted manuscripts are (or will be) peer-reviewed and published in relevant journals or books. Additional publications and conference contributions can be found in the appendix.

Accepted manuscripts

1. The skeleton of the sand dollar as a biological role model for segmented shells in building construction: a research review. 2016. In: J Knippers, KG Nickel, T Speck (eds) Biomimetic Research for Architecture and Building Construction: *Biological Design and Integrative Structures*. Springer, Cham, 217–242. 2016

   Authors: Grun TB, Koohi L, Schwinn T, Sonntag D, von Scheven M, Bischoff M, Knippers J, Menges A, Nebelsick JH

2. The taphonomy of *Clypeaster*: a paleontological tool to identify stable structures in natural shell systems. 2018. *Neues Jahrbuch für Geologie und Paläontologie*. Sonderband des 8th International Meeting on Taphonomy and Fossilization.

   Authors: Grun TB, Mancosu A, Belaústegui Z, Nebelsick JH

3. Structural design of the minute clypeasteroid echinoid *Echinocyamus pusillus*. *Royal Society Open Science*.

   Authors: Grun TB, Nebelsick JH

4. Structural stress response of segmented natural shells: a numerical case study on the clypeasteroid echinoid *Echinocyamus pusillus*. *Royal Society Interface*.

   Authors: Grun TB, von Scheven M, Bischoff M, Nebelsick JH

Submitted manuscript

5. Structural design of the echinoid's trabecular system. *PlosOne*.

   Authors: Grun TB, Nebelsick JH

EBERHARD KARLS
UNIVERSITÄT
TÜBINGEN

Faculty of Science

Personal contribution

Declaration according to § 5 Abs. 2 No. 8 of the PromO of the Faculty of Science.
Share in publications done in team work.

nr	accepted for publication	number of all authors	position of the candidate in list of authors	scientific ideas of candidate (%)	data generation by candidate (%)	analysis and interpretation by candidate (%)	Paper writing by candidate (%)
1	accepted	9	1	40	60	30	50
2	accepted	4	1	70	80	70	80
3	accepted	2	1	80	85	60	80
4	accepted	4	1	50	50	50	80
5	in review	2	1	80	90	75	90

I certify that the above statement is correct.

Date, Signature of the candidate

I / We certify that the above statement is correct.

Date, Signature of the doctoral committee or at least of one of the supervisors

Introduction

This section provides an overview of the biomimetic approach and its implementation for the multi-plated, though stable tests of clypeasteroid echinoids. The biological and paleontological background of clypeasteroids is given by a brief introduction into the Echinodermata phylum, the class of Echinoidea, and eventually the order Clypeasteroida.

Biomimetics and technical biology of echinoids

The biomimetic approach aims to understand functional principles of natural structures which can potentially be transferred to technical applications (Nachtigall 2002). A major part of this approach is technical biology, in which natural systems are analyzed using engineering techniques (Fig. 1) (Nachtigall 2002). Thereby, evolutionary optimized mechanisms can be revealed which possess the potential for the development of solutions for technical problems (e.g. Drack 2018). The technical understanding of biological structures additionally provides information for the biological relevance of these structures (Fig. 1). Technical biology is of particular interest in biology, paleontology and taphonomy, in which the structural behavior is indicative for morphological adaptations, and the preservation potential of

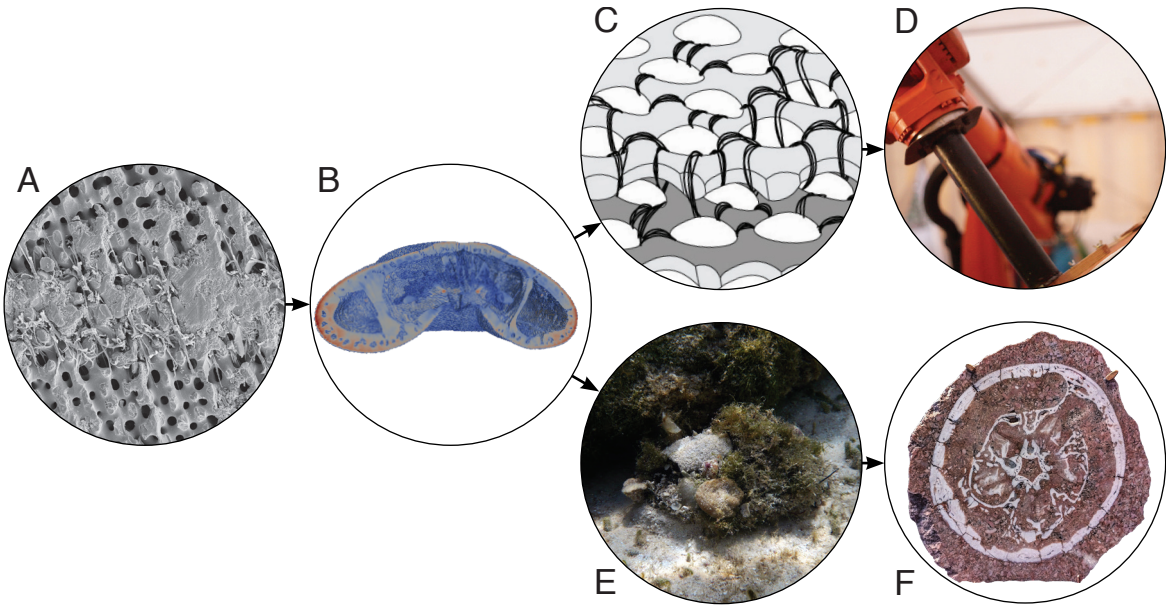

Figure 1. Biomimetic approach. (A-B) Analytics, (C-D) technical application, (E-F) technical biology and structural interpretation. (A) Identification of candidate structures which are relevant for biology, paleontology and engineering sciences. (B) Analyses of functional principles. (C) Abstraction of these principles for technical applications. (D) Proof of concept and fabrication. (E) Interpretation of environmental adaptations (biology), and (F) understanding mechanisms that are important taphonomic interpretations (paleontology). Modified from Grun et al. (2016; 2017b)

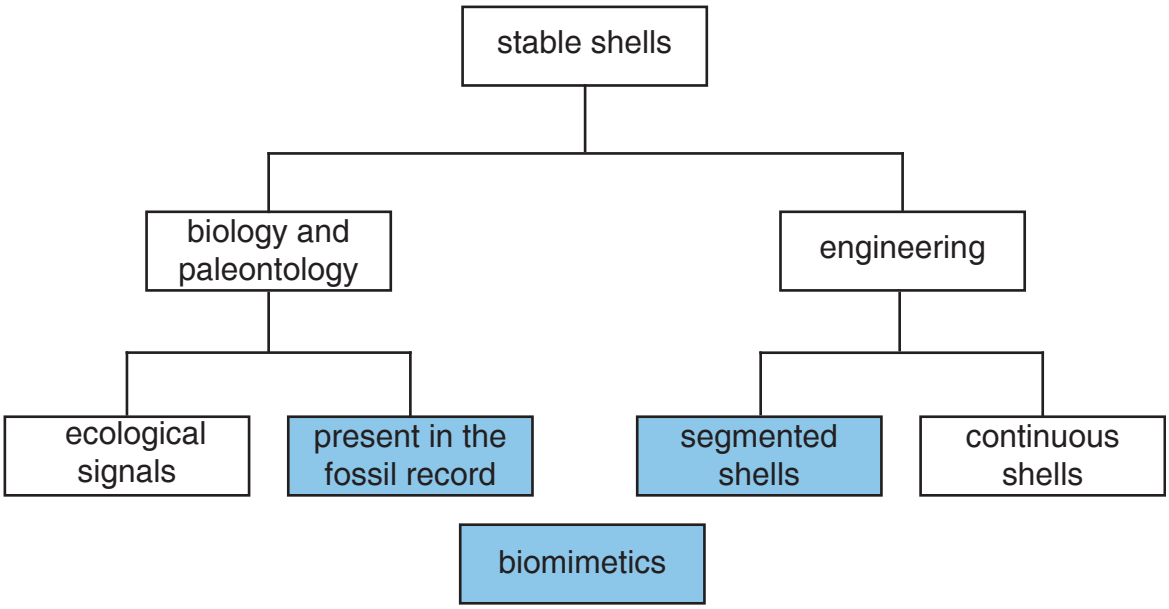

Figure 2. Diagram showing interdisciplinary interest in stable segmented shell

skeletal structures in the fossil record (e.g. Mancosu and Nebelsick 2017, Grun et al. 2018). The echinoid skeleton represents a naturally multi-plated shell construction, where single plates are, in most cases, interconnected by collagenous fibers (Nichols 1962, Nichols and Currey 1968, Klein and Currey 1970, Telford 1985a, Ellers et al. 1998). Clypeasteroids, however, developed additional or even exclusively skeletal connections between the plates and internal supports which has been discussed to increase the skeletal integrity of the tests (Seilacher 1979, Mortensen 1948, Durham 1955; 1966, Klein and Currey 1970, Telford 1985a; b, Mooi 1989, Nebelsick 1999a; 2008, Nebelsick and Kowalewski 1999, Grun et al. 2014, Grun and Nebelsick 2015; 2016, Grun et al. 2017a). The stable nature of the clypeasteroid tests (Grun et al. 2018; [2], Grun and Nebelsick [1]) make these structures of considerable interest for mechanical and biomimetic research (Fig. 2) (e.g. Bramski 1981, Telford 1985a; b, Grossmann and Nebelsick 2013a; b, Presser et al. 2010, Grun et al. 2016; 2018; [2], Klang et al. 2016, Grun and Nebelsick 2018; [1]). In addition, discovering of strengthening mechanisms provide better understanding of the structures responsible for the high preservation potential of clypeasteroid echinoids (Fig. 2). The content of this thesis thus reflects a classic example for biomimetic research, in which analyzed structural mechanisms provide information on the structural layout responsible for the extensive fossil record including the patterns found therein, and can also be the basis for the development of improved technical shell constructions (e.g. Grun et al. 2016; 2017b; 2018; [2], Grun and Nebelsick 2018; [1]).

Echinodermata

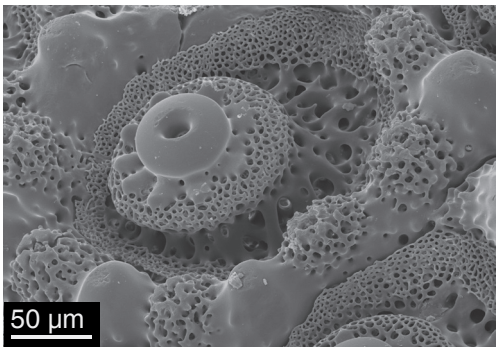

Figure 3. SEM micrograph of a tubercle of *Echinocyamus pusillus*. The entire skeleton is formed by a lattice-like meshwork, the stereom

The phylum Echinodermata includes the five extant classes crinoids (sea lilies), asteroids (sea stars), ophiuroids (brittle stars), holothuroids (sea cucumbers), and echinoids (sea urchins). With around 7,000 extant and 13,000 fossil species, echinoderms are one of the major phyla in the world's oceans (Pawson 2007, Byrne and O'Hara 2017). Their skeletons are constructed from calcareous ossicles, which are formed by the stereom, a micro-beam system (Fig. 3). This skeletal light-weight construction is a differential diagnostic feature for all echinoderms (Nichols 1962, Raup 1966, Ubaghs 1967), which is even recognizable from small fragments revealed from both recent environments and the fossil sedimentary record (e.g. Nebelsick 1992; 1999b, Kroh and Nebelsick 2010, Dynowski 2012). The echinoderms' skeletal elements are of mesodermal origin, thus representing a true internal skeleton (e.g. Hyman 1955, Raup 1966). Apart from the hemichordates, echinoderms are the only invertebrate taxon that feature such a mesodermal skeleton (Kilian and Wilt 2008), which allows for *in-situ* modifications of the skeletal constitutes (e.g. Durham 1955, Hyman 1955). Particularly the ability of skeletal rearrangement, regeneration and element insertion is common in echinoderms (e.g. Hyman 1955, Nichols 1962, Swan 1966, Dubois and Ameye 2001).

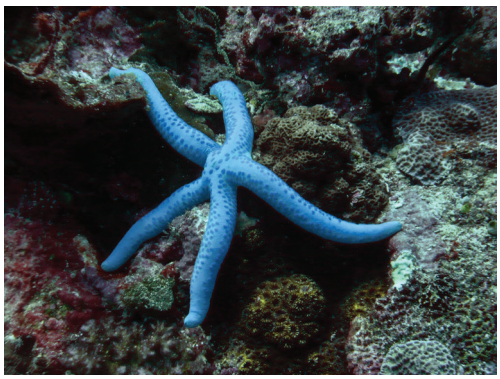

Figure 4. Blue asteroid *Linckia laevigata* (Sulawesi, Indonesia). The five-fold symmetry is well-visible

The echinoderm skeleton follows a pentamerous symmetry with typically five (Fig. 4), or a multiple of five planes of symmetry (e.g. Lang 1896). The five-fold symmetry is well-recognizable in asteroids, ophiuroids and numerous echinoids, but can be less obvious in crinoids and holothurians (e.g. Hyman 1955). The latter class consists of a dermal tube which incorporates skeletal elements (e.g. Lang 1896). Although holothurians show an internal pentamerous symmetry, the general appearance is characterized by a dorsal and ventral side, as well as an anterior and posterior end. The calyx (main body) of the crinoids

generally exhibit the five-fold symmetry, but numerous arms and cirri (holdfast) hide this symmetrical arrangement in live-condition. Although echinoderms possess an often pronounced pentamerous symmetry, they belong to the Bilateria and consequently feature a left and a right body side. This bilateral symmetry is well-recognizable in the echinoderm larvae (Lang 1896, Mortensen 1948, Durham 1955; 1966, Ubaghs 1967), which after its metamorphosis, is still visible in the position of the madreporite and the arrangement of the periproct and some skeletal elements (Lovén 1874, Durham 1966).

Echinoidea

Echinoids account for around 800 species today (Pawson 2007) and the fossil record is dating back around 450 million years into the Late Ordovician (Smith and Savill 2001, Bottjer et al. 2006, Thompson et al. 2015). In both recent and fossil echinoids, the multi-element skeletons (Fig. 5) are taxonomically important (e.g. Mortensen 1948, Durham 1955, Mooi 1989, Kroh and Smith 2010, Mooi et al. 2014), and consist of plates, spines, jaw-apparatus, skeletal discs of the tube feet, and skeletal elements of the pedicellariae (e.g. Nebelsick et al. 2015, Grun et al. 2016, Grun and Nebelsick 2018). The skeletal plates envelope internal organs of the echinoids and form a test, which functions as an external shell (Fig. 5) (Durham 1966, Raup 1966). Yet, all skeletal elements are of mesodermal origin thus being covered by an ectoderm, except for the tips of the teeth and spines of cidaroids (Fig. 6A) (Durham 1955, Hyman 1955, Märkel and Röser 1983).

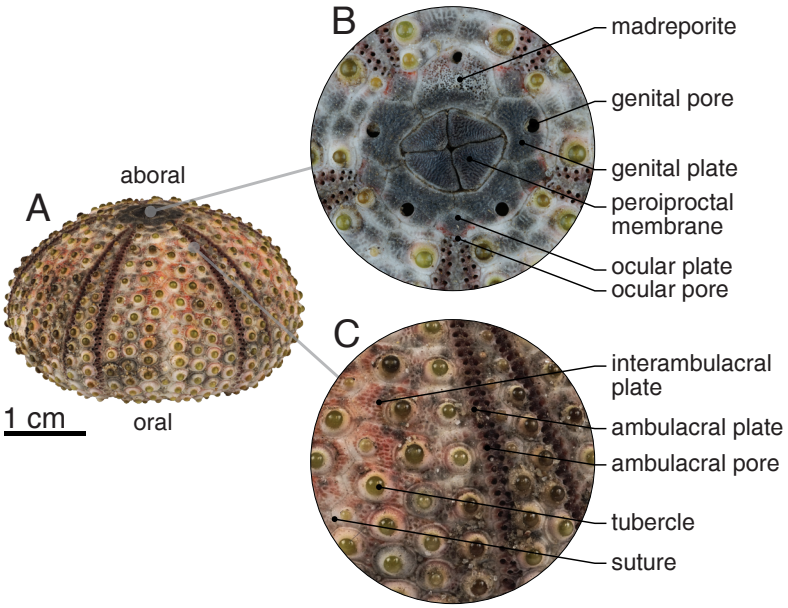

Figure 5. Denuded test of *Arbacia* sp. (A) Test in oblique view with the aboral side to the top, and the oral side to the bottom. (B) Apical disc consists of the madreporite, genital plates, genital pores, ocular plates and ocular pores. The periproct is in the center of the disc surrounded by a membrane. (C) The test consists of interambulacral plates and ambulacral plates. The latter includes the paired interambulacral pores. Sutures are the connection faces of the plates. Plates feature tubercles for spine attachment.

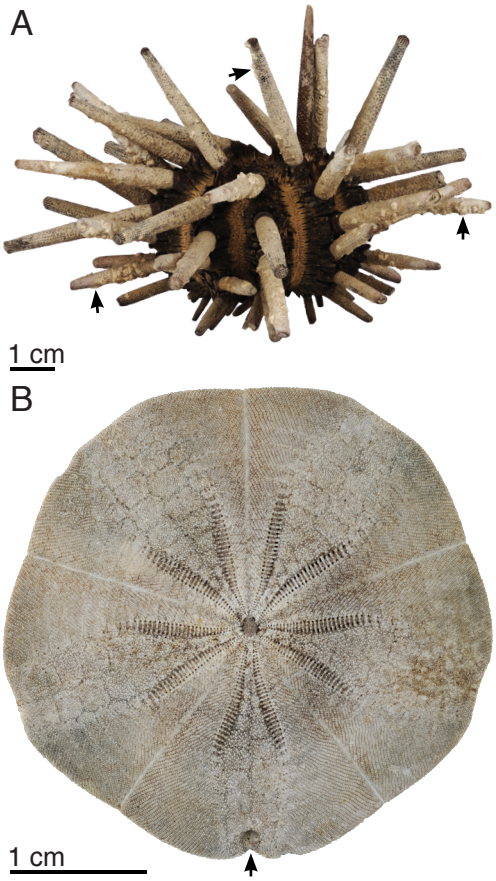

Figure 6. (A) Regular echinoid *Eucidaris* sp. Test dorsoventrally slightly flattened. Spines are not covered by a dermis and hence show encrustations (arrows). (B) Test of the irregular echinoid *Arachnoides placenta*. Test is fairly flattened with the periproctal opening posterior (arrow).

Sea urchins are dichotomously divided into "Regularia" and Irregularia (Fig. 6). "Regularia" represent a paraphyletic group with a generally globular, but often slightly dorsoventrally flattened test (Fig. 6A). The periproct lies within the apical disc of the aboral side (Fig. 5). The ambulacral system includes the paired tube-feet (Fig. 5C) for respiration, locomotion and particle transportation (e.g. Lang 1896, Hyman 1955, Nichols 1959, Ubaghs 1967, Shick 1983, Ghiold 1984, Mooi 1986a; b) and ranges from the outer limits of the apical disc towards the peristome on the oral side. Irregular echinoids (Fig. 6B) are monophyletic and known since the Sinemurian of the Lower Jurassic (Kier 1977). These representatives are often characterized by a flattened and elongated or disc-like test (Fig. 6B). The periproct migrated posteriorly out of the apical disc and can be located at any position between the apical disc on the aboral side, and the peristome on the oral side (Fig. 6B). The ambulacral system is condensed and often restricted to the aboral surface, forming a flower-like structure with five petals. These petals include the paired ambulacral pores for the tube feet and promote the pentamerous symmetry of the echinoids.

The petalodium is a taxonomically and ecologically relevant structure, which has been defined in the literature in different manners (Zachos 2015): as a synonym of the flower-like structure of the five petals (Lang 1896, Nebelsick 2008), and, in a more expansive definition (Nebelsick and Kowalewski 1999, Grun et al. 2014), which includes both the ambulacral and interambulacral areas of the aboral surface determined by the outer margins of the five petals. The term petalodium has also been used describing a single petal of the flower-like structure (e.g. Ebert 1892, Schaffer 1962, Kroh 2002). The term petal is synonymized with a petaloid (e.g. Lang 1896, Nebelsick 2008, Lopes 2011). The petals can be differently pronounced within the petalodium and, together with the often longitudinal elongated test and

the migrated periproct, demonstrate the overprinted bilateral symmetry (e.g. Hyman 1955, Grun et al. 2016). In the following thesis and companioning manuscripts, the petalodium is used in its narrow sense describing the five ambulacral petals.

Although regular echinoids often show a poor fossil record (Kier 1977), irregular sea urchins, especially the clypeasteroids, can be well-preserved in fossil sediments (Fig. 7) (Michelin 1861, Lambert 1927, Kier 1977, Mitrović-Petrović 1984, Poddubiuk 1984, Rose and Poddubiuk 1987, Mooi 1989, Dixon and Donovan 1998, Nebelsick 1999a, Kroh and Nebelsick 2003, Kroh 2005, Tsaparas et al. 2007, Belaústegui et al. 2012a; b, Mancosu and Nebelsick 2013; 2015; 2017, Mooi et al. 2014, Rahman et al. 2015, Grun et al. 2017a; 2018). The strength of the clypeasteroid test has been attributed to the circumstances that they contain internal strengthening mechanisms such as plate interlocking (Fig. 8) and buttressing, which promote their preservation potential in both modern and ancient ecosystems (Grun and Nebelsick 2018; [1]; [3], Grun et al. 2018; [2]).

Figure 7. Fossil *Clypeaster* sp. (Neogene). Well-preserved and re-mineralized test. Internal supports (black arrows) and jaw-apparatus are *in situ* and intact. Origin: Wöllersdorf, Austria. Specimen photographed at the Natural History Museum Vienna, Austria

Clypeasteroida

The order Clypeasteroida includes around 150 living and 750 fossil species (Mooi 1989) which are typically characterized by well-depressed tests (Fig. 9) (e.g. Mortensen 1948, Durham 1955; 1966). These echinoids usually live partly or entirely infaunally (e.g. Mortensen 1948, Kier and Grant 1965, Durham 1966, Hendler et al. 1995). Test of the sand dollars are generally fairly flattened and often disc-like in their outline as seen in the genera (e.g.) *Arachnoides*, *Dendraster*, *Leodia* (Fig. 9F), and *Mellita*. Several sand dollars (e.g.) *Leodia*, *Mellita* are characterized by prominent lunulae (Fig. 9F), key-hole shaped apertures penetrating the test (e.g. Mortensen 1948, Durham 1966, Mooi 1989). The function of these lunulae have been discussed enhancing the hydrodynamic behavior of the echinoid when recovered from the sediment (Telford 1983). Other sand dollars, such as the genera (e.g.) *Echinodiscus*, *Encope*, and *Heliophora* (Fig. 9B, G) feature circumferential indentations in the test, which emphasizes the bilateral symmetry of these clypeasteroids. The genera *Clypeaster*, *Echinocyamus* and *Fibularia* (Fig. 9A, C) are more vaulted than the letter mentioned echinoids (e.g. Durham 1955). Many species within the genus *Clypeaster* are marginally flattened, but feature a central elevation of the test, under which the jaw-apparatus is located. The centrally vaulted form is seen in (e.g.) *Clypeaster humilis*, *Clypeaster Ravenelii*, *Clypeaster reticulatus*, *Clypeaster subdepressus* (Fig. 9D, E).

This thesis focuses on *Clypeaster rosaceus* and *Echinocyamus pusillus*, both of which demonstrate a unique morphological setup of structural reinforcement mechanisms, as well as a large fossil record, which together makes them promising candidates in both biomechanical and paleontological studies (e.g. Grun et al. 2018).

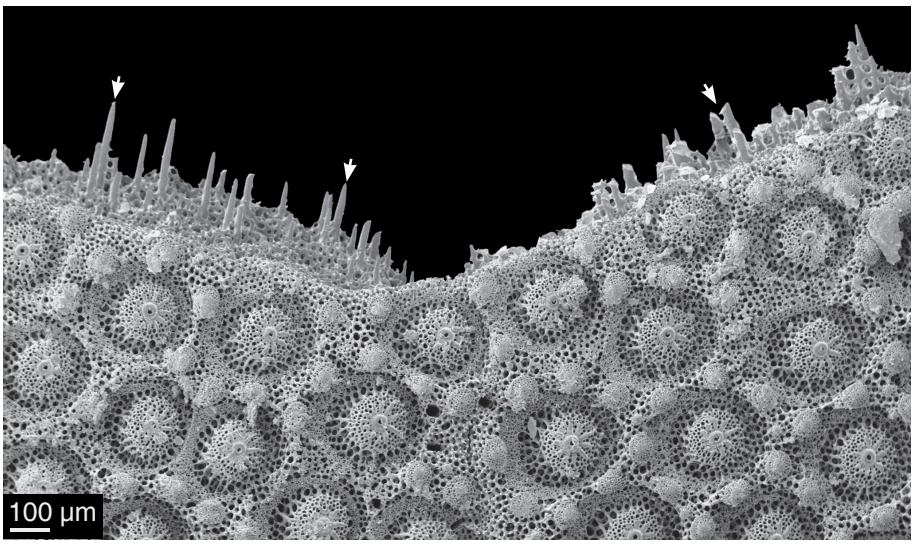

Figure 8. SEM micrograph of plate interlocking in the sand dollar *Dendraster excentricus*. Arrows indicate skeletal protrusions that reach from one plate into the stereom interspace of adjoining plates. Modified from Grun et al. (2017b)

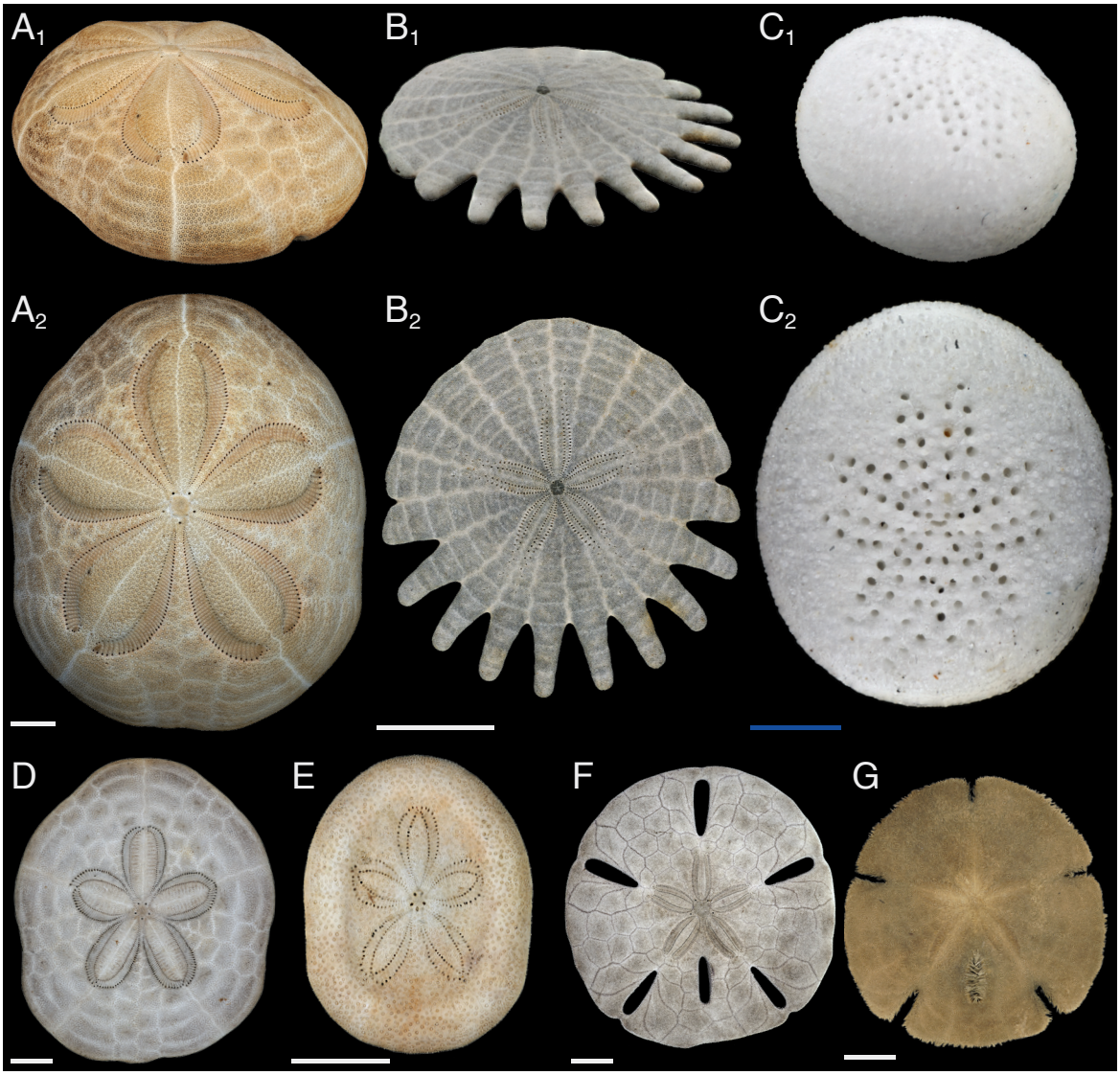

Figure 9. Diversity of clypeasteroid echinoids showing a definite bilateral symmetry. Oblique views emphasize the flatness of the clypeasteroid tests. (A1) *Clypeaster rosaceus* in oblique view. Test is dorsoventrally flattened though aborally vaulted. (A2) *Clypeaster rosaceus* in aboral view. Petalodium well-recognizable. Origin: Bahamas. (B1) *Heliophora orbiculus* in oblique view. Test fairly flattened. (B2) *Heliophora orbiculus* in aboral view. Posterior ambitus with notches. Single plates well-visible. Origin: Senegal. (C1) *Fibularia ovulum* in oblique view. Test is ovoid. (C2) *Fibularia ovulum* in aboral view, petalodium well-recognizable. Origin: Red Sea. (D) *Clypeaster humilis* in aboral view. Test is elongated and marginally flattened. The petalodium is elevated. Origin: Red Sea. (E) *Clypeaster reticularis* in aboral view. Test is elongated, the outer rim is inflated. The center is depressed, but the apical system is elevated. Origin unkown. (F) *Leodia sexiesperforata* in aboral view. Tests is fairly flattened and disc-shaped. Petalodium slightly elevated. Six lunulae penetrate the test. Origin: Bahamas. (G) *Encope michelini* in oral view with the minute spines still attached. The fairly flattened and disc-shaped test is elevated at the petalodium. Test with five notches at the ambitus and an anal lunula posterior to the apical system. Origin unknown. White scale bar = 1 cm, blue scale bar = 1 mm

Clypeaster rosaceus

Clypeaster rosaceus (Fig. 10) is one of the oldest known clypeasteroids and represents the genotype of *Clypeaster* (Mortensen 1948). The test is around 20 cm in length and covered by numerous elaborately ornamented, minute and blunt spines (Agassiz 1872, Mortensen 1948, Durham 1955; 1966, Mooi 1986c; 1989). The test is vaulted on the aboral side, and is fairly infundibulated on the oral side (Mortensen 1948, Durham 1966, Mihaljević et al. 2011, Grun et al. 2016; 2018). This echinoid is internally reinforced (Fig. 10C) by numerous pillars which connect the oral and aboral sides (Agassiz 1872, Mortensen 1948, Seilacher 1979, Grun et al. 2016; 2018). The pillars surround the jaw-apparatus and consist, as the remaining test, of multiple plates (e.g. Smith 1980, Grun et al. 2017b). The test of *Clypeaster rosaceus* is particularly reinforced by a calcareous layer on the inner surface (Fig. 10C), under which a branched canal system proceeds (Agassiz 1872, Mortensen 1948, Durham 1966, Grun et al. 2018). This skeletal layer separates the canals of the water-vascular system from the remaining body cavity, by only being connected to one another via several pores (Agassiz 1872, Schaffer 1962, Donovan 1991). This double-layer structure is part of the internal resilience system of several *Clypeaster* species (Donovan 1991).

Clypeaster rosaceus occurs in the Caribbean Sea, Gulf of Mexico and neighboring areas from shallow waters down to 285 m (Kier and Grant 1965, Kier 1975,

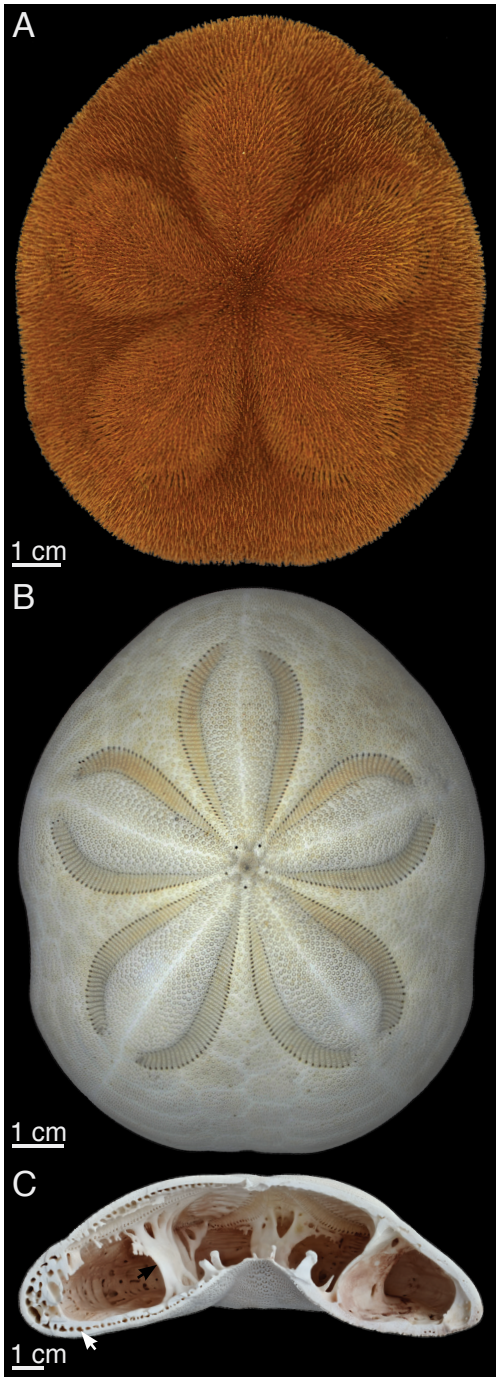

Figure 10. *Clypeaster rosaceus*. (A) Reddish skeleton is covered by minute spines. (B) Tests where spines are removed. Individual plates and the petalodium visible. (C) Lateral section. Internal supports (black arrow) bridge the oral and aboral side. Double-layer structure visible (white arrow). Modified from Grun et al. (2017b)

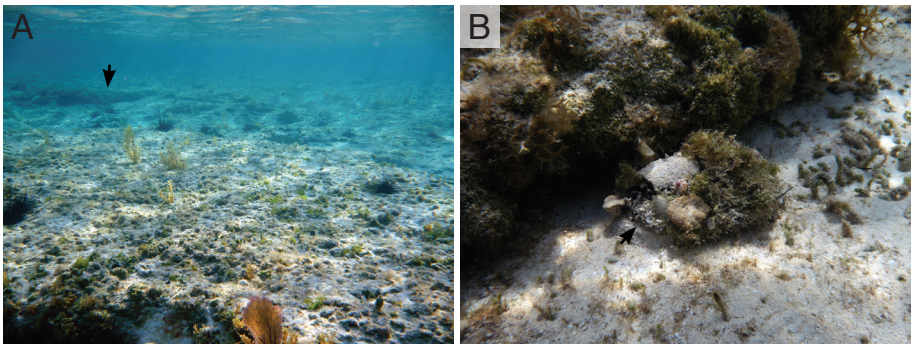

Figure 11. Habitat of *Clypeaster rosaceus*. (A) Sand pit (arrow) within an algae-dominated substrate at Fernandez Bay, San Salvador, Bahamas. (B) *Clypeaster rosaceus* (arrow) masking itself with algae, gravel, sediment and shells. Modified from Grun et al. (2017b)

Serafy 1979, Hopkins 1988, Alvarado and Solís-Marín 2013, Rodríguez-Barreras 2014, Hendler et al. 1995). This echinoid occurs in soft sediment realms of bare sand, sand patches, or sea grass meadows, where it predominantly lives epifaunally (Fig. 11) (Kier and Grant 1965, Moore 1966, Hendler et al. 1995), typically masking its reddish-brown body by available substrates including algae, coral gravel, shell fragments or small rocks (Fig. 11B) (Agassiz 1872, Nichols 1964, Kier and Grant 1965). Camouflage items are replaced on a nightly base enhancing the camouflage effect by being covered with local and currently surrounding materials (Nichols 1964, Kier and Grant 1965).

Echinocyamus pusillus

This minute echinoid is usually less than 20 mm in length (Fig. 12), dorsoventrally flattened and sub-circular to piriform in outline with the peristome slightly elevated (Fig. 12C) (Mortensen 1948, Ceranka and Złotnik 2003, Złotnik and Ceranka 2005, Grun et al. 2014, Grun and Nebelsick 2018). The test includes numerous skeletal reinforcement structures (Fig. 12C) (Mortensen 1907; 1927; 1948, Durham 1955, Nichols 1959, Telford 1985b, Grun and Nebelsick 2018; [3]). The most prominent resilience mechanism is the presence of a buttressing system (Mortensen 1948, Durham 1966, Telford 1985b, Grun and Nebelsick 2018, Grun et al. [2]). The buttresses are extensions of the interambulacral plates (Grun and Nebelsick 2018) and are restricted to the marginal areas of the test. Following the double-plate arrangement of the echinoid (Fig. 5C), the buttressing includes five double-wall buttresses. The ambulacral plates are furthermore thickened, resulting in horizontal ridges which have been discussed with respect to increasing the flexural stiffness of the test (Telford 1985b). Plates are additionally connected to one another in tight-fitting sutures, which lack stabilizing collagenous fibers (Telford 1985b).

The minute *Echinocyamus pusillus* is widely distributed in the northern hemisphere of the Atlantic Ocean, where it is documented around the Faroe Islands, Norway, British Seas,

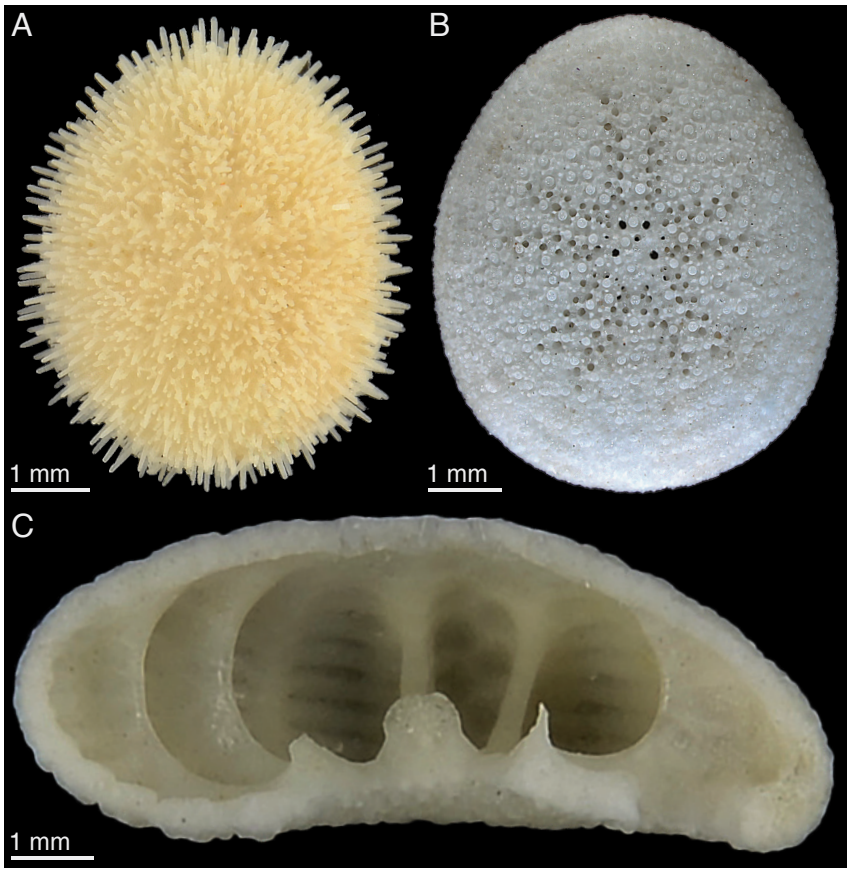

Figure 12. *Echinocyamus pusillus* from Giglio, Italy. (A) The minute skeleton is entirely covered by short spines. (B) The bright test is characterized by surface micro-structures. The petalodium is well-recognizable. (C) Buttressing is visible in lateral section (arrow). Modified from Grun et al. (2017b)

North Sea, European Atlantic coast, Azores, Mediterranean Sea, Madeira, and Cape Bojador at West Africa (Müller 1854, Agassiz 1872, Döderlein 1906, Mortensen 1907). This echinoid occurs from shallow waters (Fig. 13) down to 1250 m depth (Mortensen 1948), where it lives infaunally in various soft sediments ranging from silts (Döderlein 1906, Walther 1910) to sands (Nichols 1959; 1962, Ghiold 1982, Grun et al. 2014), and even shell-gravel (Nichols 1959; 1962). *Echinocyamus pusillus* thereby buries using both spines and tube-feet (Nichols 1959, Telford et al. 1983). In its natural habitat, this echinoid feeds on algae, debris, diatoms, foraminifers and particles covered by organic matters (Mortensen 1927, Telford et al. 1983). As a result of the small size, *Echinocyamus pusillus* can ingests single sand grains from which organic material can be digested (Telford et al. 1983).

Figure 13. Habitat of *Echinocyamus pusillus* at Campese, Giglio, Italy. Coarse sand flats are interspersed by *Posidonia oceanica* meadows (black arrow). Dark area (white arrow) is deep water not necessarily covered by sea grass

Morphological hierarchy

The echinoid skeleton follows a six-step hierarchy (Fig. 14) (Grun and Nebelsick 2018). Level 1 involves the echinoid as a whole including all skeletal elements, organic soft tissues and appendages. In this level, the echinoid is equipped with all structures necessary for being alive. Level 2 includes the denuded test, which encloses internal organs and serves as a platform for appendages. The test itself is build-up from numerous plates. Level 3 describes the single plates, jaw apparatus, and appendages such as spines, skeletal discs of the tube feet, and skeletal elements of the pedicellariae (e.g. Nebelsick et al. 2015, Grun et al. 2016, Grun and Nebelsick 2018). Level 4 represents the stereom, from which each skeletal element is formed. The stereom morphology also underlies variations according to its biological function (e.g. Smith 1980; 1990; 1984). Level 5 includes the trabeculae of the stereom. Level 6 describes the mineralogical level of the trabeculae consisting of high-magnesium calcite (Schmidt 1925, Raup 1965, Raup and Schwan 1967), which incorporates up to 0.2 weight % organic substances (Weber 1969, Emlet 1982).

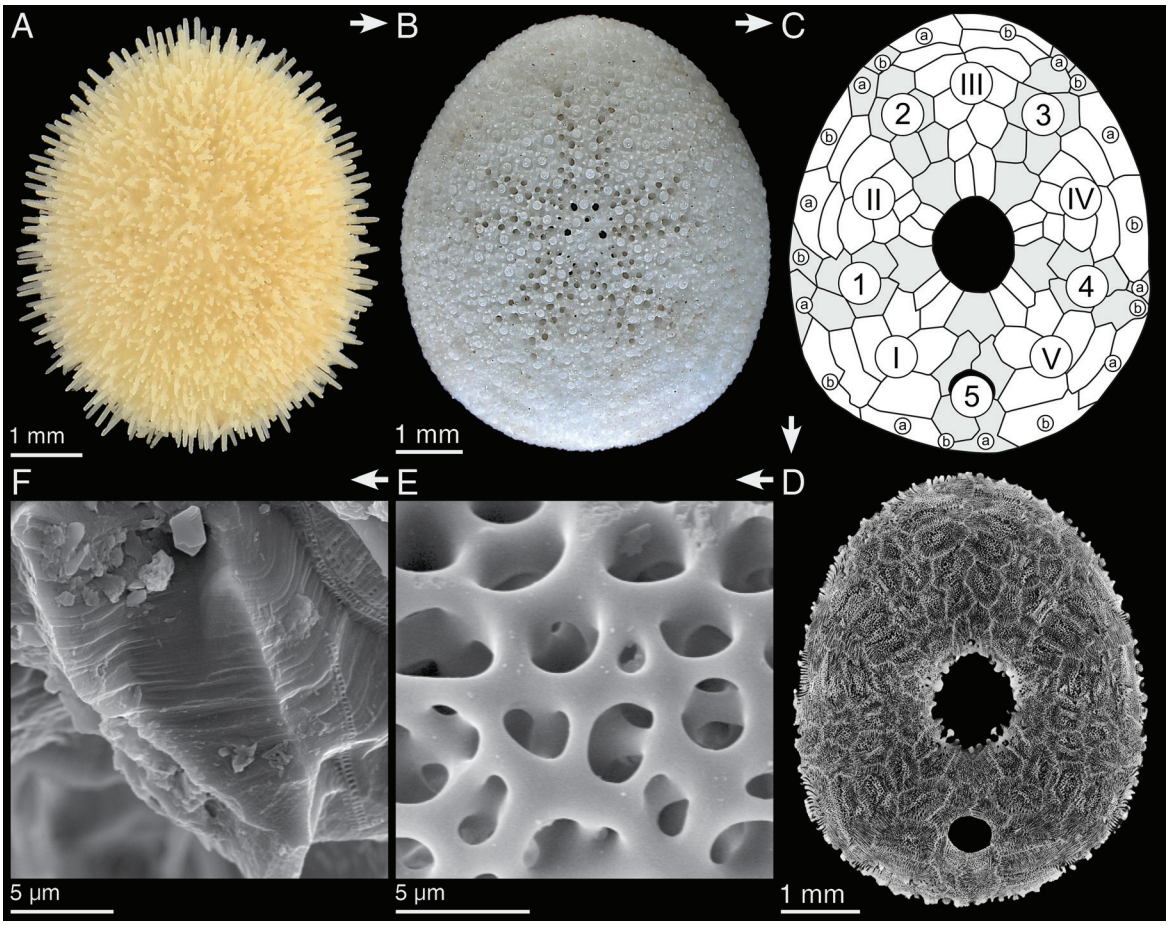

Figure 14. Hierarchical design of *Echinocyamus pusillus*. (A) Complete echinoid. (B) Denuded test. (C) Plate arrangement of the test. (D) Stereom architecture. (D) Trabecular arrangement. (F) Close-up of a broken trabecula.

Comparative loads on echinoids and buildings

Organisms and their remains are subject to various environmental loads (Fig. 15), some of which act continuously on the individuals, and some loads occur sporadically (e.g. Salvadori and Heller 1975, Grun and Nebelsick 2018). Forces can be categorized into static or dynamic loads, based on their occurrence (e.g. Salvadori and Heller 1975, Tamboli et al. 2000). Static forces are usually constant, where dynamic loads can change rapidly over time.

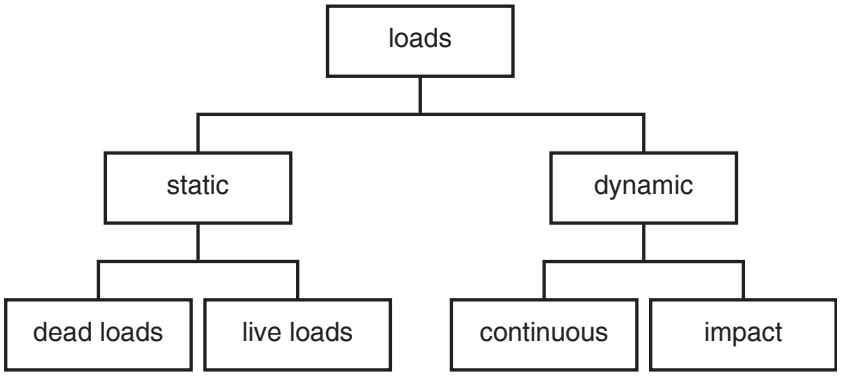

Figure 15. Load conditions that can act on both echinoids and building constructions. Modified after Salvadori and Heller (1975)

Dead loads

Dead loads are static loads defining the self-weight of a system. These loads are crucial for any structural analysis as they can represent the major load source and are permanently applied to the structure (Salvadori and Heller 1975). A constructional system is the sum of all permanently attached members such as floors, windows, ceilings, etc. (Salvadori and Heller 1975, Schodeck 1980). In the echinoid analogues, dead loads are the universe of all organic and inorganic structures produced by the individual such as the skeleton and soft tissues including the digestive tract, gonads, etc.

Live loads

These static loads can change over time and alter within a certain and often predictable amplitude. The magnitude of change is generally minor (Salvadori and Heller 1975). Typical live loads in building construction are persons, interior or seasonal loads such as snow or water accumulations on surfaces (e.g. Salvadori and Heller 1975, Schodeck 1980). Live loads in echinoids can be materials which are used for masking such as algae, coral gravel, shells (Fig. 11B) (e.g. Lewis 1958, James 2000), epibionts (e.g. Telford 1982, Queirotz et al. 2011), gut content (e.g. Telford et al. 1987, Mooi and Chen 1996), the sediment in which they

burrow (e.g. Chia 1969, Ghiold 1982) or the encountered water pressure.

Post-mortem encrustations (Fig. 16), such as epibionts, and fouling organisms, can become important stressors (e.g. Belaústegui et al. 2012b, Grun and Nebelsick 2016). Although the echinoid test is neither designed nor intended to carry such loads, it can usually carry the additional loads caused by the encrusters. Encrustation does not only increase the magnitude of live-loads, but can also increase the test stability as additional material is added, which can cross the sutures (Grun and Nebelsick 2016).

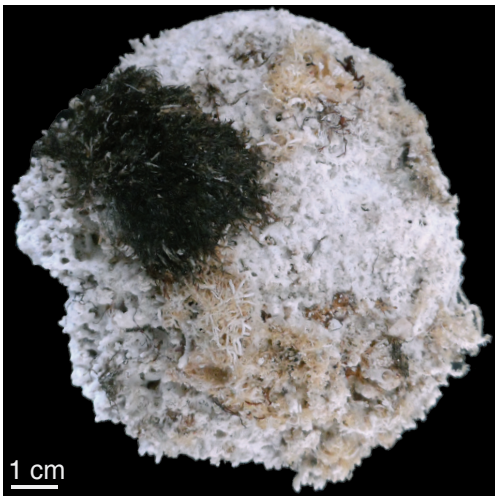

Figure 16. *Clypeaster rosaceus*, entirely fouled by calcareous and soft algae. Test collected at Fernandez Bay, San Salvador, Bahamas

Thermal loads

Thermal load are static loads in which structures contract or expand due to changes of temperature (e.g. Tamboli et al. 2000). Material contractions or expansions are typically slow and occur in low magnitudes, even during seasonal changes when temperature differences are largest (e.g. Salvadori and Heller 1975). The slightest variations in structural length due to material contraction or expansion can, however, cause high stress resultants when expansion joints are lacking. Such thermal effects are well-known from bridges that require roller supported bearings with expansion joints (e.g. Salvadori and Heller 1975). Building constructions underlie thermal stresses, when the sun exposed site warms up while the shaded part remains cool. Thermal induced loads probably play a minor role in the echinoid skeleton as changes in water temperatures in marine environments are typically minor due to a continuous water agitation. Diurnal changes are also low as a result of to the energy storage capacity of water. This is particularly the case for the infaunal living irregular echinoids, where water exchange with the environment is reduced by the sediment (Fig. 17).

Figure 17. Infaunally living *Meoma ventricosa* (Spatangoida, irregular echinoid), partly recovered from the sediment. Sand shielding the echinoid from direct sunlight

Continuous loads

Continuous loads are dynamic loads that occur in building constructions in form of wind, and in some regions, earthquakes, etc. (e.g. Schodeck 1980). These loads, unlike static loads, are uncontrolled in their amplitude and might occur unexpectedly though periodically. In the echinoid environment, such loads can be represented by wave action, currents (Fig. 18) and sediment agitation which are always present, but can change rapidly in their magnitude such as during storms, submarine earthquakes, etc.

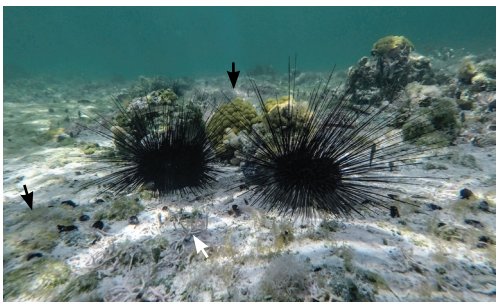

Figure 18. *Diadema antillarum* at Pigeon Creek, San Salvador, Bahamas. Daily tides cause strong currents indicated by the presence of flat-growing, non-branching algae, and corals (black arrows), as well as the accumulation of fragmented more delicate organisms (white arrow)

Impact loads

Impact loads are dynamic loads which typically occur unexpected, in an extreme magnitude and often singularly. These events can cause extensive damage and structural failure of a system (Fig. 19). Impacts in building constructions are typically related to natural disasters or in form of teardowns. In marine environments, impacts on echinoid tests are not uncommon as predators regularly crush the echinoid skeletons under total test failure (Fig. 19) and feed upon their soft tissues (e.g. Chesher 1969, Sala 1997, Gianguzza et al. 2009, Young and Bellwood 2012, Sievers et al. 2014, Grun 2016, Sievers and Nebelsick 2018).

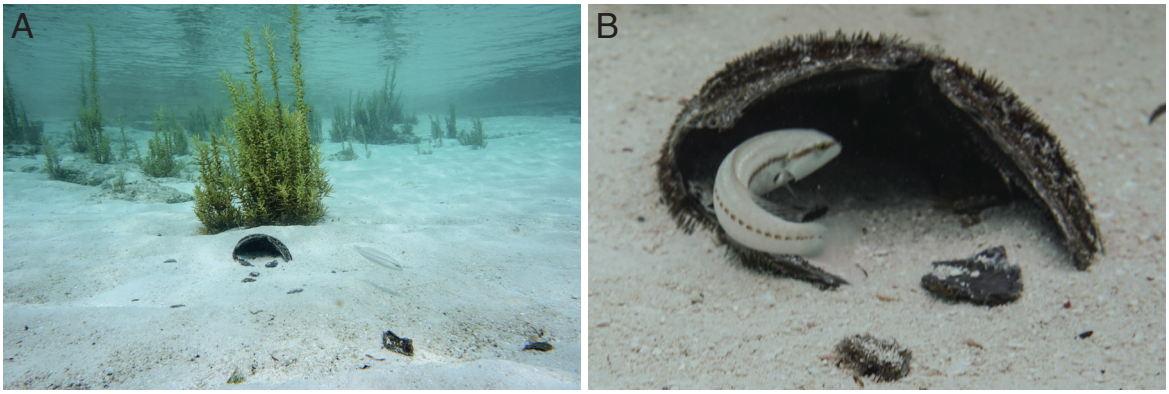

Figure 19. Crushed *Meoma ventricosa* (Spatangoida, irregular echinoid) after a predatory attack. (A) Partly buried test in shallow water environment at Sand Dollar Beach, San Salvador, Bahamas. (B) The broken tests can function as habitat for fish and other marine life

Objectives

Naturally segmented shells are important for biology, paleontology and engineering sciences for different reasons (Fig. 2) (e.g. Grun et al 2016; 2017b). The echinoid skeleton or their skeletal fragments are often preserved in the fossil record (e.g. Złotnik and Ceranka 2005, Dynowski 2012, Belaústegui et al. 2012; 2013, Rahman et al. 2015, Grun et al. 2017a; 2018). During the processes of fossilization, these skeletal hard parts are subject to various alterations such as abrasion, disarticulation, fragmentation, bioerosion and encrustation (e.g. Wilson 1988, Kidwell and Bosence 1991, Hageman et al. 2004, Hauser et al. 2008, Belaústegui et al. 2012a; b). Taphonomic modification of skeletons or their fragments occur as a result of specific environmental condition and can, when recovered from the sedimentary record, be analyzed in order to interpret the respective environments (Davies et al. 1989, Nebelsick 1999a, Kroh and Nebelsick 2010, Grun et al. 2017a). Even though the smallest skeletal fragments can provide information about the environmental conditions, complete echinoid shells are of highest interest as these structures can record biotic signals such as predatory, parasitic, and symbiotic traces (e.g. Nebelsick 1999a; 2008, Złotnik and Ceranka 2005, Rahman et al. 2015, Grun et al. 2017a) that might be lost during fragmentation. Understanding the structural mechanisms of shell strengthening and their ability to resist stress can provide an additional parameter to be correlated to environmental conditions.

The structurally relevant mechanisms that lead to a multi-plated, though stable test can be furthermore used in engineering sciences for the development of segmented light-weight constructions (Grun et al. 2016; 2017b). The aim of this thesis is the analysis of structural mechanisms responsible for the skeletal strength of the clypeasteroid tests and the mechanical principles beyond these structures. The focus predominantly lies on the study of plate arrangement, plate connection, internal supports, stereom distribution, and stereom microstructure of tests of *Clypeaster rosaceus* and *Echinocyamus pusillus*. The results are discussed with respect to the implication for biology, paleontology and engineering sciences. Although this thesis concentrates on the structural design and consequently structural mechanics of the clypeasteroids' tests, a dedicated development and optimization of engineering strategies or building components is not part of this work.

Results and discussion

This section provides an overview and discussion of the results obtained during this thesis. Results include, but are not restricted, to findings presented in the companioning manuscripts. For a detailed introduction and in-depth discussion please consult the respective manuscripts.

Clypeasteroids in architecture and building constructions

Technical shell constructions are in the focus of architectural and engineering sciences as they feature advantageous mechanical performance over non-shell constructions (e.g. Tamboli et al. 2000, Schodeck and Bechthold 2015, Grun et al. 2016). Especially thin-walled shell systems, where membrane actions dominate, are of high interest since membrane actions result in compressive and tensile forces, where bending is nearly absent. The reduction of bending moments allows for even thinner-walled and thus lighter-weight shell constructions (e.g. Schodeck and Bechthold 2015).

Conventional monolithic shells are economically challenging, since they require intensive framework during the construction process is time and material consuming (e.g. Grun et al. 2016). These monolithic constructions have thus been widely replaced by lattice systems, whose surfaces are covered by planar elements. Lattice or grid constructions, however, neither reach the architectural elegance of monolithic and double-curved constructions, nor resemble their structural performance (Malek et al. 2014, Grun et al. 2016).

A promising solution to counter the disadvantages of both the uneconomical deployment of monolithic shells, as well as the structural deficit of lattice systems, is the development of segmented shell constructions (Grun et al. 2016). Single modules of the shell structure can be pre-fabricated in manufacturing halls where environmental conditions such as light, temperature, humidity, etc. can be controlled. In on-site construction, the pre-fabricated module assemblage requires much less intensive framework and are thus more economical. Segmented shell systems, however, suffer in some structural aspects. One of the major problems is the connection of the individual modules, which is a general problem in segmented systems (e.g. Grun et al. 2016). Another important factor for the overall integrity of segmented shell constructions is the arrangement of the individual modules.

The multi-plated and light-weight tests of clypeasteroid echinoids have been shown to be promising role models for the improvement of technical segmented shell constructions

(Grun et al. 2016, Grun and Nebelsick 2018). Tests of clypeasteroid echinoids are found in large numbers and often articulated in both recent environments and the fossil sedimentary record (e.g. Grun et al. 2014; 2016; 2017a; 2018, Grun and Nebelsick 2015; 2016). The fossil echinoids thereby survived the often complex taphonomic pathways, yet still commonly feature an intact test (Grun et al. 2018). The high stability and the potential of being found in the fossil record make these echinoids interesting for both paleontology and engineering sciences and are thus in the focus of biomimetic research (Grun et al. 2016; 2018).

The test of clypeasteroids do not resemble a technical shell construction where bending is widely reduced (e.g. Telford 1985b, Grun et al. [2]). The plate-interlocking mechanisms, as well as the general test design and the plate arrangement, possess the potential to improve such technical shell systems. The structural principles which lead to the high preservation potential are thus analyzed as the basis for technical improvements for segmented technical shell constructions, where tests of *Clypeaster rosaceus* and *Echinocyamus pusillus* have now being given full consideration as candidate structures for these biomimetic research.

Load model

A crucial part of the mechanical interpretation of structures is the understanding to what loads constructions are exposed. It is, however, unrealistic to cover all possible load conditions under all possible circumstance. The following load model has been developed for *Echinocyamus pusillus* in the awareness of incorporating only general and relevant loads for clypeasteroids. *Echinocyamus pusillus* lives infaunally (Fig. 20) (Döderlein 1906, Nichols 1959; 1962, Ghiold 1982, Telford et al. 1983), in which the buried echinoid is covered by a water saturated sediment layer. This sediment causes downward forces that impinges the echinoid skeleton perpendicularly (Fig. 20B) (e.g. Gordon 1978). Depending

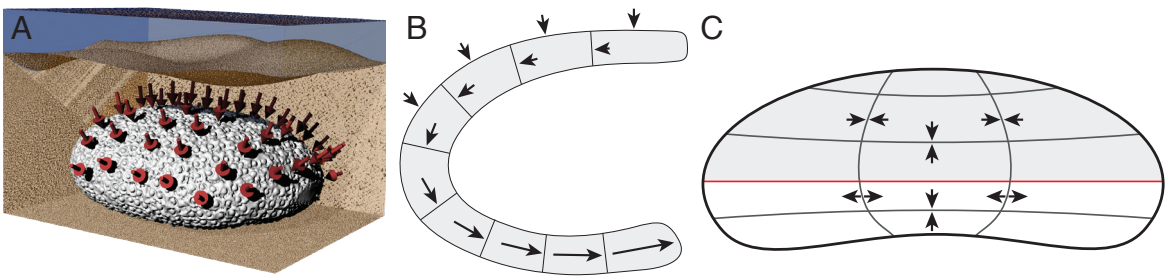

Figure 20. Load model for *Echinocyamus pusillus*. (A) The infaunal living echinoid is covered by a sediment layer which causes downward forces (red arrows). (B) Part of the test in lateral view. External arrows indicate downward stress that turns into lateral thrust within the plates. (C) Sketch of *Echinocyamus pusillus* in lateral view. Radial lines indicate radial stress, horizontal lines represent circumferential stress. The red line indicates the ambitus. Modified from Grun and Nebelsick (2018)

on the depth to which an clypeasteroid buries, the downward force that act on the skeletons vary. An example is given by the inflated irregular echinoid *Meoma ventricosa* (order Spatangoida) is covered by a quite thin sediment layer where, at times, the petalodium can be visible from above the sediment (personal observation, San Salvador, Bahamas 2015; 2017). The fairly flattened sand dollar *Leodia sexiesperforata* IS found buried a few centimeters underneath the sediment surface, never exposing the petalodium to the surface during life (personal observation, San Salvador, Bahamas 2015; 2017). The resulting downward forces can thus be different in their magnitudes due to the different depths of burrow. Additionally, the mineralogical composition of the sediment determined the specific density and weight per unit. Similarly, the sea water chemistry, particularly the salinity and temperature, determines the water's buoyancy following the Archemedian principles (Heath 1897, Wilde et al. 1970), which affects the downward forces.

The downward forces of the sediment are turned into lateral thrust in the echinoid skeleton and follow the arched-shape of the test (Gordon 1978, Telford 1985a). Resulting circumferential stresses are compressive despite their position in the test, where radial stresses above the ambitus are compressive, but become tensile below the ambitus (Fig. 20C) (Philippi and Nachtigall 1996).

Plate interlocking

Previous work on the clypeasteroids' plate connecting mechanisms have indicated that plate interlocking can contribute to the over-all test integrity (Seilacher 1979, Smith 1980, Telford 1985a; b). In-depth examinations using SEM and 3d µCT analysis resulted in the recognition of distinct interlocking types (Grun and Nebelsick 2018). The first interlocking mechanism is based on the shape of the echinoid plates (hierarchical level 3), which are arranged in a mosaic and off-set to one another (Fig. 21). This plate arrangement inhibits in-plane displacement of the plates within this mosaic. The plates

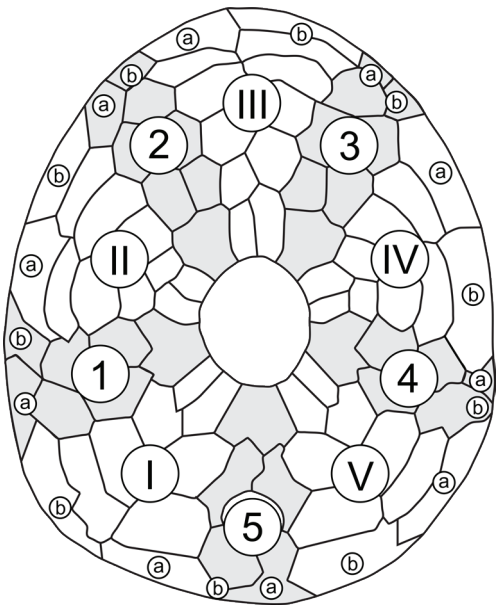

Figure 21. Mosaic of interlocking plates in *Echinocyamus pusillus*. Terminology following Lovén (1874)

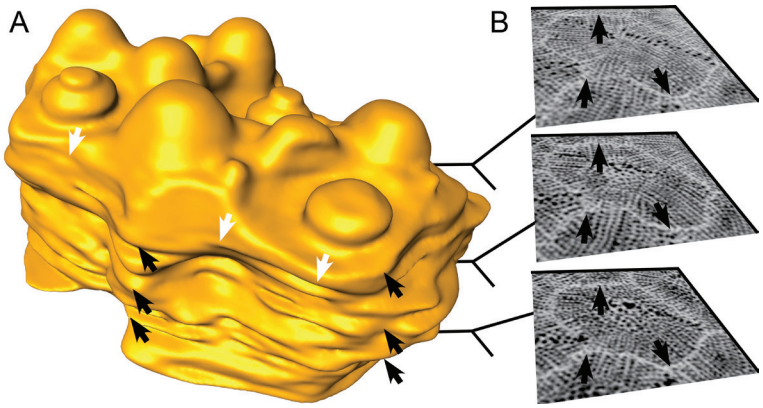

Figure 22. Sutural interlocking in *Echinocyamus pusillus*. (A) 3d surface rendering of a plate. Plate margins show a sinuous path which interlocks with adjoining plates. White arrows indicate the sinuous course in horizontal plane, black arrows in lateral direction. (B) Micro-CT sections of the segmented plate showing the different plate outlines at three intervals. Arrows correspond to black arrows in (A). From Grun and Nebelsick (2018)

themselves are furthermore vertically irregularly curved at their sutural faces (Fig. 22). This three-dimensional irregularity results in a complex spatial interlocking pattern between adjoining plates and is hence designated as sutural interlocking (Grun and Nebelsick 2018).

The second type of plate interlocking is recognized on a lower hierarchical level 5. The galleried stereom at the plate margins is highly ordered (Grun and Nebelsick 2018), meeting the statures in a perpendicular manner (Fig. 23). This constellation results in a stereom alignment in which the trabeculae of one plate is abutted to the stereom interspace of a neighboring plate. The single trabeculae then protrude from one plate into the stereom interspace of an adjoining plate thus securely interlocking both plates to one another (Fig. 23C, D). This interlocking can be promoted by the presence of collagenous fibers which additionally connects the plates via the stereom interspaces. The additional reinforcement by collagenous fibers is, however, exclusively restricted to living echinoids, as soft tissues decay rapidly after the death of an individual (e.g. Nebelsick and Kampfer 1994). Plates in *Echinocyamus pusillus* lack such a collagenous reinforcement during life (Telford 1985b) indicating that the test strength predominantly relies on the structural design of the skeleton itself (Grun and Nebelsick 2018, Grun et al. [2]). The interlocking type, where trabeculae reach from one plate into another plate is designated as trabecular interlocking (Grun and Nebelsick 2018). In *Echinocyamus pusillus*, trabecular interlocking is present in three types (Telford 1985b, Grun and Nebelsick 2018): the most prominent trabecular interlocking is recognized where long trabecular protrusions penetrate deeply into the stereom interspace of adjoining plates (Fig. 23C, D). The second type is a knob-like interdigitating where trabecular protrusions are short and do not penetrate into the opposing stereom interspace (Fig. 23F). This type of interlocking is commonly present when the stereom interspace of an adjoining plate is too narrow for trabecular penetration. This is often the case in the sutures of the buttresses, especially in the distal areas where the supports are

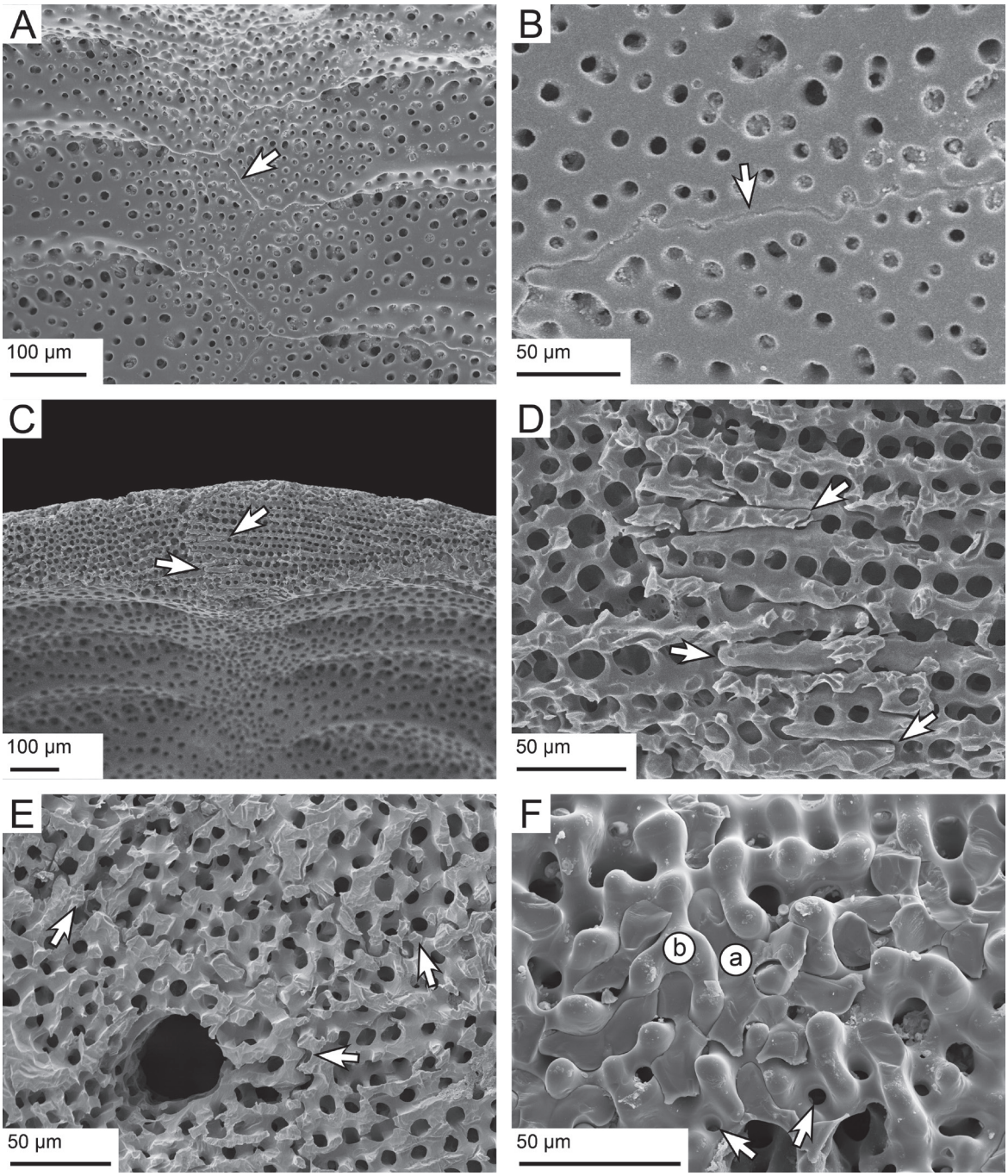

Figure 23. SEM micrographs of plate joints in *Echinocyamus pusillus*. (A) Sinuous course of sutures within a perradial boundary. (B) Sutural interlocking in detail. Knobs reaching from one into another plate, thus strengthen the interlocking. (C) Trabecular interlocking at a thickened perradial suture. (D) Trabecular interlocking in detail, where trabeculae from one plate protrude into the stereom interspace of an adjoining plate. (E) Sutural interlocking in a 3d mosaic of surrounding plates. Arrows indicate plate boundaries. (F) Orthogonal view onto a suture. Fractured trabeculae are attached and penetrate into the interspace of another plate, a and b indicate the affiliation of the involved plates. Arrows indicate narrow depressions for knob-like interlocking. From Grun and Nebelsick (2018)

thin and of high stereom density. The third type of trabecular interlocking is well-recognizable on the plates' surfaces. Single trabeculae bridge the sutures and fuse into another trabecula of the adjoining plate. Such trabecular fusions are rare, but recognizable from different areas of the test (Grun and Nebelsick 2018).

In the test of *Echinocyamus pusillus*, radial sutures are additionally thickened. The sutural thickening has been discussed with respect their function as additional buttresses that increase the test strength (Telford 1985b). The thickening furthermore increases the interface area between two plates thus promoting a more intensive interlocking and consequently strengthen the test (Fig. 23C) (Grun and Nebelsick 2018). The interlocking mechanisms revealed from *Echinocyamus pusillus* together with the sutural thickening is considered to behave as a monolithic construction, since the single plates are thus intensively interconnected that the sutures are barely weaker than the plates. This is furthermore supported by the examination of high-speed videos in which tests of *Echinocyamus pusillus* have been point-loaded until total structural failure (Fig. 24). Footages show that cracks proceed through both the plates and the sutures, indicating the sutural strength.

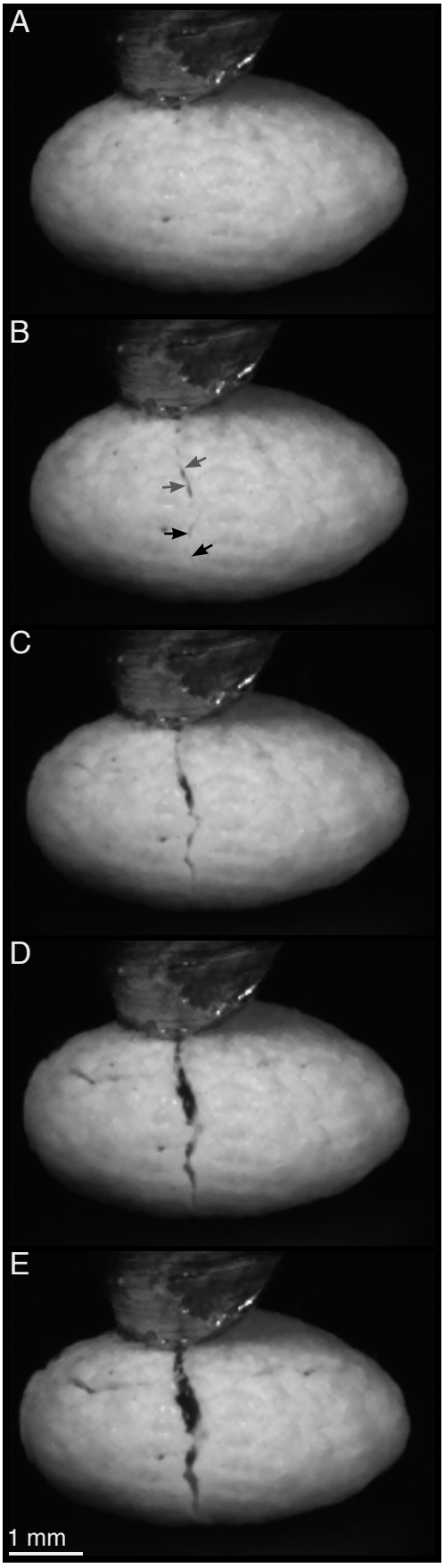

Figure 24. Crushing behavior of *Echinocyamus pusillus*. Point load is applied from above and is successively increased from (A) towards (E). (A) shows the test intact. (B) Crack start occurring. (C) – (E) Crack progression. Fracturing occurs along the sutures (black arrows) and through the plates (gray arrows)

Internal supports

Clypeasteroid echinoids, excluding family Fibulariidae, are characterized by internal supports, which bridge the oral and aboral side of the test (Mortensen 1948, Durham 1966, Mooi et al. 2014). Four types of internal supports have been identified (Fig. 25), which also correlate with the flattening of the test (Durham 1955). The first type is a pillar system found in e.g. *Clypeaster rosaceus* (Fig. 25A). These pillars are arranged around the jaw-apparatus and can be fused to thin walls. In more flattened forms, such as *Clypeaster humilis*, the pillars are still present in the center of the test, but turn into a wall-system in the flattened marginal areas. The second type is a buttress system, found in e.g. *Echinocyamus pusillus* (Fig. 25B). The buttresses are elongations of the interambulacral plates reaching from the auricles towards the outer regions of the petalodium. Following the pentamerous double-columns layout of the echinoid, the buttress system is present in five radial double-walls, or radial partitioning (Agassiz 1874). The third type is a wall-system found at the margins of e.g. *Jacksonaster depressus* (Fig. 25C). This support system involves both ambulacral and interambulacral plates, the latter of which follows a prominent radial partitioning, whereas the ambulacral supports run circumferentially. The fourth type resembles a branched meshwork of thin walls (Fig. 25D). This type is typically found in the fairly flattened sand dollars, such as *Arachnoides*, *Dendraster*, *Leodia* and *Mellita*.

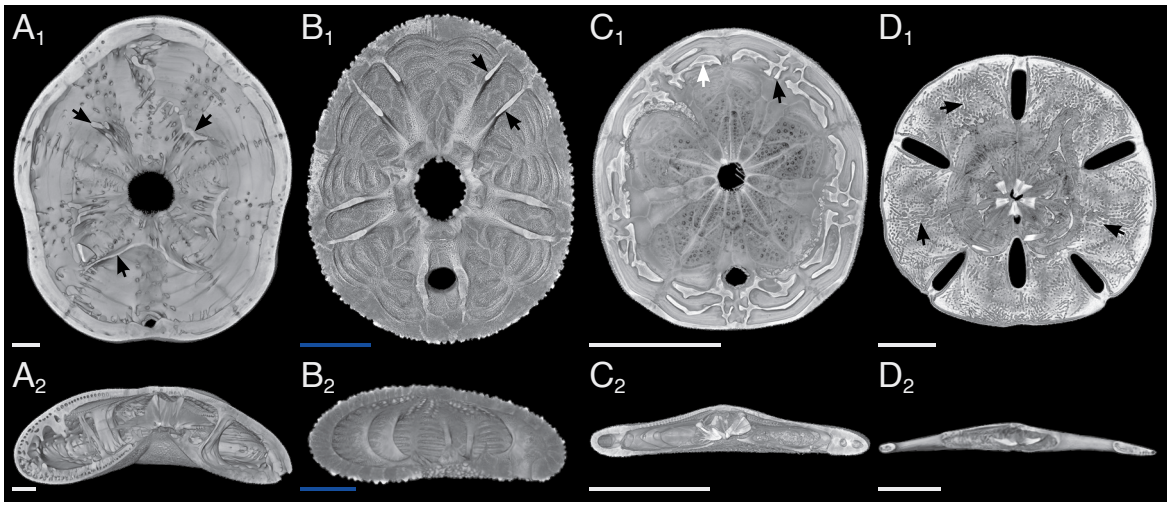

Figure 25. Micro-CT renderings of clypeasteroids in horizontal (A_1-D_1) and lateral (A_2-D_2) sections showing the internal supports. (A_1) *Clypeaster rosaceus*, supports are in the form of pillars or large walls (arrows). (A_2) The test is faulted on the aboral side and elevated on the oral side. (B_1) *Echinocyamus pusillus*, internal supports are in the form of interambulacral buttresses (arrows). (B_2) The test is faulted on the aboral side, and slightly elevated on the oral side. (C_1) *Jacksonaster depressus*, supports are in the form of marginal and branched walls. Supports in the ambulacralia are circumferentially arranged (white arrow), supports in the interambulacralia are radially arranged (black arrow). (C_2) The test is marginally flattened and elevated towards the center of the aboral side. The oral side is slightly elevated. (D_1) *Leodia sexiesperforata*, supports are in the form of a wall-like meshwork (arrows). (D_2) The test is fairly flattened, slightly elevated towards the center of the aboral side. The oral side is nearly planar. White scale bar = 1 cm, blue scale bar = 1 mm

Structural significance of internal supports

Finite element analysis of the tests of *Echinocyamus pusillus* revealed that internal supports are of high structural significance (Grun et al. [2]). This has been tested by comparing two finite element models to one another (Fig. 26). The one voxel-model still contained the internal buttresses (Fig. 26A), where in the other model, the buttresses were virtually removed (Fig. 26B). Results show that both the compressive as well as the tensile forces in the test system increased in the model where the supports were removed (Fig. 26B). The removal of internal buttresses also resulted in the occurrence of high circumferential stresses around the peristome. These findings indicate that the buttresses in *Echinocyamus pusillus* possess a load bearing capacity which reduces compressive and tensile tresses at the ambitus as well as large tensile circumferential stresses (Grun et al. [2]).

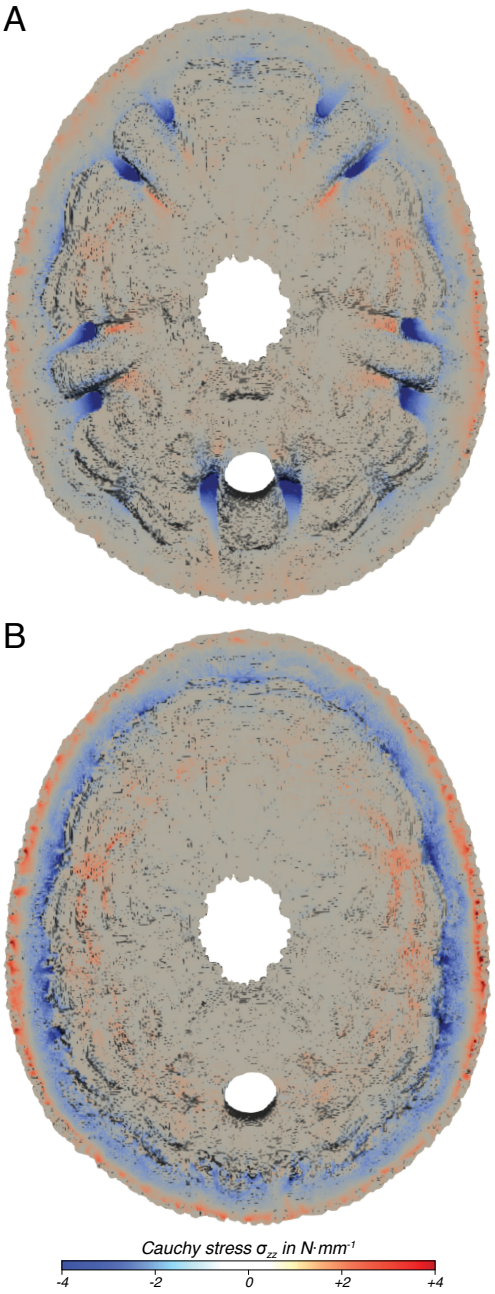

Figure 26. FE analysis on a voxel model of Echinocyamus pusillus. (A) Model with the internal supports intact. Areas of high stresses are mainly restricted to the buttresses. (B) Model in which the buttresses have been virtually removed. Stress is present on the inner surface (blue) and the outer surface (red) of the ambitus. Modified from Grun et al. [2]

Physical crushing experiments of the tests of *Echinocyamus pusillus* support the results of the finite element analysis. In the physical crushing experiments, 30 tests of *Echinocyamus pusillus* has been analyzed in three treatment groups: treatment group 1 included specimens where both organic tissues and the buttress system where present. Treatment group 2 included specimens where the organic material has been removed by a sodium hypochlorite bath. Treatment group 3 included specimens where both the organic material as well as the internal supports have been removed. First, the three treatment groups were statistically tested for the test length avoiding biases due to differences in test length

and hence the load carrying ability (Grun et al. [2]). Second, the tests were examined for their load carrying capability by uniaxial compression tests. Results show that the organic tissues do not significantly increase the test strength. A comparison between the treatment group 1 and 2 (tests with internal supports present and tests with internal supports removed) showed, that the internal supports significantly account for the test strength (Grun et al. [2]).

Stereom differentiation

The echinoid stereom has been previously classified into ten types (Smith 1980). Plates of the clypeasteroids *Clypeaster rosaceus* and *Echinocyamus pusillus* are analyzed using µCT and SEM techniques. The plates of both echinoids show a similar basic layout with an unordered labyrinthic stereom in the center and an ordered stereom at the plate's margin (Fig. 27) (Smith 1980, Grun and Nebelsick 2018; [1]). The volumetric analysis based on µCT micrographs shows that the labyrinthic stereom at the plate's center is on average of higher material density than the galleried stereom on the plate's margin (Fig. 27B, C) (Grun and Nebelsick 2018). The sutural areas, where intensive trabecular interlocking occur is of highest material density. This is, however, not surprising as trabecular protrusions of the galleried stereom reach into and thus fill the stereom interspace of the adjoining plate (Fig. 23D). The stereom density show a high variation in the buttress system of *Echinocyamus pusillus* (Fig. 28), where the proximal areas are accounts for 83.3% of stereom, and the distal area accounts for 92.0%. The high stereom density at the distal buttress area implies that the stereom interspaces are narrow thus prevent intensive trabecular interlocking between the buttress segments. Variations in the stereom density can

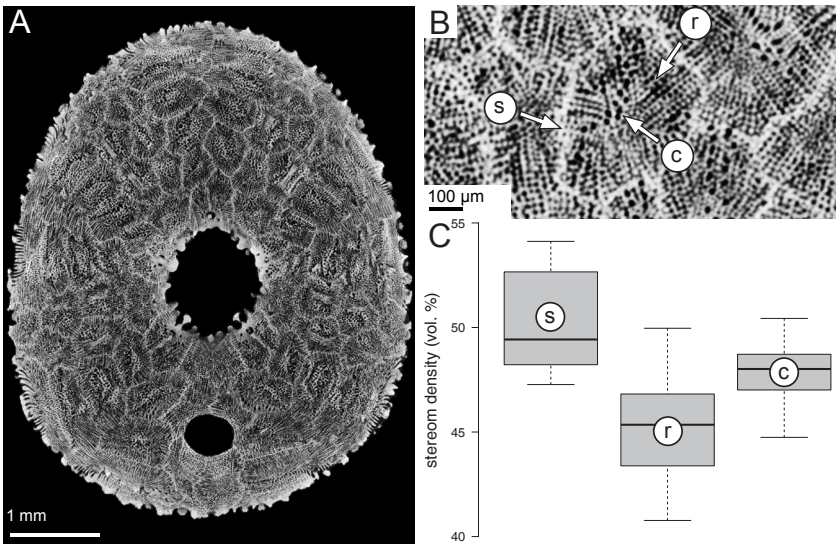

Figure 27. Stereom densities in plates of *Echinocyamus pusillus*. (A) Micro-CT section of the oral side providing an overview of the stereom differentiation. (B) Close-up of plates indicating three distinct regions of the plate. (C) Comparison of stereom densities between three plate regions. c = unordered labyrinthic stereom at the plate's center, r = directional galleried stereom at the plate's rim, s = directional galleried stereom within sutures. From Grun and Nebelsick (2018)

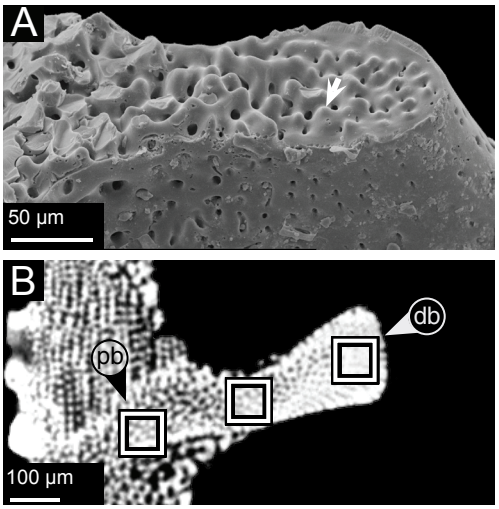

Figure 28. Buttresses in *Echinocyamus pusillus* showing the material density distribution. (A) SEM micrograph of a buttress suture. Segments are interconnected by knob-like structures (arrow). (B) Micro-CT section. Rectangles indicate areas of volumetric comparison. db = distal buttress, pb = proximal buttress. From Grun and Nebelsick (2018)

render the test stiffer or stronger. Stiffer structures usually attract and channelizes forces, whereas strengthened structures are induced by high forces. Finite element analyses applied on the test of *Echinocyamus pusillus* shows the mechanical effect of the variations in stereom density (Fig. 29) (Grun et al. [2]). Two voxel-models based on µCT scanning were generated, one of which possesses a homogeneous material distribution (Fig. 29A), and the other model possesses a heterogeneous material distribution (Fig. 29B). When the two models are under load, the stress resultants are similar in their magnitudes. The similar stress response on the load carrying behavior indicates that the material distribution in the test is less significant for the load-bearing behavior than the geometrical layout of the test. It is, however, important to recall that higher material densities at the sutures possess a structural effect: the plate interlocking mechanism, that leads to higher material densities at the sutures, results in a monolithic load carrying behavior of the test and is thus of high structural significance (Grun and Nebelsick 2018), although the higher density at the sutures (as a material parameter) has no significant effect such as functioning as a load carrying grid construction.

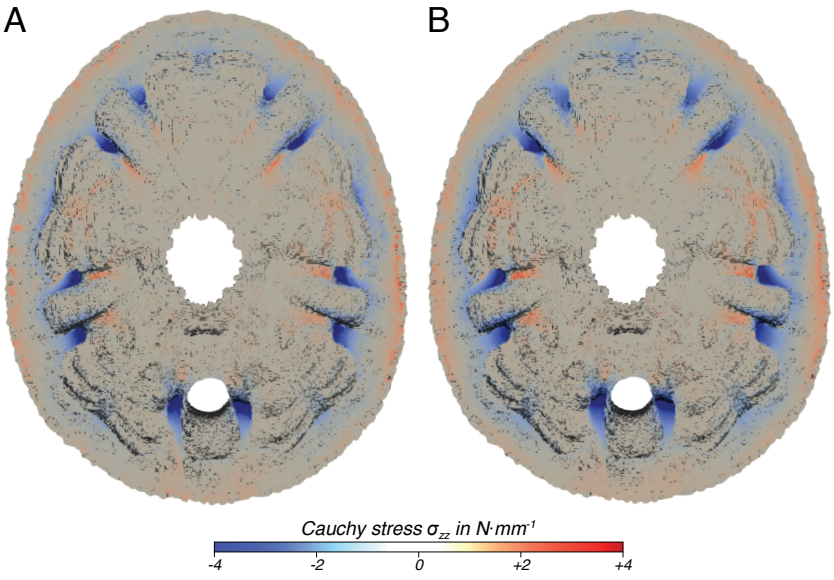

Figure 29. FE analysis of a voxel-model with different material densities. (A) Model with a heterogeneous material distribution, reflecting the true material distribution in the test. (B) Model with a homogeneous material distribution. Stresses in both models are similar, irrespectively of the material density distribution. Modified from Grun et al. [2]

Trabecular system

The echinoids trabecular system represents a micro-beam construction of calcareous struts (Fig. 30). Although the trabecular system has been intensively analyzed with the advent of scanning electron microscopy (Smith 1980; 1984; 1990), the 3d architecture of this system is hitherto practically unknown though essential to understand its structural function. The micro-architecture and the spatial design of the trabecular system is now analyzed in-depth for the first time using µCT techniques and a custom written R code (R Core Team 2017, Grun and Nebelsick [1]). In total, eight trabecular descriptors have been defined and used to analyze the trabecular architecture and topology of *Echinocyamus pusillus*. In the following section, the most important findings, including the inter-trabecular angle and the orientation of the trabeculae, are discussed.

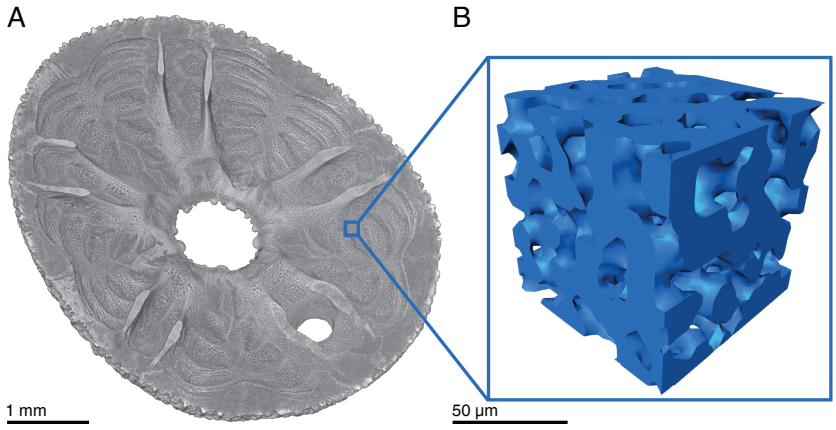

Figure 30. 3d rendering of Echinocyamus pusillus. (A) horizontal section of the test. (B) Subvolume of the stereom with an edge-length of 90 µm. Modified from Grun and Nebelsick [1]

Trabecular orientation

Echinoid plates can be subdivided in two regions, the center which is made from an unordered labyrinthic stereom, and the margins, which is made from an ordered galleried stereom (e.g. Smith 1980, Lawrence 1987, Grun and Nebelsick 2018). The unordered labyrinthic stereom is capable of resisting multi-directional stresses, where the ordered labyrinthic stereom is capable to distribute stresses along the entire test (Smith 1984, Lawrence 1987). These two plate regions have been also identified from µCT scans of *Echinocyamus pusillus* (Grun and Nebelsick 2018) and are now examined with respect to the trabecular orientation perpendicular to the plate's surface (theta-orientation), and the orientation in the plate's horizontal plane (phi-orientation) (Fig. 31) (Grun and Nebelsick [1]).

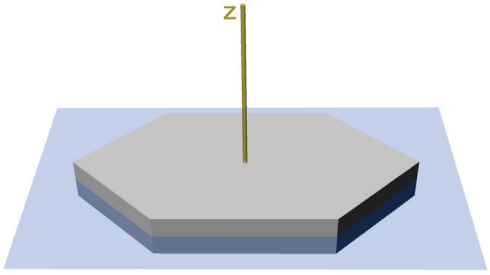

Figure 31. Definition of the plate's horizontal plane (blue) and the z-axis perpendicular to the plate's surface (yellow). From Grun and Nebelsick [1]

Results show that the average trabecular orientation perpendicular to the plate's surface is roughly 60 degrees (Fig. 32) and does not statistically differ between the labyrinthic and galleried stereom. The trabecular orientation in the plate's horizontal plane is in both labyrinthic and the galleried stereom directional in order to distribute the loads over the entire test (Fig. 33). The spatial trabecular analysis demonstrates that both the unordered labyrinthic, as well as the ordered galleried stereom are capable of resisting downward stress and can distribute loads along the entire test. This finding is not surprising, as loads, such as water pressure, are omnipresent along the entire surface of the test and not restricted to only specific parts of the plates (Grun and Nebelsick 2018).

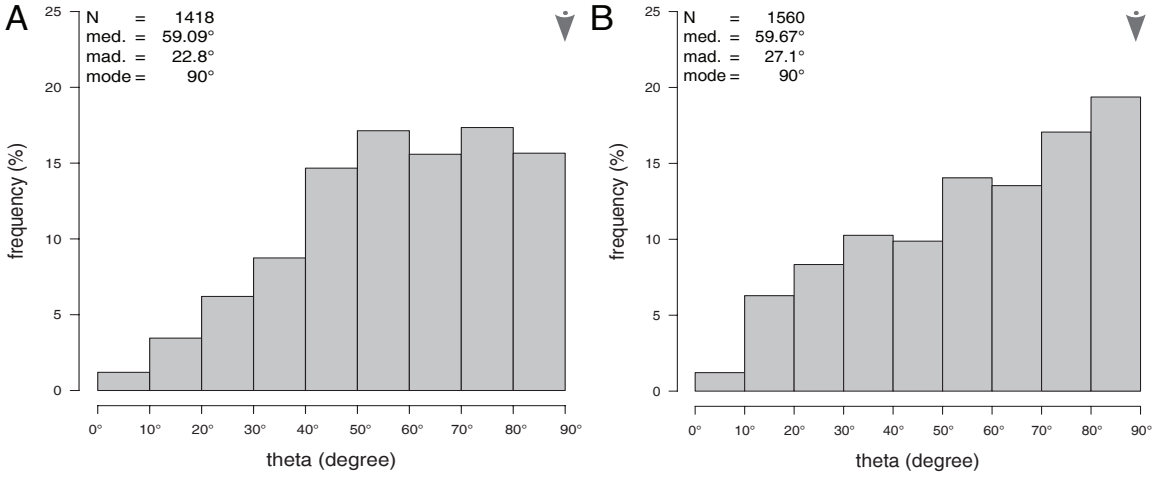

Figure 32. Trabecular orientation perpendicular to the plate's surface. (A) Orientation at the plate's center. (B) Orientation at the plate's margin. Modifies from Grun and Nebelsick [1]

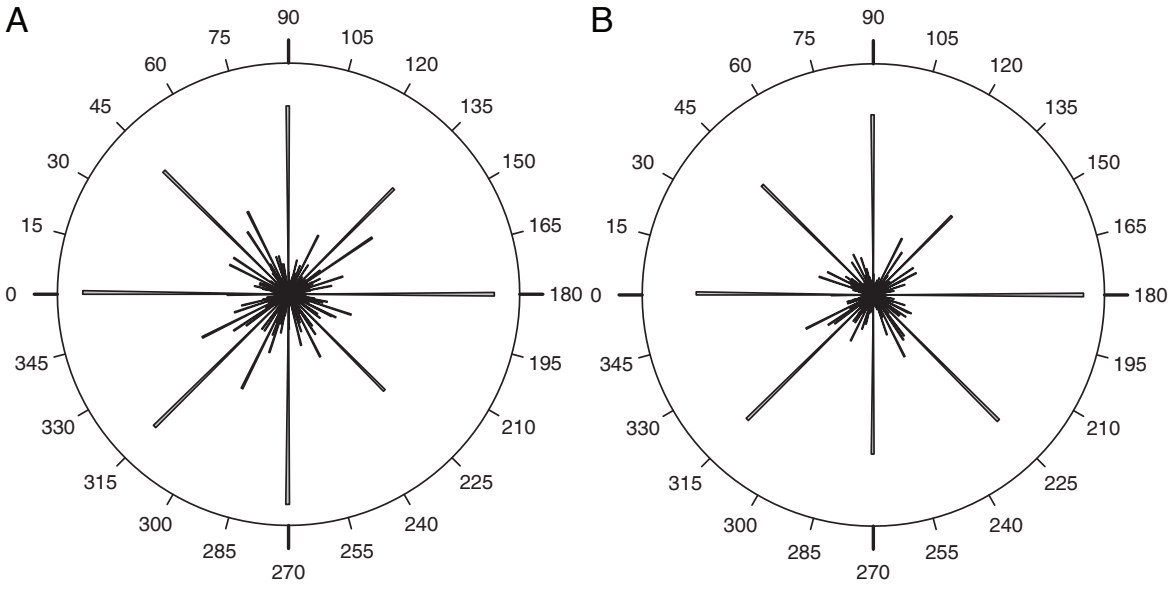

Figure 33. Rose diagrams of the trabecular orientation in the plate's horizontal plane. (A) Orientation at the plate's center. (B) Orientation at the plate's margin. Trabeculae in both plate regions are directionally orientated. Modified from Grun and Nebelsick [1]

Trabecular topology

The inter-trabecular angle, together with the number of trabeculae that intersect in one common node (node configuration) determines the trabecular topology (Fig. 34) (Reznikov et al. 2016). The trabecular topology allows for an interpretation of the ability to which degree a system is capable to resist multi-dimensional loads. For example, a beam system in 3N configuration (three trabeculae intersect in one common node) that is characterized by inter-trabecular angles of 120 degrees result in a planar and triangular segment (e.g. Reznikov et al. 2016). Such a segment can transfer only in-plane loads. A beam system in 4N configuration with inter-trabecular angles of 109.5 degrees forms a tetrahedron, which is capable of resisting spatial multi-directional loads.

Results show that the 3N configuration with an average inter-trabecular angle of 120 degrees is most common in both the labyrinthic and the galleried stereom (Tab. 1) (Grun and Nebelsick [1]). This indicates that most elements follow a roughly planar and triangular constructional motif. The second most common motif is the 4N configuration, this motif allows for resisting multi-directional loads. The high abundance of 3N configurations, however, is capable of resisting multi-directional loads when several 3N segments are connected in series with an angular off-set (Fig. 35) (Grun and Nebelsick [1]). The 3N configuration can thus cover a wide range of load directions. It is additionally highly interesting, that both the abundance of 3N and 4N motives, as well as the inter-trabecular angles of 120 degrees in the 3N configuration is not only found in the echinoid stereom, but also in the cancellous bones of vertebrates (Reznikov et al. 2016). This indicates that, especially the 3N and 120 degree motif can potentially be interpreted to represent an universal building principle in both echinoids and invertebrates (Reznikov et al. 2016, Grun and Nebelsick [1]).

Table 1. Inter-trabecular angles and node-configuration. ITA = inter-trabecular angle, N = sample size, deg = degree, sd = standard deviation. From Grun and Nebelsick [1]

	ITA	total	2N	3N	4N	5N	6N	7N	8N	9N
center	N	538	7	357	115	35	21	2	n/a	1
	fraction (%)	100.00	1.30	66.40	21.38	6.51	3.90	0.37	n/a	0.19
	mean (deg)	104.35	117.19	105.76	102.40	99.68	95.88	95.27	n/a	99.68
	sd (deg)	13.1	30.2	13.4	10.2	10.7	9.6	4.7	n/a	n/a
	mode (deg)	120.00	146.87	120.00	98.91	94.96	85.03	91.96	n/a	n/a
margin	N	589	5	369	149	38	20	4	1	n/a
	fraction (%)	100.00	0.93	68.59	27.70	7.06	3.72	0.74	0.19	n/a
	mean (deg)	102.85	117.04	103.19	102.19	102.89	99.38	92.91	113.76	n/a
	sd (deg)	13.9	20.1	13.3	15.2	12.4	15.3	5.7	n/a	n/a
	mode (deg)	120.00	150.17	120.00	100.12	99.78	100.11	100.53	n/a	n/a

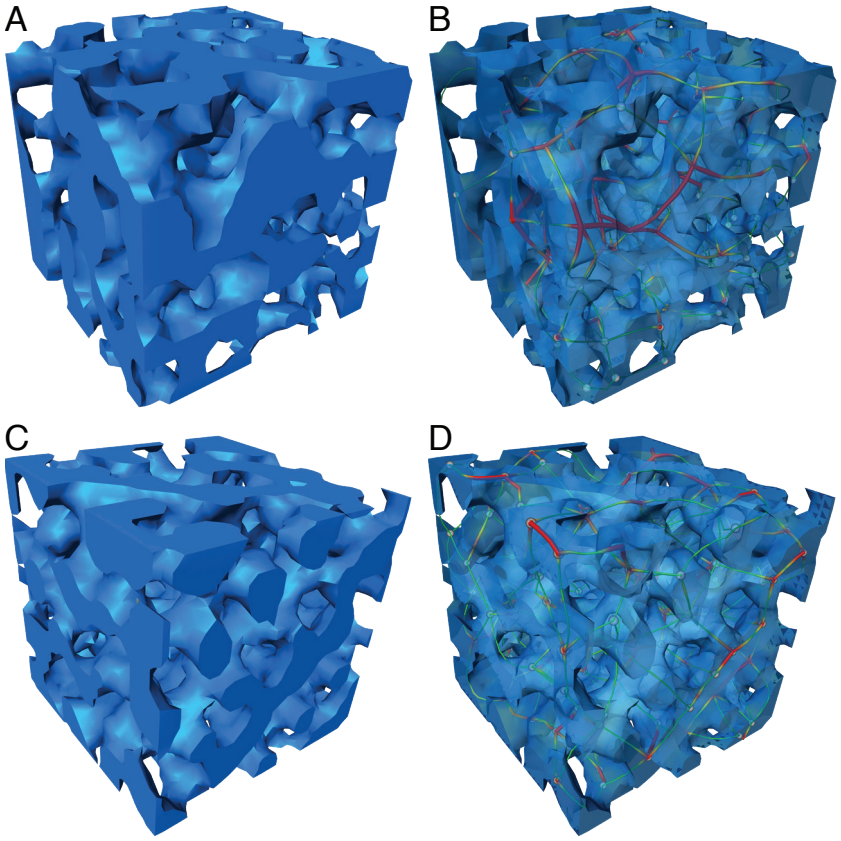

Figure 34. Rendering of the stereom of *Echinocyamus pusillus*. Trabeculae are tracked and color coded. (A) Trabecular system at the plate's center. (B) Trabeculae tracked (C) Trabeculae at the plate's margin, and (D) trabeculae tracked. Red = sturdy trabecula, green = slender trabecula. From Grun and Nebelsick [1]

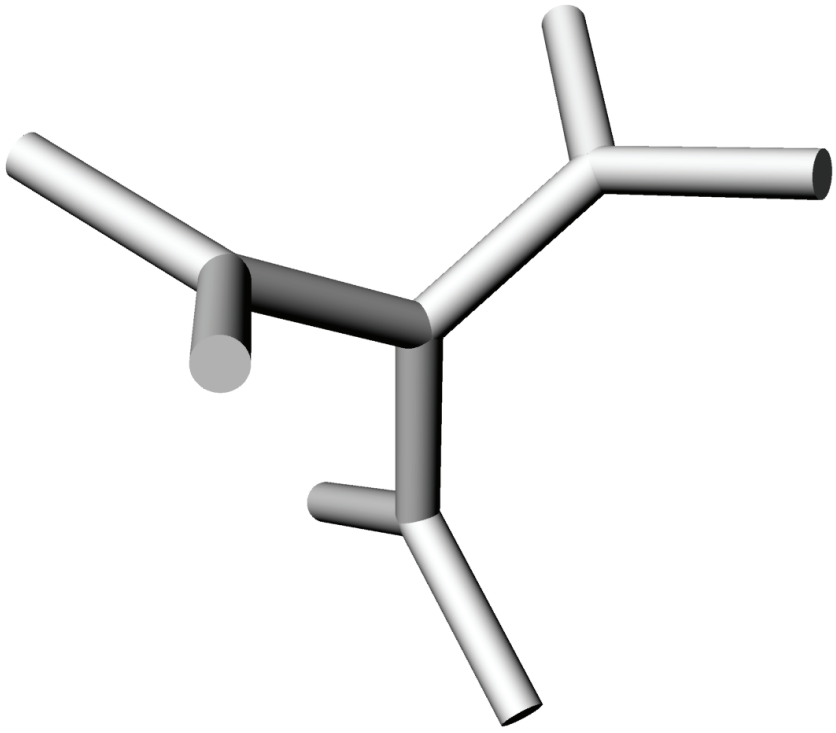

Figure 35. Constructed lattice-system built-up from multiple 3N members. All inter-trabecular angles possess an offset of 120 degrees to one another. From Grun and Nebelsick [1]

Overall test integrity

Clypeaster shows a high abundance of well-preserved tests in both recent environments and the fossil sedimentary record. Especially the preservation of the nearly triangular pie-shaped fragments is very well-recognizable (Grun et al. 2018). The test of recent *Clypeaster rosaceus* from the Bahamas were compared to fossil *Clypeaster*. In both the recent and fossil cases, the preservation as complete tests or pie-shaped fragments where most prominent (Tabs. 2, 3) (Grun et al. 2018). The tests of *Clypeaster* has thus been considered as a candidate structure for stable natural segmented shell systems. The structural reasons for the excellent preservation of the pie-shaped fragments and the reduced stability of the perradial sutures where the tests broke into the pie-shaped fragments were examined by µCT and SEM imageries. Results showed that the plate interlocking in radial sutures (Fig. 36) (adradial, interradial and perradial) are similar and can thus not be responsible for the different structural performances of the sutures (Grun et al. 2018).

The internal pillar system of *Clypeaster rosaceus* often intensively bridges the adradial and interradial sutures (Fig. 37). The bridging at the perradial sutures is, however less intensive and less frequent (Grun et al. 2018), which results in a reduced test integrity at the perradial sutures. The sutural bridging, however, only occurs on small areas and can thus not account for the major reason for a decreased test integrity and the common fragmentation along the perradial sutures. A 3d rendering of the micro-canal system revealed that the

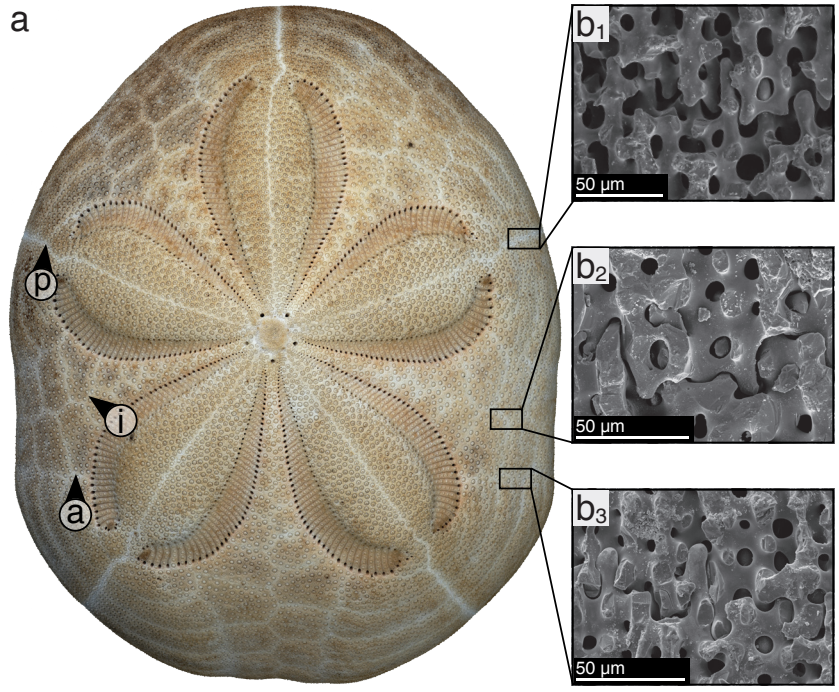

Figure 36. *Clypeaster rosaceus.* (A) Test with the three radial sutures labeled: a = adradial suture, i = interradial suture, p = perradial suture. (B) Trabecular interlocking mechanisms at the radial sutures. Modified from Grun et al. (2018)

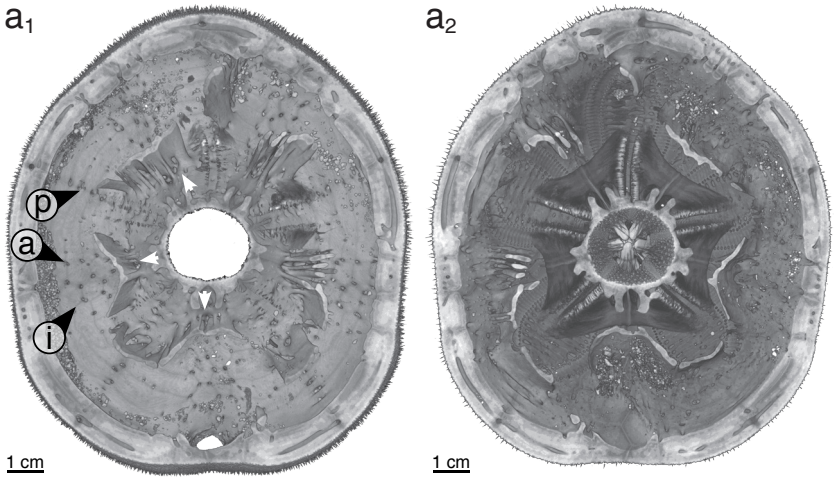

Figure 37. Micro-CT rendering of *Clypeaster rosaceus* showing the (a1) interior oral surface and the (a2) interior aboral surface with wall-like pillars at the adradial and interradial sutures, and pillars close to the perradial sutures. Wall-structures can frequently cross sutures (white arrows) where pillars rarely cross the plate borders of perradial sutures. p = perradial suture, a = adradial suture, i = interradial suture. Modified from Grun et al. (2018)

perradial sutures are undermined by radial canals of the water-vascular system (Fig. 38). These radial canals reduce the interlocking areas of the sutures, thus both the sutural interlocking as well as the trabecular interlocking (Grun and Nebelsick 2018) are reduced. Especially the decrease of trabecular interlocking weaken the structural integrity of the perradial sutures, thus leading to a preferred fragmentation site of the test (Grun et al. 2018).

The results of the fragmentation patterns reveal that both the plate interlocking mechanisms as well as the internal supports are capable to strengthen the test and resist stresses, which occur during taphonomic processes. The thereby identified structural reinforcing mechanisms can be seen as candidate structures for technical segmented shell constructions. Furthermore, the structural background of the fragmentation patterns improves the interpretation of both recent and fossil ecosystems (Grun et al. 2018).

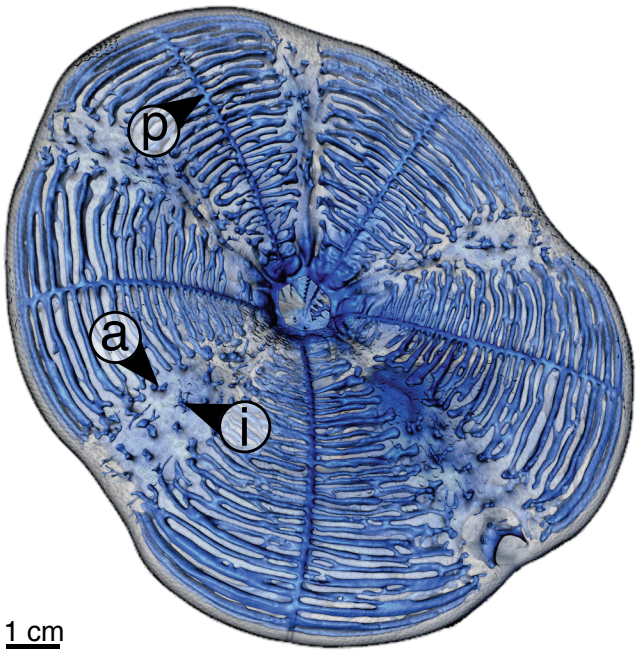

Figure 38. Micro-CT rendering of the micro-canal system of the *Clypeaster rosaceus* test in oral view. Micro-canals follow the course of perradial sutures or occur as branched stem-like structures at the adradial and interradial sutures. p = perradial suture, a = adradial suture, i = interradial suture. From Grun et al. (2018)

Table 2. Preservation of recent *Clypeaster rosaceus*. N = number of specimens. From Grun et al. (2018)

		complete N	fragmented N
overview	total	17	22
	apical disc missing	2	20
	encrusted	15	8
	pie-shaped	-	15
		N	%
fragmentation	total	22	100
	along horizontal sutures	0	0
	along radial	9	40.9
	along radial and latitudinal	12	54.5
	along perradial suture	13	59.1
	along adradial suture	0	0
	along interradial suture	0	0
	along perradial and adradial sutures	2	9.1
	along perradial and interradial sutures	2	9.1
	along adradial and interradial sutures	0	0
	along perradial, adradial and interradial sutures	3	13.6

Table 3. Preservation of fossil *Clypeaster* sp. from the Miocene of Usini (Sardinia, Italy). N = number of specimens. From Grun et al. (2018)

		N	%
	all specimens	30	100.0
complete tests	total	15	50.0
	pristine	4	13.3
	apical disc missing	5	16.7
	bioinfested	9	30.0
pie-shape fragments	total	6	20.0
	along perradial suture	5	16.7
	along adradial suture	1	3.3
	along interradial suture	1	3.3
	bioinfested	4	13.3
non-pie-shaped fragments	total	9	30.0
	along horizontal or radial suture	9	30.0
	bioinfested	5	16.7

Conclusion

The mechanical analyses of tests of *Clypeaster rosaceus* and *Echinocyamus pusillus* revealed numerous reinforcement strategies. Plate interlocking is considered as a major structural principle, which can be present as sutural interlocking or trabecular interlocking. The plate interlocking can be additionally promoted by sutural thickening, where the interface between two adjoining plates increases, thus increasing the test integrity.

Internal supports vary among species and can be divided into four types: pillars, buttresses, marginal wall-system and meshwork. Pillars, marginal wall-systems and the meshwork can cross sutures, thereby increasing the test integrity. Buttresses are restricted to the interambulacral areas. The presence of internal buttressing in *Echinocyamus pusillus* is structurally significant. When the buttresses are removed, compressive and tensile forces increase. Especially the tensile circumferential forces around the peristome increase. The organic tissues which cover the entire stereom do not contribute to the overall test integrity to a significant level.

The high preservation potential of *Clypeaster rosaceus*, especially in the form of pie-shaped fragments, is predominantly based on the sutural layout. Plate interlocking and internal supports promote the test integrity. Biologically relevant micro-canals for the transportation of fluids of the water-vascular system follow the course of the perradial sutures. Although the presence of micro-canals is important for the biological functionality of the individual, they reduce the test strength at the perradial sutures. After fragmentation of the test in pie-shaped fragments, the stability of the remaining sutures is still intact.

The micro-architecture of the stereom of *Echinocyamus pusillus* reveals that most nodes are in the 3N configuration where three trabeculae intersect in one common node. The most abundant inter-trabecular angles in 3N configuration occur in around 120 degrees indicating that these resembles a planar triangle. These triangles, when connected in series with an angular off-set, can resist loads from multiple directions. The 3N and 120 degree motif is also found in cancellous bones of many taxa of vertebrates, thus indicating an universal building principle.

The identified and analyzed reinforcement structures which have been addresses above are considered as relevant for both the understanding of structural complexity and the preservation potential of the clypeasteroid echinoids, particularly *Clypeaster rosaceus* and *Echinocyamus pusillus*.

Outlook

The mechanical analyses of test architecture and the structural involvement leading to the high preservation potential of intact tests, or their fragments, can be directly incorporated into paleontological analysis (e.g. Grun et al. 2018). The transfer of the structural reinforcement mechanisms of the analyzed clypeasteroids into architectural or engineering disciplines (Fig. 39) is more difficult. Although the identified and analyzed structures are of high significance in the clypeasteroid test, technical hurdles such as the potential of scaling or the fabrication process must be resolved. Biological and paleontological methods, however, have been shown to be advantageous in biomimetic research, their employment should be further developed in order to obtain a better understanding of the skeletal remains which are important for biological, paleontology and engineering sciences.

Figure 39. ICD / ITKE Research Pavilion 2015 at the University of Stuttgart. Developed during an interdisciplinary biomimetic course together with the University of Tübingen. From Grun et al. (2016)

References

Agassiz A (1872) Revision of the Echini. *Cambridge University Press*, Cambridge.

Alvarado JJ, Solís-Marín FA (2013) Echinoderm Research and Diversity in Latin America. *Springer*, Heidelberg.

Belaústegui Z, Nebelsick JH, Gibert de JM, Domènech R and Martinell J (2012a) A taphonomic approach to the genetic interpretation of clypeasteroid accumulations from Tarragona (Miocene, NE Spain). *Lethaia* 45:548–565.

B**elaústegui Z, Gibert de JM, Nebelsick JH, Domènech R and Martinell J (2012b)** Clypeasteroid echinoid tests as benthic islands for gastrochaenid bivalve colonization: evidence from the Middle Miocene of Tarragona (North–East Spain). *Palaeontology* 56:783–796.

Bottjer DJ, Davidson EH, Peterson KJ, Cameron RA (2006) Paleogenomics of echinoderms. *Science* 314:956–960.

Bramski C (1981) Rotationssymmetrische tropfenförmige Behälter. *Wilhelm Ernst und Sohn*, München.

Byrne M, O'Hara TD (2017) Australian Echinoderms: Biology, Ecology and Evolution. *CSIRO Publishing*, Clayton.

Ceranka T, Złotnik M (2003) Traces of cassid snails predation upon the echinoids from the Middle Miocene of Poland. *Acta Palaeontoogica Polonica* 48:491–496.

Chesher RH (1969) Contributions to the biology of *Meoma ventricosa* (Echinoidea: Spatangoida). *Bulletin of Marine Science* 19:72–110.

Chia FS (1969) Some observations on the locomotion and feeding of the sand dollar, *Dendraster excentricus* (Eschscholtz). *Journal of Experimental Marine Biology and Ecology* 3:162–170.

Davies DJ, Powell EN, Station RJ (1989) Taphonomic signature as a function of environmental processes: shell and shell beds in a hurricane-influenced inlet on the Texas coast. *Palaeogeography, Palaeoclimatology, Palaeoecology* 72:317–356.

Dixon HL and Donovan SK (1998) Oligocene echinoids of Jamaica. *Tertiary Research* 18:95–124.

Döderlein L (1906) Arktische Seeigel. In: F Römer, F Schaudinn (eds) Fauna Arctica. *Verlag von Gustav Fischer*, Jena, 374–394.

Donovan SK (1991) The taphonomy of echinoderms: calcareous multi–element skeletons in the marine environment. In: SK Donovan (ed) The Process of Fossilization. *Belhaven Press*, London, 241–269.

Drack M, Limpinsel M, de Bruyn G, Nebelsick JH, Betz O (2018) Towards a theoretical clarification of biomimetics using conceptual tools from engineering design. *Bioinspiration and Biomimetics* 13:016007.

Dubois P, Ameye L (2001) Regeneration of spines and pedicellariae in echinoderms: a review. *Microscopy Research and Technique* 55:427–431.

Durham JW (1955) Classification of Clypeasteroid Echinoids. *University of California Press*, Berkeley.

Durham JW (1966) Clypeasteroids. In: RC Moore (ed) Treatise on Invertebrate Paleontology. Part U, Echinodermata 3.2. *University of Kansas Press*, Lawrence, 450–491.

Dynowski JF (2012) Echinoid remains in shallow–water carbonates at Fernandez Bay, San Salvador Island, Bahamas. *Palaios* 27:181–189.

Ebert T (1892) Die Echiniden des nord-und mitteldeutschen Oligocäns. *Abhandlungen zur Geologischen Spezialkarte von Preußen und den Thüringischen Staaten IX. Königlich Preussische geologische Landesanstalt*, Berlin.

Ellers O, Johnson AS, Moberg PE (1998) Structural strengthening of urchin skeletons by collagenous sutural ligaments. *Biological Bulletin* 195:136–144.

Emlet RB (1982) Echinoderm calcite: a mechanical analysis from larval spicules. *Biological Bulletin* 163:264–275.

Ghiold J (1982) Observations on the clypeasteroid *Echinocyamus pusillus* (O.F. Müller). *Journal of Experimental Marine Biology and Ecology* 61:57–74.

Ghiold J (1984) Adaptive shifts in clypeasteroid evolution – feeding strategies in the soft-bottom realm. *Neues Jahrbuch für Geologie und Paläontologie* 169:41–73.

Gianguzza P, Bonaviri C, Guidetti P (2009) Crushing predation of the spiny star *Marthasterias glacialis* upon the sea urchin *Paracentrotus lividus*. *Marine Biology* 156:1083–1086.

Gordon JE (1978) Structures: Or Why Things Don't Fall Down. *Da Capo Press*, New York.

Grossmann N, Nebelsick JH (2013a) Stereom differentiation in spines of *Plococidaris verticillata*, *Heterocentrotus mammillatus* and other regular sea urchins. In: CR Johnson (ed) Echinoderms in a Changing World: Proceedings of the 13th International Echinoderm Conference. *CRC Press*, Boca Raton, 97–104.

Grossmann JN, Nebelsick JH (2013b) Comparative morphology and structural analysis of selected cidaroid and camarodont sea urchin spines. *Zoomorphology* 132:301–315.

Grun TB (2016) Echinoid test damage by a stingray predator. *Lethaia* 49:285–286.

Grun TB, Nebelsick JH (2015) Sneaky snails: how drillholes can affect paleontological analyses of the minute clypeasteroid echinoid *Echinocyamus*. In: D. Zamora, I Rábano (eds) Progress in Echinoderm Palaeobiology. *Cuadernos del Museo Geominero, 19. Instituto Geológico y Minero de España*, Madrid, 71–74.

Grun TB, Nebelsick JH (2016) Taphonomy of a clypeasteroid echinoid using a quasimetric approach. *Acta Palaeontologica Polonica* 61:689–699.

Grun TB, Nebelsick JH (2018) Structural design of the minute clypeasteroid echinoid *Echinocyamus pusillus*. *Royal Society Open Science*.

Grun TB, Nebelsick JH [1] Structural design of the echinoid's trabecular system. *PlosOne* in review.

Grun TB, Nebelsick JH [3] Looking back and forward to the iconic clypeasteroid *Echinocyamus pusillus*. *Contemporary Trends in Geoscience* in preparation.

Grun T, Sievers D, Nebelsick JH (2014) Drilling predation on the clypeasteroid echinoid *Echinocyamus pusillus* from the Mediterranean Sea (Giglio, Italy). *Historical Biology* 26:745–757.

Grun TB, Koohi L, Schwinn T, Sonntag D, von Scheven M, Bischoff M, Knippers J, Menges A, Nebelsick JH (2016) The skeleton of the sand dollar as a biological role model for segmented shells in building construction: a research review. In: J Knippers, KG Nickel, T Speck (eds) Biomimetic Research for Architecture and Building Construction: Biological Design and Integrative Structures. *Springer*, Cham, 217–242.

Grun TB, Kroh A, Nebelsick JH (2017a) Comparison of drilling predation on phosphatized and non-phosphatized echinoids (*Echinocyamus stellatus*) from Miocene offshore sediments (Globigerina Limestone Fm., Malta). *Journal of Palaeontology* 91:433–462.

Grun TB, von Scheven M, Geiger F, Schwinn T, Sonntag D, Bischoff M, Knippers J, Menges A, Nebelsick JH (2017b) Bauprinzipien und Strukturdesign von Seeigeln – Vorbilder für bioinspirierte Konstruktionen. In: J Knippers, U Schmid, T Speck (eds) Baubionik – Biologie beflügelt Architektur. Stuttgarter Beiträge zur Naturkunde C. *Staatliches Museum für Naturkunde*, Stuttgart, 82–93.

Grun TB, Mancosu A, Belaústegui Z, Nebelsick JH (2018) The taphonomy of *Clypeaster*: a paleontological tool to identify stable structures in natural shell systems. *Neues Jahrbuch für Paläontologie und Geologie*.

Grun TB, von Scheven M, Bischoff M, Nebelsick JH [2] Structural stress response of segmented natural shells: a numerical case study on the clypeasteroid echinoid *Echinocyamus pusillus*. *Royal Society Interface* in review.

Hageman SA, Kaesler RL, Broadhead TW (2004) Fusulinid taphonomy: encrustation, corrosion, compaction, and dissolution. *Palaios* 19:610–617.

Hauser I, Oschmann W, Gischler E (2008) Taphonomic signatures on modern Caribbean bivalve shells as indicators of environmental conditions (Belize, Central America). *Palaios* 23:586–600.

Hendler G, Miller JE, Pawson DL, Kier PM (1995) Sea Stars, Sea Urchins and Allies: Echinoderms of Florida and the Caribbean. *Smithsonian Institution Press*, Washington.

Heath TL (1897) The Works of Archimedes. *Cambridge University Press*, Cambridge.

Hopkins TS (1988) A review of the distribution and proposed morphological groupings of extant species of the genus *Clypeaster* in the Caribbean Sea and Gulf of Mexico. In: RD Burke, PV Mladenov, P Lambert, RL Parsley (eds) Echinoderm Biology. Proceedings of the Sixth International Echinoderm Conference. *Balkema*, Rotterdam, 337–345.

Hyman LH (1955) The Invertebrates: Echinodermata. *McGraw-Hill*, New York.

James DW (2000) Diet, movement, and covering behavior of the sea urchin *Taxopneustes roseus* in rhodolith beds in the Gulf of California, México. *Marine Biology* 137:913–923.

Kidwell SM, Bosence DWJ (1991) Taphonomy and time-averaging of marine shelly faunas. In: PA Allison, DEG Briggs (eds) Taphonomy: Releasing the Data Locked in the Fossil Record. *Plenum Press*, New York, 116–209.

Kier PM (1977) The poor fossil record of the regular echinoid. *Paleobiology* 3:168–174.

Kier PM, Grant RE (1965) Echinoid distribution and habits, Key Largo Coral Reef Preserve, Florida. *Smithsonian Miscellaneous Collections* 149:1–68.

Killian CE, Wilt FH (2008) Molecular aspects of biomineralization of the echinoderm endoskeleton. *Chemical Reviews* 108:4463–4474.

Klang K, Bauer G, Toader N, Lauer C, Termin K, Schmier S, Kovaleva D, Haase W, Berthold C, Nickel KG, Speck T, Sobek W (2016) Plant and animals as source of inspiration for energy dissipation in load bearing systems and facades. In: J Knippers, KG Nickel, T Speck (eds) Biomimetic Research for Architecture and Building Construction: Biological Design and Integrative Structures. *Springer*, Cham, 109–133.

Klein LR, Currey JD (1970) Echinoid skeleton: absence of a collagenous matrix. *Science* 196:1209–1210.

Kroh A (2002) Die Echiniden (Echinodermata) aus dem Karpatium des Korneuburger Beckens und der Kreuzstettener Bucht (Niederösterreich, Untermiozän). *Beiträge zur Paläontologie und Geologie Österreich-Ungarns* 27:305–315.

Kroh A (2005) Catalogus Fossilium Austriae. Band 2. Echinoidea neogenica. *Österreichische Akademie der Wissenschaften*, Wien.

Kroh A, Nebelsick JH (2003) Echinoid assemblages as a tool for palaeoenvironmental reconstruction – an example from the Early Miocene of Egypt. *Palaeogeography, Palaeoclimatology, Palaeoecology* 201:157–177.

Kroh A, Nebelsick JH (2010) Echinoderms and Oligo-Miocene carbonate systems: potential applications in sedimentology and environmental reconstruction. *International Association of Sedimentology Special Publications* 42:201–228.

Kroh A, Smith AB (2010) The phylogeny and classification of post-Palaeozoic echinoids. *Journal of Systematic Palaeontology* 8:147–212.

Lambert J (1927) Revision des echinides fósiles de la Catalogne. Memorias del Museo de Ciencias Naturales de Barcelona. *Serie Geológica* 1:1–102.

Lang A (1896) Text Book of Comparative Anatomy. *Macmillan and Co*, London.

Lauer C, Grun TB, Zutterkirch I, Jemmali R, Nebelsick JH, Nickel KG (2017) Morphology and porosity of the spines of the sea urchin *Heterocentrotus mamillatus* and their implications on the mechanical performance. *Zoomorphology* 137:139–154.

Lawrence J (1987) A functional morphology of echinoderms. *John Hopkins University Press*, Baltimore.

Lewis JB (1958) The biology of the tropical sea urchin *Tripneustes esculentus* Leske in Barbados, British West Indies. *Canadian Journal of Zoology* 36:607–621.

Lopes RP (2011) Fossil sand dollars (Echinoidea: Clypeasteroida) from the southern Brazil coast. *Revista Brasileira Paleontolgia* 14:201–214.

Lovén S (1874) Études sur les Échinoïdées. *PA Norstedt and Söner*, Stockholm.

Malek S, Wierzbicki T, Ochsendorf J (2014) Buckling of spherical cap gridshells: a numerical and analytical study revisiting the concept of the equivalent continuum. *Engineering Structures* 75:288–298.

Mancosu A and Nebelsick JH (2013) Multiple routes to mass accumulations of clypeasteroid echinoids: a comparative analysis of Miocene echinoid beds of Sardinia. *Palaeogeography, Palaeoclimatology, Palaeoecology* 374:173–186.

Mancosu A and Nebelsick JH (2015) The origin and paleoecology of clypeasteroid assemblages from different shelf setting of the Miocene of Sardinia, Italy. *Palaios* 30:273–387.

Mancosu A and Nebelsick JH (2017) Ecomorphological and taphonomic gradients in clypeasteroid-dominated echinoid assemblages along a mixed siliciclastic-carbonate shelf from the early Miocene of northern Sardinia, Italy. *Acta Palaeontologica Polonica* 62:627–646.

Märkel K, Röser U (1983) The spine tissues in the echinoid *Eucidaris tribuloides*. *Zoomorphology* 103:25–41.

Michelin H (1861) Monographie des Clypéastres fossiles. *Mémoire de la Société Géologique de France* 7: 101–147.

Mihaljević M, Jerjen I, Smith AB (2011) The test architecture of *Clypeaster* (Echinoidea, Clypeasteroida) and its phylogenetic significance. *Zootaxa* 2983:21–38.

Mitrović–Petrović J (1984) Importance biostratigraphique et paleoecologique du genre *Clypeaster* (Echinoidea) pour les sediments neogenes de la Yougoslavie. *Colloquium on Mediterranean Neogene marine megafaunal palaeoenvironments and biostratigraphy. Annales Géologiques des Pays Hellénique* 32:211–235.

Mooi R (1986a) Non-respiratory podia of the clypeasteroids (Echinodermata, Echinoides). *Zoomorphology* 106:21–30

Mooi R (1986b) Non-respiratory podia of the clypeasteroids (Echinodermata, Echinoides): II. Diversity. *Zoomorphology* 106:75–90

Mooi R (1986c) Structure and function of clypeasteroid miliary spines (Echinodermata, Echinoides): I. Functional morphology. *Zoomorphology* 106:212–223.

Mooi R (1989) Living and Fossil Genera of the Clypeasteroida (Echinoidea: Echinodermata): An Illustrated Key and Annotated Checklist. Smithsonian Contributions to Zoology 488. *Smithsonian Institution Press*, Washington DC.

Mooi R, Chen CP (1996) Weight belts, diverticula, and the phylogeny of the sand dollars. *Bulletin of Marine Science*, 58:186–195.

Mooi R, Kroh A and Srivastava DK (2014) Phylogenetic re-evaluation of fossil and extant micro-echinoids with revision of *Tridium*, *Cyamidia*, and *Lenicyamidia* (Echinoidea Clypeasteroida). *Zootaxa* 3857:501–526.

Moore HB (1966) Ecology of echinoids. In: RA Boolootian (ed) Physiology of Echinodermata. *John Wiley and Sons*, New York, 7–85.

Mortensen T (1907) The Danish Ingolf-Expedition IV.2 Echinoidea (II). *Bianco Luno*, Copenhagen.

Mortensen TH (1927) Handbook of the Echinoderms of the British Isles. *Humphrey Milford Oxford University Press*, Edinburgh.

Mortensen T (1948) A monograph of the Echinoidea, IV, 2. Clypeasteroida. Clypeasteridæ, Arachnoidæ, Fibulariidæ, Laganidæ and Scutellidæ. *CA Reitzel*, Copenhagen.

Müller M. 1854. Über die Gattungen der Seeigellarven. Siebente Abhandlung über die Metamorphose der Echinodermen. In: Abhandlungen der Königlichen Akademie der Wissenschaften zu Berlin. *Druckerei der Königlichen Akademie der Wissenschaften*, Berlin, 1–56.

Nachtigall W (2002) Bionik. Grundlagen und Beispiele für Ingenieure und Naturwissenschaftler. 2. Auflage. *Springer*, Berlin.

Nebelsick JH (1992) Echinoid distribution by fragment identification in the northern bay of Safaga, Red Sea, Egypt. *Palaios* 7:316–328.

Nebelsick JH (1999a) Taphonomic comparison between recent and fossil sand dollars. *Palaeogeography, Palaeoclimatology, Palaeoecology* 149:349–358.

Nebelsick JH (1999b) Taphonomy of *Clypeaster* fragments: preservation and taphofacies. *Lethaia* 32:241–252.

Nebelsick JH (2008) Taphonomy of the irregular echinoid *Clypeaster humilis* from the Red Sea: implications for a taxonomic resolution along taphonomic grades. In: WI Ausich, GD Webster (eds) Echinoderm Paleobiology. *Indiana University Press*, Bloomington, 115–128.

Nebelsick JH, Kampfer S (1994) Taphonomy of *Clypeaster humilis* and *Echinodiscus auritus* (Echinoidea, Clypeasteroids) from the Red Sea. In: B David, A Guille, JP Féral, M Roux (eds) Echinoderms through Time. *Balkema*, Rotterdam, 803–808.

Nebelsick JH, Kowalewski M (1999) Drilling predation on recent clypeasteroid echinoids from the Red Sea. *Palaios* 14:127–144.

Nebelsick JH, Dynowski JF, Grossmann JN, Tötzke C (2015) Echinoderms: hierarchically organized light weight skeletons. In: C Hamm (ed) Evolution of Lightweight Structures: Analyses and Technical Applications. *Springer*, Dodrecht, 141–156.

Nichols D (1959) The histology and activities of the tube-feet of *Echinocyamus pusillus*. *Quarterly Journal of Microscopical Science* 100:539–555.

Nichols D (1962) Echinoderms. *Hutchinson and Co*, London.

Nichols D (1964) Echinodermata: experimental and ecological. In: H Barnes (ed) Oceanography and Marine Biology: An Annual Review, Volume 2. *Allen and Uwin*, London, 393–423.

Nichols D, Currey JD (1968) The secretion, structure, and strength of echinoderm calcite. In: SM McGee, KFA Ross (eds) Cell Structures and its Interpretation. *Edward Arnold*, London, 251–261.

Pawson DL (2007) Phylum echinodermata. *Zootaxa* 1668:749–764.

Philippi U, Nachtigall W (1996) Functional morphology of regular echinoid tests (Echinodermata, Echinoidea): a finite element study. *Zoomorphology* 116:35–50.

Poddubiuk RH (1984) Evolution and Adaptation in some Caribbean Oligo-Miocene clypeasters. In: BF Keegan and BDS O´Connor (eds) Fifth International Echinoderm Conference. *Balkema*, Galway, 75–80.

Presser V, Gerlach K, Vohrer A, Nickel KG, Dreher WF (2010) Determination of the elastic modulus of high porous samples by nanoindentation: a case study on sea urchin spines. *Journal of Materials Science* 45:2408–2418.

Queiroz V, Sales L, Neves E, Johnsson R (2011) *Dissodactylus crinitichelis* Moreira, 1901 and *Leodia sexiesperforata* (Leske, 1778): first record of this symbiosis in Brazil. *Nauplius* 19:63–70.

Rahman IA, Belaústegui Z, Zamora S, Nebelsick JH, Domènech R and Martinell J (2015) Miocene *Clypeaster* from Valencia (E Spain): insights into the taphonomy and ichnology of bioeroded echinoids using x-ray micro-tomography. *Palaeogeography, Palaeoclimatology, Palaeoecology* 438:168–179.

Raup DM (1965) Crystal orientations in the echinoid apical system. *Journal of Paleontology* 39:934–951.

Raup DM (1966) The endoskeleton. In: *RA Boolootian (ed) Physiology of Echinodermata. John Wiley and Sons*, New York, 379–395.

Raup DM, Schwan EF (1967) Crystal orientation in the apical plates of aberrant echinoids. *Biological Bulletin* 133:618–629.

R Core Team (2017) R: a language and environment for statistical computing. Vienna, Austria, *R Foundation for Statistical Computing*. www.r-project.org

Reznikov N, Chase H, Ben-Zvi Y, Tarle V, Singer M, Brumfeld V, Shahar R, Weiner S (2016) Inter-trabecular angle: a parameter of trabecular bone architecture in the human proximal femur that reveals underlying topological motives. *Acta Biomaterialia* 44:65–72.

Rodríguez-Barreras R (2014) The shallow-water echinoids (Echinodermata: Echinoidea) of Cuba. *Marine Biodiversity Records* 7:1–8.

Sala E (1997) Fish predators and scavengers of the sea urchin *Paracentrotus lividus* in protected areas of the north-west Mediterranean Sea. *Marine Biology* 129:531–539.

Salvadori M, Heller R (1975) Structure in Architecture: The Building of Buildings, Second Edition. *Prentice-Hall*, Englewood Cliffs.

Schaffer H (1962) Die Scutelliden des Miozäns von Österreich und Ungarn. *Paläontologische Zeitschrift* 36:135–170.

Schodek DL (1980) Structures. *Prentice-Hall*, Englewood Cliffs.

Schodeck DL, Bechthold M (2015) Structures. *Pearson*, Noida.

Schmidt WJ (1925) Über die Lage der optischen Achse in den Kalkkörpern der Holothurien und ihre Bedeutung für die vergleichende Morphologie. *Zoologische Jahrbücher. Abteilung für Anatomie und Ontogenie der Tiere* 47:113–154.

Seilacher A (1979) Constructional morphology of sand dollars. *Paleobiology* 5:191–221.

Serafy DK (1979) Echinoids (Echinodermata: Echinoidea). *Memoirs of the Hourglass Cruises* 5:1–120.

Shick JM (1983) Respiratory gas exchange in echinoderms. In: M Jangoux, JM Lawrence (eds) Echinoderm Studies, Volume 1. *Balkema*, Rotterdam, 67–110.

Sievers D, Nebelsick JH (2018) Fish predation on a Mediterranean echinoid: identification and preservation potential. *Palaios* 33:47–54.

Sievers D, Friedrich JP, Nebelsick JH (2014) A feast for crows: bird predation on irregular echinoids from Brittany, France. *Palaios*, 29:87–94.

Smith AB (1980) Stereom Microstructure of the Echinoid Test. Special Papers in Palaeontology 25. *The Palaeontological Association*, London.

Smith AB (1990) Biomineralization in echinoderms. In: JG Carter (ed) Skeletal Biomineralization: Patterns, Processes and Evolutionary Trends. *Van Nostrand Reinhold*, New York, 413–443.

Smith AB (1984) Echinoderm Palaeobiology. *George Allen and Unwin*, London.

Smith AB, Savill JJ (2001) *Bromidechinus*, a new Ordovician echinozoan (Echinodermata), and its bearing on the early history of echinoids. *Earth and Environmental Science Transactions of the Royal Society of Edinburgh* 92:137–147.

Swan EF (1966) Growth, autotomy, and regeneration. In: RA Boolootian (ed) Physiology of Echinodermata. *John Wiley and Sons*, New York, 397–434.

Tamboli A, Xing M, Ahmed M (2000) Structural theory. In: F. Merritt, JT Ricketts (eds) Building Design and Construction Handbook, Sixth Edition. *McGraw-Hill*, New York, 232–419.

Telford M (1982) Echinoderm spine structure, feeding and host relationships of four species of *Dissodactylus* (Brachyura: Pinnotheridae). *Bulletin of Marine Science* 32:584–594.

Telford M (1983) An experimental analysis of lunule function in the sand dollar *Mellita quinquiesperforata*. *Marine Biology* 76:125–134.

Telford M (1985a) Domes, arches and urchins: the skeletal architecture of echinoids (Echinodermata). *Zoomorphology* 105:114–124.

Telford M (1985b) Structural analysis of the test of *Echinocyamus pusillus* (O. F. Müller). In: BF Keegan, BDS O'Conner (eds) Proceedings of the Fifth International Echinoderm Conference. *Balkema*, Rotterdam, 353–360.

Telford M, Harold AS, Mooi R (1983) Feeding structures, behavior and microhabitat of *Echinocyamus pusillus* (Echinoidea: Clypeasteroida). *Biological Bulletin* 165:745–757.

Telford M, Harold AS, Mooi R (1987) Feeding activities of two species of *Clypeaster* (Echinoides, Clypeasteroida): further evidence of clypeasteroid resource partitioning. *Biological Bulletin* 172:324–336.

Thompson JR, Petsios E, Davidson EH, Erkenbrack EM, Gao F, Bottjer DJ (2015) Reorganization of sea urchin gene regulatory networks at least 268 million years ago as revealed by oldest fossil cidaroid echinoid. *Scientific Reports* 5:15541.

Tsaparas N, Drinia H, Antonarakou A, Marcopoulou-Diakantoni A and Dermitzakis MD (2007) Tortonian *Clypeaster* fauna (Echinoidea: Clypeasteroida) from Gavdos Island (Greece). *Bulletin of the Geological Society of Greece* 40:225–237.

Ubaghs G (1967) General characters of Echinodermata. In: RC Moore (ed) Treatise on Invertebrate Paleontology. Part S, Echinodermata 1. *University of Kansas Press*, Lawrence, 3–60.

Walther J (1910) Die Sedimente der Taubenbank im Golf von Neapel. In: G Reimer (ed) Abhandlungen Der Königlich Preussischen Akademie Der Wissenschaften. *Reichsdruckerei*, Berlin, 1–49.

Weber JN (1969) The incorporation of magnesium into the skeletal calcites of echinoderms. *American Journal of Science* 267:537–566.

Wilde P, Holden J, Isselhardt C (1970) Non-destructive wet weighing of marine sediments. *Marine Geology* 8:173–178.

Wilson MVH (1988) Taphonomic processes: information loss and information gain. *Geoscience Canada* 15:131–148.

Young MAL, Bellwood DR (2012) Fish predation on sea urchins on the Great Barrier Reef. *Coral Reefs* 31:731–738.

Zachos LG (2015) Holistic morphometric analysis of growth of the sand dollar *Echinarachnius parma* (Echinodermata: Echinoidea: Clypeasterida). *Zootaxa* 4052:151–179.

Złotnik M, Ceranka T (2005) Patterns of drilling predation of cassid gastropods preying on echinoids from the middle Miocene of Poland. *Acta Palaeontologica Polonica* 50:409–428.

Appendix I:

Further contributions

Further publications

The following manuscripts have been written during the time of this PhD thesis, but are not directly related to the topic. These manuscripts are not attached, except for the co-authored paper dealing with the spines of *Heterocentrotus mamillatus*, as this paper employed similar methods and possesses a biomimetic background.

Morphology and porosity of the spines of the sea urchin *Heterocentrotus mamillatus* and their implications on the mechanical performance. 2017. *Zoomorphology* 137:139–154.

Authors: Lauer C, **Grun TB**, Zutterkirch I, Jemmali R, Nebelsick JH, Nickel KG

Recognizing traces of snail predation on the Caribbean sand dollar *Leodia sexiesperforata*. 2017. *Palaios* 32:448–461.

Author: Grun TB

Habitat and behavioral shift of *Cassis tuberosa*. 2017. *American Malacological Bulletin* 35:55–58.

Authors: Grun TB, Nebelsick JH

Comparison of drilling predation on phosphatized and non-phosphatized echinoids (*Echinocyamus stellatus*) from Miocene offshore sediments (Globigerina Limestone Fm., Malta). 2017. *Journal of Palaeontology* 91:433–462.

Authors: Grun TB, Kroh A, Nebelsick JH

Echinoid test damage by a stingray predator. 2016. *Lethaia* 49:285-286.

Author: Grun TB

Taphonomy of a clypeasteroid echinoid using a quasimetric approach. 2016. *Acta Palaeontologica Polonica* 61:689–699.

Authors: Grun TB, Nebelsick JH

Sneaky snails: How drillholes can affect paleontological analyses of the minute clypeasteroid echinoid *Echinocyamus*. 2015. In: D Zamora, I Rábano (eds) Progress in Echinoderm Palaeobiology. *Cuadernos del Museo Geominero, 19. Instituto Geológico y Minero de España*, Madrid, 71–74.

Authors: Grun TB, Nebelsick JH

Conference contributions

The following conference contributions are a directly related to the topic of this PhD thesis.

Computational analytics: exploring the structural test design of *Echinocyamus pusillus*. 2018. *International Echinoderm Conference*. Nagoya, Japan.

Authors: Grun TB, Nebelsick JH

Biomechanics of *Echinocyamus pusillus*: the relevance of internal buttressing. 2018. *International Echinoderm Conference*. Nagoya, Japan.

Authors: Grun TB, von Scheven M, Bischoff M, Nebelsick JH

Echinoids in 3d: understanding mechanisms that strengthen light-weight skeletons. 2017. *Geological Society of America Abstract with Program* 49:

Authors: Grun TB, Nebelsick JH

Clypeaster under pressure: strengthening structures and virtual modulations of an echinoid's test. 2017. *Geological Society of America Abstract with Program* 49:

Authors: Grun TB, von Scheven M, Bischoff M, Nebelsick JH

Taphonomy as a proxy for stable shell constructions. 2017. *International Meeting on Taphonomy and Fossilization: Taphos*. Vienna, Austria.

Authors: Grun TB, Nebelsick JH

Post-mortem encrustation patterns of *Clypeaster rosaceus* tests from San Salvador, The Bahamas and their effects on preservation potential. 2017. *International Meeting on Taphonomy and Fossilization: Taphos*. Vienna, Austria.

Authors: Zille S, **Grun TB**, Nebelsick JH

The significance of internal supports and plate interlocks for the test integrity and the preservation potential of clypeasteroid echinoids. 2016. *Geological Society of America Abstract with Program* 48:212

Authors: Grun TB, Nebelsick JH

Morphology and crushing behavior of the minute clypeasteroid *Echinocyamus pusillus*. 2016. *Geological Society of America Abstract with Program* 48:184

Authors: Grun TB, Nebelsick JH

Echinocyamus test morphology - a minute echinoid as a biological role model for biomimetics. 2016. *Book of Abstracts: European Conference on Echinoderms*. Sopot, Poland.

Authors: Grun TB, Nebelsick JH

Smashing echinoids: *Echinocyamus* on the chopping block. 2016. *Book of Abstracts: European Conference on Echinoderms*. Sopot, Poland.

Authors: Grun TB, Nebelsick JH

Structures and Sutures in *Clypeaster rosaceus*. 2016. *Book of Abstracts: European Conference on Echinoderms*. Sopot, Poland.

Authors: Grun TB, Amariei AE, Nebelsick JH

From the womb to the tomb - accompanying a Caribbean sand dollar through its life. 2015. *Geological Society of America Abstracts with Program* 47:427.

Author: Grun TB

Taphonomy of *Clypeaster rosaceus* as a model for the preservation potential of a 3-dimensional multi-element skeleton. 2015. *Geological Society of America Abstract with Program* 47:575

Authors: Grun TB, Nebelsick JH

Stabilizing instable skeletons: mapping plate connections and internal supports of clypeasteroid echinoids and their implication for preservation potentials in the rock record. 2015. *Geological Society of America Abstract and Program* 47:575.

Authors: Nebelsick JH, **Grun TB**, Stoll N, Schaich C

Further conference contributions

The following conference contributions have been presented during the time of the PhD thesis, but are not directly related to its topic.

Learning from the present, understanding the past: drill hole recognition for the fossil record. 2017. *International Meeting on Taphonomy and Fossilization: Taphos*. Vienna, Austria.

Author: Grun TB

Geographic and temporal gradients of circumalpine Oligo-Miocene carbonates based on high resolution quantification of component diversity. 2016. *Geological Society of America Abstract with Program* 48:249

Authors: Nebelsick JH, Bassi D, Nietsch F, **Grun TB**

Coding the echinoid skeleton - a quasimetric description of complex taphonomic pathways. 2016. *Geophysical Research Abstracts. European Geosciences Union General Assembly*. Vienna, Austria.

Authors: Grun T, Nebelsick J

Quantifying component diversities along temporal and geographic gradients in Cenozoic circumalpine carbonates. 2016. *Geophysical Research Abstracts. European Geosciences Union General Assembly*. Vienna, Austria.

Authors: Nebelsick J, Bassi D, Nietsch F, **Grun T**

Drilling predation, an ecological tool through time. 2015. *International Echinoderm Conference*. Playa del Carmen, Mexico. 40–41.

Authors: Grun TB, Nebelsick JH

Taphonomy and Echinoids: a quasimetric approach to quantify taphonomic alterations. 2015. *International Echinoderm Conference*. Playa del Carmen, Mexico. 104–105.

Authors: Grun TB, Nebelsick JH

Taphonomic pathways and environmental differentiation based on the clypeasteroid echinoid *Echinocyamus*. 2015. *Geophysical Research Abstract. European Geosciences Union General Assembly*. Vienna, Austria.

Authors: Grun T, Nebelsick J

Microfacies quantification: assessing component diversity among circumalpine Paleogene and Neogene carbonates. 2015. *Geophysical Research Abstract. European Geosciences Union General Assembly*. Vienna, Austria.

Authors: Nebelsick J, Bassi D, Nietsch F, **Grun T**

Book review and report

These contributions have been written during the time of PhD, but are not directly related to the topic.

Fortey: Fossils – The Key to The Past. 2017. *Priscum* 24:18–19.

Author: Grun TB

8th International Meeting on Taphonomy and Fossilization TAPHOS 2017. 2018. *The Palaeontological Association Newsletter* 97:59–60.

Author: Grun TB

Public outreach

The following contributions are directly related to the work of this thesis with the aim to introduce young scientists and the public to biomimetic research.

Museum exhibition

Baubionik – Biologie beflügelt Architektur. Rosensteinmuseum, Staatliches Museum für Naturkunde Stuttgart. October 19th, 2017 – May 6th, 2018.

Companion volume for the exhibition

Bauprinzipien und Strukturdesign von Seeigeln – Vorbilder für bioinspirierte Konstruktionen. 2017. In Baubionik – Biologie beflügelt Architektur. Stuttgarter Beiträge zur Naturkunde C. J Knippers, U Schmid, T Speck (eds). 82–93. Stuttgart: *Staatliches Museum für Naturkunde*.

Authors: Grun TB, von Scheven M, Geiger F, Schwinn T, Sonntag D, Bischoff M, Knippers J, Menges A, Nebelsick JH

DAAD RISE supervision

The German Academic Exchange Service (Deutscher Akademischer Austausch Dienst) organizes Research Internships in Science and Engineering that allow students to participate in scientific research projects.

Lectureships

The following courses have been taught as course instructor with lectureship for both bachelor and master students in Geosciences.

Aktuopaläontologisches Geländepraktikum 2016, May 14th – May 21st.
Institute for Marine Biology, Campese, Giglio, Italy

Aktuopaläontologisches Geländepraktikum 2016, October 5th – October 14th. Giglio, Italy.
Institute for Marine Biology, Campese, Giglio, Italy

Courses and workshops

The following courses and workshops have been attended with direct implications for this thesis.

Taphonomy and Ecology of Tropical Environments 2015
Institution: *Gerace Research Centre*, *College of the Bahamas*; *University of Florida*

Historical Ecology and Conservation Paleobiology 2016
Institution: *University of Vienna*

Taphonomy and Ecology of Tropical Environments 2017
Institution: *Gerace Research Centre*, *University of the Bahamas*; *University of Florida*

Ecological Modelling in Palaeontology 2018
Institution: *University of Vienna*

Appendix II:

Manuscripts

Manuscript 1

The skeleton of the sand dollar as a biological role model for segmented shells in building construction: a research review

Chapter 11
The Skeleton of the Sand Dollar as a Biological Role Model for Segmented Shells in Building Construction: A Research Review

Tobias B. Grun, Layla Koohi Fayegh Dehkordi, Tobias Schwinn, Daniel Sonntag, Malte von Scheven, Manfred Bischoff, Jan Knippers, Achim Menges, and James H. Nebelsick

Abstract Concrete double-curved shell constructions have been used in architectural design and building constructions since the beginning of the twentieth century. Although monolithic shells show a high stiffness as their geometry transfers loads through membrane forces, they have been mostly replaced by the more cost-efficient lattice systems. As lattice systems are covered by planar glass or metal panes, they neither reach the structural efficiency of monolithic shells, nor is their architectural elegance reflected in a continuous curvature. The shells of sand dollars' – highly adapted sea urchins – combine a modular and multi-plated shell with a flexible, curved as well as smooth design of a monolithic construction. The single elements of the sand dollars' skeleton are connected by calcite protrusions and can be additionally supported by organic fibres. The structural efficiency of the sea urchin's skeleton and the principles behind them can be used for innovations in engineering sciences and architectural design while, at the same time, they can be used to illustrate the biological adaptations of these ecologically important animals

T.B. Grun (✉) • J.H. Nebelsick
Department of Geosciences, University of Tübingen, Hölderlinstraße 12, 72074 Tübingen, Germany
e-mail: tobias.grun@uni-tuebingen.de; nebelsick@uni-tuebingen.de

L. Koohi Fayegh Dehkordi • M. von Scheven • M. Bischoff
Institute for Structural Mechanics (IBB), University of Stuttgart, Pfaffenwaldring 7, 70550 Stuttgart, Germany
e-mail: koohi@ibb.uni-stuttgart.de; mvs@ibb.uni-stuttgart.de; bischoff@ibb.uni-stuttgart.de

T. Schwinn • A. Menges
Institute for Computational Design (ICD), University of Stuttgart, Keplerstraße 11, 70174 Stuttgart, Germany
e-mail: tobias.schwinn@icd.uni-stuttgart.de; achim.menges@icd.uni-stuttgart.de

D. Sonntag • J. Knippers
Institute of Building Structures and Structural Design (ITKE), University of Stuttgart, Keplerstraße 11, 70174 Stuttgart, Germany
e-mail: d.sonntag@itke.uni-stuttgart.de; j.knippers@itke.uni-stuttgart.de

J. Knippers et al. (eds.), *Biomimetic Research for Architecture and Building Construction*, Biologically-Inspired Systems 9, DOI 10.1007/978-3-319-46374-2_11

within their environments. The structure of the sand dollar's shell is investigated using modern as well as established imaging techniques such as x-ray micro-computed tomography (μCT), scanning electron microscopy and various optical imaging techniques. 3D models generated by μCT scans are the basis for Finite Element Analysis of the sand dollar's shell to identify possible structural principles and to analyse their structural behaviour. The gained insights of the sand dollar's mechanical properties can then be used for improving the state-of-the-art techniques of engineering sciences and architectural design.

11.1 Introduction

During the early twentieth century, iconic concrete shells were built with a double-curved geometry adapted to transferring loads through membrane forces. Today, monolithic shells are mostly replaced by grid shells consisting of cost-efficient lattice systems covered by planar glass or metal panes. These systems neither reach the structural efficiency of monolithic shells, nor is their architectural elegance reflected in a continuous curvature. The assembly of on-site segmented shells from prefabricated elements is a useful alternative. It reduces building time on-site and potentially lowers costs due to prefabrication and allows for a smooth surface curvature. Structural segment joining is necessary but can conflict with the desired membrane state for load bearing by reducing bending stiffness in the joints and lowering the capacity for the transfer of normal or shear forces. Heterogeneities in membrane stiffness can also trigger the bending of homogeneous shells in a pure membrane state. The properties and arrangement of the joints are thus of crucial importance for the load-bearing behaviour of segmented shells.

The shells of sand dollars, which are highly adapted sea urchins, are currently being studied as a biological concept generator. These shells consist of modular polygonal plates linked at their edges by calcite protrusions and organic fibres. Sand dollars show a variety of geometric variations with respect to overall shape and plate arrangements. The high load-bearing capacity of the sand dollar skeleton is well adapted to turbulent environments. These echinoids show morphological features that are also required from many shells in building construction: a mainly flat curvature, apertures and column-like connections between the upper and the lower half of the shell. The sand dollar thus serves as a suitable model for shells in building construction.

Analyses of the functional morphology of various sand dollars by focusing on the lightweight stereom of the plates, the connective joints and the role of organic and inorganic components provide insights into the biological principles of sand dollar adaptions. The examined material and structural properties can be used as a basis for Finite Element Analysis (FEA) leading to a better understanding of the functional morphology of the shell. The physical representation of the skeleton and joints by additive fabrication processes and the influence of additive manufacturing on the joints might represent innovations in building constructions of shells.

Various conditions for load transfer and stiffness at the joints and geometrical restrictions for the segments will be considered as variable parameters in the process. This design methodology can be used to investigate the various geometries of sand dollar species as the result of evolutionary adaptions to the mechanical conditions of their respective habitats and to develop design recommendations for joint pattern layouts for segmented shells in building construction. Investigations of possible ways to transfer the above-mentioned performative qualities and morphological principles of the sand dollar to building construction can be performed. Biological principles in modular shell systems allow high degrees of geometrical adaptability and structural efficiency attributable to component differentiation.

11.2 Clypeasteroid Echinoids as Biological Role Models

11.2.1 Hierarchically Organised Skeletons of Echinoids

Echinoids are hierarchically organised marine invertebrates featuring a multi-element skeleton. The animals exhibit five hierarchical levels (e.g. Nebelsick et al. 2015) including (1) the whole individual, (2) the multi-plated skeleton, (3) single skeletal plates, (4) a microstructure of various stereom types of which the single plates are constructed and (5) the nanostructure of the biomineralised stereom.

The highest organisational level is represented by the whole echinoid including all soft and hard parts of the individual. The skeleton is of mesodermal origin and is, in most cases, entirely covered by soft epidermis (e.g. Hyman 1955). Although it is an endoskeleton, the sea urchin test (calcareous skeleton without appendages) functions as an external skeleton (e.g. Goldberg 1992) protecting vital internal organs from both biotic (e.g. predators) and abiotic (e.g. strong water agitation) stress. The test also serves as a substrate for various surface appendages including spines, which are mounted on tubercles of the test surface, and pedicellariae, which are microscopic jaw-like structures that can remove particles and organisms from the echinoid surface. In addition, the echinoid skeleton features numerous apertures in the test including the peristome (mouth), periproct (anus), genital pores, ocular pores, the pore pairs for the respiratory tube feet of the ambulacral system and, in clypeasteroids, secondary unipores, which represent single holes for accessory tube feet. A further skeletal feature found inside the test is the complex jaw apparatus bearing self-sharpening teeth.

The skeleton itself consists of multiple rows of single plates that are interconnected by soft tissue such as collagenous filaments, as found in regular echinoids and, furthermore, interlocking skeletal protrusions in clypeasteroid echinoids (e.g. Seilacher 1979). Most regular echinoids, which show pronounced pentameral symmetry, possess similarly shaped plates throughout the skeleton, although these can be highly variable in some groups of irregular echinoids. Sea urchins feature two dominant types of plates in distinct double rows, the ambulacralia and the

interambulacralia. Ambulacral plates bear the pores for the respiratory tube feet. In clypeasteroids, these pores are concentrated in a well-developed flower-like pattern on the dorsal surface. In addition, calcareous elements are present in spines, the jaw apparatus, and within diverse supporting structures on and within the test.

Every individual skeletal plate is constructed of a lightweight stereom, a sponge- or lattice-like three-dimensional trabecular system that is comparable with the microstructure of the bones of vertebrates (Millott 1967). The trabeculae are synthesised by specialised cells. Although biomineralisation occurs in various steps, each single plate behaves as a single crystal under polarisation, which combines both the advantages of a monolithic structure and a modular and multi-element construction (e.g. Raup 1959).

11.2.2 Morphological Details of Clypeasteroids

The echinoids are divided into two groups, the regular and irregular echinoids, based on their symmetry and position of the periproct (anus). In the mostly spherical regular echinoids, which show a generally pentamerous symmetry, the peristome (mouth) is oriented towards the oral (ventral) side, whereas the periproct is located on the aboral (dorsal) side. In the irregular echinoids, a prominent bilateral symmetry is developed and the periproct moves outside of the apical disc. In one group of irregular echinoids, namely the clypeasteroids, the periproct is positioned on the oral side of the test between the posterior ambitus (the "rim" of echinoids) and the centrally positioned peristome.

Clypeasteroids show a high degree of morphological variability (e.g. Müller 1854; Lang 1896; Mortensen 1948). Typical infaunal living individuals, such as the genera *Leodia*, *Mellita* and *Scutella* and some *Clypeaster* species, are highly flattened, whereas the epifaunal *Clypeaster rosaceous* is domed (Fig. 11.1). Exceptional features of the clypeasteroid test are the internal supports, buttress- or pillar-like structures that connect the oral and aboral plated surfaces of the test (Fig. 11.1d, e). Buttresses generally occur within the interambulacral fields, whereas pillars are restricted to the ambulacral fields (Mooi 1989). The morphology of these structures can be related to the overall test shape with flattened skeletons tending to form delicate needle-like (e.g. *Clypeaster subdepressus*) or labyrinthic (e.g. *Leodia sexiesperforata*) structures, whereas domed echinoids (e.g. *Clypeaster rosaceus*) are characterised by more robust and occasionally coalesced internal supports (e.g. Mortensen 1948; Mihaljević et al. 2011).

An additional important morphological feature of some especially flattened and discoidal sand dollars are the lunulae, which are round to slit-like holes (e.g. *Leodia*, *Mellita*) or indentations (e.g. *Rotula*, *Encope*) in the skeleton (Fig. 11.1b). Lunulae can occur in various numbers and can either grow during ontogenesis or arise by resorption of skeletal material (e.g. Hyman 1955). The clypeasteroids are further characterised by (1) the presence of respiratory tube feet in a flower-like petalodium

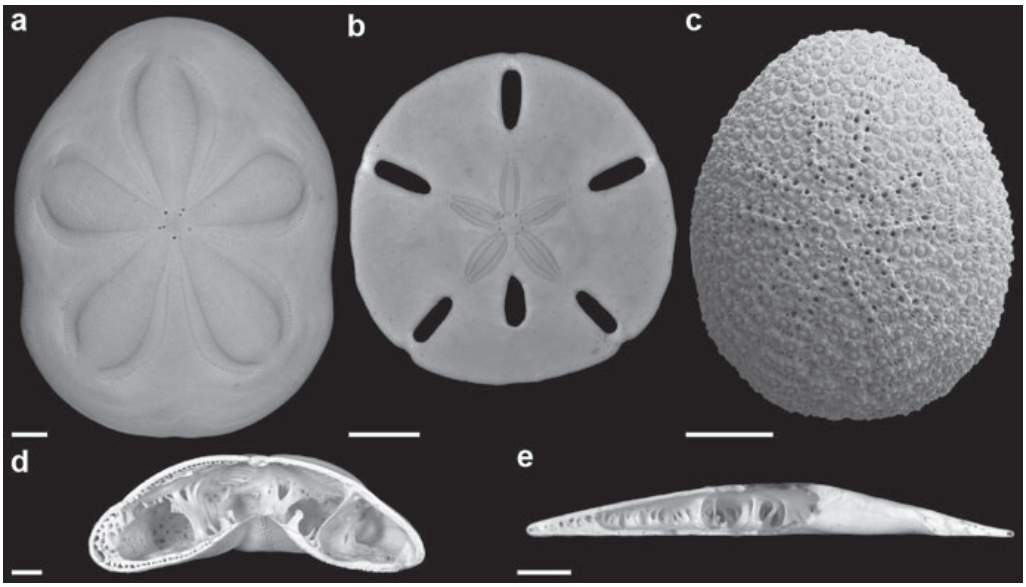

Fig. 11.1 Photographs of clypeasteroid echinoids. (**a**) *Clypeaster rosaceus*, (**b**) *Leodia sexiesperforata* and (**c**) *Echinocyamus pusillus* in aboral view. (**d**) Domed *Clypeaster rosaceus* featuring an inflated peristome. (**e**) Highly flattened *Mellita tenuis* in section with the anterior to the left. *Scale bars* (**a**, **b**, **d**, **e**) = 1 cm, *scale bar* (**c**) = 1 mm

on the aboral surface, (2) secondary tube feet distributed across the whole skeleton, (3) highly differentiated minute spines on the surface of the test, (4) a branching system of food grooves on the oral surface leading to the peristome, and (5) a highly modified jaw apparatus found inside the test.

The morphological variability of clypeasteroids is clearly shown by the species *Clypeaster rosaceus*, *Echinocyamus pusillus* and *Leodia sexiesperforata* (Fig. 11.1). The sea-biscuit *Clypeaster rosaceus*, one of the largest known clypeasteroids, is characterised by its inflated shape. It lives epifaunally on top of the sea floor and masks itself by using available materials such as algae and sediment particles. The test shape is moderately domed and the oral surface shows a bell-shaped indentation around the mouth. The oral and aboral surfaces are interconnected by massive pillars. Furthermore, a second internal wall is present that is partly perforated to supply the water vascular system between the two test layers (Mortensen 1948).

The minute sand dollar *Echinocyamus pusillus* is one of the smallest clypeasteroids rarely exceeding 15 mm in length. It is moderately domed and its oral surface is slightly indented. *Echinocyamus pusillus* features buttresses instead of pillars as internal supports. It lives infaunally in a wide variety of substrates and depths (Ghiold 1982; Grun et al. 2014; Grun and Nebelsick 2015).

The six-holed sand dollar *Leodia sexiesperforata* is a discoidal, highly flattened, medium-sized echinoid that burrows through the sediment just underneath the surface feeding on organic material. The distal areas of the skeleton near the ambitus are characterised by a dense meshwork of labyrinthic internal support structures.

11.2.3 Functional Morphology and Habitat Adaptation

Echinoids are highly adapted to their marine environments. Their habitats range from rocky areas with rough breaker zones and high water agitation to those characterised by soft bottom sediments and slow currents (see Mortensen 1948; Schultz 2006). Adaptations to the environment can be seen in the high variability of skeletal morphologies and behaviour in both regular and irregular echinoids.

Most clypeasteroids live shallowly buried within soft sediment, although some adopt an upright position stuck into the sediment (Timko 1976; Lawrence et al. 2004). *Clypeaster rosaceus*, in contrast, shows an epifaunal life style on the sediment surface (Kier and Grant 1965). These various life styles are accompanied by morphological adaptations of the echinoids shell including general shape and internal structures. Infaunal living genera are generally characterised by highly flattened skeletons that are discoidal. Numerous minute spines cover the surfaces of these echinoids and fullfil a variety of purposes (see Smith 1984; Mooi 1986). The function of lunulae, the hole- to slit-like apertures in some sand dollar tests, has been discussed in detail by Smith and Ghiold (1982) who concluded that lunulae, on the one hand, can increase the food gathering capacity of the animal by shortening the transportation distance from the aboral surface to the peristome (Goodbody 1960; Ghiold 1979; Seilacher 1979; Smith 1980; Alexander and Ghiold 1980) and, on the other hand, can improve the hydrodynamic stability of these near surface dwelling sand dollars (Telford 1981). Telford et al. (1985), however, argued that their observations conclusively showed that food material is collected by surface podia on the oral surface alone.

Most clypeasteroids possess internal supports connecting the oral and aboral plates of the test. These buttress- and pillar-like structures have been interpreted as increasing the overall test stability of the extremely flattened form of some sand dollars, which can inhabit high energy environments (e.g. Seilacher 1979). There are, however, no empirical studies that have investigated the role of internal supports on the stability of clypeasteroid sea urchins. Furthermore, the role of spines, as shown for regular echinoids (Nichols 1962; Strathmann 1981) has barely been explored. In addition, the significance of soft tissues, which not only cover the plates, but also interconnect them, for the stability of clypeasteroids is poorly understood.

Not only are macroscopic morphological features of interest with respect to the stability of the echinoids, but also their plate arrangements, their mode of jointing, and their microstructure. A high variation of stereom types in echinoid plates and spines is exhibited (e.g. Smith 1980; Grossmann and Nebelsick 2013). These diverse stereom types are highly variable with respect to arrangement and density. They are adapted for various tasks including support, the interlocking of muscle tissue and the provision of surfaces for spine articulations and space fillers (Smith 1980). A further feature seen at the microscopic level are skeletal extensions that reach from one plate

into neighbouring plates, thus potentially increasing interlocking (e.g. Seilacher 1979). Again, few studies have revealed the distribution and morphology of these interlocking features or the way that they contribute to the general strength of the test.

Functional morphological aspects are present at all hierarchical levels (see Nebelsick et al. 2015) enabling the echinoid to adapt to various environments. Biomimetic investigations might reveal more detailed insights into these evolutionary adaptive strategies and such discovered functional principles can potentially be transferred from nature and used to inspire construction techniques in architectural applications. Furthermore, structural analysis and developmental strategies employed during building processes can be used in a reverse biomimetic approach to improve the knowledge of the adaptations of sea urchins and their skeletons to the specific environments in which they live.

11.3 Biomimetic Steps from Echinoid Role Models to Building Constructions

11.3.1 Modelling of Skeletons as a Tool for Structural Analysis

Computational simulations of organisms, such as echinoids, can be difficult because of their complexity and highly structured body plan. A detailed description of the model including every morphological detail is thus not practicable. To obtain a meaningful model, concrete questions and working hypotheses have to be tested in order to be verified or falsified. For the mechanical modelling of sand dollars envisaged here, the most important questions concern the role of the specific geometry and segmentation of the skeleton, the mechanical properties of the joints, the role of the trabeculae and the relationship of these components to the environments to which the sand dollars are exposed.

The simulations are based on three models of the sand dollar, a full model, a reduced model and an abstracted model. The aim of a full or detailed model, which is pursued at the beginning of this research project, is to strive for a best possible approximation of the actual geometric, topological and material properties of the sand dollar. Reduced and abstracted models are later derived from the lessons learned with the full model. The reduced model preserves the basic mechanical and structural features of the full model at significantly lower computational expense, whereas the abstracted model represents the principal underlying structural concept with the aim of implementation in architecture. Questions that are addressed here are whether certain mechanical functionalities are intrinsically related to the pattern layout, the properties of the joints and the overall geometric and topological features of the segmented skeleton, including the trabeculae.

One fundamental problem of modelling organisms, as opposed to engineering structures, is that no protocol is available specifying the geometry, constructional

details and materials used. The same is true for loads and boundary conditions. Instead, two complementary methods gain such information by using measurements and making feasible assumptions. Such information forms the basis for the finite element modelling described in this section.

For the material behaviour, assumptions are made based on available data from the literature for the stiffness and strength of the base material and physical tests. In this context, we have to stress that the notions of "material" and "structure" are somewhat ambiguous, because neither of them can exist without the other. This means that, for instance, a certain porosity of the stereom might be advocated for material behaviour and related parameters specifying stiffness, strength etc. Porosity can be regarded as a structural feature, given a sufficient geometric fidelity. In this case, the different material parameters characterising the base material are relevant.

The skeleton of clypeasteroid echinoids consists of high magnesium calcium carbonate, for which material properties, such as Young's modulus (around $7{\cdot}10^7$ kN/m^2 for the solid base material, neglecting porosity), can be taken from the literature. The porosity of the stereom is partly represented in the identified geometry but needs to be extended for a proper reduction of the related moduli.

Today, mechanical problems in engineering are mostly solved with the finite element method, a numerical method that approximately solves partial differential equations. A major technical issue when deriving a finite element model is the generation of a feasible mesh. Powerful tools exist for mesh generation given the Computer Aided Design (CAD) data of the geometry. For the problem at hand, this means that, first, a CAD model has to be extracted from the raw data, which can be automatically processed by meshing software in a second step. Both steps are not trivial and, in general, cannot be performed in a fully automatic manner. The automatically generated mesh generally needs manual refinements. In addition to employing such a surface mesh, the use of voxel-based finite element meshes (Fig. 11.2) is possible, which can be created from the raw data. In this case, every finite element geometrically represents a regular hexahedron. The grey scale can be related to the density or porosity and can thus provide hints towards realistic material properties.

Such a voxel-based approach has both advantages and disadvantages when compared with a standard CAD-FEM transition. The voxel model is limited in smoothness because of the resolution of the CT-images and the available soft- and hardware. The obvious disadvantage is the poor geometric representation of the surface contour, which potentially compromises accuracy of the computational results. A decisive advantage is also the possibility of a direct transfer from raw data to a numerical model. Additionally, for linear analyses, the underlying element stiffness matrices have the same generic format. At this point, which of the advantages and disadvantages of both approaches will prevail is not yet clear. For the time being, both concepts are pursued in parallel.

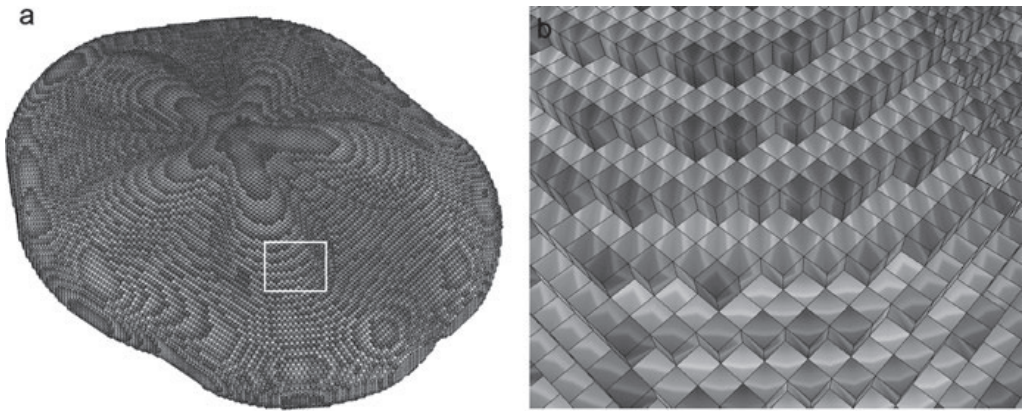

Fig. 11.2 Voxel-based mesh (Cartesian grid) of *Clypeaster rosaceus*. (**a**) Oblique view of the mesh. The region within the square shows (**b**) single voxels in detail containing material density information represented in different *grey* values

11.3.2 Morphospace and Optimisation of Skeletal Structures

In evolutionary biology, the morphological features of an individual are the observable instances of a theoretical solution space (Eble 2004). Morphological spaces or "morphospaces" constitute formal spaces defined by multiple dimensions that each correspond to a variable parameter of morphology. Morphospaces serve as computational and conceptual tools that allow the vast variation of organismal form in living nature to be described and associated (Mitteroecker and Huttegger 2009). In computational design, the generation of form is based on algorithmic processes that operate within specific variable ranges of selected parameters. The combined variance range of each parameter in the computational model can be conceptualised as delineating an n-dimensional space that is similar to the morphospaces of theoretical morphology in biology. In this case, individual building elements are represented as n-dimensional points.

In order to address the problem of the exploration into fabrication-related design, a method for evaluating design-spaces has already been developed in previous work and allows for the quantification of the available design space associated with a particular fabrication setup. The so-called *Machinic Morphospace Method* adopts and transfers the method from the field of evolutionary biology to architectural design in order to describe the morphological variance of building elements together with the machine constraints necessary for their fabrication within one methodological framework (Menges 2013). This transfer allows the representation of the variable parameter range of both form generation and materialisation in one theoretical morphospace. In this theoretical space, different regions can be distinguished such as the *Producible region of Possible Form* (PPF) as a subset of the *Geometrically Possible region of Form* (GPF) defined by the computational design process (Fig. 11.3) (Menges 2013). In the context of digital fabrication, the PPF

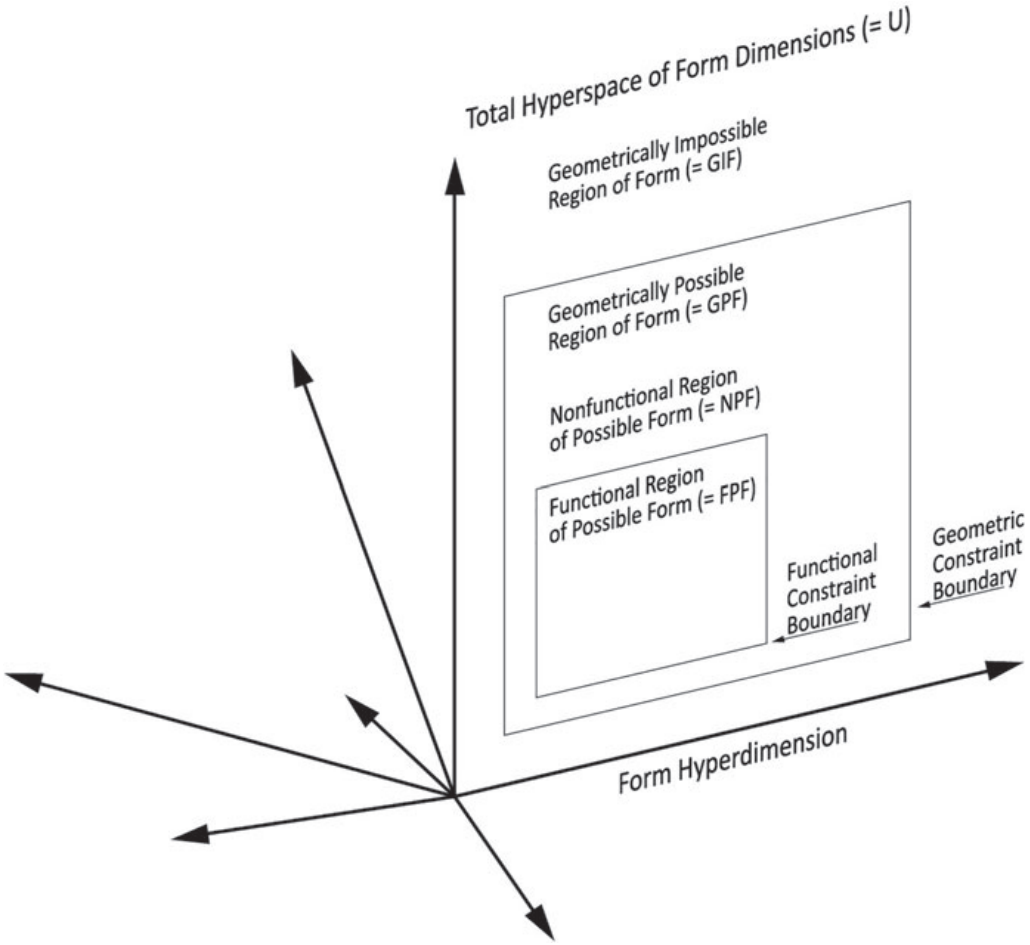

Fig. 11.3 Regions of a hyper-dimensional theoretical morphospace in which each dimension represents one parameter of form (Menges 2013)

relates a specific machine configuration to a space of possible producible outcomes, its machinic morphospace (Schwinn et al. 2012). While ongoing technological advances, such as the advent of robotics, increase the capacities of digital fabrication and, in consequence, expand the space of producible forms, the search space for the *Functional region of Possible Form* (FPF), as the subset of the GPF, increases proportionally. On the one hand, such correlations increase the possibility that a particularly functional region of form is contained within a producible region determined by a particular fabrication setup. On the other hand, the correlations also offer the possibility for the determination of fabrication requirements with respect to morphological parameters.

Based on the premise of biological evolution as an adaptive agent, a biomimetic design approach based on the analysis of biological role models and on the transfer of morphological features into the context of architectural and structural design provides a filter for identifying particularly functional regions of the producible form

(Krieg et al. 2011). In the context of the design of segmented shells, the machinic morphospace method in conjunction with a biomimetic design approach has proven to be a viable strategy as described in the case studies below.

11.3.3 Optimisation of Shell Structures in Architecture

Numerous strategies for shape finding and the optimisation of shell structures have been developed including the experimental work of Heinz Isler (Chilton 2000) and the analytical methods of Bletzinger and Ramm (1999) and Arnout et al. (2012). Insights into form finding and the optimisation of shell structures inspired by nature have been explored in previous research (e.g. Ramm et al. 1993). Most existing work on form finding deals with homogeneous smooth shell structures. Monolithic concrete shells are of less relevance for today's architecture mainly because of the extensive effort needed for individually customising complex reinforcement layouts. An alternative might be the erection of shells from prefabricated segments; this offers many advantages for prefabrication, transportation and on-site assembly. Only a few studies exist on the optimal joint layout for segmented shells. Some preliminary studies have, however, demonstrated possible applications (Fildhuth et al. 2012; Breitenberger et al. 2013). The major difficulties lie in the choice of a parameterised tessellation taking into account fabrication constraints, the choice of suitable optimisation algorithms, the coupling of optimisation algorithms with finite element software and the generation of a functional interface.

In the case of the structural optimisation of segmented shells, the objective functions are generally non-linear with respect to the design variables and are non-continuous. Evolutionary algorithms, which are metaheuristic search and optimisation processes, have shown promise in optimising such problems as they only require the evaluation of the objective function itself. Although not converging as rapidly as gradient-based methods, they tend to have fewer problems with discontinuities. In the context of segmented shells, it might be necessary to deal with multiple objective functions. This is true for the biological role model (e.g. mechanical stability, functional aspects and ontogenesis) as for the architectural counterpart (stiffness, weight, forces in the joints and stability). Evolutionary algorithms can deal with several objective functions at once without the need of preliminary reduction to one objective function; they can directly sample the Pareto-front and are therefore particularly suitable for multi-criteria optimisation. A comprehensive overview concerning evolutionary algorithms for multi-objective optimisation is given by Fonseca and Fleming (1995) and Deb (2011).

For the optimisation of grid shells, Dimcic and Knippers (2011) have used a standard evolutionary optimisation algorithm. An evolutionary optimisation algorithm has also been used by Fildhuth et al. (2012) to minimise tension forces in adhesive joints under various geometric conditions for glass panes and overall shell geometry. This has proved to be a suitable method as it handles discontinuities of a

segmented shell and can be adjusted to various fitness criteria and penalty functions. The evolutionary methodology also requires the identification of essential geometric parameters and their constraints in order to describe the diversity of the studied skeletons.

The optimality of a sea urchin skeleton under various loading conditions has been analysed through parametric studies (Philippi and Nachtigall 1996). In this study, the mechanical response of a regular sea urchin shell to external loading was calculated by using Finite Element Analysis. The results were used to link shell shape to mechanical behaviour. The influence of the joints between the various shell segments was, however, not taken into account. Few studies of the mechanical behaviour of the shell are available for irregular sea urchins.

Today, new computational tools are available allowing an advanced optimisation of segmented shells in architecture. In order to study the biological role model with respect to its optimality, the data of the 3D model needs to be processed and reduced to a manageable data size. Thus, all relevant geometrical and mechanical characteristics need to be identified in order to generate a parametric design model. The definition of geometric parameters is established with the goal of modelling the biological diversity of the sand dollar's plate layout and morphological features, such as the length, width and height, plate topology, shell curvature, the quantity and position of skeletal apertures, and the quantity and position of internal supports. The 3D design model of the skeleton is therefore extended towards a parametric model that allows the description of natural diversity by variation of the design parameters. The goal is to keep the geometrical and mechanical model as simple as possible in order to reduce the amount of parameters and therefore computation time.

11.4 Examples for Echinoid Skeletons as Potential Models for Biomimetic Architecture

11.4.1 Potential for Building Construction

Continuous shells, if properly designed, can be highly efficient and aesthetic structures and have therefore a high potential in the field of architecture. In order to avoid disadvantages such as expensive and material-consuming formwork, which is presented by continuous shells during construction, segmented shells might be an interesting alternative to monolithic shells.

Segmented shells have been built from glass (Blandini 2005; Almegaard et al. 2007; Bagger 2010) or wood (La Magna et al. 2013) with only limited use at larger scales. Since connections between adjacent segments can hardly deal with forces occurring in the constructions, segmented shells are still restricted to an academic research level. The main reason for this is the lack of applicable joint constructions satisfying conditions of sufficient structural load transfer and the restricted adaptability to various geometric and static situations. Only a few studies

on this subject can be found (Wester 1990; Veer et al. 2003), which either use adhesives for joining or apply combined mechanical and adhesive techniques. Joints between prefabricated segments nearly always weaken shell structures as they disturb the continuity of their stiffness. Joints can also reduce the capacity to transfer bending moments or membrane forces. The structural capacity of joints not only impacts the overall load-bearing behaviour of the shell, but also determines the efficient arrangement of the segments on the 3D surface. Their geometry and dimensions are usually restricted by specific fabrication conditions and transport and assembly options. Usually, size, aspect ratios, corner angles and curvature are limited. Simple engineering considerations for regular shell geometries are not possible for the complex interactions present in 3D shapes.

In order to profit from load-bearing behaviour via membrane forces, shells should (1) have a continuous smooth curvature, (2) be extremely thin compared with their span dimensions, (3) have continuous equal stiffness (no sudden changes in thickness), and (4) have membrane-specific support boundary conditions. The last-mentioned condition is often difficult to achieve as it might result in lateral bending and constraints in the case of settlement or temperature loads. Here, the arrangement of joints might reduce such interior constraints (Fildhuth and Knippers 2011).

11.4.2 Application in Demonstrators

In previous work, the Institute for Computational Design (ICD) and the Institute for Building Structures and Structural Design (ITKE) at the University of Stuttgart, Germany, in collaboration with the Department of Geosciences at the University of Tübingen, Germany, have examined the architectural and structural potential of transferring morphological principles from the skeletons of echinoids to lightweight construction and, specifically, to the design of segmented shells in architecture.

In a first study in 2011, a temporary pavilion was built that explored the biomimetic transfer of four essential morphological principles to architecture. These principles were identified in the skeleton of echinoids and are related to (1) hierarchical organisation, (2) plate arrangement, (3) differentiation of plate morphology, and (4) plate connection.

One of the most prominent features of the plate morphology of the sea urchin is the arrangement of polygonal plates in the shell, an arrangement that is based on a three-plate principle. This principle describes the fact that, on each node, three-plate edges intersect that allow the sea urchin's shell to work as a pure plate structure (Wester 2002), which consists of rigid plates interconnected by shear-resistant hinges. The three-plate principle potentially avoids instable structural configurations and has been transferred to the computational design model of the above-mentioned pavilion resulting in a modular system in which three edges are assured to meet at one point.

Similar to the biological role model in which plates are connected by microscopic calcite protrusions along the plate edges, primarily shear forces and normal forces

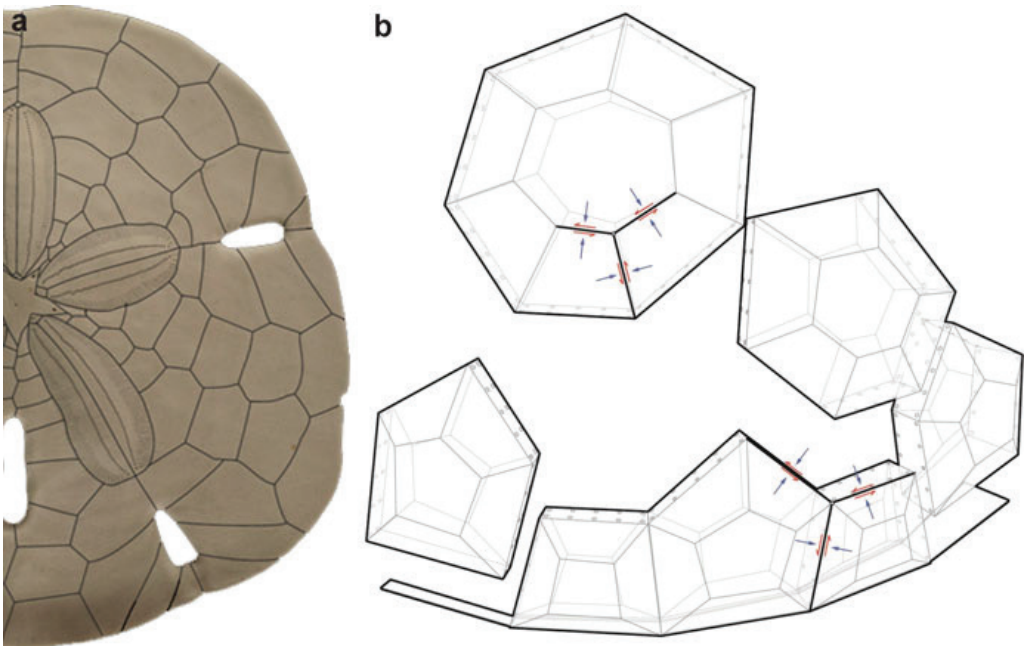

Fig. 11.4 ICD/ITKE Research Pavilion 2011 showing (**a**) the biological three-plate principle (Photo: Wolfgang Gerber, Department of Geosciences, University of Tübingen, Germany) and (**b**) the technological transfer in terms of plate arrangement and module assembly

are transferred at the connection level. Because of the three-plate principle, the transfer of bending moments globally is still possible but requires a certain bending stiffness of the segments, as can be provided by a double-layer structure of each element.

As with most biological structures, sea urchins and thus sand dollars exhibit a strict hierarchical organisation (e.g. Nebelsick et al. 2015). This principle has also been transferred to the research pavilion in which, at the plate level, finger joints have been glued together to form polyhedral modules, which, in turn, are assembled together with simple screw joints. At each hierarchical level, the three-plate principle has been respected (Fig. 11.4). Achieved by computational design methods and customised Computer Aided Manufacturing methods (CAM) (La Magna et al. 2013), the pavilion's overall form includes surface regions with strongly varying Gaussian curvature and various module and plate sizes in order to demonstrate the flexibility of the proposed prototypical building system. Whereas the arrangement and shape of the modules was further developed according to general design and engineering considerations, the transfer of these principles insured that, at the plate level, primarily in-plane forces occurred, which led to a highly efficient lightweight structure made entirely of only 6.5 mm thin plywood plates (Fig. 11.5).

In a follow-up project, the biomimetic transfer of the previously identified principles was further developed and also transferred from an academic to a building construction context resulting in the Landesgartenschau Exhibition Hall. Its main

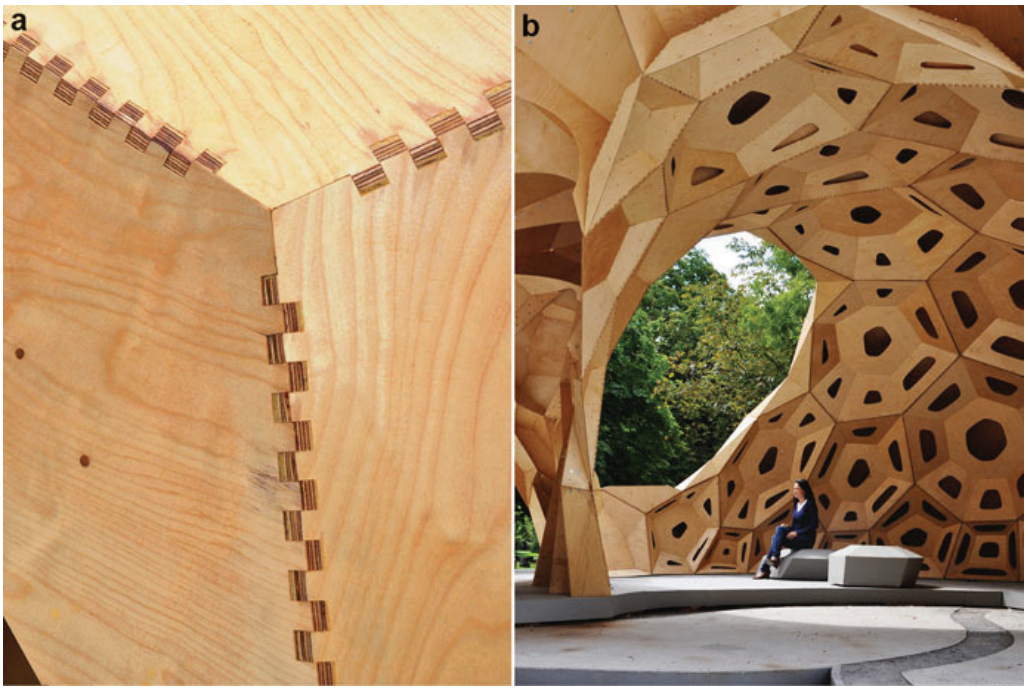

Fig. 11.5 ICD/ITKE Research Pavilion 2011 showing (**a**) plate connection details of finger joints and (**b**) the interior view (Knippers et al. 2013)

innovations compared with the previous research pavilion were (1) the single layered structural design, (2) the technical development of the joint detail with respect to structural performance, fabrication and assembly (Krieg et al. 2015), (3) the constructive development with regards to thermal insulation and weather proofing, (4) the integration of quality control into the fabrication and assembly process (Schmitt and Schwieger 2015) and, (5) the agent-based generation scheme for plate structures with its focus on material stock and producibility (Schwinn et al. 2014).

Completed in 2014, the complex plate structure consisting of 243 geometrically unique polygonal plates also complies with the three-plate principle. As a single layered structure made from 50 mm thin beech veneer plywood, the exhibition hall works as a pure plate structure spanning 11 by 17 m (Fig. 11.6). Although only connected by hinges, trivalent polygonal plate structures can transfer bending moments at the global level via out-of-plane shear forces (Li and Knippers 2015). This is also possible in planar configurations, leading, however, to high local force concentrations. Therefore, transition regions between synclastic and anticlastic regions are especially critical because of the lack of curvature and the resulting pattern.

In order to cover the double-curved design surface of the shell with only a single layer of planar stock material, a subdivision scheme involving the Tangent Plate Intersection (TPI) method (Wang and Liu 2009) was implemented as part of an agent-based modelling approach. In this multi-agent model, each agent corresponds

Fig. 11.6 Landesgartenschau Exhibition Hall in Schwäbisch Gmünd, Germany. Interior view showing the polygonal plate layout of the single-layered segmented shell (Krieg et al. 2015)

to exactly one input point for the TPI method and, correspondingly, to one plate in the segmented shell. Through the definition of parameterised behaviours on the level of each individual agent, the entire model can autonomously be steered towards producibility taking into account the planarity requirement, available stock material sizes, and workspace constraints of the fabrication setup (Fig. 11.7). Whereas the consideration of structural performance is technically possible in this kind of approach, the arrangement of the plates in this example primarily reflects geometrical and fabrication constraints, as the optimisation of the joint layout based on mechanical criteria had not previously been implemented.

In 2015, the ICD and the ITKE in collaboration with the work group Invertebrate Paleontology and Paleoclimatology at the Department for Geosciences, University of Tübingen (IPPK) and the work group for Evolutionary Biology of Invertebrates, Institute for Evolution and Ecology at the University of Tübingen, Germany started the development of a demonstrator in the form of a temporary research pavilion. Starting from the previous findings, the aim was (1) to revise some of the earlier biomimetic transfers with respect to the design of segmented shells, (2) to identify additional performative biological principles, and (3) further to improve the ratio of self-weight to loadbearing capacity of segmented timber shells.

The biological principles that have been further investigated include (1) the double-layer shell structure as found in the irregular echinoid species *Clypeaster rosaceus*, (2) the principles of hierarchical material organisation and geometric differentiation (Gruber and Jeronimidis 2012), which can be found in many

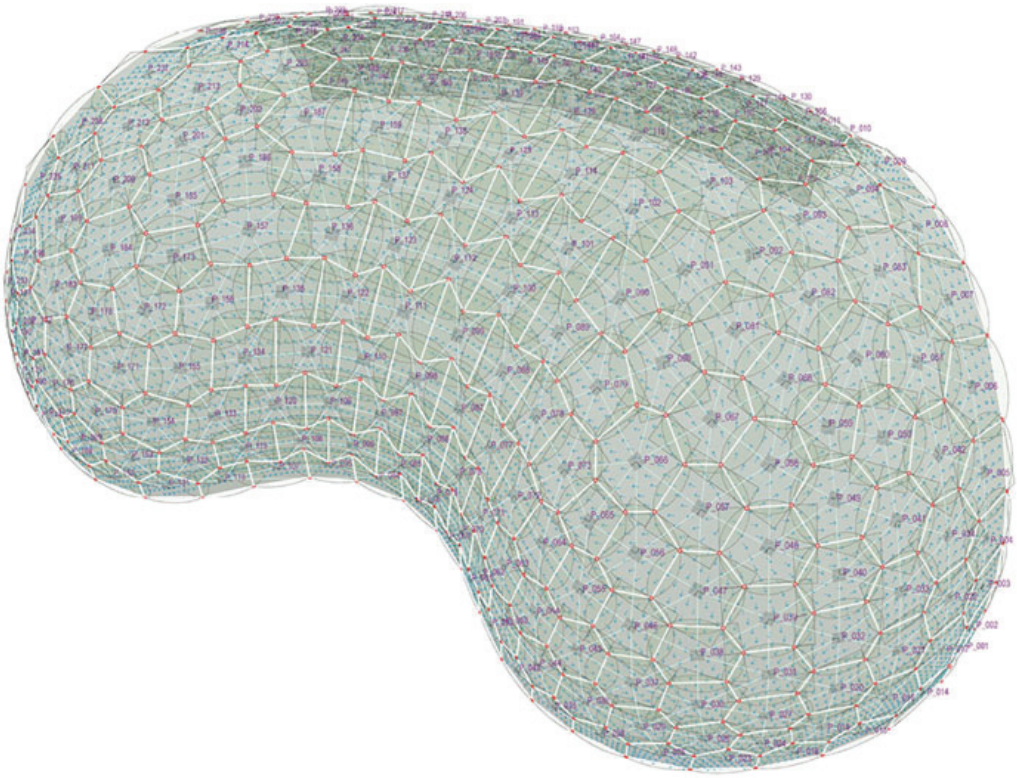

Fig. 11.7 Landesgartenschau Exhibition Hall in Schwäbisch Gmünd, Germany. Agent-based model of shell segmentation by using Tangent Plane Intersection (Schwinn and Menges 2015)

biological structures, and (3) the finger-jointing principle between building modules. New principles that have been identified as part of this research are based on (1) the differentiation of material composition of the echinoid shell, (2) the fibrous connections between shell segments, (3) the growth principles of plate addition and plate accretion (Raup 1968; Pearse and Pearse 1975; Abou Chakra and Stone 2011), and (4) morphological features such as plate morphology and shell openings, which can be observed in clypeasteroid echinoids and might be relevant in an architectural context.

Similar to the 2011 research pavilion, this demonstrator features a double-layered timber construction that is closely related to the constructional morphology of the sand dollar as a biological concept generator. Because of the double-layered nature of the structure, no bending moments need to be transferred between segments. Therefore, the joints between segments consist not only of finger joints, which transfer shear forces and compressive normal forces, but also of laces, which bear the tensile forces in between the segments.

Indeed, the joints of several irregular sea urchin species not only are formed of calcareous protrusions in form of finger joints, but also have often collagen fibres connecting the plates, which are able to withstand tensile forces (see Ellers et al. 1998). Although not necessary for overall stability, as the shell can work

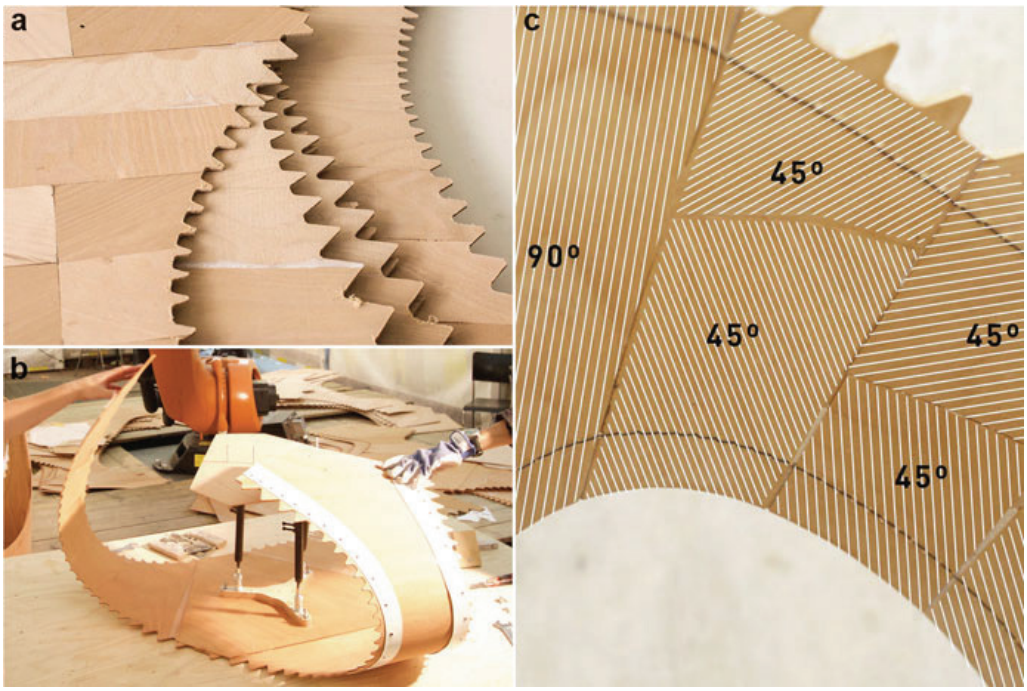

Fig. 11.8 6 ICD/ITKE Research Pavilion 2015. Process of active bending of (**a**) custom laminated veneer strips into (**b**) segments following (**c**) an angle pattern derived from stiffness requirements achieving desired curvature

as a pure plate structure, these fibres seem to be necessary for growth, assembly and robustness (Wester 2002). Echinoid shell growth occurs under maintenance of the structural integrity and mechanical stability of the test. This is a challenging task, as the increase in size of plates is often not possible without creating structural discontinuities. For pure plate structures, forces would be transferred mainly parallel to plate edges and thus perpendicular to the growth direction (Wester 2002). Moreover, during growth, fibres can be shown to play an important role in maintaining structural integrity (Ellers et al. 1998) with the flexible tissue allowing the creation of gaps into which new material can be inserted without the test collapsing. This principle of fibrous connection has been used as an inspiration when using textile connection techniques, such as sewing or lacing, for construction purposes.

The idea of transferring forces via textile connectors has been applied to construction at two levels of hierarchy. On a first level, thin sheets of beech veneer are laminated and bent to form extremely lightweight building modules of only 4 to 6 mm in thickness (Fig. 11.8). Traditionally, layers of veneer are bonded by using glue; however, in the case of bending glue-laminated veneer, delamination can be critical because the sheets need to be joined in a deformed position, thus the high pressures typically required for lamination cannot be achieved. Sewing layers of veneer together therefore presents an interesting alternative, as the yarn can

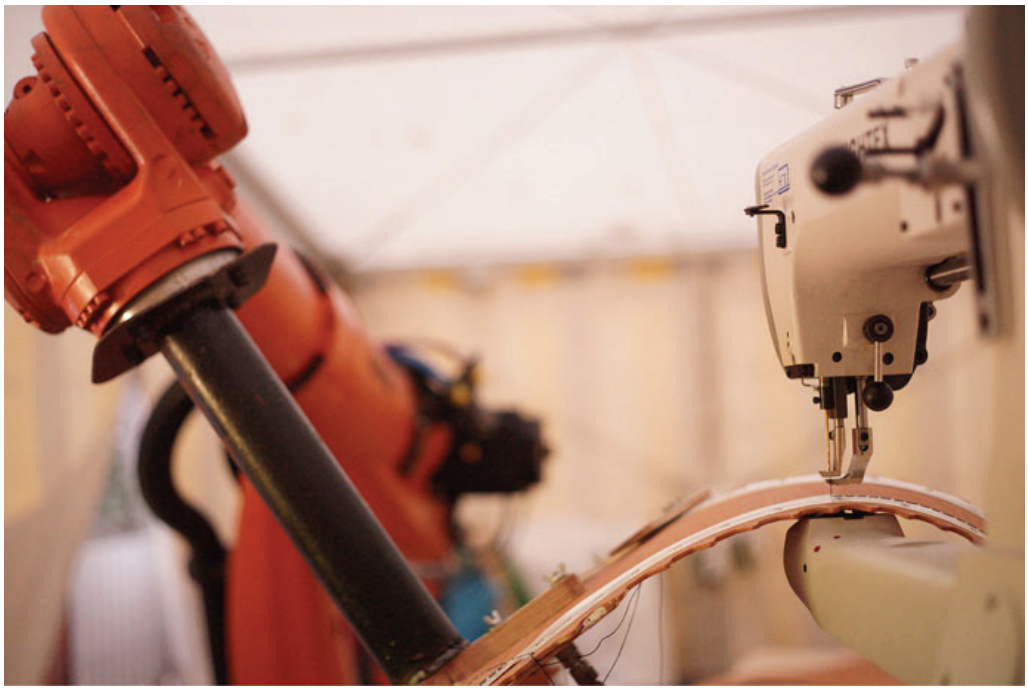

Fig. 11.9 ICD/ITKE Research Pavilion 2015. Robotic sewing of laminated veneer strips

continuously transfer forces between the sheets. The sewing only locally damages the material and, for timber constructions in general, many small connectors are preferable to a few large ones (Herzog et al. 2003). It is also at this local level that the principle of material differentiation with respect to mechanical requirements, as can be found in the calcite tests of echinoids, comes into play: the wooden strips are built up by laminating several veneer sheets, adjusting the thickness and grain orientation to stiffness requirements derived from the global segment layout and the resulting different local stresses that occur in each individual building module. Each module, in turn, is formed by three individually laminated strips, which are joined together by robotic sewing of the timber veneer laminates (Fig. 11.9).

The fibrous connective elements serve mainly for maintaining the structural integrity and for assembly, similar to the biological role models, but they can also transfer larger tensile forces in regions with low curvature. The laced connection is particularly suitable to variable connection angles, which arise from the module geometry. Furthermore, the connection allows flexible adjustment to tolerances during assembly, as they can be tensioned after assembly (Fig. 11.10).

Regular sea urchins grow by plate addition originating from the apical disc and by the incremental growth of individual plates by the accretion of calcite material (for an overview of echinoid growth, see Zachos 2009; Abou Chakra and Stone 2011). These principles have been abstracted and transferred by using a parametric circle packing approach as part of the computational design process (Fig. 11.11). In this process, circles are additively seeded from user-defined locations on a

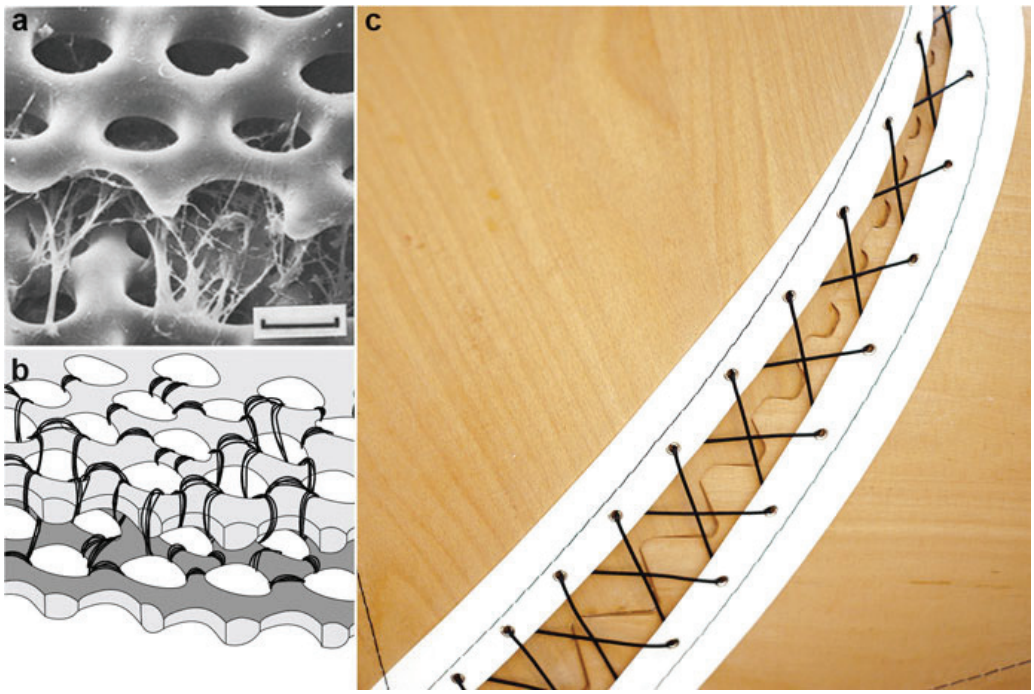

Fig. 11.10 ICD/ITKE Research Pavilion 2015. Principle of (**a**) collagen fibres connecting two adjacent plates of an echinoid test (Telford 1985), which has been (**b**) abstracted into a manufacturable system and transferred to (**c**) a connection detail between timber segments by using lacing

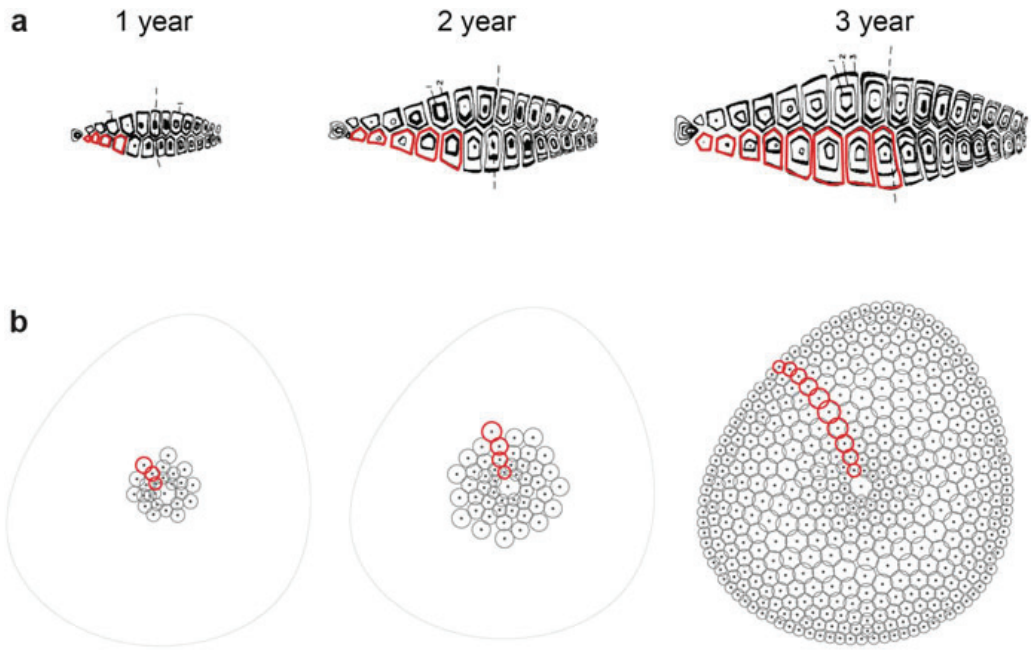

Fig. 11.11 ICD/ITKE Research Pavilion 2015. (**a**) Analysis of the growth process in echinoid plates (modified from Pearse and Pearse 1975) serving as (**b**) a form and pattern-generating algorithm for shell constructions

three-dimensional reference surface. After the circles have been seeded, they continue to grow, i.e. increase in radius, and to be pushed away from the seed origin until a previously defined surface area is filled with tangent circles. The diameters of the circles increase proportionally with time resulting in a configuration in which larger circles are located further away from the origin. The resulting topology of plate origins and shared edges forms the basis for the arrangement of the building modules and satisfies the requirements of the three-plate principles identified in previous case studies.

Morphological features such as lunulae and internal supports, which can be found in clypeasteroids, are particularly relevant in the context of architecture and shell design. Apertures are usually considered detrimental to the structural integrity of shells as they disrupt the continuity of the shell surface; however, they are useful from an architectural and daylighting point of view. Sand dollars, which incorporate lunulae, adjust the plate arrangement in order to accommodate the resulting discontinuity of the shell. This principle might be transferred to the demonstrator through the arrangement and geometry of the modules resulting in a characteristic arrangement of openings in the shell (Fig. 11.12). Supports as found in clypeasteroids are usually avoided in shell structures as they lead to force concentrations and require the thickening of the surface in the area around the support points. Clypeasteroids feature internal supports in the shell that obviously serves as a structural support of the plated skeleton. Transferred into the architectural context, openings and supports can significantly extend the solution for the space and range of applications for segmented shell structures. In the case of the research pavilion 2015, the double-layered shell gradually transforms into a plate-and-support system highlighting the flexibility of the proposed lightweight building system. Its capacity to transform between structural systems constitutes one of its most significant innovations, as this has not been achieved in any of the previous case studies (Fig. 11.12).

11.5 Conclusions

The hierarchically organised and segmented skeletons of the sand dollar feature a variety of adaptations with respect to their mode of life. These morphological and structural modulations are highly adapted to the specific conditions of the environment. The morphological response to mechanical stress caused by biotic and abiotic factors can be seen as form and principle generators in clypeasteroid construction. The adoption and abstraction of biological principles can improve building constructions, since buildings are possibly subject to similar loading conditions as echinoids.

The use of new methods and techniques such as high resolution x-ray micro-computed tomography, 3D imaging tools and advanced Finite Element Analyses enables the examination of the biological role model in detail. Computational simulations based on 3D data can provide insights into mechanical properties of

Fig. 11.12 ICD/ITKE Research Pavilion 2015. The front view showing the transition from shell to plate-and-pillar system (Photo: Roland Halbe)

morphological features and their structural adaptation. 3D models and specific material parameters are necessary for such advanced computational analyses. The model used here is based on x-ray micro-computed tomography records and has been post-processed producing both a surface polygon mesh and a voxel mesh that includes material density parameters. The mesh models can be additionally divided based on echinoid plate distribution and morphology including the connections between single plates.

Previous research on the echinoid skeleton has revealed various principles for segmented shells, such as the hierarchical organisation of the shell, which allows for a modular building concept by using prefabricated modules. The three-plate rule, meaning that three plates always meet in a single node, potentially avoids instable structural configurations. The development of a double-layered shell is the basis of a light-weight structure that not only results in an optimised weight of the building, but also in maximum material economisation. One of the most important developments in the clypeasteroid echinoids are the internal support structures that connect the oral and aboral surfaces. These structures vary in position and morphology with respect to the overall echinoid shape, which is correlated to the mode of life and ambient environmental conditions.

11.6 Outlook

The analyses of echinoids and, especially, the clypeasteroids have shown that these biological role models exhibit meaningful principles that can be transferred into building constructions and design. Mechanical and structural attributes of the

echinoid skeleton, however, need to be investigated in more detail in order to obtain a more precise understanding of the revealed principles and the possible detection of new principles.

Further research will be performed by using more detailed models for simulations and material parameters that can be physically evaluated. Such focused analyses are predestined to reveal not only obvious principles on a macroscopic scale, but also latent principles that might be of major interest for structural engineering, form finding and functional morphological interpretations.

Acknowledgements This work has been funded by the German Research Foundation (DFG) as part of the Transregional Collaborative Research Centre (SFB/Transregio) 141 'Biological Design and Integrative Structures'/project A07. We also thank The Paleontological Society, The Gerace Research Centre, Hartmut Schultz (Scanning Electron Microscopy Lab, Department for Geosciences, University of Tübingen), Wolfgang Gerber (Photo Lab, Department for Geosciences, University of Tübingen), Ellen Struve (Applied Geosciences, University of Tübingen), Raouf Jemmali (German Aerospace Center, Stuttgart, Germany) and Rolf Pohmann (Max-Planck Institute for Biological Cybernetics, Tübingen, Germany). Thanks to the European Fund for Regional Development and the Cluster Forst und Holz Initiative. We also thank Theresa Jones for proof reading and Roland Halbe.

References

Abou Chakra M, Stone JR (2011) Holotestoid: a computational model for testing hypotheses about echinoid skeleton form and growth. J Theor Biol 285:113–125

Alexander DE, Ghiold J (1980) The functional significance of the lunules in the sand dollar *Mellita quinquiesperforata*. Biol Bull 159:561–570

Almegaard H, Bagger A, Gravesen J, Jüttler B, Šír Z (2007) Surfaces with piecewise linear support functions over spherical triangulations. Proc Math Surf XII 4647:42–63

Arnout S, Firl M, Bletzinger KU (2012) Parameter free shape and thickness optimisation considering stress response. Struct Multidiscipl Optim 45:801–814

Bagger A (2010) Plate shell structures of glass. Dissertation, University of Denmark

Blandini L (2005) Structural use of adhesives in glass shells. Dissertation, Universität Stuttgar

Bletzinger KU, Ramm E (1999) A general finite element approach to the form finding of tensile structures by the updated reference strategy. Int J Space Struct 14:131–145

Breitenberger M, Blenzinger KU, Wüchner R (2013) Isogeometric layout optimization of shell structures using trimmed NURBS surfaces. In: Proceedings of World Congress on Structural and Multidisciplinary Optimization, Orlando, 19—24 May

Chilton J (2000) Heinz Isler. The engineer's contribution to contemporary architecture. Thomas Telford Ltd, Reston

Deb K (2011) Multi-objective optimization using evolutionary algorithms. Kan Gal Rep 2011003:1–24

Dimcic M, Knippers J (2011) Structural optimization of grid shells. In: Proceedings of The International Association for shell and spacial structures, London, 20—23 September

Eble G (2004) The macroevolution of phenotypic integration. In: Pigliucci M, Perston K (eds) Phenotypic integration, studying the ecology and evolution of complex phenotypes. Oxford University Press, Oxford, pp 253–273

Ellers O, Johnson AS, Moberg PE (1998) Structural strengthening of urchin skeletons by collagenous sutural ligaments. Biol Bull 195:136–144

Fildhuth T, Lippert S, Knippers J (2012) Design and joint pattern optimisation of glass shells. In: Proceedings of The International Association for Shell and Spacial Structures, Seoul, 20—24 May

Fildhuth T, Knippers J (2011) Geometrie und Tragverhalten von doppelt gekrümmten Ganzglasschalen aus kalt verformten Glaslaminaten. Stahlbau 80:31–44

Fonseca CM, Fleming PJ (1995) An overview of evolutionary algorithms in multiobjective optimization. Evol Comput 3:1–16

Ghiold J (1979) Spine morphology and its significance in feeding and burrowing in the sand dollar *Mellita quinquiesperforata* (Echinodermata: Echinoidea). Bull Mar Sci 29:481–490

Ghiold J (1982) Observations on the clypeasteroid *Echinocyamus pusillus* (O.F. Müller). J Exp Mar Biol Ecol 61:57–74

Goldberg WM (1992) The biology of reefs and reef organisms. The University of Chicago Press, Chicago

Goodbody I (1960) The feeding mechanism in the sand dollar *Mellita sexiesperforata* (Leske). Biol Bull 119:80–86

Grossmann JN, Nebelsick JH (2013) Stereom differentiation in spines of *Plococidaris verticillata*, *Heterocentrotus mammillatus* and other regular sea urchins. In: Johnson C (ed) Echinoderms in a Changing World. Proceedings of the 13th International Echinoderm Conference, Tasmania. CRC Press, London, pp 97—104

Grun T, Sievers D, Nebelsick JH (2014) Drilling predation on the clypeasteroid echinoid *Echinocyamus pusillus* from the Mediterranean Sea (Giglio, Italy). Hist Biol 26:745–757

Grun T, Nebelsick JH (2015) Sneaky snails: how drillholes can affect paleontological analyses of the minute clypeasteroid echinoid *Echinocyamus*? In: Zamora S, Rábano I (eds) Progress in echinoderm paleobiology. Publicaciones del Instituto Geológico y Minero de España, Madrid, pp 71–73

Gruber P, Jeronimidis G (2012) Has biomimetics arrived in architecture? Bioinspir Biomim 7:1–2

Herzog T, Natterer J, Schweitzer R (2003) Holzbau Atlas. Birkhäuser, Basel

Hyman LH (1955) The Invertebrates. Volume IV: Echinodermata. McGraw-Hill, New York

Kier PM, Grant RE (1965) Echinoid distribution and habits, Key Largo Coral Reef Reserve, Florida. Smithsonian Inst 149:1–62

Knippers J, Menges A, Gabler M, La Magna R, Waimer F, Reichert S, Schwinn T (2013) From nature to fabrication: biomimetic design principles for the production of complex spatial structures. In: Hesselgren L, Sharma S, Wallner J, Baldassini N, Bompas P, Raynaud J (eds) Advances in architectural geometry 2012. Springer, Wien, pp 107–122

Krieg OD, Schwinn T, Menges A, Li J, Knippers J, Schmitt A, Schwieger V (2015) Biomimetic lightweight timber plate shells: computational integration of robotic fabrication, architectural geometry and structural design. In: Block P, Knippers J, Mitra NJ, Wang W (eds) Advances in architectural geometry 2014. Springer, Cham, pp 109–125

Krieg OD, Dierichs K, Reichert S, Schwinn T, Menges A (2011) Performative architectural morphology: Finger-joined plate structures integrating robotic manufacturing, biological principles and location-specific requirements. In: Gengnagel C, Kilian A, Palz N, Scheurer F (eds) Computational design modelling: proceedings of the design modelling symposium berlin 2011. Springer, Berlin, pp 259–266

La Magna R, Gabler M, Reichert S, Schwinn T, Waimer F, Menges A, Knippers J (2013) From nature to fabrication: biomimetic design principles for the production of complex spatial structures. Int J Space Struct 28:27–39

Lang A (1896) Text-book of comparative anatomy, volume 2. MacMillan and Co, London

Lawrence JM, Herrera J, Cobb J (2004) Vertical posture of the clypeasteroid sand dollar *Encope michelini*. J Mar Biol Assoc UK 84:407–408

Li JM, Knippers J (2015) Pattern and form – their influence on segmental plate shells. In: Proceedings of The International Association for Shell and Spacial Structures, Amsterdam, 17—20 August

Menges A (2013) Morphospaces of robotic fabrication. In: Brell-Çokcan S, Braumann J (eds) Robarch 2012: robotic fabrication in architecture, art and design. Springer, Wien, pp 28–47
Mihaljević M, Jerjen I, Smith AB (2011) The test architecture of *Clypeaster* (Echinoidea, Clypeasteroida) and its phylogenetic significance. Zootaxa 2983:21–38
Millott N (ed) (1967) Echinoderm biology. Academic, New York
Mitteroecker P, Huttegger SM (2009) The concept of morphospaces in evolutionary and developmental biology: mathematics and metaphors. Biol Theory 4:54–67
Mooi R (1986) Structure and function of clypeasteroid miliary spines (Echinodermata, Echinoides). Zoomorphology 106:212–223
Mooi R (1989) Living and fossil genera of the Clypeasteroida (Echinoidea, Echinodermata): an illustrated key and annotated checklist. Smithsonian Institution Press, Washington, DC
Mortensen T (1948) A monograph of the Echinoidea IV. CA Reitzel, Copenhagen
Müller J (1854) Über den Bau der Echinodermen. Druckerei der Königlichen Akademie der Wissenschaft, Berlin
Nebelsick JH, Dynowski JF, Grossmann JN, Tötzke C (2015) Echinoderms: hierarchically organized light weight skeletons. In: Hamm C (ed) Evolution of light weight structures. Analyses and technical applications. Springer, Dordrecht, pp 141–154
Nichols D (1962) Echinoderms. Hutchinson and Co, London
Pearse JS, Pearse VB (1975) Growth zones in the echinoid skeleton. Amer Zool 15:731–753
Philippi U, Nachtigall W (1996) Functional morphology of regular echinoid tests (Echinodermata, Echinoida): a finite element study. Zoomorphology 116:35–50
Ramm E, Bletzinger KU, Reitinger R (1993) Shape optimization of shell structures. Revue Européenne des Éléments 2:377–398
Raup DM (1959) Crystallography of echinoid calcite. J Geol 67:661–674
Raup DM (1968) Theoretical morphology of echinoid growth. J Paleo 42:50–63
Schmitt A, Schwieger V (2015) Quality control of robotics made timber plates. In: Fédération Internationale Géometès, Sofia, 17—21 May
Schultz H (2006) Sea urchins I: a guide to worldwide shallow water species, 3rd edn. Heinke and Peter Schultz, Hemdingen
Schwinn T, Menges A (2015) Fabrication agency: Landesgartenschau Exhibition Hall. Archit Des 85:92–99
Schwinn T, Krieg OD, Menges A (2014) Behavioral strategies: synthesizing design computation and robotic fabrication of lightweight timber plate structures. In: Proceedings of the 34th annual conference of the Association for Computer Aided Design in Architecture, Los Angeles, 23—25 October
Schwinn T, Krieg OD, Menges A, Mihaylov B, Reichert S (2012) Machinic morphospaces: biomimetic design strategies for the computational exploration of robot constraint spaces for wood fabrication. In; Proceedings of the 32nd annual conference of the Association for Computer Aided Design in Architecture, San Francisco, 18—21 October
Seilacher A (1979) Constructional morphology of sand dollars. Paleobiology 5:191–221
Smith AB (1980) The structure and arrangement of echinoid tubercles. Philos Trans R Soc B 289:1–54
Smith AB (1984) Echinoid palaeobiology. George Allen and Unwin, London
Smith AB, Ghiold J (1982) Roles for holes in sand dollars (Echinoidea): a review of Lunulae function and evolution. Paleobiology 8:242–253
Strathmann RR (1981) The role of spines in preventing structural damage to echinoid tests. Paleobiology 7:400–406
Telford M (1981) Hydrodynamic interpretation of sand dollar morphology. Bull Mar Sci 31:605–622
Telford M (1985) Domes, arches and urchins: the skeletal architecture of echinoids (Echinodermata). Zoomorphology 105:114–124
Telford M, Mooi R, Ellers O (1985) A new model of podial deposit feeding in the sand dollar, Mellita quinquiesperforata (Leske): the sieve hypothesis challenged. Biol Bull 169:431–448

Timko PL (1976) Sand dollars as suspension feeders: a new description of feeding in *Dendraster excentricus*. Biol Bull 151:247–259

Veer FA, Wurm J, Hobbelman GJ (2003) The design, construction and validation of a structural glass dome. In: Proceedings of glass processing days, Tampere, 15—18 June

Wang W, Liu Y (2009) A note on planar hexagonal meshes. In: Emiris IZ, Sottile F, Theobald T (eds) The IMA volumes in mathematics and its applications. Springer, New York, pp 221–233

Wester T (1990) A geodesic dome-type based on pure plate action. Int J Space Struct 5:155–167

Wester T (2002) Nature teaching structures. Int J Space Struct 17:135–147

Zachos LG (2009) A new computational growth model for sea urchin skeletons. J Theor Biol 259:646–657

Manuscript 2

The taphonomy of *Clypeaster*: a paleontological tool to identify stable structures in natural shell systems

The taphonomy of *Clypeaster*: a paleontological tool to identify stable structures in natural shell systems

Tobias B. Grun[1], Andrea Mancosu[2], Zain Belaústegui[3], James H. Nebelsick, Tübingen[1]

[1] Department for Geosciences, University of Tübingen, Hölderlinstraße 12, 72074 Tübingen, Germany; tobias.grun@uni-tuebingen.de

[2] Dipartimento di Scienze Chimiche e Geologiche, Università degli studi di Cagliari, Via Trentino 51, 09127 Cagliari, Italy; andrea.mancosu@gmail.com

[3] Departament de Dinàmica de la Terra i de l'Oceà, Universitat de Barcelona, Martí i Franquès, 08028 Barcelona, Spain; zbelaustegui@ub.edu

[1] Department for Geosciences, University of Tübingen, Hölderlinstraße 12, 72074 Tübingen, Germany; nebelsick@uni-tuebingen.de

Key words: Echinoid, Clypeasteroidea, Bahamas, fragmentation, fossil, Recent, biomimetics, method, stability, test strength

Abstract

The stability of echinoid skeletons is highly dependent on the strength of the connections between individual elements, such as the plates of the test, which contribute to the construction of these modular organized organisms. Herein, the irregular echinoid genus *Clypeaster* (Lamarck 1801) is studied with respect to constructional details of the skeleton, which in turn is of interest as a model for engineered architectural and segmented domes. The preservation of the sea biscuit *Clypeaster rosaceus* (Linnaeus 1758) from the Bahamas was studied in detail using micro-CT and scanning electron microscopic methods. Furthermore, field data concerning their preservation is compared to that of Miocene *Clypeaster* species from the Mediterranean area. The results show that three structural elements affect the test strength: (1) skeletal protrusions which interlock adjoining plates; (2) internal supports crossing plate boundaries and joining the aboral and oral sides of the test; and (3) micro-canals which show a differentiated distribution within the test. The stabilizing features lead to the preservation of denuded complete tests on the sea floor for extended periods of time allowing for extensive bioinfestation of shells. Furthermore, when fragmentation occurs, it preferentially follows the perradial sutures within the ambulacra resulting in typical pie-shaped fragments that are found in both fossil and Recent environments. The potential for using the preservation of shells for biomimetic research is discussed.

INTRODUCTION

Domed structures, such as the Pantheon in Rome, demonstrate an exceptional structural strength due to the effective distribution of applied stresses (e.g., Tamboli et al. 2000; Grun et al. 2017b). Modern architecture therefore employs segmented shell constructions, which combine enhanced strength performance, optimization in material-use, and a reduction of assembling time (e.g., Grun et al. 2016). Individual segments of such a shell construction can be pre-fabricated in assemblage halls where ambient environmental parameters such as humidity, temperature, and light can be controlled. Therefore, seasonal effects including weather- and natural light conditions do not affect the fabrication process. The economization of materials as well as the time needed for fabrication and assemblage can also lead to a substantial reduction of building costs. Segmented shells, however, are characterized by the inherent disadvantage that the connections between individual elements represent weak-points of the construction (e.g., Gordon 1978; Grun et al. 2016, 2017b). It is thus of great interest to investigate modular domed skeletons, such as those represented by echinoids, as role models for structural engineering and structural design. Inversely, recognizing engineering principles in the construction of an echinoid skeleton can be important with respect to their preservation in the fossil record. The high preservation potential and taphonomy of clypeasteroids in general, including that of *Clypeaster* (Lamarck 1801), has been the subject of various studies (Seilacher 1979; Telford 1985a, b; Nebelsick 1995; Kroh & Nebelsick 2003; Belaústegui et al. 2012; Mancosu & Nebelsick 2013, 2015, 2017). Although some strengthening mechanisms in clypeasteroid echinoids have been identified (Seilacher 1979; Telford 1985a, b), the direct correlation between distinctive fragmentation patterns and underlying skeletal structures has yet to be addressed. To fill this gap, Recent skeletons of *Clypeaster rosaceus* (Linnaeus 1758) are analyzed with respect to their architectural design and stability using scanning electron microscopy (SEM) and x-ray micro-computed tomography (µCT). Recent *Clypeaster rosaceus* tests have been analyzed using *in situ* underwater photography in their natural habitat for identifying stable structures of the skeleton. In addition, structural implications are examined with respect to the preservation of *Clypeaster* tests in the fossil record. Finally, the possibility of using the taphonomic pathways of shell preservation as a biomimetic tool is explored.

Echinoid tests as hierarchical modular skeletons

Echinoid skeletons are hierarchical organized multi-element systems representing segmented shells constructions (Smith 1984; Telford 1985a; Lawrence 1987; Nebelsick et al. 2015; Grun et al. 2016). As organic tissues decay rapidly after the death of an individual, the structural strength and test integrity of the multi-plated skeletons prevalently rely on the structural design of the plates and the plate's interlocking mechanisms (Telford 1985a; Lawrence 1987; Kidwell & Baumiller 1990; Grun et al. 2016).

Considering its construction as a modular skeleton, it is not surprising that the echinoid skeleton has thus come into the focus of theoretical modeling and as basis for morphological research (Seilacher 1979; Telford 1985a, b; Philippi & Nachtigall 1996; Philippi 2001; Chakra & Stone 2011; Mihaljević et al. 2011; Zachos 2015; Grun et al. 2016; Grun et al. 2017b) in which the biological role models were analyzed in order to develop technical processes and products (e.g. Drack et al. 2018).

Recent *Clypeaster rosaceus*

The irregular echinoid *Clypeaster rosaceus* (Fig. 1) is one of the best known echinoid species occurring in the warm waters of the Caribbean Sea and neighboring areas (Kier & Grant 1965; Kier 1975; Serafy 1979; Hopkins 1988; see also numerous citations within Alvarado & Solís-Marín 2013 and Rodríguez-Barreras 2014). *Clypeaster rosaceus*, as other species of the genus *Clypeaster*, features a prominent internal support system, and also often a double-layered wall (Mortensen 1948).

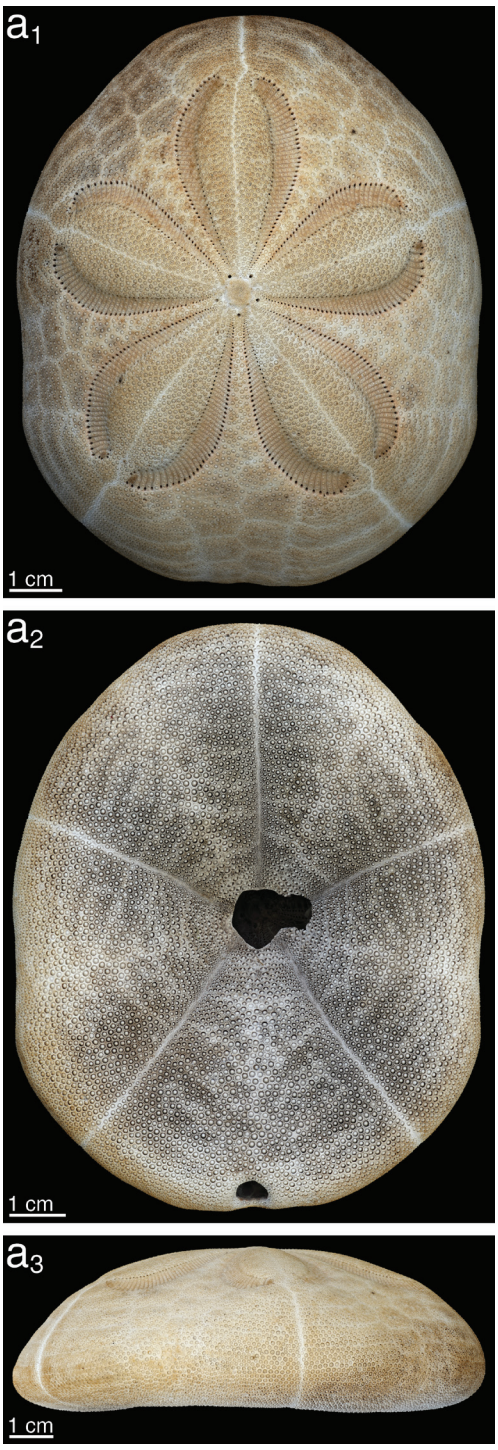

Figure 1. Photographs of *Clypeaster rosaceus* from the Bahamas. (a1) aboral, (a2) oral, (a3) lateral view [GPIT/EC/00743:SSI-FDB-CR-15].

The test of *Clypeaster rosaceus* differs from that of other extant members of this genus in that it features a highly tumid margin with a elevated petalodium on the aboral side of the test. Furthermore, the oral side possesses a deeply sunken infundibulum which contains the peristome. In contrast to other *Clypeaster* species, it mostly lives epibenthically on the sea surface covering itself with material from the sea floor, although it can also occur slightly or rarely fully buried within the sediment (Moore 1966; Hendler et al. 1995). It has been described as an epibenthic feeder subsiding on dead leaves of the sea grass *Thalassia testudinum* (Telford et al. 1987), and on the green algae *Halimeda* sp. (Kampfer & Ott 1995). *Clypeaster rosaceus* is also known from Plio-Pleistocene sedimentary rocks of the Caribbean and Florida (Poddubiuk 1984; Donovan et al. 1994; Portell & Oyen 2002).

Fossil Clypeaster

Clypeaster is one of the most characteristic fossils of Cenozoic sedimentary sequences showing a wide variation of morphotypes, and occurring in both siliciclastic and carbonate environments since the Eocene (Michelin 1861; Lambert 1927; Mitrović-Petrović 1984; Poddubiuk 1984; Rose & Poddubiuk 1987; Dixon & Donovan 1998; Kroh & Nebelsick 2003; Kroh 2005; Tsaparas et al. 2007; Belaústegui et al. 2012; Mancosu & Nebelsick 2013, 2015, 2017). This genus can occur dispersed among other biogenic components and in mass occurrences, which can be common for clypeasteroid in general (Nebelsick & Kroh 2002; Belaústegui et al. 2012; Mancosu & Nebelsick 2013). The high preservation potential of fossil *Clypeaster* and clypeasteroids in general have long been related to the presence of both interplate connections and internal supports (Seilacher 1979; Poddubiuk 1984; Grun et al. 2016). Furthermore, the high preservation potential of denuded *Clypeaster* tests after death has an influence on the ambient environment in that the skeletons serve as secondary hard substrate for encrustation and bioerosion (Belaústegui et al. 2013, 2017; Rahman et al. 2015; Mancosu & Nebelsick 2017).

Geometry and sutures of the *Clypeaster* skeleton

Sutures. — As a typical post-Paleozoic echinoid, the skeleton of *Clypeaster rosaceus* is divided into ten rows of ambulacral and interambulacral plates resulting in 20 plate rows, since ambulacralia and interambulacralia are furthermore subdivided into two plate rows each (Fig. 2). Plate boundaries can be often recognized on the test surface, where sutures

extending radially from the apical disc o the peristome, and latitudinal sutures which are circumferentially arranged around the test. Radial sutures show a zig-zag pattern as opposing plates on each side of the suture alternating with one another and can be categorized into three types (Zachos 2008): (1) perradial sutures occur between ambulacral plates (Fig. 2); (2) adradial suture between ambulacral and an interambulacral plate rows; and (3) interradial sutures between interambulacral plates. Sutures differ in length depending on their position on the test.

Plate interlocking. — The plates of clypeasteroids are typically interconnected by collagenous fibers and skeletal protrusions (Moss & Meehan 1967; Seilacher 1979; Telford 1985a, b). Especially the skeletal protrusions, that can vary along species, are interpreted to be of high significance for the test integrity and the high preservation potential in clypeasteroids (e.g., Seilacher 1979).

Internal supports. — The internal support system is characteristic for clypeasteroids (Mortensen 1948; Roman 1952; Mooi 1989; Mihaljević et al. 2011) and is present in all its representatives except the family Fibulariidae (Gray 1855) (Mortensen 1948; Mooi et al. 2014). These prominent morphological characters can either be part of the ambulacral zone, where buttresses protrude into the cavity of the echinoid as in, for example *Echinocyamus pusillus* (Müller 1776) (e.g., Mortensen 1948; Grun et al. 2016, 2017b), or belong to the interambulacral zones, where they constitute solitary pillars (Mooi 1989).

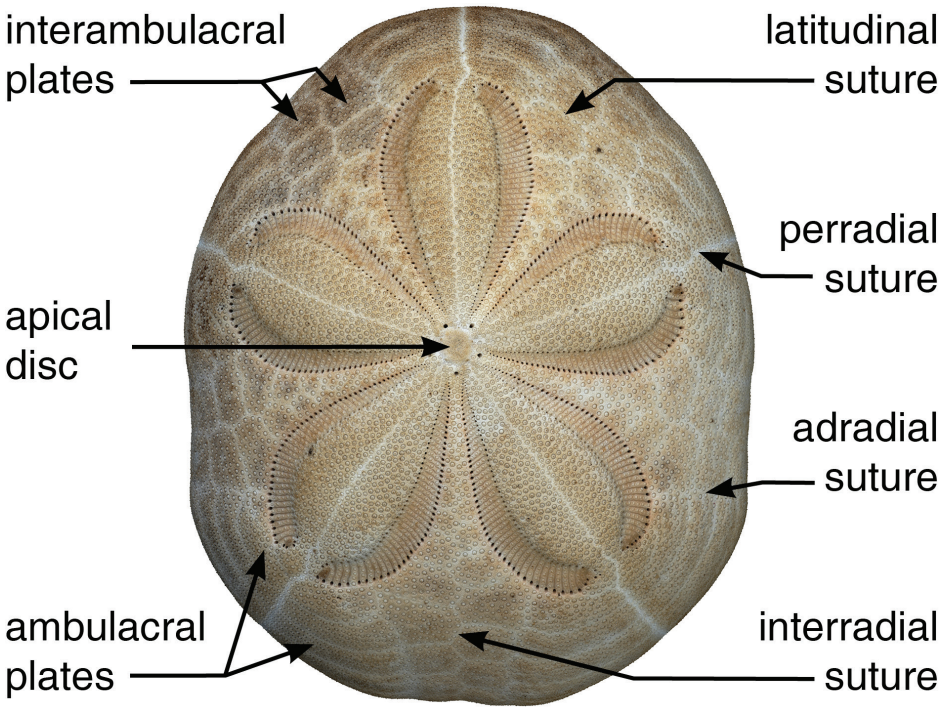

Figure 2. Morphology of the test of *Clypeaster rosaceus*, showing plate and suture arrangement. [GPIT/EC/00743:SSI-FDB-CR-15].

Double-wall structure. — *Clypeaster rosaceus* is characterized by a thick test wall, which is interspersed by the micro-canals (Schaffer 1962) of the water-vascular system (e.g., Durham 1966). The network of the micro-canals results in a double-wall structure which has been interpreted to increase test stability (Donovan 1991).

MATERIAL AND METHODS

Material

Recent *Clypeaster rosaceus* from the Caribbean: Complete tests and fragments of *Clypeaster rosaceus* were exhaustively searched, *in situ* photographed and collected by SCUBA and snorkeling in shallow near-shore environments down to 15 m depth during June and July 2017 at Fernandez Bay, west-coast of San Salvador, Bahamas "(24°01'15.0"N 74°31'25.3"W, Fig. 3). Material was analyzed and stored at the University of Tübingen, Germany under repository GPIT/EC/00744. Specimens used for µCT scans and SEM were collected during July and August 2015 at Fernandez Bay, San Salvador, Bahamas and are stored under repository GPIT/EC/00743 at the University of Tübingen, Germany. Coordinates are obtained from Google Maps 2016.

Representative fossil occurrences rich in *Clypeaster* and their fragments have recently been studied from the Miocene of Sardinia and Spain. A number of localities were studied in detailed with respect to their paleoecology as well as bioinfestation for the Early Miocene of Sardinia (Mancosu & Nebelsick 2013, 2015, 2017) and the middle Miocene of Spain (Belaústeguietal. 2012, 2017, Rahman et al. 2015).

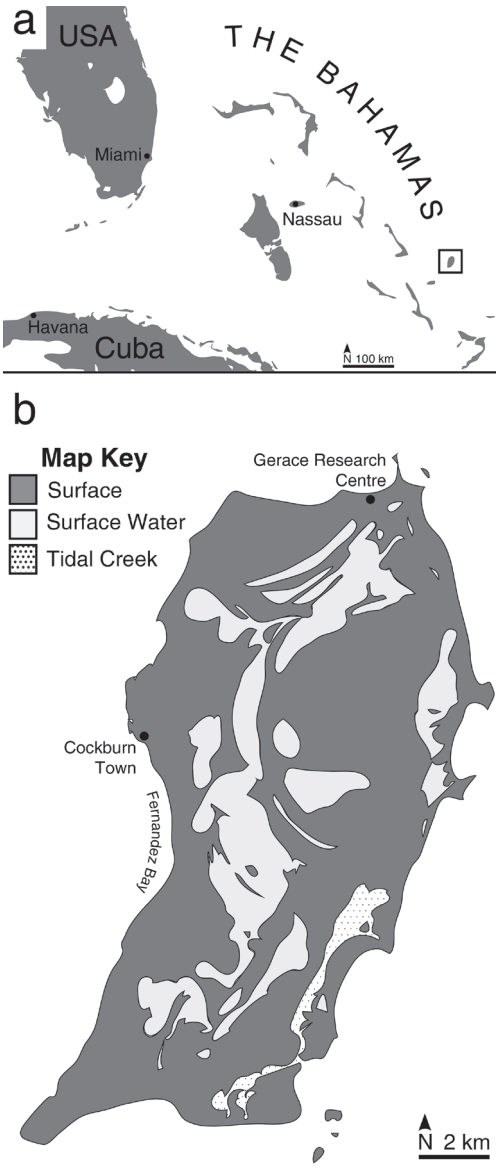

Figure 3. Map of the (a) Bahamas and (b) San Salvador Island showing the sample site Fernandez Bay.

Methods

A total of 39 *Clypeaster rosaceus* tests or fragments were photographed *in situ* and then collected. The images of *in situ* documented specimens are analyzed for fragmentation patterns, which can be present along the perradial, adradial, and interradial sutures (Fig. 2). Furthermore, the presence of bioinfestation on both intact and fragmented *Clypeaster rosaceus* test were recorded and differentiated with respect to encrustation by either soft bodied (e.g. fleshy algae) or calcareous organisms (e.g. encrusting coralline algae) as a proxy for sea surface residence times. Specimens found in the fossil record were respectively investigated for the preservation, fragmentation patterns, and bioinfestation. Results from fossil occurrences are then compared to those found in Recent environments.

Computed tomography. — Tests of Recent *Clypeaster* rosaceous were analyzed for internal supports [GPIT/EC/00743:SSI-FDB-CR-126] and the micro-canal system [GPIT/EC/00743:SSI-FDB-CR-28] using μCT, which were obtained at the German Aerospace Center (Deutsches Zentrum für Luft-und Raumfahrt) using a v-tomex L450 (General Electric Company Corporation, Boston, MA, USA) with an isotropic voxel resolution of 15 microns. Micro-CT scans are processed using Avizo 9.4.0 (Thermo Fisher Scientific, Waltham, MA, USA).

Scanning electron microscopy. — Plate interlocking was analyzed from scanning electron microscopic images obtained at the Department of Geosciences, University of Tübingen, using a Leo 1450VP (Carl Zeiss AG, Oberkochen, Germany) SEM. Samples for SEM were extracted from a complete and denuded *Clypeaster rosaceus* [GPIT/EC/00743:SSI-FDB-CR-4] test using a Dremel 300i rotary tool (Dremel, Racine, WI, USA) with a Dremel EZ Speedclic diamond cutting wheel (Dremel, Racine, WI, USA). Samples were cleaned for 30 min in an ultrasonic bath (Bandelin DT106, Bandelin Electronic, Berlin, Germany) and were dried in a Heraeus LUT6050 (Kendro Laboratory Products, Hanau, Germany) convection oven at around 60ºC. Samples were fixed on aluminum stubs (Plano GmbH, Wetzlar, Germany) using Leit-C-Plast (Plano GmbH, Wetzlar, Germany). The samples were platinum-sputtered in a Bal-Tec SCD 005 sputter coater (Bal-Tec, Balzers, Lichtenstein).

Image processing

Image stacking was performed using Zerene Stacker 1.04 (Zerene Systems, Richland, WA, USA). Photographs were adjusted for brightness and contrast using Adobe Photoshop CC 2017 (Adobe Systems, San José, CA, USA); line drawings were generated in Adobe Illustrator CC 2017 (Adobe Systems, San José, CA, USA) and figures were processed using Adobe InDesign CC 2017 (Adobe Systems, San José, CA, USA).

RESULTS

Recent *Clypeaster rosaceus* from the Bahamas. — Of the 39 collected specimens (Tab. 1), 15 (38.5%) were complete, though completely denuded, with the apical discs attached to the test (Fig. 4a). Two specimens (5.1%) were complete yet lacking the apical disc. Two fragmented specimens consisting of larger clusters (5.1%) showed the apical disc. The apical disc was, however, never present on single pie-shaped fragments.

Fossil Clypeaster. — Findings from the fossil record show that both complete and pie-shaped fragments are preserved (Fig. 5). The domed Miocene fossilized *Clypeaster* species from Spain are embedded in a coarse grained shelly environment which is comparable to some of the substrates in which *Clypeaster rosaceus* was found in Recent environments of San Salvador (Fig. 4c). In total, 30 fossil specimens from the Miocene of Usini (Sardinia, Italy) were analyzed (Tab. 2). From these, 15 tests (50.0%) were complete, although only five samples (33.3%) had the apical disc attached to the test and four individuals (26.7%) were seen as pristine. The 15 complete specimens showed bioinfestation in 9 tests (60.0%).

Fragmentation Patterns

Recent *Clypeaster rosaceus* from the Bahamas. — Out of the 21 tests which show fragmentation, 13 (61.9%) are fragmented along the perradial sutures (Fig. 4b, c), thus representing the most prominent fragmentation sites among *Clypeaster rosaceus* specimens. Exclusive fragmentation along the interradial sutures (between interambulacral plates) and adradial sutures (between ambulacral and interambulacral plate rows) is absent. Complex fragmentation patterns occur on perradial and adradial sutures as well as on perradial and interradial sutures in two individuals (each 9.5%). In three tests (14.3%), perradial, adradial and interradial sutures are subject to fragmentation. In a single specimen (4.8%), it was not possible to analyze adradial and interradial fragmentation patterns due to destruction during transportation.

Table 1. Preservation of Recent *Clypeaster rosaceus*. N = number of specimens

		complete	fragmented
overview	N	17	22
	apical disc missing	2	20
	encrusted	15	8
	pie-shaped	-	15
		N	%
fragmentation	total	22	100
	along horizontal sutures	0	0
	along radial	9	40.9
	along radial and latitudinal	12	54.5
	along perradial suture	13	59.1
	along adradial suture	0	0
	along interradial suture	0	0
	along perradial and adradial sutures	2	9.1
	along perradial and interradial sutures	2	9.1
	along adradial and interradial sutures	0	0
	along perradial, adradial and interradial sutures	3	13.6

Table 2. Preservation of fossil *Clypeaster* sp. from the Miocene of Usini (Sardinia, Italy). N = number of specimens

		N	%
	total specimens (N)	30	100.0
complete specimens	total (N)	15	50.0
	pristine	4	13.3
	apical disc missing	5	16.7
	bioinfested	9	30.0
pie-shape fragments	total (N)	6	20.0
	along perradial suture	5	16.7
	along adradial suture	1	3.3
	along interradial suture	1	3.3
	bioinfested	4	13.3
non-pie-shaped fragments	total (N)	9	30.0
	along horizontal or radial suture	9	30.0
	bioinfested	5	16.7

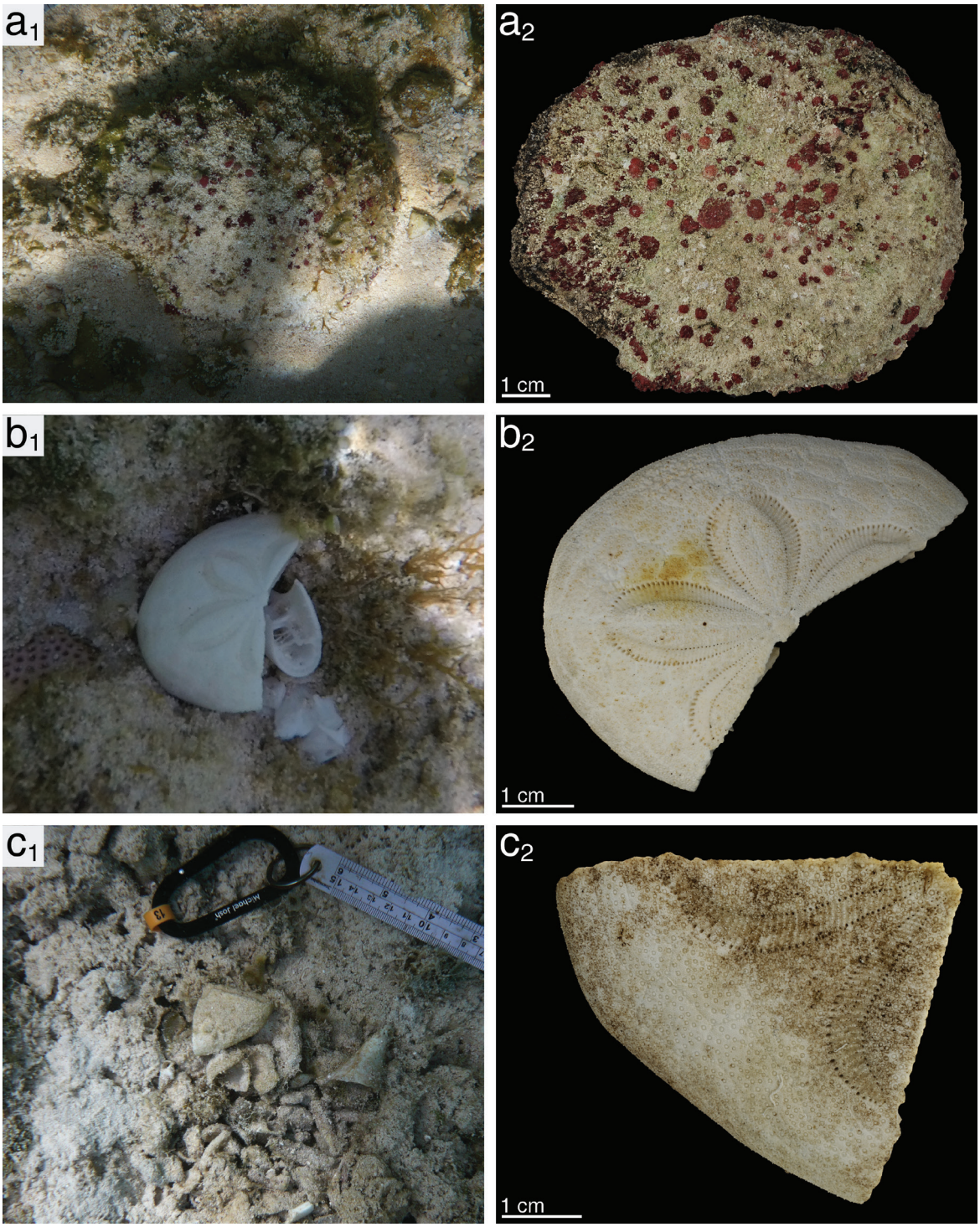

Figure 4. *Clypeaster rosaceus* from the Bahamas. (a1) complete and encrusted specimen *in situ* and (a2) recovered [GPIT/EC/00744:SSII-FDB-CR-1]. (b1) fragmented specimen with the apical disc still attached *in situ* and (b2) recovered [GPIT/EC/00744:SSII-FDB-CR-2]. (c1) pie-shaped fragment *in situ* embedded in a rubble bed (compare Fig. 2b) and the (c2) pie-shaped fragment recovered [GPIT/EC/00744:SSII-FDB-CR-3].

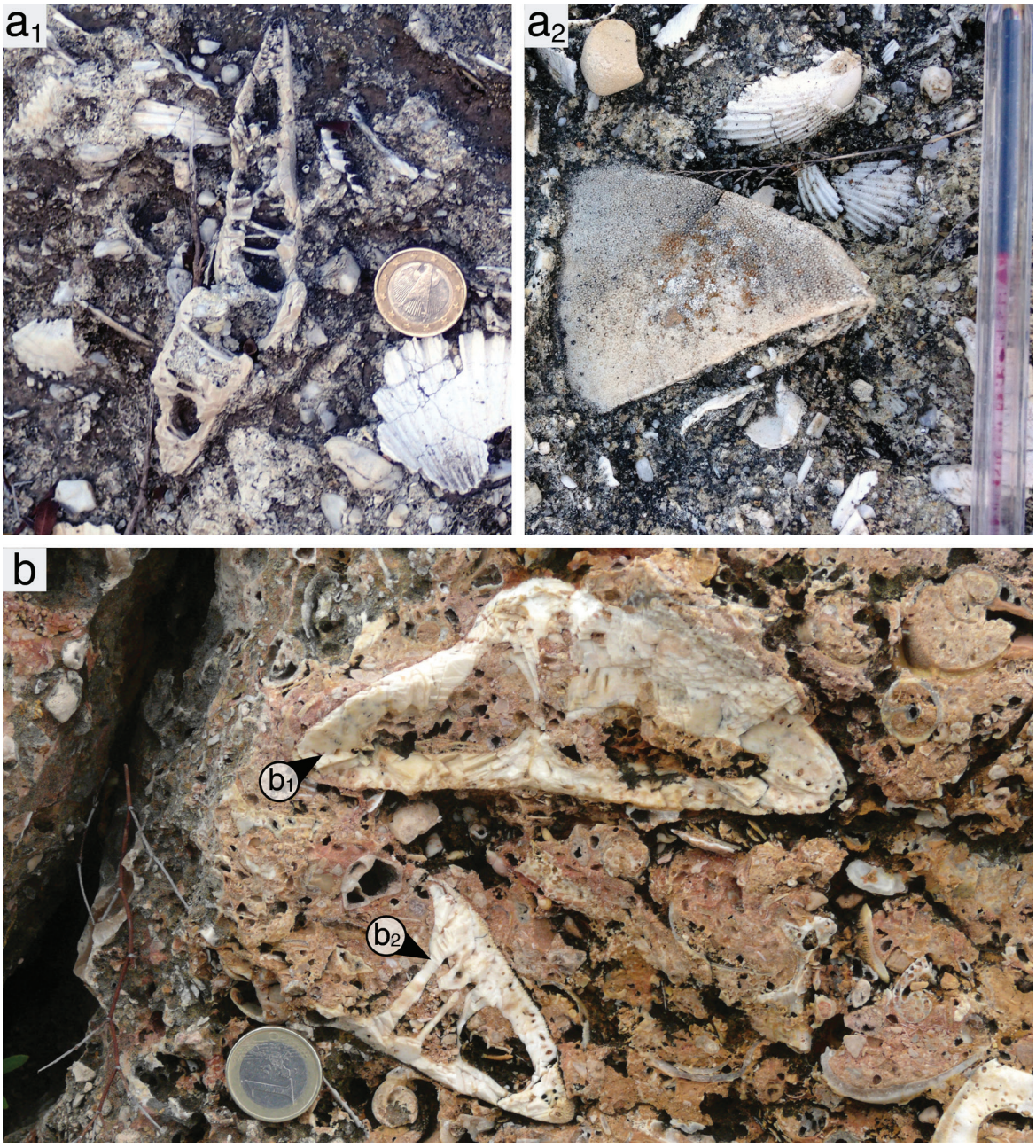

Figure 5. Miocene *Clypeaster* sp.: (a) Early Miocene, Bancali, Sardinia, Italy. (a1) Cross section through a complete (?) skeleton showing thick walls and internal supports. (a2) a pie-shaped fragment consisting a 1/5th of the test. (b) Middle Miocene, L'Arrabassada, Tarragona, north-east Spain: (b1) a complete (?) domed specimen showing thick walls. (b2) a large fragment showing internal pillars extending from the oral to the aboral side of the test.

Out of 22 fragmented specimens, 15 tests (68.2%) were found as pie-shaped fragments representing 1/5th of the skeleton (Fig. 4c). These pie-shaped fragments consist of a complete double-row of interambulacral plates embraced by two single-rows of ambulacral plates (Figs. 2, 4c). The fragments include both the oral and aboral surfaces of the test, and are often found *in situ* on the sea floor.

Fossil *Clypeaster* from Italy. — Out of the 30 fossil samples (Tab. 2), 15 specimens (50.0%) show inter-plate fragmentation with six specimens (40.0%) in pie-shape and nine specimens (60.0%) showing complex lateral and radial fragmentation patterns resulting in small and non-pie-shaped pieces. Five of these non-pie-shaped fragments (33.3%) showing bioinfestation. The six pie-shaped fragments (40.0%) show fragmentation along the perradial suture in five cases (83.3%). A single specimen (16.7%) show additional partial fragmentation along the adradial and interradial sutures. From the six pie-shaped fragments, four fragments (66.7%) showed bioinfestation.

Important morphological structures

Plate connections. — Individual plates in the *Clypeaster rosaceus* test are interconnected by stereom protrusions (Fig. 6). These stereom protrusions penetrate from one plate into the stereom interspace of adjoining plates forming a tight fitting interlock. This interlocking mechanism is found in all three radial suture types (perradial, adradial and interradial), and is similar with respect to size and density (Fig. 6).

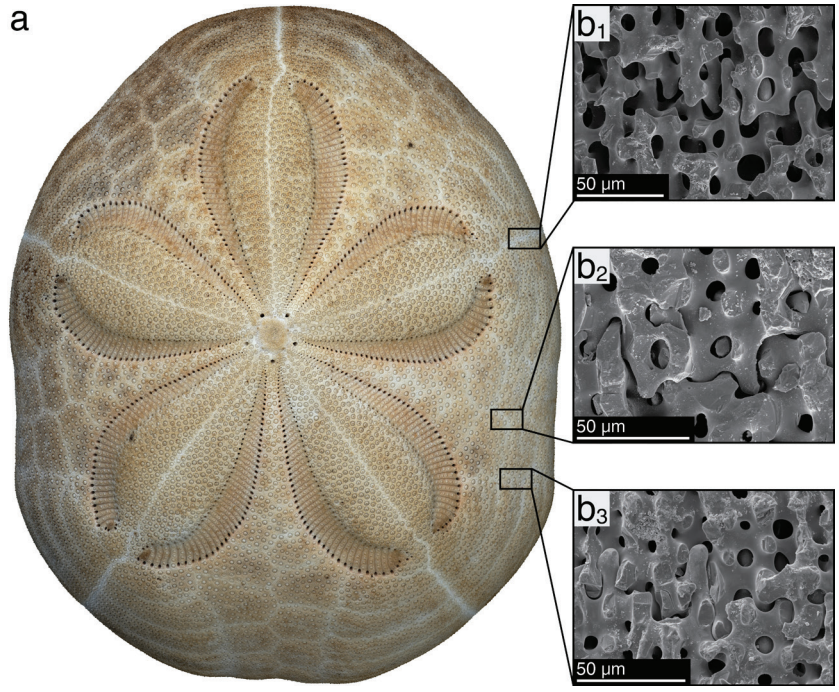

Figure 6. Interlocking sutures of *Clypeaster rosaceus* from the Bahamas. (a) Photograph of the aboral side [GPIT/EC/00743:SSI-FDB-CR-15]. Sutural connections of the (b1) perradial suture, (b2) interradial suture, and (b3) adradial suture [GPIT/EC/00743:SSI-FDB-CR-4].

Internal supports. — The internal support system of *Clypeaster rosaceus* consists of multiple wall-like pillars, which are aggregated around the jaw-apparatus (Fig. 7). The pillars are commonly extensive and thin-walled, but can also be arranged as branched arch systems (Fig. 8). The analyses of the internal pillar system indicate that pillars arise from both the oral and aboral interambulacral plates, and reach towards one another. The base of the pillars cross both interradial and adradial sutures. The perradial sutures are, however, rarely crossed or reached by internal supports (Figs. 7, 8).

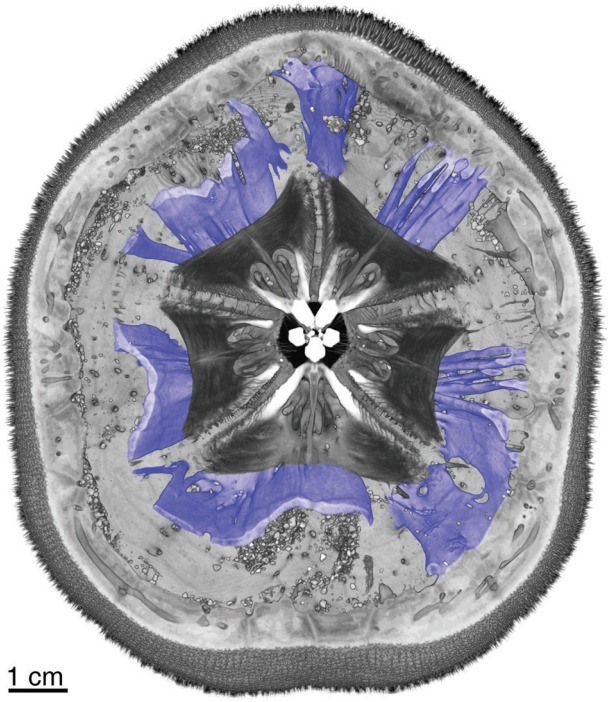

Figure 7. Micro-CT reconstruction of *Clypeaster rosaceus* in aboral view showing the lantern surrounded by the internal supports (blue colored) [GPIT/EC/00743:SSI-FDB-CR-28].

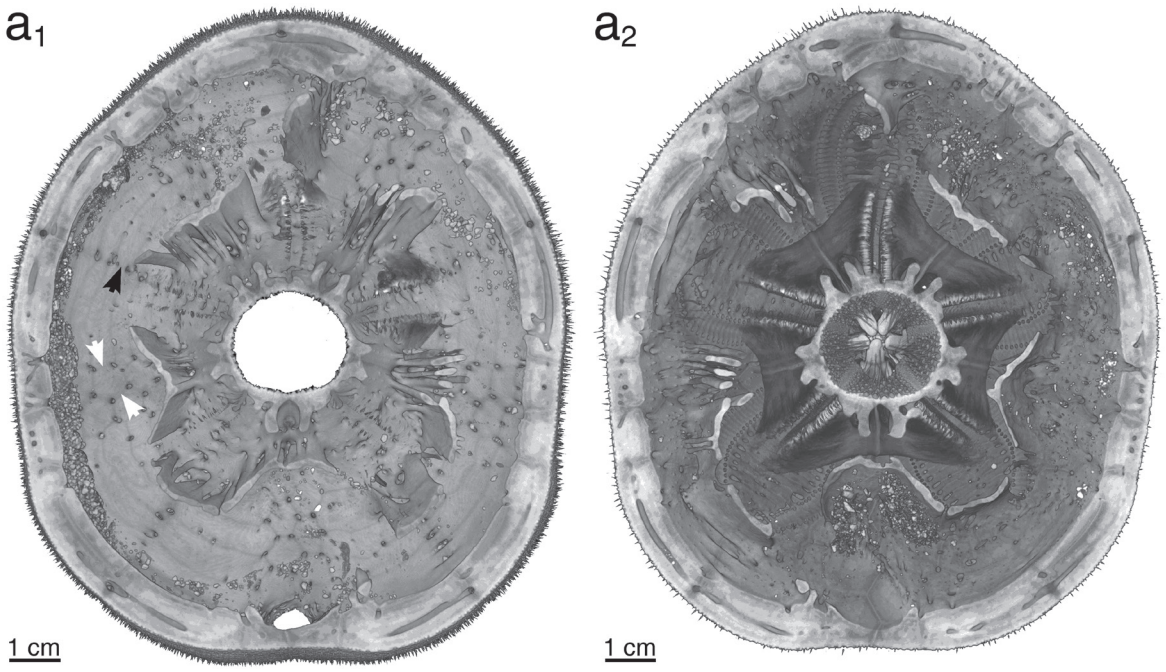

Figure 8. Micro-CT reconstruction of *Clypeaster rosaceus* showing the (a1) interior oral surface and the (a2) interior aboral surface with wall-like pillars at the adradial and interradial sutures, and pillars close to the perradial sutures. Wall-structures can frequently cross adradial and interradial sutures (white arrows) where pillars rarely cross the plate borders of perradial sutures (black arrow) [GPIT/EC/00743:SSI-FDB-CR-28]. p = perradial suture, a = adradial suture, i = interradial suture.

Micro-canal system. — The double-walled test structure of *Clypeaster* is a result of a micro-canal system (Fig. 9) characterized by longitudinal channels within the ambulacral plates and horizontal canals along the perradial sutures. The interambulacral plates feature a massive double-wall structure with only single branch-like channels connecting the interior of the test to the exterior of the test (Fig. 9).

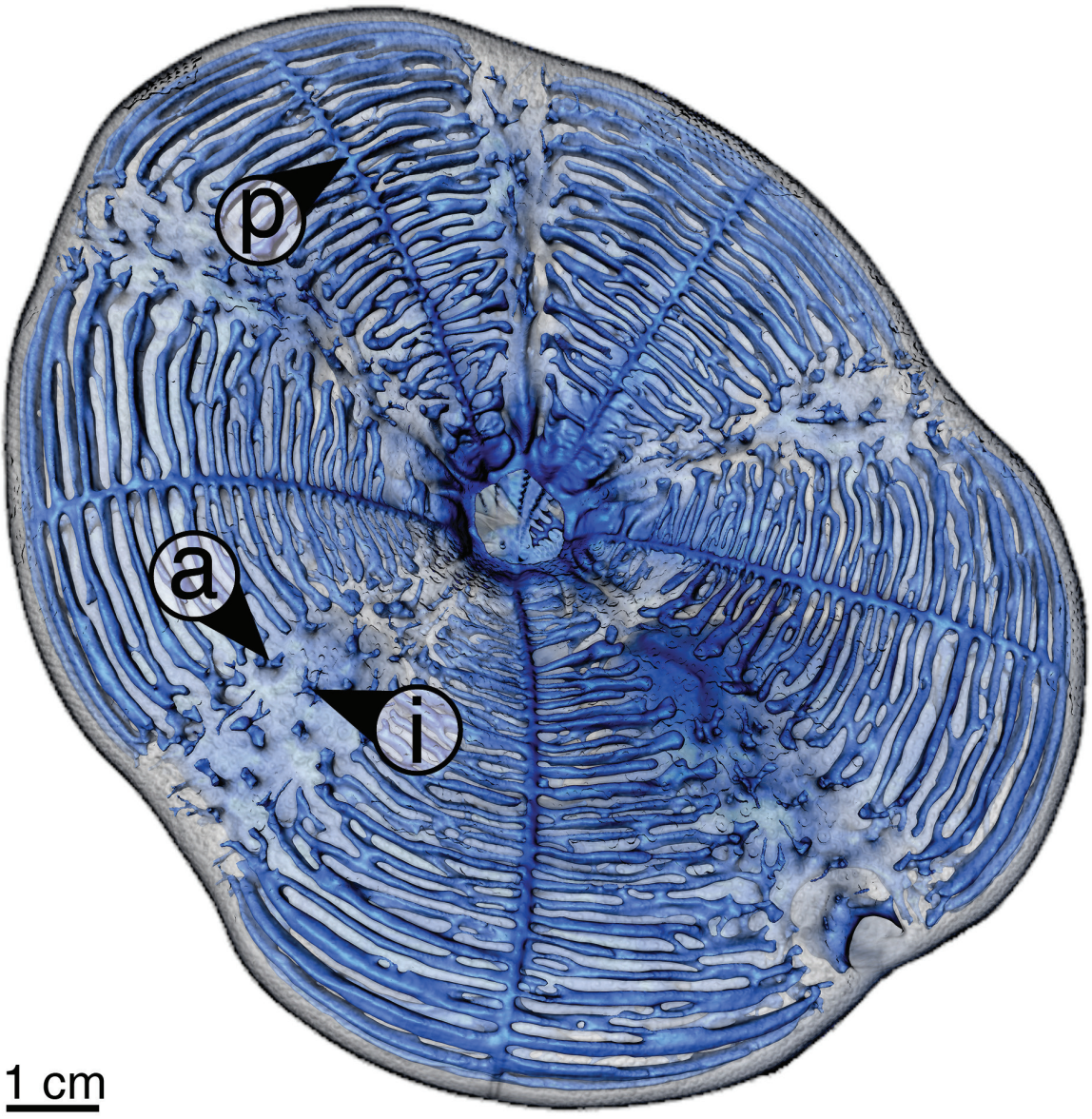

Figure 9. Micro-CT reconstruction of the micro-canal system of the *Clypeaster rosaceus* test in oral view. Micro-canals follow the course of perradial sutures or occur as branched stem-like structures at the adradial and interradial sutures [GPIT/EC/00743:SSI-FDB-CR-126]. p = perradial suture, a = adradial suture, i = interradial suture.

DISCUSSION

General preservation potential of the *Clypeaster* skeleton

The *in situ* observations on Recent *Clypeaster rosaceus* indicate that the dead test feature a good preservation potential. As described for *Clypeaster humulis* (Leske 1778) in the Red Sea (Nebelsick & Kampfer 1994; Nebelsick 2008), *Clypeaster* tests are robust enough to survive a whole range of processes along a complex taphonomic gradient ranging from pristine examples, across encrusted, bioeroded and abraded tests to highly corroded, albeit still recognizable specimens. Although the number of complete individuals is high, the majority of collected material shows fragmentation. Complex fragmentation patterns, where fragmentation occurs on more than one suture type, are rare. This indicates that the individual pie-shaped segments exhibit a high intrinsic stability, which is also reflected in the fossil record where along with complete *Clypeaster* tests, pie-shaped fragments can be present.

In almost 50% of the collected complete *Clypeaster rosaceus* specimens from the Recent, encrustation is present suggesting an extensive surface residence time and biotic interactions. This is again reflected in the fossil record where the long surface residence times of fossil *Clypeaster* were extensive enough to allow for complex bioinfestation including both encrustation and bioerosion (Belaustegui et al. 2013, 2017; Rahman et al. 2015; Mancosu & Nebelsick 2017).

Fragmentation patterns

Upon fragmentation, tests of *Clypeaster rosaceous* typically separate along the perradial sutures (Figs. 2, 4b, c). Interradial and adradial sutures are less commonly affected by fragmentation reflecting the fact that these sutures show a higher structural performance over those of the perradial sutures even though SEM analyses show that plates at the perradial, adradial and interradial sutures are all interconnected by stereom protrusions (Fig. 6). The plate interlocking mechanisms of the three suture types appears similar in terms of protrusion morphology and magnitude (Fig. 6), thus can be interpreted as not crucial for the observed differences in structural performance. The presence of the micro-canal system, which follows the perradial sutures, reduces the test thickness and the interlocking area between the ambulacral rows, thus destabilizing the entire suture.

The layout of internal supports is highly different among sutures. The base of internal supports crossing the adradial and interradial sutures provides additional reinforcement to the plate joint. This is not common in the perradial sutures (Figs. 7, 8). Furthermore, internal supports bridge the gap between the adoral and oral surfaces within the interambulacralia, but bridging is rare for sutures of the ambulacral plate rows. The presence and disposition of the internal supports thus dictate the stability of test areas with weak perradial zones within the ambulacralia and strengthened interradial sutures between the ambulacralia, and interambulacralia as well as adradial sutures within the interambulacralia. The differences in micro-canal distribution and the arrangement of internal supports eventually result in the typical pie-shaped fragments broken along the perradial sutures within the ambulacralia, which can also be observed in the fossil record (Fig. 5).

Taphonomy as a tool for biomimetic research

Taphonomic signals such as fragmentation and encrustation are used in this study as a primary indicator of the stability of multi-plated shells. In both fossil and Recent *Clypeaster*, a general trend in the production of pie-shaped fragments was observed. The results suggest that there is a direct correlation between skeletal architecture and fragmentation patterns. Taphonomic studies consequently not only have the potential to interpret environmental signals and patterns of alterations (Nebelsick 1999; Kroh & Nebelsick 2010; Grun et al. 2017a), but can also be employed as a powerful tool for biomimetic research as they reflect underlying principles of skeletal architectural design.

The concept behind biomimetic research is the finding of evolutionary optimized principles in natural systems, that can improve existing technical solutions or lead to novel developments to encounter technical problems (Drack et al. 2018). The basis of biomimetic research hence entails the identification of evolutionary optimized systems. The example employed in this study, shows that the interpretation of taphonomic states can be used as a method to reveal such systems. Although the analyzed tests of *Clypeaster* are taphonomically altered by fragmentation and bioinfestation in both Recent and fossil occurrences, it is shown the pie-shaped fragments exhibit a remarkable strength. The integrity of these pie-shaped fragments indicates that one or more strengthening principles act on these fragments. Therefore, taphonomy can be applied as a tool for identifying stable shells in natural environments as the basis for further biomimetic research.

CONCLUSIONS

(1) Taphonomic processes can be used to identify biomimetically relevant structures. The observed preservation of *Clypeaster* in both Recent and fossil environments is indicative of stabilizing features within the shell which are reflected in taphonomic patterns.

(2) The general stability of the *Clypeaster* skeleton is enhanced by interplate interfingering joints consisting of pegs which reach from one plate to another, as well as robust internal supports which join the oral and aboral sides of the skeleton. The latter are mainly restricted to the interambulacral plate rows.

(3) Tests of *Clypeaster rosaceus* predominantly fragmentize along specific radially arranged sutures. The fragmentation pattern shows that these skeletons underlie specific constructional principles with less stable perradial sutures and more stable adradial and interradial sutures.

(4) The micro-canal system along perradial sutures can decrease post-mortem test integrity, particularly since radially arranged canals are present in the ambulacralia.

Acknowledgments

The work of T. B. Grun and J. H. Nebelsick is funded by the German Research Foundation (DFG) as part of the Transregional Collaborative Research Centre (SFB/Transregio) 141 “Biological Design and Integrative Structures” project A07. We thank The Paleontological Society, The Gerace Research Centre, Hartmut Schultz (Scanning Electron Microscopy Lab, Department for Geosciences, University of Tübingen), and Raouf Jemmali (German Aerospace Center, Stuttgart, Germany). We also thank Martin Zuschin for organizing the Taphos Meeting 2017 in Vienna, as well as Stephen K. Donovan and Andreas Kroh for their reviews.

REFERENCES

Alvarado, J.J. & Solís-Marín, F.A. (2013): Echinoderm Research and Diversity in Latin America. – 658 pp.; Heidelberg (Springer).

Belaústegui, Z., Nebelsick, J.H., Gibert de, J.M., Domènech, R. & Martinell, J. (2012): A taphonomic approach to the genetic interpretation of clypeasteroid accumulations from Tarragona (Miocene, NE Spain). – Lethaia, 45: 548-565.

Belaústegui, Z., Gibert de, J.M., Nebelsick, J.H., Domènech, R. & Martinell, J. (2013): Clypeasteroid echinoid tests as benthic islands for gastrochaenid bivalve colonization: Evidence from the Middle Miocene of Tarragona (North-East Spain). – Palaeontology, 56: 783-796.

Belaústegui, Z., Muñiz, F., Nebelsick, J.H., Domènech, R. & Martinell, J. (2017): Echinoderm ichnology: bioturbation, bioerosion and related processes. – Journal of Paleontology, 91: 643-661.

Chakra, M.A. & Stone, J.R. (2011): Classifying echinoid skeleton models: testing ideas about growth and form. – Paleobiology, 37: 686-695.

Dixon, H.L. & Donovan, S.K. (1998): Oligocene echinoids of Jamaica. – Tertiary Research, 18: 95-124.

Donovan, S.K. (1991): The taphonomy of echinoderms: calcareous multi-element skeletons in the marine environment. – In: Donovan, S.K. (Ed.): The Process of Fossilization: 241-269; London (Belhaven Press).

Donovan, S.K., Dixon, H.L., Pickerill, R.K. & Doyle, E.N. (1994): Pleistocene echinoid (Echinodermata) fauna from southeast Jamaica. – Journal of Paleontology, 68: 351-358.

Drack, M., Limpinsel, M., de Bruyn, G., Nebelsick, J.H. & Betz, O. (2018): Towards a theoretical clarification of biomimetics using conceptual tools from engineering design. – Bioinspiration & Biomimetics, 13: 016007.

Durham, J.W. (1966): Clypeasteroids. Treatise on invertebrate paleontology, Part U, Echinodermata 3.2. – 328 pp.; Lawrence (University of Kansas Press).

Gordon, J.E. (1978): Structures: or why things don't fall down. – 395 pp.; New York (Da Capo Press).

Gray, J.E. (1855): Catalogue of the Recent Echinida, or Sea Eggs, in the Collection of the British Museum. Part I.-Echinida Irregularia. - 69 pp.; London (Woodfall and Kinder).

Grun, T.B., Koohi, L., Schwinn, T., Sonntag, D., von Scheven, M., Bischoff, M., Knippers, J., Menges, A. & Nebelsick, J.H. (2016): The skeleton of the sand dollar as a biological role model for segmented shells in building construction: A research review. – In: Knippers, J., Nickel, K.G. & Speck, T. (Eds.): Biologically-Inspired Design and Integrative Structures: Analysis, Simulation and Implementation in Architecture: 217-242; Cham (Springer).

Grun, T.B., Kroh, A. & Nebelsick, J.H. (2017a): Comparative drilling predation on time-averaged phosphatized and non-phosphatized assemblages of the minute clypeasteroid echinoid Echinocyamus stellatus from Miocene offshore sediments (Globigerina Limestone Fm., Malta). – Journal of Paleontology, 91: 633-462.

Grun, T.B., von Scheven, M., Geiger, F., Schwinn, T., Sonntag, D., Bischoff, M., Knippers, J., Menges, A. & Nebelsick, J.H. (2017b): Bauprinzipien und Strukturdesign von Seeigeln - Vorbilder für Bioinspirierte Konstruktionen. – In: Knippers, J., Schmid, U. & Speck, T. (Eds.): Baubionik: Biologie beflügelt Architektur. Stuttgarter Beiträge zur Naturkunde Serie C, Band 82: 82-93; Stuttgart (Staatliches Museum für Naturkunde Stuttgart).

Hendler, G., Miller, J.E., Pawson, D.L. & Kier, P.M. (1995): Sea stars, sea urchins, and allies: echinoderms of Florida and the Caribbean. – 390 pp.; Washington D.C. (Smithsonian Institution Press).

Hopkins, T.S. (1988): A review of the distribution and proposed morphological groupings of extant species of the genus *Clypeaster* in the Caribbean Sea and Gulf of Mexico. – In: Burke, R.D., Mladenov, P.V., Lambert, P. & Parsley, R.L. (Eds.): Echinoderm Biology. Proceedings of the Sixth International Echinoderm Conference: 337-345; Rotterdam (A.A. Balkema).

Kampfer, S. & Ott, J. (1995): Nutrition and feeding preferences of the Caribbean echinoid *Clypeaster rosaceus* (Echinodermata: Echinoidea). – In: Eleftheriou, A., Ansell, A. & Smith, Ch. (Eds.): Biology and Ecology of Shallow Coastal Waters: 309-313; Fredensborg (Olsen & Olsen).

Kidwell, S.M. & Baumiller, T. (1990): Experimental disintegration of regular echinoids: roles of temperature, oxygen, and decay thresholds. – Paleobiology, 16: 247-271.

Kier, P.M. (1975): The echinoids of Carrie Bow Cay, Belize. – Smithsonian Contributions to Zoology, 206: 1–45.

Kier, P.M. & Grant, R.E. (1965): Echinoid distribution and habits, Key Largo Coral Reef Preserve, Florida. – Smithsonian Miscellaneous Collections, 149: 1-68.

Kroh, A. (2005): Catalogus Fossilium Austriae. Band 2. Echinoidea neogenica. – 210 pp.; Wien (Österreichische Akademie der Wissenschaften).

Kroh, A. & Nebelsick, J.H. (2003): Echinoid assemblages as a tool for palaeoenvironmental reconstruction - An example from the Early Miocene of Egypt. – Palaeogeography, Palaeoclimatology, Palaeoecology, 201: 157-177.

Kroh, A. & Nebelsick, J.H. (2010): Echinoderms and Oligo-Miocene Carbonate Systems: Potential applications in sedimentology and environmental reconstruction. – International Association of Sedimentology Special Publications, 42: 201-228.

Lamarck, J.B. (1801): Système des animaux sans vertèbres. – 452 pp.; Paris (Deterville).

Lambert, J. (1927): Revision des echinides fósiles de la Catalogne. -Memorias del Museo de Ciencias Naturales de Barcelona. Serie Geológica, 1:71, 1–102.

Lawrence, J. (1987): A functional biology of echinoderms. – 340 pp.; Baltimore (John Hopkins University Press).

Leske, N.G. (1778): Jacobi Theodorie Klein Naturalis Dispositio Echinodermatum. – 278 pp.; Lipsiae (Gleditsch).

Linnaeus, C. (1758). Systema Naturae per regna tria naturae, secundum classes, ordines, genera, species, cum characteribus, differentiis, synonymis, locis. Editio decima, reformata. – 824 pp.; Holmiae (Laurentius Salvius).

Mancosu, A. & Nebelsick, J.H. (2013): Multiple routes to mass accumulations of clypeasteroid echinoids: a comparative analysis of Miocene echinoid beds of Sardinia. – Palaeogeography, Palaeoclimatology, Palaeoecology, 374: 173-186.

Mancosu, A. & Nebelsick, J.H. (2015): The origin and paleoecology of clypeasteroid assemblages from different shelf setting of the Miocene of Sardinia, Italy. – Palaios, 30: 273-387.

Mancosu, A. & Nebelsick, J.H. (2017): Ecomorphological and taphonomic gradients in clypeasteroid-dominated echinoid assemblages along a mixed siliciclastic-carbonate shelf from the early Miocene of northern Sardinia, Italy. – Acta Palaeontologica Polonica, 62: 627-646.

Mihaljević, M., Jerjen, I. & Smith, A.B. (2011): The test architecture of *Clypeaster* (Echinoidea, Clypeasteroida) and its phylogenetic significance. – Zootaxa, 2983: 21-38.

Michelin, H. (1861): Monographie des Clypéastres fossiles. – Mémoire de la Société Géologique de France (série 2), 7: 101-147.

Mitrović-Petrović, J. (1984): Importance biostratigraphique et paleoecologique du genre *Clypeaster* (Echinoidea) pour les sediments neogenes de la Yougoslavie. - Colloquium on Mediterranean Neogene marine megafaunal palaeoenvironments and biostratigraphy. – Annales Géologiques des Pays Hellénique, 32: 211-235.

Mooi, R. (1989): Living and fossil genera of the Clypeasteroida (Echinoidea: Echinodermata): an illustrated key and annotated checklist. – Smithsonian Contributions to Zoology, 488: 1-51.

Mooi, R., Kroh, A. & Srivastava, D.K. (2014): Phylogenetic re-evaluation of fossil and extant micro-echinoids with revision of Tridium, Cyamidia, and Lenicyamidia (Echinoidea Clypeasteroida). – Zootaxa, 3857: 501-526.

Moore, H. (1966): Ecology of echinoids. – In: Boolootian, R.A. (Ed.): Physiology of Echinodermata: 73-85; New York (John Wiley & Sons).

Mortensen, T. (1948): A monograph of the Echinoidea, IV, 2. Clypeasteroida. Clypeasteridæ, Arachnoidæ, Fibulariidæ, Laganidæ and Scutellidæ. – 471 pp.; Copenhagen (Clypeaster A. Reitzel).

Moss, M.L. & Meehan M.M. (1967): Sutural connective tissues in the test of an echinoid: Arbacia punctulata. – Acta Anatomica, 66: 279-304.

Müller, O.F. (1776): Zoologicæ prodromus, seu animalium Daniæ et Norvegiæ indigenarum characteres, nomina, et synonyma imprimis popularium. – 282 pp.; Havniæ (Typis Hallageriis).

Nebelsick, J.H. (1995): Actuopalaeontological investigations on echinoids: The potential for taphonomic interpretation. – In: Emson, R.H., Smith, A.B. & Campbell, A.*Clypeaster* (Eds.): Echinoderm Research: 209-214; Rotterdam (A.A. Balkema).

Nebelsick, J.H. (1999): Taphonomic comparison between recent and fossil sand dollars. – Palaeogeography, Palaeoclimatology, Palaeoecology, 149: 349-358.

Nebelsick, J.H. (2008): Taphonomy of the irregular echinoid *Clypeaster humilis* from the Red Sea: Implications for taxonomic resolution along taphonomic grades. – In: Ausich, W.I. & Webster, G.D. (Eds.): Echinoderm Paleobiology: 115-128; Bloomington (Indiana University Press).

Nebelsick, J.H. & Kroh, A. (2002): The Stormy Path from Life to Death Assemblages: The Formation and Preservation of Mass Accumulations of Fossil Sand Dollars. – Palaios, 17: 378-394.

Nebelsick, J.H. & Kampfer, S. (1994): Taphonomy of *Clypeaster humilis* and *Echinodiscus auritus* from the Red Sea. – In: David, B., Guille, A., Féral, J.P. & Roux, M. (Eds.): Echinoderms through time: 803-808; Rotterdam (Balkema).

Nebelsick, J.H., Dynowski, J.F., Grossmann, J.N. & Tötzke, C. (2015): Echinoderms: Hierarchically organized light weight skeletons. – In: Hamm, C. (Ed.): Evolution of Lightweight Structures: Analyses and Technical Applications, Biologically-Inspired Systems: 141-156; Dordrecht (Springer).

Philippi, U. (2001): Finite Element-Analyse von Seeigelschalen. – In: Reinhardt, H.W. & Reiner, R. (Eds.): Natürliche Konstruktionen in Raum und Zeit: 185-189; Stuttgart (Institut für Werkstoffe im Bauwesen).

Philippi, U. & Nachtigall, W. (1996): Functional morphology of regular echinoid tests (Echinodermata, Echinoida): a finite element study. – Zoomorphology, 116: 35-50.

Poddubiuk, R.H. (1984): Evolution and Adaptation in some Caribbean Oligo-Miocene Clypeasters. – In: Keegan, B.F. & O´Connor, B.D.S. (Eds.): Fifth International Echinoderm Conference: 75-80; Balkema (Galway).

Portell, R.W. & Oyen, C.W. (2002): Pliocene and Pleistocene Echinoids Florida Fossil Invertebrates Gainesville Florida. – Paleontological Society, 3: 1-30.

Rahman, I.A., Belaústegui, Z., Zamora, S., Nebelsick, J.H., Domènech, R. & Martinell, J. (2015): Miocene *Clypeaster* from Valencia (E Spain): Insights into the taphonomy and ichnology of bioeroded echinoids using X-ray micro-tomography. – Palaeogeography, Palaeoclimatology, Palaeoecology, 438: 168-179.

Rodríguez-Barreras, R. (2014): The shallow-water echinoids (Echinodermata: Echinoidea) of Cuba. – Marine Biodiversity Records, 7: 1-8.

Roman, J. (1952): Sur les structures internes des Clypéastres. – Bulletin de la Société Géologique de France, 11: 403-416.

Rose, E.P.F. & Poddubiuk, R.H. (1987): Morphological variation in the Cenozoic echinoid *Clypeaster* and its ecological and stratigraphical significance. – Annales Instituti Geologici Publici Hungarici, 70: 463-469.

Schaffer, H. (1962): Die Scutelliden des Miozäns von Österreich und Ungarn. – Paläontologische Zeitschrift, 36: 135-170.

Schodek, D.L. & Bechthold, M. (2013): Structures, 7th Edition. Harlow (Pearson), 549 pp.

Seilacher, A. (1979): Constructional morphology of sand dollars. – Paleobiology, 5: 191-221.

Serafy, D.K. (1979): Echinoids (Echinodermata: Echinoidea). – Memoirs of the Hourglass Cruises, 5: 1-120.

Smith, A. (1984): Echinoid Palaeobiology: Special Topics in Paleontology, Special Topics in Palaeontology. – 191 pp.; London (George Allen and Unwin).

Tamboli, A., Xing, M. & Ahmed, M. (2000): Structural theory. – In: Merritt, F. & Ricketts, J.T. (Eds.): Building Design and Construction Handbook, 6th Edition: 232-419; New York (Mc-Graw-Hill).

Telford, M. (1985a): Domes, arches and urchins: the skeletal architecture of echinoids (Echinodermata). – Zoomorphology, 105: 114-124.

Telford, M. (1985b): Structural analysis of the test of Echinocyamus pusillus (O. F. Müller). – In: Keegan, B.F. & O'Conner, B.D.S. (Eds.): Proceedings of the Fifth International Echinoderm Conference: 353-360; Rotterdam (Balkema).

Telford, M., Mooi, R. & Harold, A.S. (1987): Feeding activities of two species of *Clypeaster* (Echinoides, Clypeasteroida): Further evidence of clypeasteroid resource partitioning. – Biological Bulletin, 172: 324-336.

Tsaparas, N., Drinia, H., Antonarakou, A., Marcopoulou-Diakantoni, A. & Dermitzakis, M.D. (2007): Tortonian *Clypeaster* fauna (Echinoidea: Clypeasteroida) from Gavdos Island (Greece). – Bulletin of the Geological Society of Greece, 40: 225-237.

Zachos, L.G. (2008): A New Theoretical Model for Growth of the Echinoid Test. – 191 pp.; Unpublished Ph.D. thesis, University of Austin, Texas.

Zachos, L.G. (2015): Holistic morphometric analysis of growth of the sand dollar Echinarachnius parma (Echinodermata: Echinoidea: Clypeasteroida). – Zootaxa, 4052: 151-79.

Manuscript 3

Structural design of the minute

clypeasteroid echinoid *Echinocyamus pusillus*

Structural design of the minute clypeasteroid echinoid *Echinocyamus pusillus*

Tobias B. Grun* and James H. Nebelsick

Department of Geosciences, University of Tübingen, Hölderlinstraße 12, 72074 Tübingen, Germany

Keywords: Echinoid skeleton, multi-element shell, structural hierarchy, plate joints, internal supports, stereom architecture

Summary

The clypeasteroid echinoid skeleton is a multi-plated, light-weight shell construction produced by biomineralization processes. In shell constructions, joints between individual elements are considered as weak points, yet, these echinoid skeleton shows an extensive preservation potential in both Recent and fossil environments. The remarkable strength of the test is achieved by skeletal reinforcement structures and their constructional layouts.

Micro-computed tomography and scanning electron microscopy are used for structural and volumetric analyses of the echinoid's skeleton. It is shown, that strengthening mechanisms act on different hierarchical levels from the overall shape of the skeleton to micro-skeletal interlocking. The tight-fitting and interlocking plate joints lead to a shell considered to behave as a monolithic structure. The plate's architecture features distinct regions interpreted as a significant load transferring system. The internal support system follows the segmentation of the remaining skeleton, where sutural layout and stereom distribution are designed for effective load transfer. The structural analysis of the multi-plated, yet monolithic skeleton of *Echinocyamus pusillus* reveals new aspects of the micro-morphology and its structural relevance for the load-bearing behaviour. The analysed structural principles allow *Echinocyamus pusillus* to be considered as a role model for the development of multi-element, light-weight shell constructions.

Introduction

Organisms have developed various strategies to reinforce their skeletons during evolution [1]. Some of these skeletons are of high interest for technical solutions as their underlying constructional principles can be transferred to architecture and engineering disciplines. Hereby, existing solutions for technical problems can be improved, or, new strategies for structural optimisation can be developed [2–4]. Especially dome-shaped objects [5,6], as well as the suturing and interlocking between skeletal elements in both vertebrate and invertebrate skeletons have been analysed with respect to their mechanical design and function [7,8].

In architecture and engineering sciences, structural configurations are obviously of major interest with domes, for example, demonstrating a remarkable strength. In modern architecture, in which building conventions underlie stringent economic constraints, framework and material-intensive domes have often been replaced by cost-efficient, but less performative grid-shells covered by pre-fabricated, planar elements [9,10]. Such grid-based constructions, in which building parameters, e.g. grid-size, determine structural stability, are restricted in their architectural degree of freedom [10]. These disadvantages can be countered by the development of segmented shell constructions, which combine the advantages of structural strength and freedom of design. Segmented shells also represent an economically optimised processes by using pre-fabricated elements [10]. The multi-plated echinoid skeleton can be used as a biological role model for developing constructional principles that can be transferred into biomimetic solutions for improved segmented designs [9].

The echinoid role model

The echinoid (Echinodermata: Echinoidea) skeleton is constructed of multiple biomineralized plates [11], which are securely interconnected by soft tissues and, in some cases, skeletal interlocks [12–17]. The hierarchical organisation of echinoids additionally allows for the separation and functional interpretation of principles along the skeletal configuration [18]: the complete individual includes all skeletal elements, soft tissues, and appendages (hierarchical level 1). The denuded echinoid test (hierarchical level 2), which encloses the internal organs, serves as a platform for appendages and is made of multiple plates (hierarchical level 3). Individual skeletal elements consist of a lattice-like stereom (hierarchical level 4) with a highly differentiated morphology, density and function [11,19,20]. The stereom

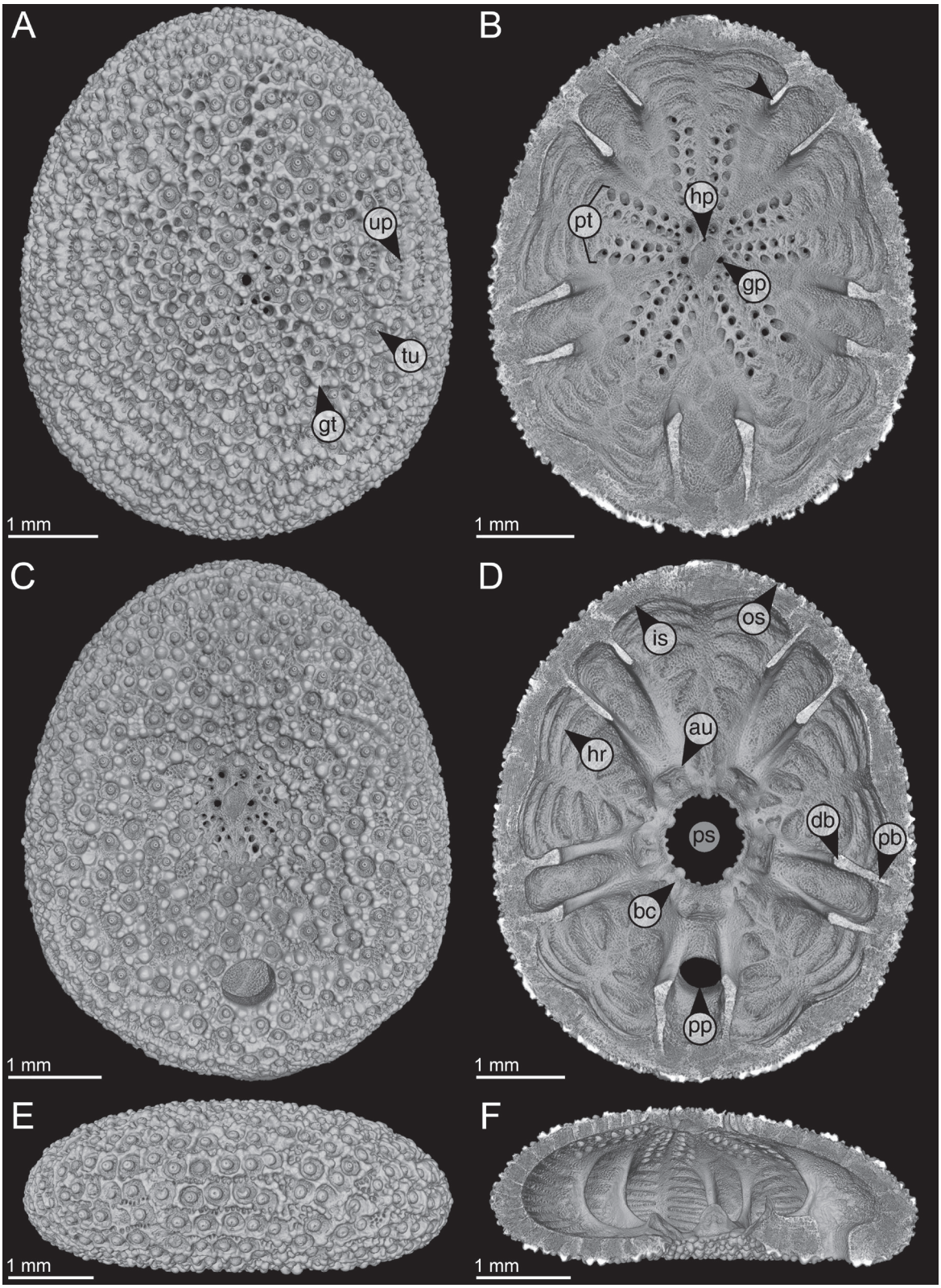

Figure 1. *Echinocyamus pusillus*. Micro-CT based volume rendering of the denuded test [GPIT/EC/00740:gg-al-1.73]. (A) View of the aboral side. (B) Horizontal section with view onto the internal aboral surface. (C) View of the oral side. (D) Horizontal section with view onto the internal oral surface. (E) Lateral view, anterior to the left. (F) Lateral section showing internal test structures. au = auricle, bc = basicoronal ring, bu = buttress, db = distal buttress, gp = genital pore, gt = glassy tubercle, hp = hydropore, hr = horizontal rib, is = inner surface, os = outer surface, pb = proximal buttress, ps = peristome, pt = petal, pp = periproct, tu = tubercle, up = unipore.

is made up of trabeculae (hierarchical level 5) consisting of high-magnesium calcite struts [21–23], which represents a composite material (hierarchical level 6) with 0.1 to 0.2 weight % organic substances [24,25].

The architecture of the sea urchin skeleton has been in the focus of technical analysis for the last decades [9,14–16,26–30]. In-depth studies have been made on the test's microstructure using scanning electron microscopy and increasingly micro-computed tomography [11,19,20,31–38]. The most comprehensive technical studies on the echinoid skeleton provided for a detailed theoretical and mechanical background, which were discussed with respect to dome structures and their static properties [15,26,28]. The plate connections and internal supports were also described as structures that support the test under compression loads, whereas connective tissues counteract tension stress in most echinoids [15,16].

Clypeasteroid echinoids (Echinoidea: Clypeasteroidea) are usually flattened sea urchins featuring various internal support systems such as pillars, buttresses and ridges [9,15,16,31,38]. These echinoids can be abundant in high-energy environments and the fossil record, where they are frequently well-preserved [39–42]. The occurrence of *Echinocyamus pusillus* under these conditions demonstrate the remarkable test strength, which is attributed to the presence of skeletal reinforcements [9,43,44].

The clypeasteroid genus *Echinocyamus* is characterized by a minute test size typically less than 20 mm in length [45–50]. *Echinocyamus* is abundant in Recent and fossil environments distributed around Europe, West-Africa, south-eastern USA, as well as from the Indo-Pacific, where it occurs from shallow waters to the deep-sea [48,51–59]. The common species *Echinocyamus pusillus* (Fig. 1) has been broadly described with regard to its morphology [45,54,59–61] and ecology [46,62–65]. One exceptional characteristic of this echinoid is that it lacks collagenous fibres within its sutures [15,16]. The stability of the test therefore relies primarily on the skeletal construction [16].

Although it has been shown that echinoids can in general be used as role models in engineering sciences [9,14–18,26,28,30,35], only little research has yet focused on the technical aspects of the unique *Echinocyamus pusillus* test in particular [16]. Major aspects responsible for the test stability such as the three-dimensional (3d) interaction of test structures and variations in the stereom density remained hitherto unaddressed. The skeletal features that lead to this remarkable test strength are explored here in detail using x-ray micro-computed tomography (μCT) and scanning electron microscopy (SEM). The use of 3d techniques combined with high-resolution SEM imagery allows for in-depth analyses of structures and

their interactions for a novel functional interpretation. The understanding of the strengthening mechanisms is not only important as the basis for technical analyses and potential biomimetic applications, but also a contribution to palaeontology where these echinoids are used to reconstruct ancient ecosystems and biotic interactions [43,46,47,50,66].

Load-model

Echinocyamus pusillus is known to live infaunally and burrows in various substrates ranging from silts to coarse sands [53,63–65,67,68]. The skeleton is covered by a thin sediment layer [64] which causes downwards loads on the test. The roughly dome-shaped test is considered to behave as a 3d array of arches [15], on which downward forces are turned into lateral thrust [69] (Fig. 2). The flattening of these arches causes additional thrust in the test [15]. The load-model used here is simplified, disregarding possible lateral loads caused by water agitation and the respective sediment movement. Water pressure has been shown to have no effect on the echinoid skeleton, as the pressure within the skeleton is similar to that of the outside [70].

Finite element analyses based on slightly oblate regular sea urchin skeletons revealed that circumferential forces are compressive along the entire tests, increasing from the area of origin to the oral side (bottom) of the test [26,28] (Fig. 2). The radial forces result in compressive stress at the area of origin and along horizontal elastic trusses, whereas radial forces in all other areas result in tensile stress [26].

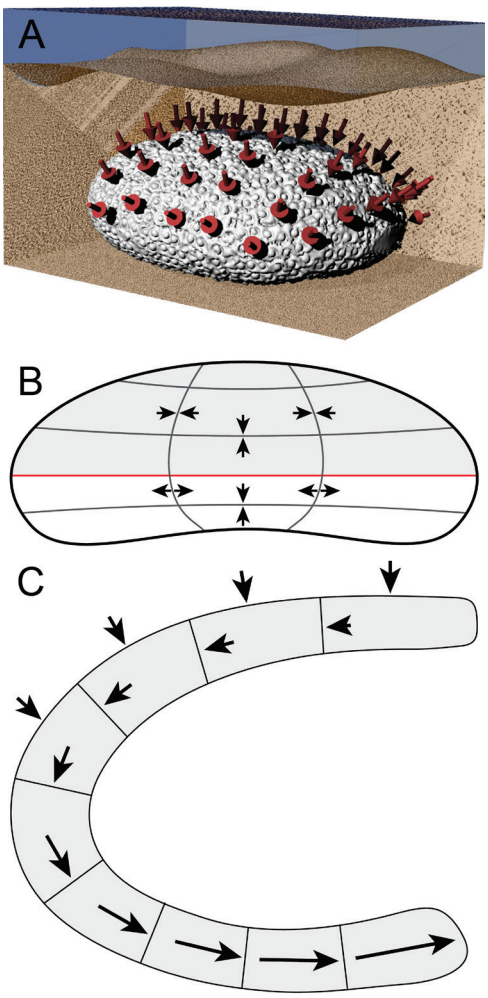

Figure 2. Load conditions in *Echinocyamus pusillus*. (A) Test rendered in a hypothetical environment, buried within the sediment. Arrows indicate the loaded areas [GPIT/EC/00740:gg-al-1.73]. (B) Sketch of *Echinocyamus pusillus* in lateral view. Radial lines indicate the course of radial stress. Horizontal lines represent the course of latitudinal stress. The red line indicates the ambitus. (C) Sketch of a part of the test in lateral view. External arrows indicate downward stress that turns into lateral thrust within the plates.

Materials and Methods

Materials

Denuded tests of *Echinocyamus pusillus* were collected in the summer of 2010 during SCUBA dives around Giglio (Tyrrhenian Sea, Italy: 42°21'07.9"N 10°52'52.1"E) and from beach sediments at Riccione (Adriatic Sea, Italy: 44°01'17.9"N 12°38'13.6"E) in September 2014. The samples are stored at the Department of Geosciences, University of Tübingen, Germany, under repository GPIT/EC/00740 for Giglio and GPIT/EC/00741 for Riccione. GPS data are obtained from Google Maps 2017.

Methods

The test of *Echinocyamus pusillus* is analysed using μCT) and SEM with respect to the (1) test design, including radial curvature, plate arrangement and thickness, (2) plate architecture, including stereom types and stereom density, (3) interlocking mechanisms on different hierarchical levels, and (4) internal support system with respect to stereom differentiation and sutural layout.

Micro-computed tomography

Specimen GPIT/EC/00740:gg-al-1.73 was cleaned for 30 min in a Bandelin DT106 (Bandelin Electronic, Berlin, Germany) ultrasonic bath and then air-dried. The scan [71] was generated with a Phoenix Nanotom 180 nF (General Electric Company Corporation, Boston, MA, USA) at the German Aerospace Center (Deutsches Zentrum für Luft- und Raumfahrt), Stuttgart, Germany. The isotropic voxel resolution is 3 μm (voltage = 80 kV, power = 180 μA, exposure time = 800 ms, projections = 2000).

Scanning electron microscopy

Complete tests of *Echinocyamus pusillus* [GPIT/EC/00741] were placed on separate aluminium specimen stubs (Plano GmbH, Wetzlar, Germany) in either the horizontal (oral side down) or lateral (right side down) position. Tests were attached to the stubs by partially impressing the echinoid skeleton into hand-warm Leit-C-Plast (Plano GmbH, Wetzlar, Germany) on a Leit-Tabs (Plano GmbH, Wetzlar, Germany) base. The non-Leit-C-Plast embedded part of the skeleton was then ground in the horizontal or lateral plane employing a Dremel 300i rotary tool (Dremel, Racine, WI, USA) equipped with a Dremel EZ Speedclic

diamond cutting wheel (Dremel, Racine, WI, USA). The ground surface was additionally fine-sanded with 1200-grit sandpaper. Grinding residues were removed by compressed air. Samples GPIT/EC/00741:RI-n.5, RI-1.6 and RI-1.19 were additionally placed for 1 s in hydrochloric acid (2.8 mol/L) to expose the interlocking mechanism more clearly. Acid-treated samples were washed three times in water to stop the reaction and removing the acid. Samples were then cleaned in a 30 min Bandelin DT106 (Bandelin Electronic, Berlin, Germany) ultrasonic bath. Samples were dried in a Heraeus LUT6050 (Kendro Laboratory Products, Hanau, Germany) convection oven at 60ºC and then platinum-sputtered on a planetary rotation disc for 120 s using a Baltek SCD 005 sputter coater (Bal-Tec, Balzers, Lichtenstein). Samples were scanned with a Leo 1450VP (Carl Zeiss AG, Oberkochen, Germany) scanning electron microscope at the Department of Geosciences, University of Tübingen, in the secondary electron (SE1) mode at 9 or 15 kV. Micrographs are recorded to a resolution of 2048 x 1536 pixels per inch (ppi) for standard images and 3072 x 2304 ppi for a high-resolution overview [GPIT/EC/00741:RI-1.19].

Test design

The µCT scan was rendered in Avizo 9.2.0 (Thermo Fisher Scientific, Waltham, MA, USA). The radial curvature was determined from µCT sections through the centre of the test. In these sections, the centre of each plate was identified. When the connecting line between the plate centre points matches a monotonic curve progression along the entire section, the test is considered convex. The plate arrangement is described from horizontal µCT sections visualized in Avizo. The sections are examined for the sutural course throughout the test in 3d space. The plate thicknesses are determined from horizontal µCT sections and measured orthogonal to the test surface. The measurements were obtained from three sections and for all 20 plate columns, resulting in 3 x 10 data points from ambulacral plates and respectively 3 x 10 data points from interambulacral plates. The sutures were measured at the boundaries between ambulacral plates (perradial suture), between interambulacral plates (interradial sutures), as well as between ambulacral and interambulacral plates (adradial sutures). Perradial and interradial sutures occur five times on each of the three slices (3 x 5 data points), whereas adradial sutures occur ten times on each of the three slices (3 x 10 data points).

The thickness measurements are statistically tested for differences among the corresponding regions using a Kruskal-Wallis H test followed by a pairwise Benjamini, Hochberg and Yekutieli p-adjusted Wilcoxon post-hoc analysis [72]. Statistical analyses are computed using the R software environment (R Foundation, Vienna, Austria) version 3.3.2 [73].

Plate architecture

The main stereom types found within the plates are assigned to established stereom types [19]. The plates' outer surfaces are excluded from this analysis due to the complex microstructures involving numerous stereom types [19] that do not contribute to the overall test stability. Stereom densities are analysed using three subvolumes with an edge length of 30 voxels (90 μm) along transects from the centre to the plate boundaries (supplementary material). Three transects per plate (three plates in total) at an angle of roughly 120° to one another are used.

The subvolumes are processed and analysed in Avizo 9.2.0. The delineate sharpening filter (size = 3 pixels) of Avizo was used to enhance the contrast between air and the stereom within each raw-subvolume. The de-noised subvolumes were then binarized applying the build-in auto-thresholding function on each 3d subvolume (mode = min-max, criterion = factorisation). This automated method of thresholding ensures repeatability of the procedure and eliminates experimenter bias. The built-in analyse function reports the amount of positive (stereom) and negative (non-material) voxels for each 3d volume. Stereom density is the sum of positive voxels divided by the total number of voxels within the subvolume.

Stereom density distributions are statistically tested for differences among the three plate regions using a Kruskal-Wallis H test followed by a pairwise Benjamini, Hochberg and Yekutieli p-adjusted Wilcoxon post-hoc analysis [72]. Statistical analyses are computed using the R software environment [73].

Interlocking mechanisms

Interlocking mechanisms are analysed from two hierarchical levels: the plates and the stereom. The plates are examined with respect to the 3d morphology and the resulting interaction with neighbouring plates along the sutures. Sutures were observed from translations throughout the μCT section. A suture is recognised as sinuous, when the plate's margins are curved, thus allowing for interlocking with neighbouring plates. The plate's

microarchitecture is examined for the stereom types involved in the plate [19]. The segmentation of a single ambulacral plate from the oral side was performed in Avizo in manual mode, using the brush-tool with masking enabled (masking range: 82-255). The surface was rendered and smoothed (unconstrained smoothening, smoothening extent = 9). The surface was additionally smoothed using the smooth surface command (iterations = 10, lambda = 0.9).

The interaction between plates on the microstructural stereom level are analysed for interlocking mechanisms based on SEM images. The mechanism of interlocking between plates is divided into three categories: (1) rod-like trabecular protrusions penetrate deeply into the stereom interspace of adjoining plates, (2) knob-like trabecular protrusions interlock with depressions formed by the opposing plate's stereom without penetration into the stereom interspace, and (3) the trabecular protrusions of one plates interlock with the trabeculae of the neighbouring plates developing a form-closed interlocking hook.

Internal support system

The buttress system is analysed for its overall morphology, including its course, length and plate involvement, as well as for its sutural layout, and variations in stereom density. Based on µCT and SEM data, the origin of the buttresses' plates is examined together with its course throughout the test. Length measurements are based on a horizontal µCT section. The sutural layout is examined for its position and interlocking mechanisms. The stereom density of the buttresses is measured at three intervals between the proximal end of one buttress with a subvolume edge length of 20 voxels (60 µm). The measurements, volumetric, and statistical analyses follow the protocols under "plate architecture".

Figure processing

Images are adjusted for brightness, contrast, and colour using Photoshop CC 2017 (Adobe Systems, San Jose, CA, USA). Figure 2A was rendered with the 3d modelling software Rhinoceros 5 (McNeel, Seattle, WA, USA) using a surface model of the echinoid's tests based on µCT scan processed in Avizo. Line-drawings are generated in Adobe Illustrator CC 2017 (Adobe Systems, San Jose, CA, USA). Zerene Stacker 1.04 (Zerene Systems, Richland, WA, USA) is used to stack figure 4A (mode: DMAP, rendering: Lanczos8 16 x 16) from four µCT sections. Figure 8A is stitched from two SEM micrographs using Autostitch (University of British Columbia, Vancouver, BC, Canada). Figures were processed using Adobe InDesign CC 2017 (Adobe Systems, San Jose, CA, USA).

Results

Test design

The test of *Echinocyamus pusillus* is sub-elliptical in shape in top view (Fig. 1A). In radial section, the test is flattened and convexly shaped without concave elements (Fig. 1F). The test's radial curvature is convex over the entire surface including the region around the slightly infundibulate peristome. The nearly dome-shaped form of the test represents a double-curved shell construction. The test's outer surface shows numerous microscopic surface features including tubercles, glassy tubercles, genital and ocular pores, single hydropore, ambulacral pores, unipores, the centrally located peristome, as well as the periproct that lies between the two posterior buttresses on the oral surface (Fig. 1). The paired ambulacral pores of the petals as well as serially arranged unipores lie flush with the outer test surface. The basicoronal ring consists of five fused basicoronal interambulacral plates and five pairs of narrow basicoronal ambulacral plates (Fig. 1D).

The test of *Echinocyamus pusillus* varies in thickness (Fig. 3). The ambulacral plates are on average 260.74 ±47.9 µm (N = 30) thick and thinner than the elongated interambulacral plates (buttresses) with an average thickness of 872.48 ±132.3 mm (N = 30) (Fig. 3, Tab. 1). The plates of the anterior ambulacra (II, III, IV) are on average thinner than those of the posterior ambulacra (I, V) (Tab. 1). The perradial suture between ambulacral plates measures on average 380.94 ±41.0 µm (N = 15) in thickness. The interradial sutures between interambulacral plates show an average thickness of 346.25 ±60.4 µm (N = 15). Adradial sutures between ambulacral and interambulacral plates are 343.50 ±72.3 µm (N = 15) thick on average. A Wilcoxon test shows that suture areas are thicker than the centre of the ambulacral plates ($W = 1670$, $p < 0.001$, $N = 90$). A pairwise Benjamini, Hochberg and Yekutieli p-adjusted Wilcoxon post-hoc analysis indicates that the average plate thickness at the perradial and interradial sutures does not show statistical differences ($p = 0.103$, $N = 30$). This also applies to the comparison between perradial and interradial sutures ($p = 0.433$, $N = 30$), and between adradial and interradial sutures ($p = 1.000$, $N = 30$).

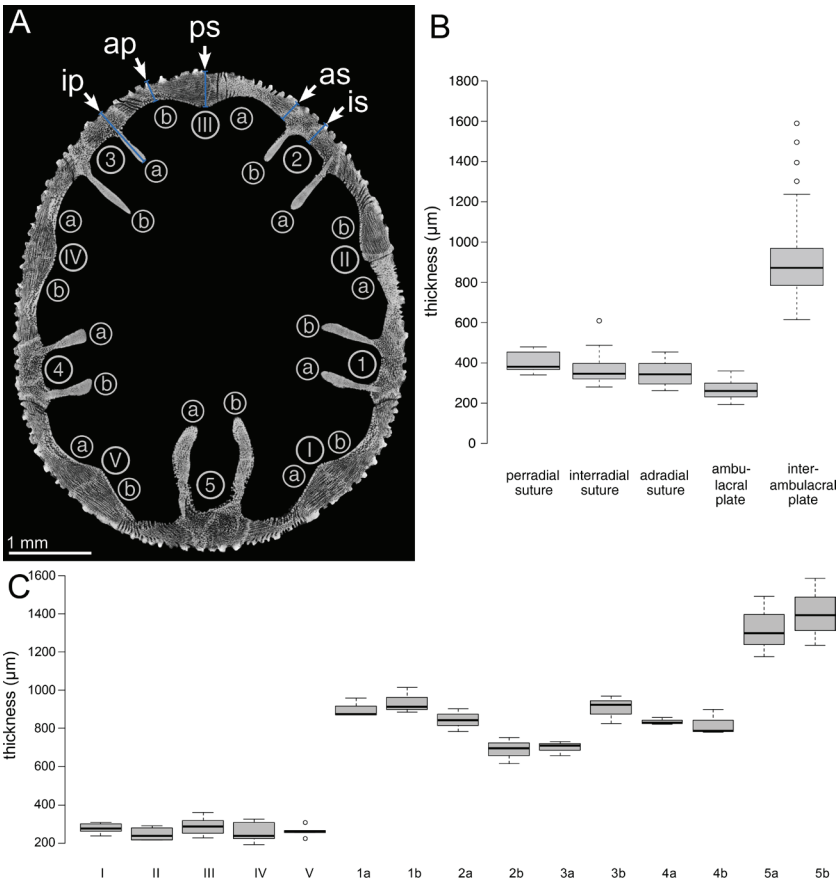

Figure 3. Analyses of test thickness. (A) Horizontal µCT section of *Echinocyamus pusillus* indicating measurement points for plate thickness. ap = ambulacral plate, as = adradial suture, ip = interambulacral plate, is = interradial suture, ps = perradial suture. Roman numerals indicate ambulacral plates, Arabic numerals indicate interambulacral plates. Small letters indicate the position of the plate according to Lovén [77] [GPIT/EC/00740:gg-al-1.73]. (B) Boxplot diagram comparing thicknesses of perradial, adradial, and interradial sutures with the thickness of ambulacral and interambulacral plates. (C) Boxplot diagram showing the thicknesses of plates. Ambulacral plates a and b are pooled to a single value (I – V). Interambulacral buttress length is given for each plate individually for plates a and b (1 – 5).

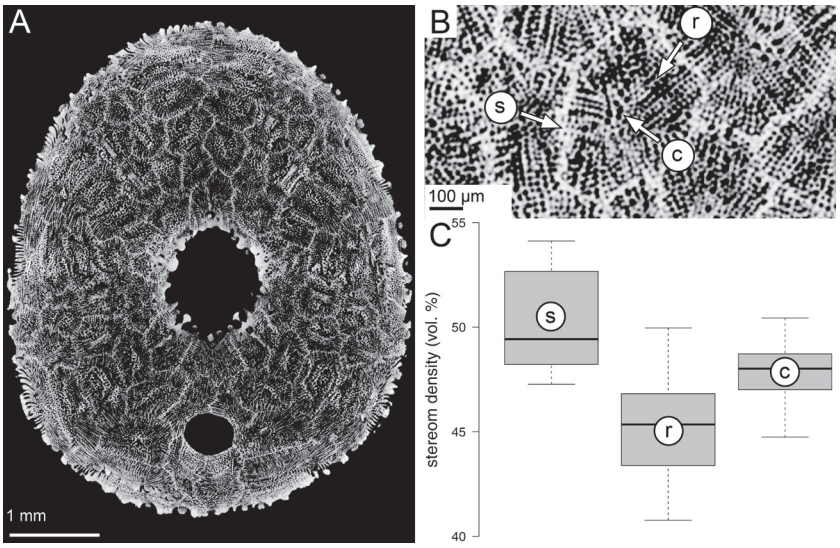

Figure 4. Stereom differentiation in *Echinocyamus pusillus* [GPIT/EC/00740:gg-al-1.73]. (A) Micro-CT section of the oral side showing the mosaic of plates. (B) Close-up indicating three analysed regions of the plate: c = unordered labyrinthic stereom at the plate's centre, r = directional galleried stereom at the plate's rim, s = directional galleried stereom within sutures. (C) Comparison between three prominent areas of the plates.

Plate architecture

The skeletal plates are subdivided into two clearly differentiated regions: the (1) plate's centre consisting of the unordered labyrinthic stereom, and the (2) surrounding distal plate areas consisting of galleried stereom (Fig. 4). The latter is constructed by highly ordered parallel struts, which run perpendicular to the plate sutures. The galleried stereom at the sutures is of higher stereom density than that of the remaining plate as indicated by the brighter grey level in the µCT section (Fig. 4).

The analysed ambulacral plates show an average stereom density of 48.0 vol.% (N = 27) (Fig. 4, Tab. 1). Stereom densities vary between the labyrinthic stereom at the plates' centre, (48.0 vol.%, N = 9), the galleried stereom at the centre surrounding areas of the plates (45.3 vol. %, N = 9), and the galleried stereom at the sutures (49.4 vol.%, N = 9). A Kruskal-Wallis H test followed by a Benjamini, Hochberg and Yekutieli p-adjusted Wilcoxon pairwise comparison indicates that the stereom densities differ between the galleried stereom at the plate sutures and the galleried stereom at the plate distal area ($p = 0.015$, N = 27). The average density of the galleried stereom at the suture is different than that on the plate's centre. This difference is, however, not significant ($p = 0.127$, N = 27). The density of the galleried stereom at the plate's suture likewise differs from that on the plate's centre, though not significantly ($p = 0.127$, N = 27).

Table 1. Thickness and stereom density measurements of the test of *Echinocyamus pusillus*. mad = median absolute deviation, N = sample size.

		median	mad	min.	max.	N
plate thickness (µm)	**ambulacral**	260.74	47.94	193.10	359.83	30
	buttress	872.48	132.26	614.91	1586.68	30
suture thickness (µm)	**perradial**	380.94	40.96	340.52	479.65	15
	interradial	346.25	60.36	280.49	607.03	15
	adradial	343.50	72.28	262.14	454.35	15
stereom density (%)	**suture**	49.43	3.20	47.27	54.12	9
	galleried stereom	45.35	2.92	40.77	49.96	9
	labyrinthic stereom	48.01	1.49	44.74	50.43	9
	total	48.01	2.89	40.77	54.12	27

Interlocking mechanisms

Plate interlocking occurs on two hierarchical levels. The irregular outline of the plates (Fig. 5) is integrated into a complex mosaic of plates (Fig. 4). Sutural interlocking can be seen on the inner surface of the test, where plate edges feature a high degree of sinuosity leading to an interdigitation of plates (Fig. 6). The outer surface of the test shows intense intergrowth where individual plates and plate boundaries are hardly visible, because they are masked by surface microstructures, such as tubercles and glassy tubercles (Fig. 1). Trabecular interlocking occurs where trabeculae of the galleried stereom meet the suture in a perpendicular direction (Fig. 6). These interlockings can be present as interdigitating rod-like structures, where trabeculae penetrate deeply into the opposing stereom interspaces, or knob-like structures, that interlock with the adjoining plate's surfaces. Rod- and knob-like interlockings are distributed over the entire area of the sutures. Fusion between single trabeculae of adjoining plates can be present, but is rare.

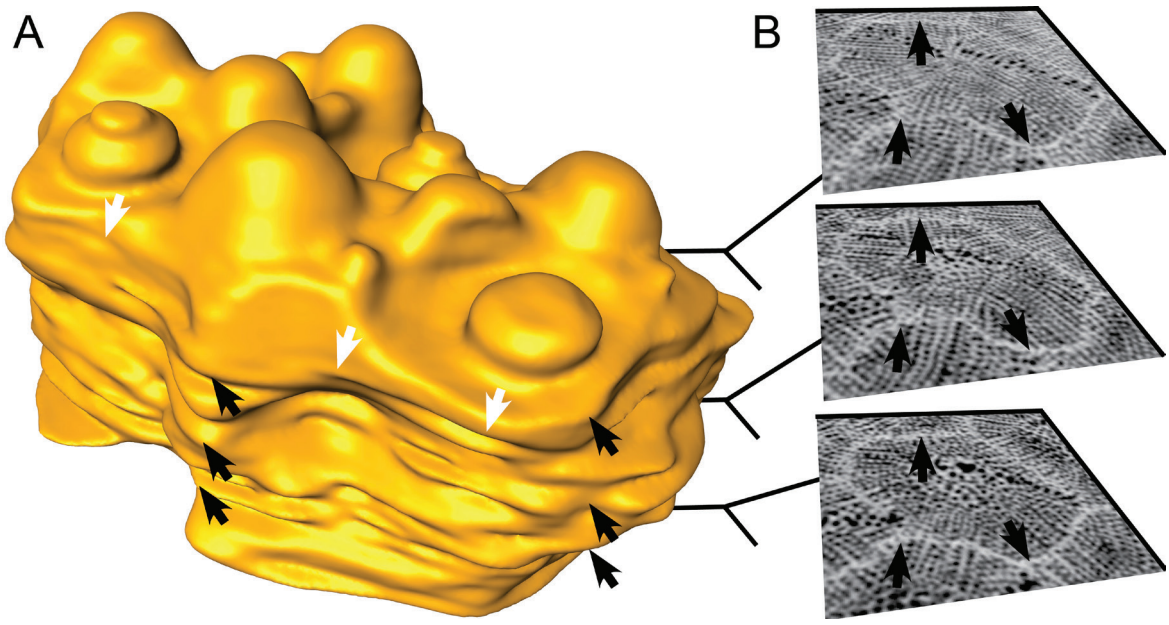

Figure 5. Plate shape of *Echinocyamus pusillus* [GPIT/EC/00740:gg-al-1.73]. (A) 3d surface rendering of a single segmented plate. Sutures follow a sinuous path in all directions. White arrows indicate the sinuous course in horizontal plane, black arrows in lateral direction. (B) Micro-CT sections of the segmented plate showing the different plate outlines at three intervals. Arrows correspond to black arrows in (A).

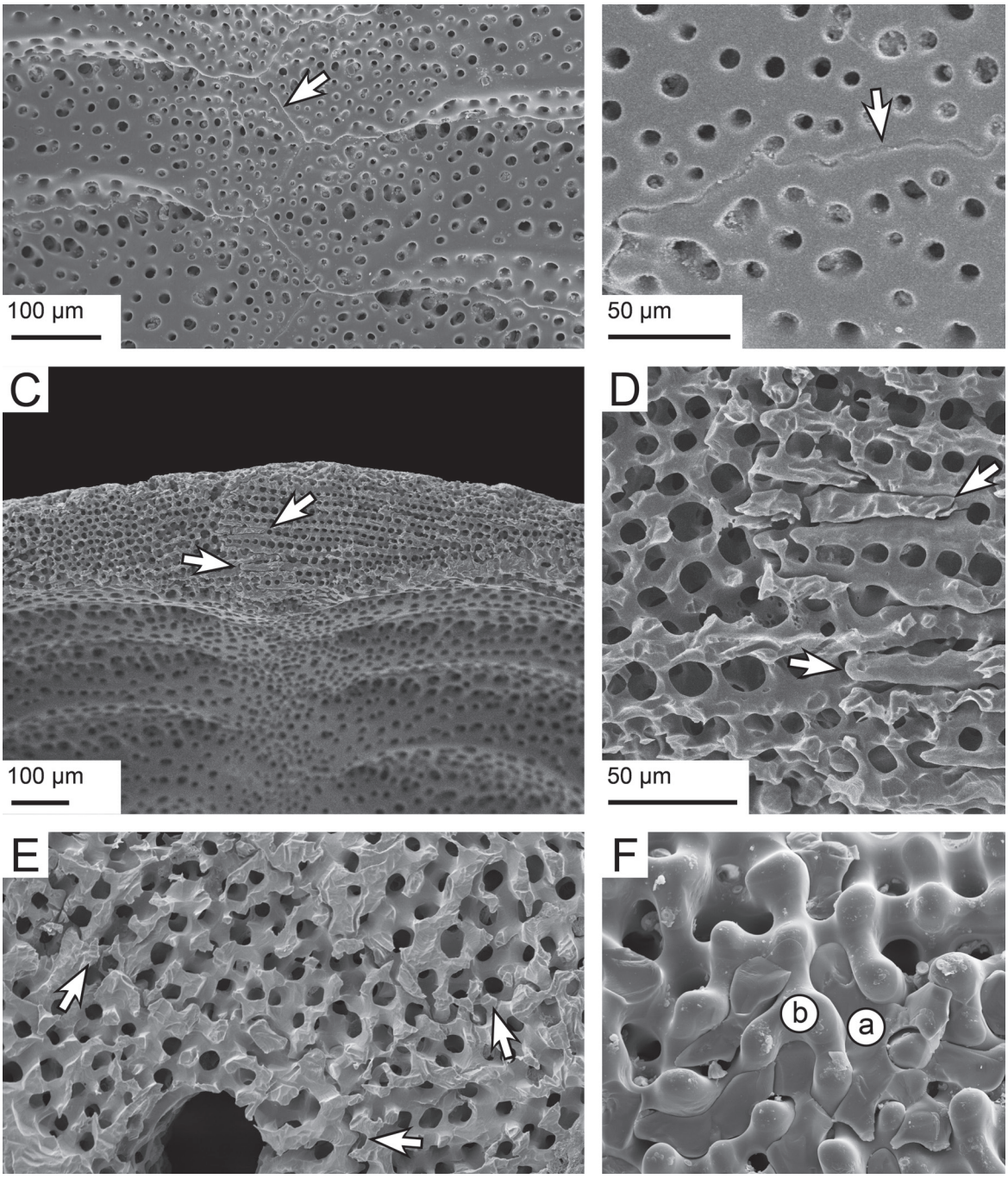

Figure 6. SEM micrographs of plate joints in *Echinocyamus pusillus*. (A) Sinuous course of sutures within a perradial boundary [GPIT/EC/00741:RI-n.4]. (B) Sutural interlocking in detail. Knobs reaching from one into another plate can increase test strength [GPIT/EC/00741:RI-n.4]. (C) Trabecular interlocking at a thickened perradial suture [GPIT/EC/00741:RI-n.5]. (D) Trabecular interlocking in detail, where trabeculae from one plate protrude into the stereom interspace of an adjoining plate [GPIT/EC/00741:RI-n.5]. (E) Sutural interlocking in a 3d mosaic of surrounding plates. Arrows indicate plate boundaries [GPIT/EC/00741:RI-1.6]. (F) Orthogonal view onto a suture. Fractured trabeculae are attached and penetrate into the interspace of another plate, a and b indicate the affiliation of the involved plates. Arrows indicate narrow depressions for knob-like interlocking [GPIT/EC/00741:RI-n.4].

Internal support system

The internal support system in *Echinocyamus pusillus* consists of two structural elements: the radial buttress system and longitudinal ribs (Fig. 1D, 1F). The buttress system is exclusively constructed from elongated interambulacral plates emerging from the outer limits of the petals and extending towards the fused auricles at the basicoronal ring. Buttresses are segmented by horizontal or slightly inclined sutures (Fig. 7). These sutures are interconnected by rod-like and knob-like trabecular protrusions at the proximal regions, and exclusively by knob-like trabecular protrusions at the distal regions (Fig. 8). The buttresses are longest at the ambitus. In horizontal section, individual buttresses are club-shaped and merge with the interambulacral plates in a V-shape (Fig. 7). Buttresses vary in length between 614.91 µm and 1586.68 µm (Tab. 1). The posterior buttresses 5a and 5b (Fig. 3) that enclose the periproct are longest (Tab. 2). Buttresses 2b and 3a are shorter than 2a and 3b, and buttresses 1b and 4a are longer than 1a and 4b.

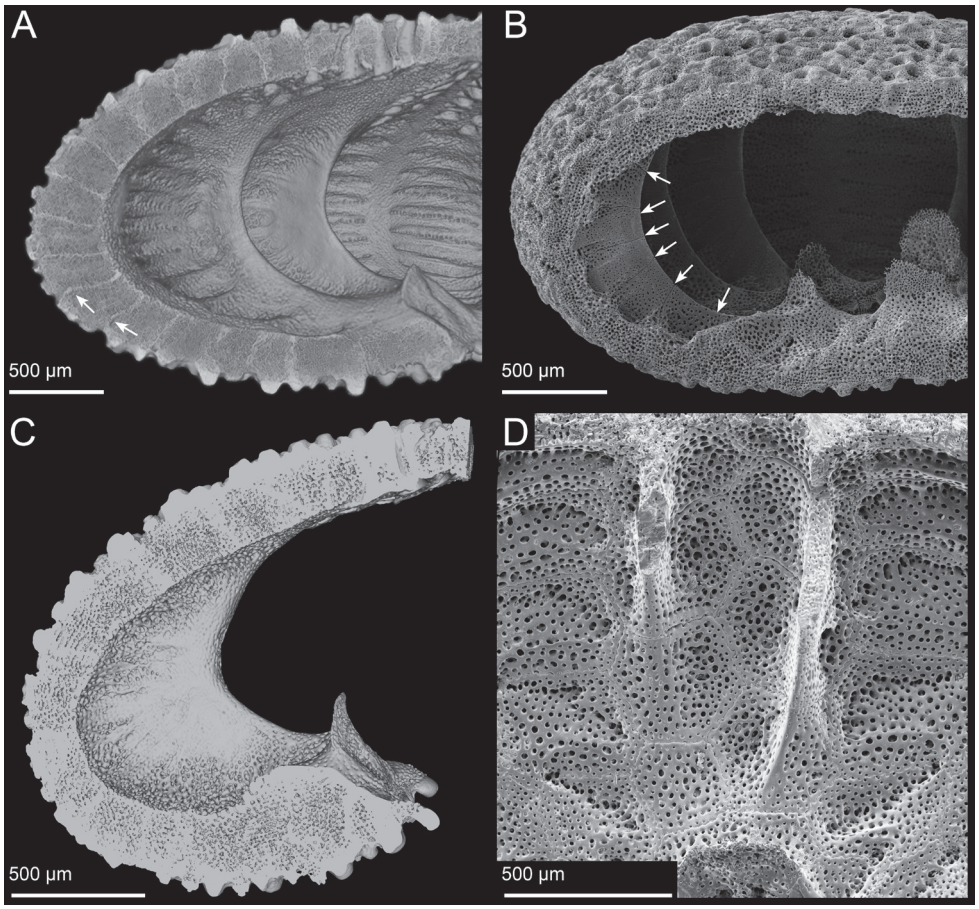

Figure 7. Internal buttress system in *Echinocyamus pusillus*. (A) Lateral section of a µCT based volume rendering showing the internal supports emerging from fused auricles. Arrows indicate sinuous course of plate boundaries [GPIT/EC/00740:gg-al-1.73]. (B) SEM micrograph of segmented buttresses. Arrows indicate plate sutures [GPIT/EC/00741:RI-1.19]. (C) Micro-CT section of a single buttress showing its widest extent at the ambitus. (D) SEM micrograph of two internal buttresses showing the supports as protrusions of interambulacral plates [GPIT/EC/00741:RI-1.2].

Whereas buttresses are extensions of the interambulacral plates, longitudinal ribs are extensions of the ambulacral plates running perpendicular to the internal buttress systems (Fig. 7). These ribs extend from the buttresses into the thickened and planar perradial sutures (Fig. 1). The ribs are most prominent at the oral side, becoming gradually less protuberant towards the petalodium. The plates and ribs are offset, causing a discontinuous suture in the horizontal direction. The stereom density of the buttress varies along its length (Fig. 8). The distal region is of highest density (92.0% stereom), the centre is of lowest density (68.3% stereom), and the proximal end of intermediate density (83.3% stereom).

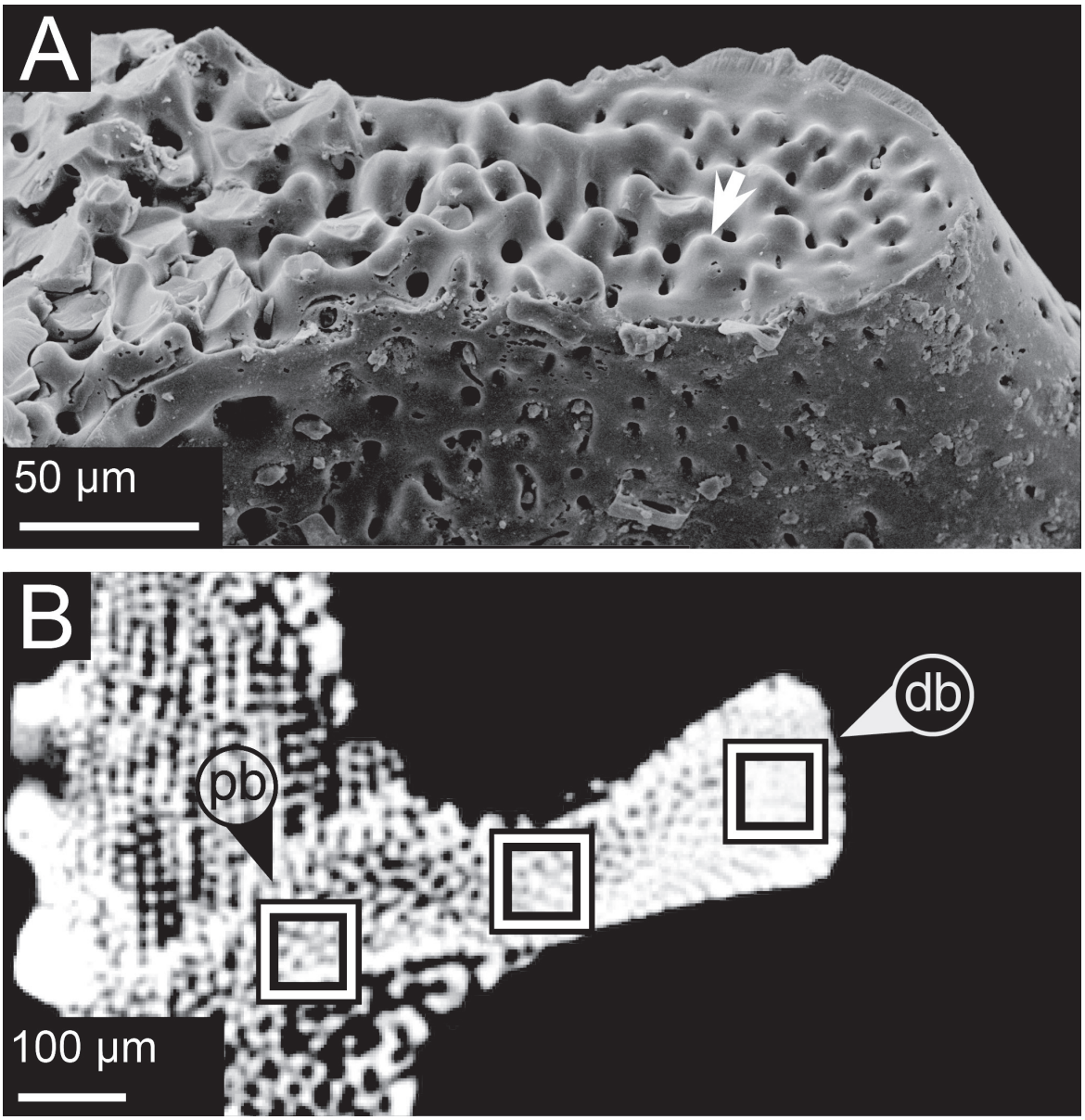

Figure 8. Horizontal section of buttresses in *Echinocyamus pusillus*. (A) SEM micrograph of a buttress suture. Individual buttress segments are interconnected by knob-like structures [GPIT/EC/00741:RI-1.29]. (B) Micro-CT section indicating the stereom density distribution within a buttress. Location of rectangles indicate areas used for stereom density comparison [GPIT/EC/00740:gg-al-1.73]. db = distal buttress, pb = proximal buttress.

Table 2. Plate thickness (µm) measurements of the test of *Echinocyamus pusillus*. mad = median absolute deviation, N = sample size. Roman numerals indicate ambulacral plates, Arabic numerals indicate interambulacral plates. Small letters indicate the position of the plate according to Lovén [77].

	median	mad	min.	max.	N
Ia	277.89	42.02	236.87	306.23	30
Ib	275.64	22.25	260.63	299.24	30
IIa	258.55	44.64	216.20	288.66	30
IIb	219.29	5.16	215.81	278.14	30
IIIa	260.85	16.92	249.44	319.52	30
IIIb	311.87	71.11	225.34	359.83	30
IVa	246.34	35.82	222.18	324.03	30
IVb	231.47	56.89	193.10	306.19	30
Va	264.62	15.17	254.39	305.59	30
Vb	257.12	11.82	223.36	265.09	30
1a	874.99	7.46	869.96	958.87	30
1b	912.49	37.75	887.03	1015.76	30
2a	842.63	85.43	785.01	904.77	30
2b	697.39	80.83	614.91	751.91	30
3a	710.37	30.22	657.91	730.75	30
3b	924.85	64.83	826.74	968.58	30
4a	830.73	12.69	822.17	857.39	30
4b	787.20	8.42	781.52	899.82	30
5a	1299.45	182.06	1176.65	1493.49	30
5b	1392.38	230.08	1237.19	1586.68	30

Discussion

Test design

The overall radial test curvature of *Echinocyamus pusillus* is convex (Fig. 1). This shape is not interrupted by any indentation throughout the test. The radially convex curvature allows for transmission of radial forces along the plates without changes in their direction and thus contributes to a stable test construction. The test of *Echinocyamus pusillus* features numerous apertures including the prominent peristome and periproct as well as ambulacral pores, unipores, genital pores, ocular pores, and the single hydropore. The unipores are abundant at the longitudinal sutures and can be considered as potential weak points in the test [16]. The peristome is a large aperture in the echinoid skeleton [26], which needs reinforcement. In *Echinocyamus pusillus*, this is achieved by the fused auricles of the basicoronal ring, which thicken the peristome's margin (Fig. 1D). This structural reinforcement distributes stress around the aperture [26]. Additionally, the buttress system merges into the fused auricles (Fig. 1D). This construction not only reinforces the basicoronal ring by further thickening, but also represents a T-beam construction that provides strength against bending [74].

The echinoid skeleton typically represents a light-weight structure [18]. The overall test density and thus the amount of structural material in the test of *Echinocyamus pusillus* is less than 50%. Those areas where higher stresses are expected to occur, such as in the buttress system, show corresponding higher stereom densities. In contrast, lower densities are present where less stress is expected to occur such as in the centre of plates and buttresses.

Plate architecture

The plates of *Echinocyamus pusillus* incorporate two stereom types, a centrally located region of unordered labyrinthic stereom, and a surrounding area of strictly-ordered galleried stereom (Fig. 4B). The labyrinthic stereom can distribute stress equally in multiple directions of the plate's plane [75], which reduces the accumulation of stress. The galleried stereom is able to transfer load forces directionally along its longitudinal struts, which lie perpendicular to the sutures. The combination of these two stereom types is an important structural feature of the plates. Applied downward loads are firstly transferred into lateral thrust. This thrust is then distributed equally along the roughly dome-shaped shell, which reduces stress accumulation in a specific area. The galleried stereom can transfer stress to a neighboring plate where it, again, is further distributed onto surrounding plates.

Interlocking mechanisms

In segmented shell constructions, plate joints are usually considered as weak points, where stress accumulation can lead to structural failure [30]. The plate joints in *Echinocyamus pusillus* show three strengthening mechanisms: (1) sutural interlocking based on the irregular and sinuous course of plate boundaries at the hierarchical level of individual plates, (2) trabecular interlocking based on rod-like, knob-like or hook-like trabecular protrusions at the hierarchical level of the stereom (Fig. 6), and (3) thickening of the contact areas between adjoining plates (Fig. 3).

Sutural interlocking relies on the shape of the entire plate. The irregular boundary regions between plates lead to a 3d interlocking along the mosaic of plates (Fig. 5). Such a 3d interlocking reduces the degree of freedom for plate movement. Trabecular interlocking is present on a lower hierarchical level where trabeculae of one plate reache into the stereom interspace of another (Fig. 6). Knob-like interlocking are found when the abutting stereom interspace is too narrow for the trabeculae to penetrate (Fig. 6F). At the internal surface of the test, knobs, hooks, and occasionally fusion of single trabeculae between neighbouring plates can increase the strength of plate cohesion (Fig. 6) [16,49]. Sutures at the inner surface are predominantly present as clear plate boundaries, whereas sutures on the outer surface are often tightly connected to one another, resulting in a homogeneous surface.

Sutural thickening increases the area of plate connections. An increase in the contact area of adjoining plates can thus boost the performance of both the sutural, as well as the trabecular interlocking mechanisms by providing a larger contact area. The thickened sutures act

as additional internal buttresses, enhancing stress transmission between the oral and aboral side [16]. The sutural design in *Echinocyamus pusillus* is considered to have a high significance for the shell strength. These three strengthening mechanisms lead to extensive plate connections with tight-fitting sutures. These interlocking mechanisms result in a segmented construction that behaves as a monolithic structure, characterised by a load transfer with reduced stress accumulation on the sutures. The monolithic behaviour, combined with the advantages of the two incorporated stereom types, results in a segmented shell construction with beneficial load transfer performance.

Internal support system

The internal support system is one of the most prominent reinforcement structures of the test and contains the buttresses as well as longitudinal ribs [16,75] (Fig. 1). The constructional design conjoins the top and bottom of the test with buttresses sharing the loads. The presence of buttresses therefore reduces tensile stress at the lower parts (Fig. 2) allowing for test flattening [16,75]. The buttress arrangement follows the bilateral symmetry of the test (Fig. 3). The fact that one buttress of a corresponding pair is shorter than the other has an ontogenetic origin as in juvenile clypeasteroids, the interambulacral plates are inserted into the double-plate column one-by-one [61], becoming an a or b plate (Fig. 3A).

The multi-plated buttress system is formed from elongated interambulacral plates with sutures perpendicular to the surface (Fig. 7B). These sutures are inclined to the test's horizontal plane such that lateral thrust, that follows the arched ring, meets the sutures in a perpendicular direction (Fig. 2C). Sutures, onto which stress impinges perpendicularly, is subject to less shear stress [76]. In addition, plates of the buttresses are interconnected by knob-like stereom protrusions which prevent horizontal movement between plates. The microstructure of the buttresses also reveals a load carrying design; the outer regions of the buttresses located towards the centre of the test show a higher density than the buttresses' limbs (Fig. 8). The structurally reinforced distal areas of the buttress system can improve the load transfer while maintaining structural integrity.

Conclusion

(1) The skeleton of *Echinocyamus pusillus* is subject to various load conditions. Due to the buried, infaunal mode of live, the weight of the sediment represents a continuous force acting on the skeleton.

(2) The skeleton is a light-weight construction with an average stereom density of less than 50%. Despite this fact, the test shows a high preservation potential in the fossil record, indicating a remarkable strength.

(3) Skeletal strength is achieved by multiple reinforcements along the hierarchical levels including (a) the arrangement of plates in a mosaic pattern, (b) stereom differentiation within a plate, which responds to different stresses, (c) sutural interlocking due to an irregular plate outline, (d) various trabecular interlockings of neighbouring plates, (e) sutural thickening boosts area of interlocking mechanisms, and (f) internal support system that adds to the resilience of the test.

(4) Plate interlocking leads to a construction that behaves as a monolithic structure. Together with the functional differentiation of the stereom within the plates and the double-curved form, the test exhibits an advantageous load-bearing performance.

(5) The skeletal adaptations of *Echinocyamus pusillus* contain numerous reinforcing structures that can be of high interest as role model in civil-engineering. An in-depth analysis of the test strengthening structures and the transfer into technical applications can enhance the development of biologically inspired segmented light-weight constructions.

Acknowledgments

The authors thank Raouf Jemmali for μCT scanning and Hartmut Schulz for support with the SEM. The constructive and detailed comments by Alexander Ziegler, one anonymous reviewer and the editors are greatly appreciated.

Funding Statement

The authors thank the German Research Foundation (Deutsche Forschungsgemeinschaft, Bonn, Germany) for funding this research within the Collaborative Research Centre SFB/Transregio 141: Biological Design and Integrative Structures.

Data Accessibility

The unprocessed μCT data of *Echinocyamus pusillus* are accessible via the dryad digital repository under doi:10.5061/dryad.rg54h: www.doi.org/10.5061/dryad.rg54h [71].

Competing Interests

The authors have no competing interests.

Authors' Contributions

TBG carried out 3d and SEM imaging as well as statistical analyses. TBG and JHN analysed and interpreted micrographs. TBG and JHN coordinated and drafted the manuscript. All authors gave final approval for publication.

Ethics

An ethical assessment was not required to collect empty and denuded tests of *Echinocyamus pusillus*. Approval from the institutional animal ethics committee was not necessary. Permission to collect samples of empty and denuded tests of *Echinocyamus pusillus* was not required at the time. No 'Animal Care Protocol' was required. Permission to carry out fieldwork was not required.

References

[1]Weiner S, Wagner HD. 1998 The material bone: structure-mechanical function relations. Annu. Rev. Mater. Sci. 28, 271–298. (10.1146/annurev.matsci.28.1.271)

[2]Gebeshuber IC, Drack M. 2008 An attempt to reveal synergies between biology and mechanical engineering. Proc. IMechEchinocyamus 222, 1281–1287. (doi: 10.1243/09544062JMES890)

[3]Gruber P. 2008 The signs of life in architecture. Bioinsp. Biomim. 3, 1–9. (doi: 10.1088/1748-3182/3/3/023001)

[4]Gebeshuber IC, Gruber P, Drack M. 2009 A gaze into to crystal ball: biomimetics in the year 2059. Proc. IMechEchinocyamus 223, 2899–2918. (doi: 10.1243/09544062JMES1563)

[5]Bramski C. 1981 Rotationssymmetrische tropfenförmige Behälter. Berlin, Germany: Wilhelm Ernst and Sohn.

[6]Nandakumar CG, Rajagopalan K. 1989 A bar finite element analogy for echinodome shells. Comput. Struct. 33:1085–1088. (doi: 10.1016/0045-7949(89)90444-6)

[7]Krauss S Monsonego-Ornan E, Zelser E, Fratzl P, Shahar R. 2009 Mechanical function of a complex three-dimensional suture joining the bony elements in the shell of the red-eared slider turtle. Adv. Mater. 21, 407–412. (doi: 10.1002/adma.200801256)

[8]Malik IA, Barthelat F. 2018 Bioinspired sutured materials for strength and toughness: pullout mechanisms and geometric enrichments. Int. J. Solids Struct. (doi: 10.1016/j.ijsolstr.2018.01.004)

[9]Grun TB, Koohi L, Schwinn T, Sonntag D, von Scheven M, Bischoff M, Knippers J, Menges A, Nebelsick JH. 2016 The skeleton of the sand dollar as a biological role model for segmented shells in building construction: a research review. In Biologically-inspired Design and Integrative Structures: Analysis, Simulation and Implementation in Architecture (eds J Knippers, KG Nickel, T Speck), pp. 217–242. Cham, Switzerland: Springer. (doi: 10.1007/978-3-319-46374-2_11)

[10]Malek S, Wierzbicki T, Ochsendorf J. 2014 Buckling of spherical cap gridshells: a numerical and analytical study revisiting the concept of the equivalent continuum. Eng. Struct. 75, 288–298. (doi: 10.1016/j.engstruct.2014.05.049)

[11]Smith AB. 1990 Biomineralization in echinoderms. In Skeletal biomineralization: patterns, processes and evolutionary trends (ed JG Carter), pp. 413–443. New York, NY: Van Nostrand Reinhold. (doi: 10.1029/SC005p0117)

[12]Duncan PM. 1882 On some points in the morphology of the test of the Temnopleuridæ. Zool. J. Linn. Soc. 16, 343–358. (doi: 10.1111/j.1096-3642.1882.tb02585.x)

[13]Pearse JS, Pearse VB. 1975 Growth zones in the echinoid skeleton. Amer. Zool. 15, 731–753. (doi: 10.1093/icb/15.3.731)

[14]Seilacher A. 1979 Constructional morphology of sand dollars. Paleobiology 5, 191–221. (doi: 10.1017/S0094837300006527)

[15]Telford M. 1985 Domes, arches and urchins: the skeletal architecture of echinoids (Echinodermata). Zoomorphology 105, 114–124. (doi: 10.1007/BF00312146)

[16]Telford M. 1985 Structural analysis of the test of *Echinocyamus pusillus* (O. F. Müller). In Echinodermata: Proceedings of the fifth international echinoderm conference, Galway 24–29 September 1984 (eds BF Keegan, BDS O'Connor), pp. 353–360. Rotterdam, Netherlands: Balkema.

[17]Ellers O, Johnson AS, Moberg PEchinocyamus 1998 Structural strengthening of urchin skeletons by collagenous sutural ligaments. Biol. Bull. 195, 136–144. (doi: 10.2307/1542821)

[18]Nebelsick JH, Dynowski JF, Grossmann JN, Tötzke C. 2015 Echinoderms: hierarchically organized light weight skeletons. In Evolution of Lightweight Structures: Analyses and Technical Applications (ed C Hamm), pp. 141–156. Dodrecht, Netherlands: Springer. (doi: 10.1007/978-94-017-9398-8_8)

[19]Smith AB. 1980 Stereom microstructure of the echinoid test. Spec. Pap. Palaeontol. 25, 1–81.

[20]Smith AB. 1984 Echinoid palaeobiology. London, United Kingdom: George Allen and Unwin.

[21]Schmidt WJ. 1925 Über die Lage der optischen Achse in den Kalkkörpern der Holothurien und ihre Bedeutung für die vergeleichende Morphologie. Zool. Jahrb. Abt. Anat. Ontog. Tiere 47, 113–154.

[22]Raup DM. 1965 Crystal orientations in the echinoid apical system. J. Paleont. 39, 934–951.

[23]Raup DM, Swan EF. 1967 Crystal orientation in the apical plates of aberrant echinoids. Biol. Bull. 133, 618–629.

[24]Weber JN. 1969 The incorporation of magnesium into the skeletal calcites of echinoderms. Am. J. Sci. 267, 537–566. (doi: 10.2475/ajs.267.5.537)

[25]Emlet RB. 1982 Echinoderm calcite: a mechanical analysis from larval spicules. Biol. Bull. 163, 264–275. (doi: 10.2307/1541265)

[26]Philippi U, Nachtigall W. 1996 Functional morphology of regular echinoid tests (Echinodermata, Echinoida): a finite element study. Zoomorphology 116, 35–50. (doi: 10.1007/s004350050007)

[27]Currey JD. 1999 The design of mineralised hard tissues for their mechanical functions. J. Exp. Biol. 202, 3285–3294.

[28]Philippi U. 2001 Finite Element-Analyse von Seeigelschalen. In Natürliche Konstruktionen in Raum und Zeit (eds HW Reinhardt, R Reiner), pp. 185–189. Stuttgart, Germany: Institut für Werkstoffe im Bauwesen.

[29]Tsafnat N, Fitz Gerald JD, Le HN, Stachurski ZH. 2012 Micromechanics of sea urchin spines. PLoS ONE 7, e44140. (doi: 10.1371/journal.pone.0044140)

[30]Li JM, Knippers J. 2015 Segmental timber plate shell for the Landesgartenschau exhibition hall in Schwäbisch Gmünd – the application of finger joints in plate structures. Int. J. Space Struct. 30, 123–139. (doi: 10.1260/0266-3511.30.2.123)

[31]Dotan A, Fishelson L. 1985 Morphology of spines of Heterocentrotus mammillatus (Echinodermata: Echinoidae) and its ecological significance. In Echinodermata: Proceedings of the fifth international echinoderm conference, Galway 24–29 September 1984 (eds BF Keegan, BDS O'Connor), pp. 253–260. Rotterdam, Netherlands: Balkema.

[32]Mooi R. 1986 Structure and function of clypeasteroid miliary spines (Echinodermata, Echinoides). Zoomorphology 106, 212–223. (doi: 10.1007/BF00312042)

[33]Grossmann JN, Nebelsick JH. 2013 Comparative morphological and structural analysis of selected cidaroid and camarodont sea urchin spines. Zoomorphology 132, 301–315. (doi: 10.1007/s00435-013-0192-5)

[34]Grossmann JN, Nebelsick JH. 2013 Stereom differentiation in spines of Plococidaris verticillata, Heterocentrotus mammilatus and other regular sea urchins. In Echinoderms in a Changing World: Proceedings of the 13th International Echinoderm Conference, January 5-9 2009, University of Tasmania, Hobart Tasmania, Australia (ed C Johnson), pp. 97–104. Boca Raton, FL: CRC Press. (doi: 10.1201/b13769-12)

[35]Klang K, Bauer G, Toader N, Lauer C, Termin K, Schmier S, Kovaleva D, Haase W, Berthold C, Nickel KG, Speck T, Sobek W. 2016 Plants and animals as source of inspiration for energy dissipation in load bearing systems and facades. In Biologically-inspired Design and Integrative Structures: Analysis, Simulation and Implementation in Architecture (eds J Knippers, KG Nickel, T Speck), pp. 109–133. Cham, Switzerland: Springer. (doi: 10.1007/978-3-319-46374-2_7)

[36]Schmier S, Lauer C, Schäfer I, Klang K, Bauer G, Thielen M, Termin K, Berthold C, Schmauder S, Speck T, Nickel KG. 2016 Developing the experimental basis for an evaluation of scaling properties of brittle and >quasi-brittle< biological materials. In Biologically-inspired Design and Integrative Structures: Analysis, Simulation and Implementation in Architecture (eds J Knippers, KG Nickel, T Speck), pp. 277–294. Cham, Switzerland: Springer. (doi: 10.1007/978-3-319-46374-2_14)

[37]Toader N, Sobek W, Nickel KG. 2017 Energy absorption in functionally graded concrete bioinspired by sea urchin spines. J. Bionic. Eng. 14, 369–378. (doi: 10.1016/s1672-6529(16)60405-5)

[38]Ziegler A, Lenihan J, Zachos LG, Faber C, Mooi R. 2016 Comparative morphology and phylogenetic significance of Gregory's diverticulum in sand dollars (Echinoidea: Clypeasteroida). Org. Divers. Evol. 16, 141–166. (doi: 10.1007/s13127-015-0231-9)

[39]Nebelsick JH, Kroh A. 2002 The stormy path from live to death assemblages: the formation and preservation of mass accumulations of fossil sand dollars. Palaios 17, 378–393. (doi:10.1669/0883-1351(2002)017<0378:TSPFLT>2.0.CO;2)

[40]Belaústegui Z, De Gibert JM, Nebelsick JH, Domenèch R, Martinell J. 2013 Clypeasteroid echinoid tests as benthic islands for gastrochaenid bivalve colonization: evidence from the Middle Miocene of Tarragona, North-east Spain. Palaeontology 56, 783–796. (doi: 10.1111/pala.12015)

[41]Mancosu A, Nebelsick JH. 2017 Ecomorphological and taphonomic gradients in clypeasteroid-dominated echinoid assemblages along a mixed siliciclastic-carbonate shelf from the early Miocene of northern Sardinia, Italy. Acta Paleontolog. Pol. 62, 627–646. (doi: 10.4202/app.00357.2017)

[42]Mancosu A, Nebelsick JH. 2017 Palaeoecology and taphonomy of spatangoid-dominated echinoid assemblages: a case study from the Early-Middle Miocene of Sardinia, Italy. Palaeogeogr. Palaeoclimatol. Palaeoecol. 466, 334–352. (doi: 10.1016/j.palaeo.2016.11.053)

[43]Grun TB, Nebelsick JH. 2016 Taphonomy of a clypeasteroid echinoid using a new quasimetric approach. Acta Palaeontol. Pol. 61, 689–699. (doi: 10.4202/app.00200.2015)

[44]Kroh A, Nebelsick JH. 2003 Echinoid assemblages as a tool for palaeoenvironmental reconstruction – an example from the Early Miocene of Egypt. Palaeogeogr. Palaeoclimatol. Palaeoecol. 203, 157–177. (doi: 10.1016/S0031-0182(03)00610-2)

[45]Mortensen T. 1948 A Monograph of the Echinoidea IV.2 Clypeasteroida. Copenhagen, Denmark: C.A. Reitzel.

[46]Nebelsick JH, Kowalewski M. 1999 Drilling predation on recent clypeasteroid echinoids from the Red Sea. Palaios 14, 127–144. (doi: 10.2307/3515369)

[47]Ceranka T, Złotnik M. 2003 Traces of cassid snails predation upon the echinoids from the Middle Miocene of Poland. Acta Palaeontol. Pol. 48, 491–496.

[48]Złotnik M, Ceranka T. 2005 Patterns of drilling predation of cassid gastropods preying on echinoids from the middle Miocene of Poland. Acta Palaeontol. Pol. 50, 409–428.

[49]Grun T, Sievers D, Nebelsick JH. 2014 Drilling predation on the clypeasteroid echinoid *Echinocyamus pusillus* from the Mediterranean Sea (Giglio, Italy). Hist. Biol. 26, 745–757. (doi: 10.1080/08912963.2013.841683)

[50]Grun TB, Kroh A, Nebelsick JH. 2017 Comparative drilling predation on time-averaged phosphatized and non-phosphatized assemblages of the minute clypeasteroid echinoid Echinocyamus stellatus from Miocene offshore sediments (Globigerina Limestone Fm., Malta). J. Paleo. 91, 633–462. (doi: 10.1017/jpa.2016.123)

[51]van Phelsum, M. 1774 Brief aan Cornelius Nozeman, over de Gewelvslekken of Zeeegelen. Rotterdam, Netherlands: R. Arrenberg.

[52]Agassiz A. 1872 Revision of the Echini. Part I. Cambridge, NY: Cambridge University Press. (doi: 10.5962/bhl.title.40080)

[53]Döderlein L. 1906 Arktische Seeigel. Fauna Arctica, Vierter Band. Jena, Germany: Verlag von Gustav Fischer.

[54]Mortensen T. 1907 The Danish Ingolf-Expedition IV.2 Echinoidea (II). Copenhagen, Netherlands: Bianco Luno.

[55]Kier PM. 1968 Echinoids from the Middle Eocene Lake City Formation of Georgia. Smithson. misc. collect. 153, 1–45.

[56]Nisiyama S. 1968 The echinoid fauna from Japan and adjacent regions part II. Palaeontological Society of Japan Special Papers 13, 1–491.

[57]Mironov AN, Sagaidachny AY. 1984 Morphology and distribution of the Recent echinoids of the genus Echinocyamus (Echinoidea: Fibulariidae). Transactions of the P. P. Shirshov Institute of Oceanology 119, 179–204.

[58]Zachos LG. 2005 Eocene dispersal of the echinoid genus Echinocyamus in the southeastern United States. Southeastern Geol. 43, 215–227.

[59]Ceranka T. 2007 Symmetry disorders of the test of the Miocene echinoid Echinocyamus from Poland. Acta Palaeontol. Pol. 52, 503–518.

[60]Mortensen T. 1927 Handbook of the Echinoderms of the British Isles. London, United Kingdom: Humpherey Milford Oxford University Press. (doi: 10.5962/bhl.title.6841)

[61]Durham JW. 1955 Classification of clypeasteroid echinoids. Berkeley, LA: University of California Press.

[62]Koehler R. 1889 Résultats des campagnes scientifiques accomplies sur son yacht par Albert Ier, prince souverain de Monaco. Monaco, Principauté de Monaco: Imprimerie de Monaco. (doi: 10.5962/bhl.title.2169)

[63]Nichols D. 1959 The histology and activities of the tube-feet of *Echinocyamus pusillus*. Journal of Cell Science 100, 539–555.

[64]Ghiold J. 1982 Observations on the clypeasteroid *Echinocyamus pusillus* (O.F. Müller). J. Exp. Mar. Biol. Ecol. 61, 57–74. (doi: 10.1016/0022-0981(82)90021-1)

[65]Telford M, Harold AS, Mooi R. 1983 Feeding structures, behavior and microhabitat of *Echinocyamus pusillus* (Echinoidea: Clypeasteroida). Biol. Bull. 165, 745–757. (10.2307/1541476)

[66]Grun TB, Nebelsick JH. 2015 Sneaky snails: How drillholes can affect paleontological analyses of the minute clypeasteroid echinoid Echinocyamus. In Progress in Echinoderm Palaeobiology (eds D Zamora, I Rábano), pp. 71–74. Madrid, Spain: Cuadernos del Museo Geominero, 19. Instituto Geológico y Minero de España.

[67]Walther J. 1910 Die Sedimente der Taubenbank im Golf von Neapel. In: Abhandlungen Der Königlich Preussischen Akademie Der Wissenschaften (ed G. Reimer), pp. 1–49. Berlin, Germany: Reichsdruckerei.

[68]Nichols D. 1962 Echinoderms. London, United Kingdom: Hutchinson and Co.

[69]Gordon JEchinocyamus 1978 Structures: or why things don't fall down. New York, NY: Da Capo Press.

[70]Ellers O, Telford M. 1992 Causes and consequences of fluctuating coelomic pressure in sea urchins. Biol. Bull. 182, 424–434.

[71]Grun TB, Nebelsick JH. 2018 Data from: Structural design of the minute clypeasteroid echinoid *Echinocyamus pusillus*. Dryad Digital Repository. (doi: 10.5061/dryad.rg54h)

[72]Warton DI, Duursma RA, Falster DS, Taskinen S. 2012 Smatr 3 - an R package for estimation and inference about allometric lines. Methods Ecol. Evol. 3, 257–259. (doi: 10.1111/j.2041-210X.2011.00153.x)

[73]R Core Team. 2016 R: a language and environment for statistical computing. Vienna, Austria: R Foundation for Statistical Computing.

[74]Tamboli A, Xing M, Ahmed M. 2000 Structural theory. In Building Design and Construction Handbook, Sixth Edition (eds F Merritt, JT Ricketts), pp. 232–419. New York, NY: Mc-Graw-Hill.

[75]Lawrence J. 1987 A functional biology of echinoderms. Baltimore, MD: John Hopkins University Press. (doi: 10.1002/iroh.19890740316)

[76]Schodek DL. 1980 Structures. Englewood Cliffs, NJ: Prentice-Hall.

[77]Lovén S. 1874 Études sur les échinoïdées. K. vet. akad. Handl. 11, 1–91.

Manuscript 4

Structural stress response of segmented natural shells:

a numerical case study on the clypeasteroid echinoid *Echinocyamus pusillus*

Structural stress response of segmented natural shells: a numerical case study on the clypeasteroid echinoid *Echinocyamus pusillus*

Tobias B. Grun[1], Malte von Scheven[2], Manfred Bischoff[2] and James H. Nebelsick[1]

[1] University of Tübingen, Department of Geosciences, Hölderlinstraße 12, 72074 Tübingen, Germany
[2] University of Stuttgart, Institute for Structural Mechanics, Pfaffenwaldring 7, 70569 Stuttgart, Germany
Corresponding author: tobias.grun@uni-tuebingen.de

Key words

Biomechanics, skeleton, computed tomography, finite element analysis, voxel-based, load carrying behaviour

Abstract

The skeleton of *Echinocyamus pusillus* is considered as an exceptional model organism for structural strength and skeletal integrity within the echinoids as demonstrated by the absence of supportive collagenous fibres between single plates and the high preservation potential of their skeletons. The structural principles behind this stable, multi-plated, light-weight construction remains hardly explored. In this study, high resolution x-ray micro-computed tomography, finite element analysis and physical crushing tests are used to examine the structural mechanisms of this echinoid's skeleton. The virtual model of *Echinocyamus pusillus* shows that the material is heterogeneously distributed with high material accumulations in the internal buttress system and at the plate boundaries. Finite element analysis indicates that the heterogeneous material distribution is less important for the skeletal strength than the geometry of the skeleton itself. This numerical approach also demonstrates that the internal buttress system is of high significance for the overall skeletal stability of this flattened echinoid. Results of the finite element analyses with respect to the buttress importance were evaluated by physical crushing tests. These uniaxial compression experiments support the results of the simulation analysis. Additionally, the crushing tests demonstrate that organic tissues do not significantly contribute to the skeletal stability. The strength of the echinoid shell, hence, predominantly relies on its structural design.

Introduction

Sea urchins (Echinodermata, Echinoidea) have increasingly become the focus of structural analyses as their light-weight skeletons feature a remarkable load-carrying property (e.g. Stratham 1962, Telford 1985a; b, Lawrence 1987, Philippi and Nachtigall 1996, Philippi 2001, Grossmann et al. 2013 a; b, Nebelsick et al. 2015, Grun et al. 2016; 2017, Klang 2016, Schmier et al. 2016, Lauer et al. 2017, Toader et al. 2017, Nickel et al. 2018). The echinoid skeleton is a hierarchically organized (e.g. Nebelsick et al. 2015) and multi-plated construction that functions as a protective shell for internal organs. The light-weight skeletons are built from a lattice-like stereom with a porosity of up to 50 % (Philippi and Nachtigall 1996). The plates of most echinoid skeletons are securely interconnected by collagenous fibres (e.g. Telford 1985a; b, Lawrence 1987), which often disarticulate quickly after soft tissues decay. The clypeasteroid echinoids feature additional strengthening mechanisms that enhances skeletal integrity: in addition to the collagenous fibres, these echinoids developed skeletal protrusions bridging the sutures between plates (e.g. Seilacher 1979, Grun and Nebelsick 2018, Grun et al. 2018). The skeletons of this echinoid group are common and often well-preserved in both recent environments and the fossil sedimentary record (Nebelsick and Kowalewski 1999, Złotnik and Ceranka 2005, Kroh and Nebelsick 2010, Mancosu and Nebelsick 2013; 2015; 2017a; b, Grun et al. 2014; 2017), which is indicative for a structurally resilient skeletal architecture (Grun et al. 2018). The minute *Echinocyamus pusillus* represents a particular case within the clypeasteroid echinoids as collagenous fibres between the plates are entirely absent (Telford 1985b).

Echinocyamus pusillus feature four structural strengthening mechanisms, the buttress system, plate thickening at the sutures, transversal ridges, and the previously mentioned plate interlocks (Telford 1985b, Gun and Nebelsick 2018). The internal buttress system consists of five pairs of radially wall-like buttresses which extends from the interambulacral basicoronal plates towards the outer margins of the petals (e.g. Agassiz 1841, Forbes 1852, Mortensen 1907; 1927, Durham 1955; 1966, Telford 1985b, Nebelsick and Kowalewski 1999, Grun et al. 2014; 2016, Grun and Nebelsick 2016) (Fig. 1). Buttresses and plate thickening have been interpreted to strengthen the skeleton when loads are applied by bridging the oral and aboral side of the echinoid (Forbes 1852, Smith 1980, Telford 1985b, Nebelsick and Kowalewski 1999, Grun et al. 2014; 2016, Grun and Nebelsick 2016). Furthermore, the traversal ridges of the ambulacral plates which range from the peristome to

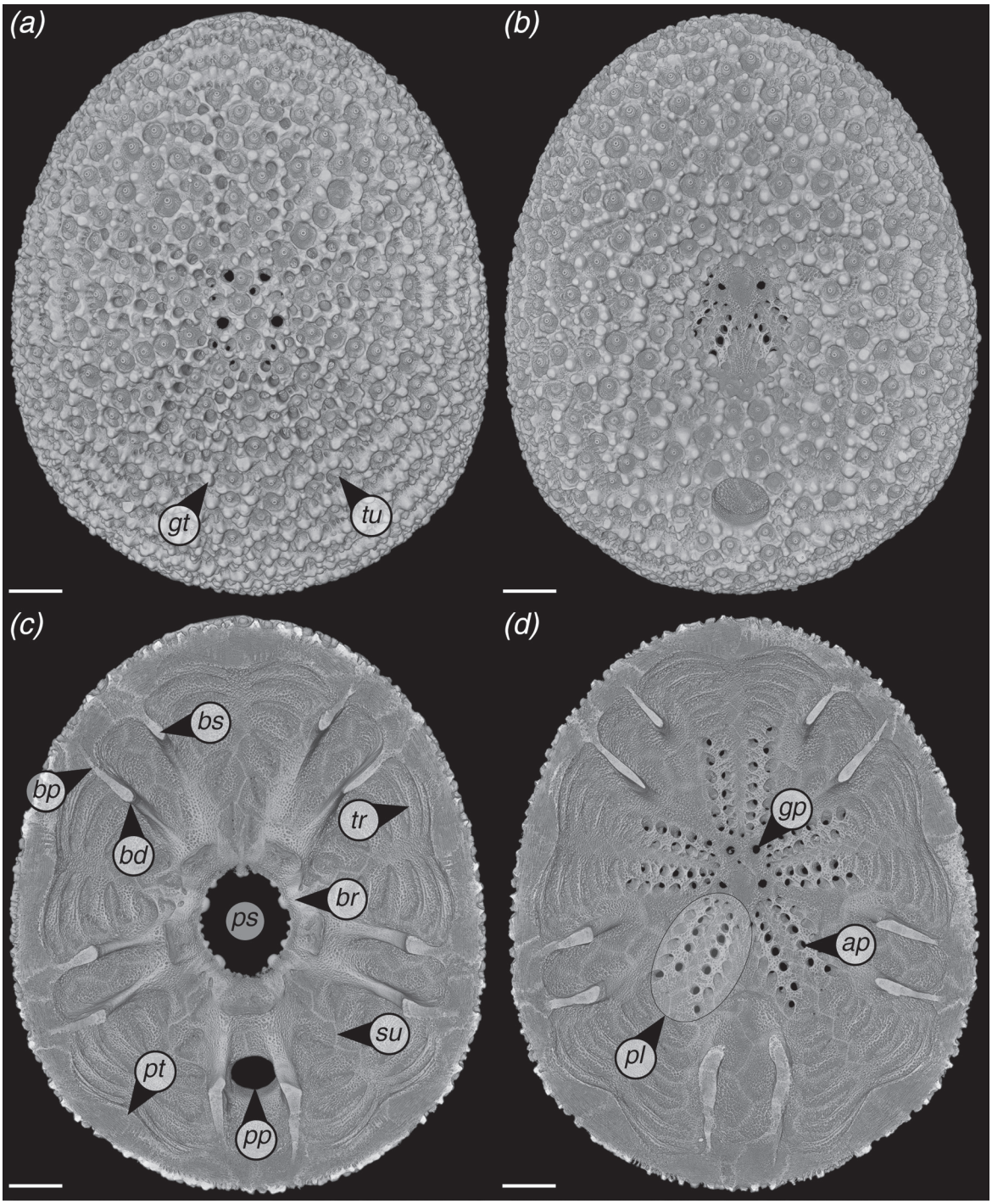

Figure 1. Micro CT rendering of *Echinocyamus pusillus* from Giglio island, Italy. (a) Skeleton in aboral view. The ambulacral system and micro-structures such as the tubercles and glassy tubercles are visible. (b) Skeleton in oral view with the prominent peristome and periproct visible. (c) Top view of the oral side. The internal supports are visible, as well as the basicoronal ring around the peristome. (d) View on the inner part of the aboral side. Pores and the limits of the buttresses are visible. ap = ambulacral pore, bd = distal region of the buttress, bp = proximal area of the buttress, br = basicoronal ring, bs = buttress, gp = genital pore, gt = glassy tubercle, pl = petal, ps = peristome, pt = plate thickening, pp = periproct, su = suture, tr = transversal ridge, tu = tubercle. Scale bar = 500 µm

the outer limits of the petals and are thought to increase the flexural stiffness of the skeleton (e.g. Telford 1985b). Along with the internal supports, this clypeasteroid features tight-fitting and interdigitating plate joints (e.g. Smith 1980, Telford 1985b, Grun and Nebelsick 2018). These internal reinforcements render tests of *Echinocyamus pusillus* resistant to destruction (e.g. Telford 1985b, Nebelsick and Kowalewski 1999, Grun et al. 2014; 2016, Grun and Nebelsick 2016; 2018).

Despite these findings, there have been to date little, if any, analytical or numerical studies concerning the density distribution and structural parameters important for the strengthening mechanisms of the clypeasteroid skeletons. The identification and analysis of structural strengthening mechanisms based on the echinoid skeleton are crucial for developing new techniques in building constructions of segmented shells. Reciprocally, understanding the basis for enhanced skeletal integrity can be useful in reconstructing both fossilisation pathways and the role of these clypeasteroids in ancient ecosystems. This study, accordingly, investigates structural aspects of the morphology of the clypeasteroid echinoid *Echinocyamus pusillus* with respect to the significance of the internal support systems and further strengthening mechanisms. High-resolution 3D x-ray micro-computed tomography (µCT) are used to obtain a digital model of the echinoid's skeleton. The 3D model serves as the basis for material density mapping and a finite element model. Physical crushing tests were additionally conducted to examine the structural importance of the internal buttresses and organic materials.

The role model *Echinocyamus pusillus*

The minute irregular echinoid *Echinocyamus pusillus* features a flattened and subcircular skeleton (Fig. 1), which rarely exceeds a length of 20 mm (Mortensen 1948). With the skeleton entirely covered by minute spines (e.g. Ghiold 1982), this infaunally living echinoid burrows through soft substrates using both spines and tube-feet (Nichols 1959). *Echinocyamus pusillus* inhabits a wide range of environments including muddy (Döderlein 1906), silty (Walther 1910), sandy (Nichols 1959; 1962, Ghiold 1982, Grun et al. 2014), shell-gravel (Nichols 1959; 1962), as well as poorly sorted sediments (Telford et al. 1983). In coarse sandy environments, the echinoid lives between gravel particles, masking itself by carrying sand grains on its aboral side (e.g. Nichols 1959, Telford 1983). The spines have been shown to absorb up to 20% of occurring loads (Telford 1985b).

The abundance of well-preserved skeletons from both fossil and recent environments, as well as the initial structural analyses of *Echinocyamus pusillus* (e.g. Telford 1985b) demonstrates that the skeleton of this echinoid can be considered as a valuable role model for biomimetic research on segmented shells.

Previous finite element analyses on echinoids

The complex skeletal geometry and the varying thicknesses of the skeleton limited structural simulations and thus the understanding of biomechanical principles of the echinoid skeleton in the past. Only few finite element analyses have been conducted on simplified and abstracted echinoid skeleton models (Philippi and Nachtigall 1996, Philippi 2001), hence, the understanding of form and its mechanical function is poorly known, although the high skeletal variability of these organisms has been described in detail (e.g. Smith 2005). Initial studies on the stress distribution have been performed on simplified computer aided geometric design model (CAGD) of regular echinoids (Philippi and Nachtigall 1996, Philippi 2001). Such a model allows for parameterization of predetermined characters by keeping computational time low. The often closely spherical regular echinoids feature a pentamerous symmetry that allows a subdividing of the entire skeleton into five nearly identical units. Analyses of a single unit can then be interpreted on the entire skeleton without losing information as the skeleton is made from five of these pieces (e.g. Philippi and Nachtigall 1996). The pivotal analysis of Philippi and Nachtigall (1996) and Philippi (2001) indicated that loads can be effectively carried by the double-curved design, though loading was not crucial for the echinoid shape. It was assumed that tensile stress due to the interaction of the tube-feet with the substrate required for locomotion is a significant driver for the specific test form.

In *Echinocyamus pusillus*, methods and results employed by Philippi and Nachtigall (1996) and Philippi (2001) cannot be applied: the skeleton of this clypeasteroid follows an overprinted bilateral symmetry resulting in a skeleton that cannot be reduced to a number of similar segments. Additionally, *Echinocyamus pusillus* lives buried within the sediment where it uses spines for burrowing, resulting in various skeletal adaptations not found in regular echinoids. As high-resolution imaging-techniques and computational resources have increased over the past decades together with the development of advanced finite element methods, a much more detailed investigation of echinoid skeletons can be applied. In this study, the skeleton of *Echinocyamus pusillus* is analysed for the first time for its mechanical performance using an accurate 3D model based on µCT scans.

Material and methods

Material

Denuded skeletons of *Echinocyamus pusillus* were collected in Summer 2010 during scuba dives around the island of Giglio (Tyrrhenian Sea, Italy: 42°21'07.9"N 10°52'52.1"E) and from beach sediments at Riccione (Adriatic Sea, Italy: 44°01'17.9"N 12°38'13.6"E) in September 2014. Additional specimens conserved in alcohol (70% vol.) were obtained from the Alfred-Wegener-Institut, Helmholtz-Zentrum für Polar- und Meeresforschung, Helgoland, Germany, collected in the North Sea. Samples are stored at the Department of Geosciences, University of Tübingen, Germany, under repository GPIT/EC/00740 for Giglio, and GPIT/EC/00756 for Helgoland. Coordinates are obtained from Google Maps 2017.

Methods

3D Models — An x-ray micro-computed tomography (µCT) scan of *Echinocyamus pusillus* [specimen GPIT/EC/00740:gg-al-1.73] was obtained by a Phoenix Nanotom (General Electric Company Corporation, Boston, MA, USA) at the German Aerospace Center (Deutsches Zentrum für Luft- und Raumfahrt), Stuttgart, Germany. The scan was performed with an isotropic voxel size of 3 µm, and scanning parameters as follow: voltage = 80 kV, power = 180 µA, exposure time = 800 ms, projections = 2000. The µCT 3D scan was recorded to an 8-bit grey-scale system with 878 image slices in the in the X-Y (horizontal) plane in JPG file format and a resolution of 1934 x 2320 pixels.
The µCT imagery was rendered in FEI Avizo in Version 9.4.0 (Thermo Fisher Scientific, Waltham, MA, USA) with active grey values ranging between 42 and 255 for the final model. The grey-scaled model was transferred into a colour-coded model by re-assigning threshold grey-values to a RGB colour space (Fig. 2, Tab. 1).

Voxel Finite Element Model — Based on the µCT imaginary, a finite element model (Zienkiewicz et al. 2005, Richmond et al. 2005, Rayfield 2007) for the structural analysis of an *Echinocyamus pusillus* specimen was generated. This process was automated in the numerical computing environment MATLAB (MathWorks, Natick, USA) and consists of the voxel-based reconstruction (Keyak et al. 1990, van Rietbergen et al. 1995, Lengsfeld et al. 1998) of the three-dimensional geometry including information about the density, removal of floating parts of material and the generation of different loads and

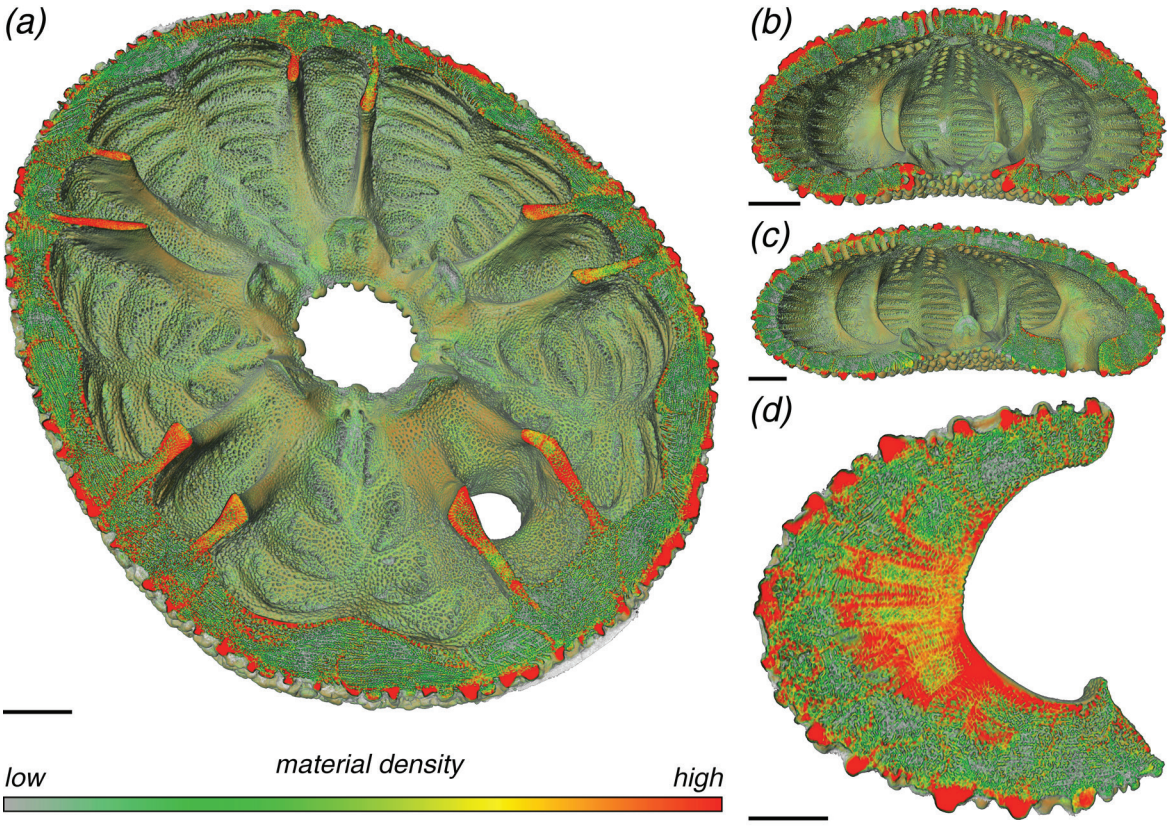

Figure 2. Colour coded 3D rendering of *Echinocyamus pusillus*. (a) Section showing the material distribution within the plates and the internal supports in horizontal and oblique view. Red indicates high material densities at the outer surface (tubercles and glassy tubercles), sutures and within the buttress system. (b) Frontal section of the skeleton. Plate centres are dominated by a low material density (green). (c) The lateral section shows that material densities are similarly distributed along the longitudinal axis. (d) A detailed section of a single buttress shows that the material density is highest (red) in direction to the peristome and along the suture areas. The average stereom of the buttress is dominated by intermediate dense (yellow) material. Scale bar = 500 µm

boundary conditions. To reduce the computational effort for the finite element simulation, 4x4x4 pixels are combined to produce one voxel element with averaged material properties, represented by the grey values of each pixel. The resulting model (Fig 3a) consists of 7,927,311 voxels, 10,450,890 nodes and 31,230,685 degrees of freedom.

Table 1. Conversion values from grey-scale to RGB colour space applied to the active grey values range between 42 and 255

	colour		
grey	R	G	B
42.00	255	255	255
95.25	170	170	170
148.50	0	214	42
201.75	254	255	0
255.00	255	24	0

Philippi and Nachtigall (1996) performed tests to obtain material properties for the regular echinoid *Echinus esculentus*. Their value for the Young's modulus of non-perforated interambulacral areas of E = 9.50 kN/mm² is used here as a base value. Poisson's ratio was assumed to be ν = 0.2, a value characterizing brittle biomaterials. The organic material was not considered for the virtual tests as physical tests have shown that organic tissues does not affect the mechanical behaviour

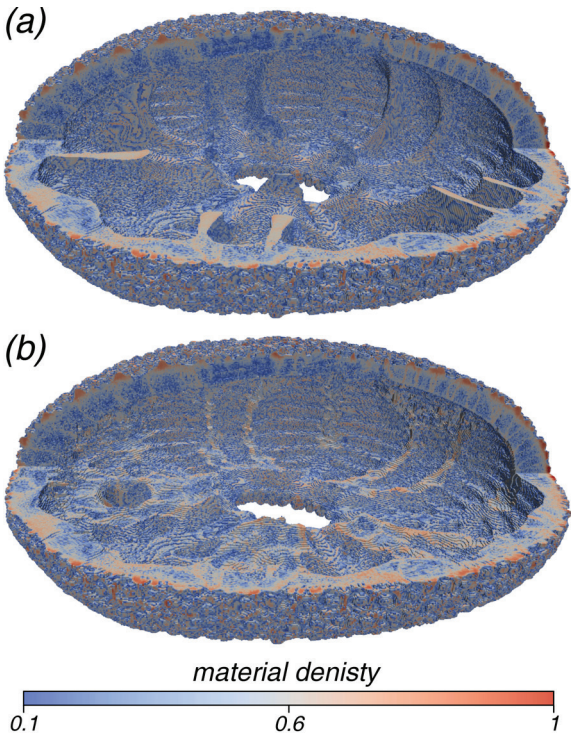

Figure 3. Voxel model of *Echinocyamus pusillus*. (a) Original geometry including the buttresses and heterogeneous material distribution. (b) Modified geometry without the buttresses and heterogeneous material distribution

of the skeleton.

To include the non-homogeneous material distribution in the finite element analysis, the grey values from µCT scans were linearly related to the density of the material. For the dependence of Young's modulus on the density or porosity of the material, a nonlinear relation (Pabst et al. 2006, Nickel et al. 2018) is used,

$$E(p) = E_0(1-p)^2$$

with E_0 denoting the base value for the Young's modulus and p the porosity of the material.

The finite element analysis of the voxel model is performed using our in-house research code "NumPro" taking advantage of the regular voxel structure for computational efficiency (Yang et al. 2012, Nguyen and Schillinger 2018). The matrix-vector-product used in the preconditioned conjugate gradient method, used for equation solving, is implemented in a matrix-free way (Carey et al. 1988) using pre-calculated products on voxel-level. Furthermore, the implementation is parallelized by openMP using a shared memory approach.

Virtual tests — To understand the structural load carrying behaviour of the skeleton of *Echinocyamus pusillus*, virtual experiments are conducted. Hereby, variations of the geometry and model parameters can be examined that are not available for real physical tests. To investigate the significance of the material distribution in the structure and the buttress system for load carrying behaviour, four different test cases are examined:

A original geometry including the buttresses; heterogeneous material distribution
B original geometry including the buttresses; homogeneous material distribution
C modified geometry without the buttresses; heterogeneous material distribution
D modified geometry without the buttresses; homogeneous material distribution

In case C and D the buttresses are removed during generation of the voxel model, resulting in an approximately constant skeleton thickness (Fig. 3b). For the homogeneous material distribution, the same amount of material of the original model is distributed homogeneously to keep the total mass constant.

Loads and boundary conditions are defined similar to the physical crushing tests. A ring shaped area on the lower side of the skeleton is supported in vertical direction and a circular area on the upper side is loaded by a constant pressure with a resultant force of 1.6 N in vertical direction. A linear static analysis is sufficient to obtain the stress distribution in the skeleton and determine load carrying characteristics.

Physical crushing tests — The physical crushing tests are performed to evaluate results obtained by finite analysis methods. Additionally, these uniaxial compression experiments are used to identify the role of organic tissues around the stereom. Therefore, skeletons of *Echinocyamus pusillus* [GPIT/EC/00756] were analysed for the force needed until the skeletal structures fail. Three treatment groups are compared to identify the effect of organic material in the skeleton and the presence of the internal buttress system. Samples of all treatment groups possess all appendages and tissues, and are stored in Ethanol (70%). Skeletons are prepared by gently milling the aboral side down to a third of the skeleton's height. This procedure ensures that forces are applied on both the ambitus and the internal supports directly. Treatment group 1 includes skeletons, where the jaw apparatus and organs of the skeleton cavity were removed by tweezers. In treatment group 2 and treatment group 3, all organic material was removed in a 60 min bath in a 12% solution of sodium hypochlorite after it was washed under running tap-water. The buttress system of treatment group 3 was removed using pointed tweezers.

The uniaxial compression tests were performed using a PCE-FB dynamometer (PCE Instruments, Meschede, Germany). For these experiments, samples are placed on an aluminium sample stub (Plano GmbH, Wetzlar, Germany) mounted on a height-adjustable stage. During elevation of the stage, samples are pressed against a plate stamp of the measuring device. The elevation stops when the skeleton is crushed. A Kruskal-Wallis H test is used to compare skeleton lengths among treatment groups to ensure that the three treatment groups are similar in size. The resulting forces for skeletal failure along the treatment groups are compared by a Kruskal-Wallis H test followed by a pairwise Benjamini, Hochberg and Yekutieli p-adjusted Wilcoxon post-hoc analyses to identify possible effects of the organic

material and internal supports with respect to the skeletal strength. The comparative crushing analysis conducted in the present study does not aim to provide absolute numbers for the skeleton's load bearing capacity, but compares the original skeleton morphology of *Echinocyamus pusillus* to manipulated structures with the goal of recognizing the importance of organic tissues and internal buttressing for skeletal strength. Measurements are reported in Newton (N) using the median for the measure of central tendency, and the median absolute deviation (mad) for the measure of dispersion.

Results

Material distribution

The colour-coded 3D model of *Echinocyamus pusillus* (Fig. 2) shows the material density distribution of the structural elements. The outer surface of the skeletons is of high material density (red). These structures can be identified as tubercles and glassy tubercles that mostly consist of imperforated stereom. In horizontal section (Fig. 2a), plates mostly consist of low (green) or intermediate (yellow) material density. In the sutural areas where plates are interconnected to one another, the density is higher (yellow to red).

In frontal section (Fig. 2b), the outer surface of plates where tubercles and glassy tubercles are present show a high material density in contrast to the plate's inner areas which typically show lower material densities. The inner transversal ridges show higher material densities along with that of plate boundaries. Material densities are similarly distributed over the entire width of the skeleton. In lateral section (Fig. 2c), material densities are similarly distributed over the longitudinal axis.

The material density found in the buttress system shows a generally higher stereom density than in the remaining skeleton (Fig. 2a). Areas of high material density are thereby mainly accumulated in the buttress areas towards the peristome as shown in the section of an individual buttress (Fig. 2d). Sutural areas are of high material density whereas most of the central buttress is dominated by intermediate to high material density. The modified skeletons, where internal supports have been virtually removed, show an approximately constant skeletal thickness. (Fig. 3b).

Virtual tests

The vertical displacement caused by applied loadings is compared for the four test cases (A-D) of the model. The displacements for the original skeleton geometry with the buttress system present and heterogeneous material distribution (case A, Fig. 4a) and with the buttress system present and homogeneous material distribution (case B, Fig. 4b) are practically identical. In contrast, the displacement for the modified geometry without the buttresses are around 57% larger for both heterogeneous and the homogeneous models (cases C and D, Fig. 4c-d) than for the original geometry.

In the comparison of the distribution of normal stresses in vertical direction σzz in horizontal section of the original skeleton of *Echinocyamus pusillus*, it can be observed that the maximum compressive stress occurs in the buttress areas towards the peristome for both the heterogeneous and homogeneous model (Fig. 5a-b). For the models without buttresses, larger bending stresses with high tension on the outer surface are visible in the finite element graph (Fig. 5c-d). The tensile stress in circumferential direction (stress σyy) in the upper and lower part of the horizontal section is also larger for the modified geometry without the buttresses (Fig. 6).

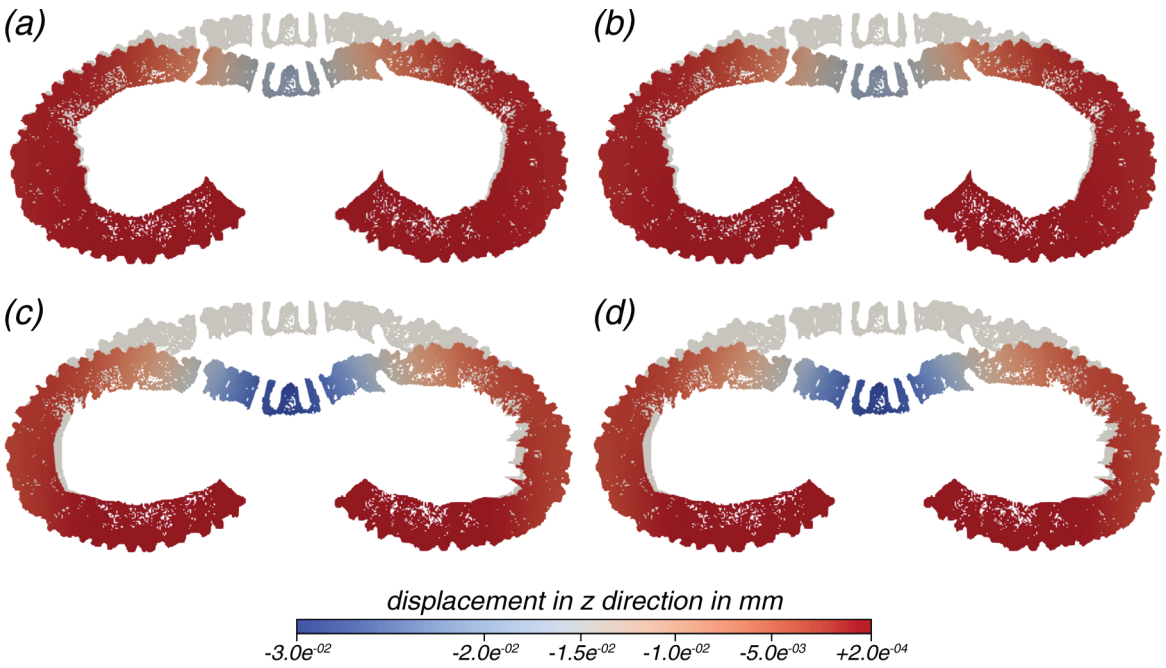

Figure 4. Undeformed (grey) and deformed (coloured) section of the voxel model of *Echinocyamus pusillus*. Deformation is scaled by a factor of 25. The colours show the magnitude of the vertical displacement. (a) Original geometry including the buttresses with heterogeneous material distribution. (b) Original geometry including the buttresses with homogeneous material distribution. (c) Modified geometry without the buttresses with heterogeneous material distribution. (d) Modified geometry without the buttresses with homogeneous material distribution

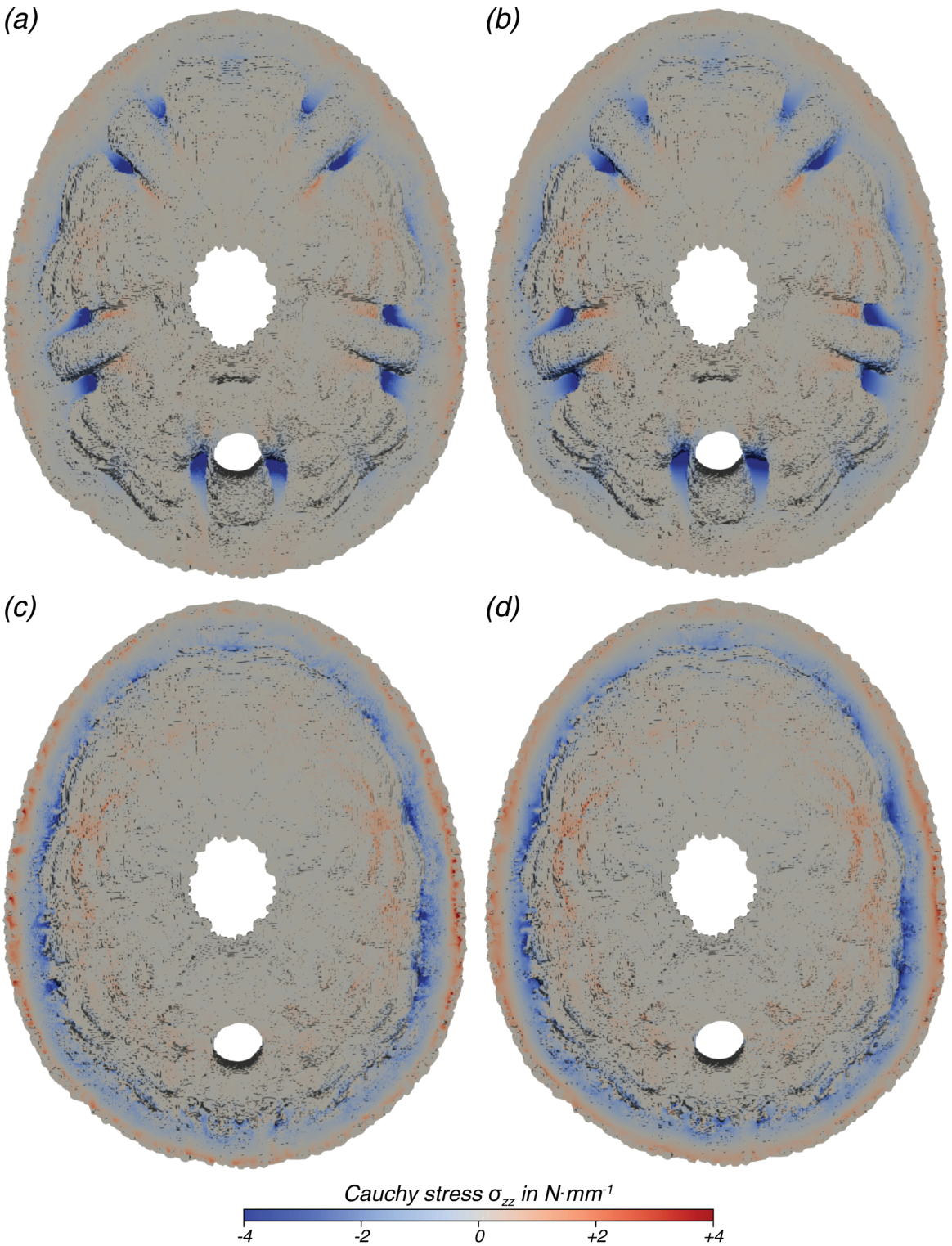

Figure 5. Contour plot of the Cauchy stresses in z direction in a section of the voxel model of *Echinocyamus pusillus*. (a) Original geometry including the buttresses with heterogeneous material distribution. (b) Original geometry including the buttresses with homogeneous material distribution. (c) Modified geometry without the buttresses with heterogeneous material distribution. (d) Modified geometry without the buttresses with homogeneous material distribution

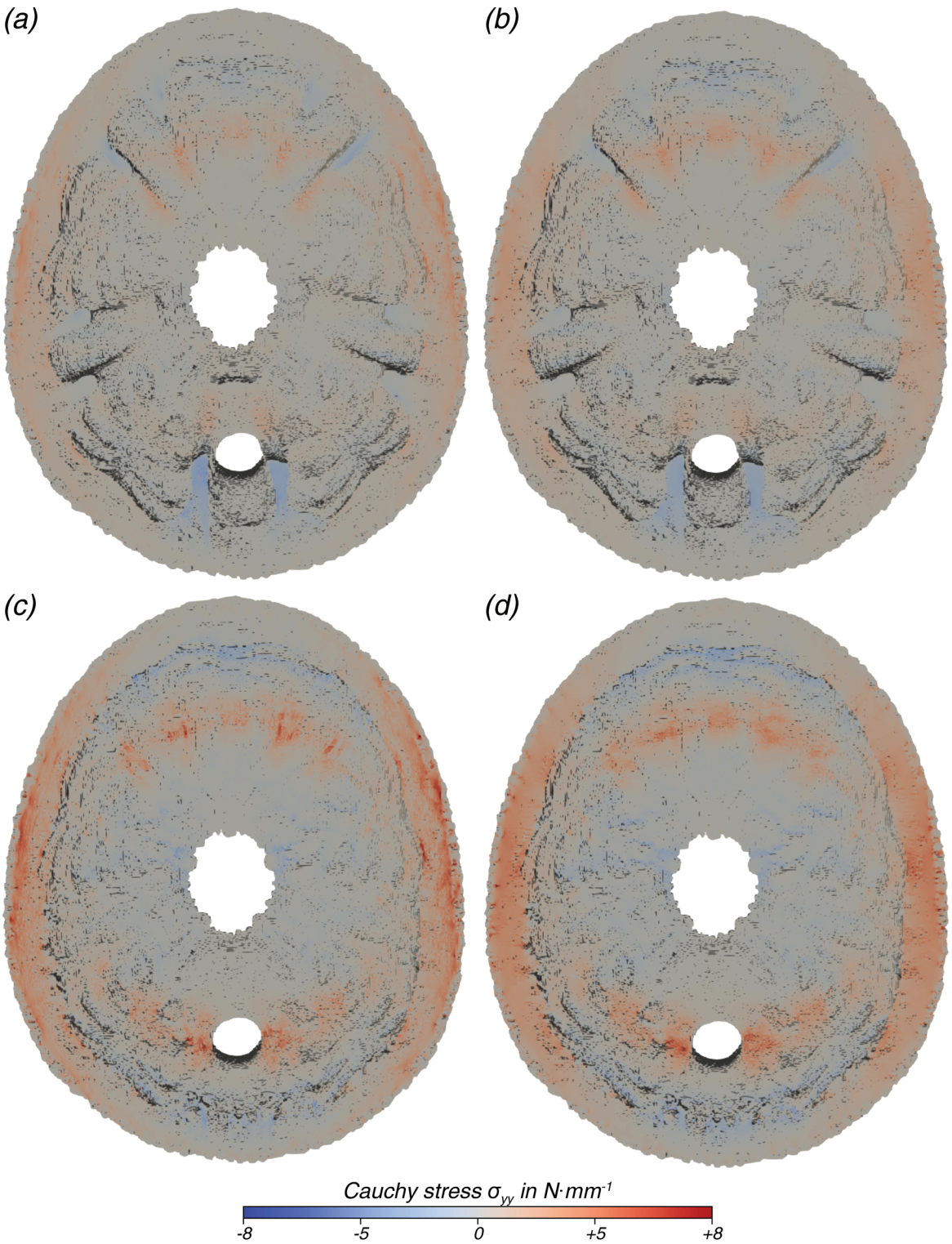

Figure 6. Contour plot of the Cauchy stresses in y direction in a section of the voxel model of *Echinocyamus pusillus*. (a) Original geometry including the buttresses with heterogeneous material distribution. (b) Original geometry including the buttresses with homogeneous material distribution. (c) Modified geometry without the buttresses with heterogeneous material distribution. (d) Modified geometry without the buttresses with homogeneous material distribution

Physical crushing tests

A Kruskal-Wallis H test compared 30 *Echinocyamus pusillus* skeletons indicating that the three treatment groups do not statistically differ in their average skeleton length ($\chi^2 = 1.29, p = 0.526, N = 30$) (Fig. 7a). A Kruskal-Wallis H test followed by a pairwise post-hoc analysis shows that the force needed until the skeleton crushes does not statistically differ between the group with organic material with internal supports present and the group where organic material was removed, but internal supports are present (p = 1.000, N = 20). The group with organic material and internal supports present maintain higher force loadings than skeletons where both organic material and internal supports were removed (p = 0.006, N = 20). Similarly, the test group without organic material, but with internal supports present, shows a higher force load capacity than the test group where both the organic material and internal supports were removed (p = 0.025, N = 20).

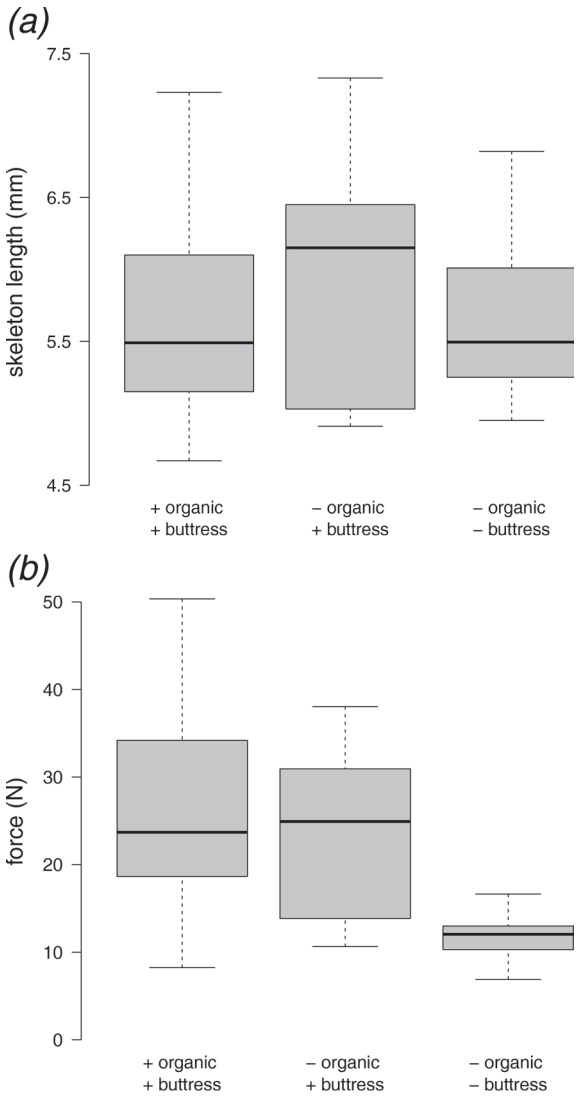

Figure 7. Box plots of statistical analyses for the load bearing capacity of the skeleton along three treatment groups. (a) Skeleton length comparison indicating that the analysed skeletons are of similar size classes along the treatment groups. (b) The comparison of force applied until structural failure occurs indicates that buttressing is a structural important parameter

The test group where organic material and the internal supports were present shows an average force load capacity of 23.70 N (Fig. 7b, Tab. 2). The test group where organic material was removed, but internal supports are still present, shows an average force load capacity of 24.93 N. The test group where both the organic material and the internal supports were removed shows an average force load capacity of 12.05 N.

Discussion

Material distribution

The skeleton of *Echinocyamus pusillus* possesses a high variation in material distribution (Fig. 2). Variations in material distribution of the stereom reflect both mechanical aspects and infrastructure for the physiological functionality. The outer surface of the skeleton is covered by tubercles for spine attachment and glassy tubercles of high material density. The distribution of tubercles and glassy tubercles has been discussed to increase skeletal integrity, as these micro-structures can cross plate boundaries (Lawrence 1987). The material distribution within the skeletal plates shows accumulations on the plate sutures, where plates are connected to one another (Fig. 2). These areas are recognizable as yellow to red zones in the colour-coded images indicating that interdigitating plates (Telford 1985b, Grun and Nebelsick 2018) locally increase the material density. This plate interlocking results in a monolithic shell behaviour and is thus important for the structural integrity of the skeleton (Grun and Nebelsick 2018). The highest material accumulation can be found in the buttress system. These structures have also been shown to transfer most of the applied stress (Fig. 5).

The approximately constant skeleton thickness of the modified model (Fig. 3) is a relevant criterion for the finite element analyses, as highly varying thicknesses can affect the stress distribution and hence the results. The voxel renderings show that the areas, where buttress elements have been removed, are in the range of thickness of the original skeleton geometry.

Mechanical load bearing behaviour

The investigation of the four models of the virtual test does not give any information about the strength of the skeleton of *Echinocyamus pusillus* in its natural environment, but the results can be used to understand the load bearing behaviour of the skeleton. Furthermore, by comparison of the heterogeneous and homogeneous models, reasons for the material distribution can be deduced.

The vertical displacement caused by the applied loading is directly related to the overall stiffness of the skeleton of *Echinocyamus pusillus*. By comparing the displacements for the four test cases of the virtual tests, the influence of different parameters on the stiffness can be evaluated. The displacements for the original skeleton geometry with heterogeneous (A)

and homogeneous (B) material distribution are practically identical (Fig. 4a-b). This indicates that the qualitative load bearing behaviour of the skeleton does not primarily depend on the material distribution. Instead, the stiffness of the skeleton is mostly dependant on the overall geometry, which represents a structural property rather than a material property. This result does not imply that the density distribution has no effect on the structural load carrying behaviour of the skeleton. It does, however, indicate that the geometrical effect is of much greater significance for the structural behaviour of the skeleton.

The importance of the geometry and the buttresses for the overall stiffness can also be observed by comparing the displacements of the original geometry (Fig. 4a-b) and the modified geometry (Fig. 4c-d). Without the buttresses, the displacements are around 57% larger for the heterogeneous and the homogeneous models than for the original geometry.

The maximum compressive normal stress in vertical direction σzz in a horizontal section through the original skeleton of *Echinocyamus pusillus* (Fig. 5a-b) occurs in the buttress areas towards the peristome for both the heterogeneous and homogeneous model. In structural mechanics, usually stiffer material attracts forces. For *Echinocyamus pusillus*, however, the stress concentration in the buttresses is not caused by the higher density in these areas, as it can also be observed for the homogeneous model. The stress distribution is rather due to the geometry and therefore a structural property. Consequently, the higher density of the material in the buttress areas towards the peristome is caused by the high stresses to obtain a higher strength (as opposed to stiffness) of the material.

The positive effect of the buttresses on the load bearing behaviour is obvious in the comparison of the stress distribution: for the model without buttresses, larger bending stresses with high tension are present on the outside of the skeleton (Fig. 5c-d). This bending is caused by the local loading but is also due to the fact that for this thick shell the ratio between membrane stiffness and bending stiffness is not as large as for thin shells. The tensile stress in circumferential direction (stress σyy in the upper and lower part of the horizontal section) is also much larger without the buttresses (Fig. 6). If the vertical load is carried by the pure shell of the modified geometry, large tension in circumferential direction is needed for equilibrium. The buttresses cause a load bearing behaviour more similar to a rib vault resulting in much lower tension in circumferential direction.

Physical crushing tests

The uniaxial compression tests show, that internal buttressing is relevant for the skeletal stability (Fig. 7). This result supports the outcome of the finite element analysis which salso upports the interpretation that the internal supports do in fact strengthen the skeleton of *Echinocyamus pusillus*. A structural strengthening behaviour has often been attributed to the buttressing structures (e.g. Schaffer 1962, Seilacher 1979, Telford 1985b, Lawrence 1987, Grun et al. 2014), yet, these assumptions have neither been testes physically, nor virtually. This is, however, not surprising as the naturally grown shells vary in geometry, thickness, curvature, and porosity, parameters which are crucial for property determination (e.g. Greven and Magin 2004).

Although it has been previously shown that collagenous fibres are absent within the plates' sutures (Telford 1985b), the presence of soft tissues such as the epidermis which covers the entire skeleton, as well the stroma within the stereom interspace (Märkel 1990), have not been analysed in this context. Results of the physical crushing tests show that organic tissues do not contribute to a significant increase in skeletal strength (Fig. 7). This is an important result, as it demonstrates that the load bearing capacity of this echinoid's skeleton predominantly relies on the structural design, rather than on supportive tissues. This fact makes the skeleton of *Echinocyamus pusillus* an attractive role model for structural engineering, where segmented shells become increasingly important (e.g. Grun et al. 2016; 2017).

Table 3. Measurements of *Echinocyamus pusillus* skeleton length and forces needed until structural failure. N = Newton

treatment		group 1	group 2	group 3
		+ organic + buttresses	- organic + buttresses	- organic - buttresses
skeleton length (mm)	median	5.49	6.15	5.50
	mad	0.83	1.10	0.45
	min.	4.67	4.91	4.95
	max.	7.23	7.33	6.82
force (N)	median	23.70	24.93	12.05
	mad	8.52	13.31	2.48
	min.	8.25	10.65	6.90
	max.	50.35	38.05	16.65
Nr. of specimens		10	10	10

Conclusion

(1) Material distribution in the skeleton of *Echinocyamus pusillus* is heterogeneous with high material accumulations in the sutures and the buttress system (Figs. 2, 3).

(2) Finite element analyses show that models of the skeletons with heterogeneous material distribution behave similar to those models with homogenous material distribution (Figs. 4-6). This result thus implies that the geometrical effect of the skeleton is of much greater structural significance to the load carrying behaviour than the material distribution, although the heterogeneous material distribution still contributes to the structural resilience of the skeleton.

(3) Finite element analyses furthermore show that internal buttressing is crucial for load transfer and minimizing bending and tension of the skeleton. The removal of the buttresses causes compressive and tensile forces with especially high tensile circumferential forces occurring around the peristome (Fig. 6).

(4) Physical crushing tests support that the results of finite element analysis are plausible. The uniaxial compression experiments also indicate that organic tissues have no significant effect on the skeletal strength (Fig. 7). Thus the structural strength of the skeleton of *Echinocyamus pusillus* predominantly relies on its skeletal design.

Acknowledgments

The authors acknowledge support by the state of Baden-Württemberg through bwHPC and Raouf Jemmali (German Aerospace Center) for micro-tomographic scanning. We thank three reviewers for their constructive comments.

Funding

This work has been funded by the Deutsche Forschungsgemeinschaft (DFG, German Research Foundation) as part of the Transregional Collaborative Research Centre (SFB/Transregio) 141 ‘Biological Design and Integrative Structures’.

Ethics

An ethical assessment was not required for collecting empty and denuded skeletons as well as for obtaining alcohol samples of *Echinocyamus pusillus* from the Alfred-Wegener Institute. Approval from the institutional animal ethics committee is not necessary. No living animals were used; no animals were particularly euthanized for this research. All alcohol samples were collections of the Alfred-Wegener-Institut Helmholtz Zentrum für Polar-und Meeresforschung. Permission to collect samples of empty and denuded skeletons of *Echinocyamus pusillus* was not required at the time. No 'Animal Care Protocol' was required. Permission to carry out fieldwork was not required.

Data accessability

The μCT data of *Echinocyamus pusillus* are accessible via dryad digital repository under doi:10.5061/dryad.rg54h: www.doi.org/10.5061/dryad.rg54h (Grun and Nebelsick 2018).

Competing interests

The authors have no competing interests.

Authors' contribution

All authors had the idea for this study and developed the research. TBG carried out the physical test as well as statistical analyses; MvS carried out voxel-based finite element analysis. TBG and MvS generated 3d renderings. All authors discussed and interpreted the results, coordinated and drafted the manuscript. All authors gave final approval for publication.

References

Agassiz L. 1841 Monographies d'Échinoderms vivans et fossiles. Échinites. Famille des Clypéasteroides. Second Monographie. Des Scutelles. Neuchâtel, Switzerland: Imprimerie de Petitpierre.

Agassiz A. 1872 Revision of the echini. Part I. Cambridge, UK: Cambridge University Press.

Carey GF, Barragy E, McLay R, Sharma M. 1988 Element-by-element vector and parallel computations. Commun. Appl. Numer. Methods 4, 299 – 307.

Döderlein L. 1906 Arktische Seeigel. Fauna Arctica, Vierter Band. Jena, Germany: Verlag von Gustav Fischer.

Durham JW. 1955 Classification of clypeasteroid echinoids. University of California Press in Geological Sciences 31,73 – 198.

Durham JW. 1966 Clypeasteroids. In Treatise on Invertebrate Paleontology, volume U3.2 (ed RC Moore), pp. 450 – 491. Lawrence, KS: University of Kansas Press.

Forbes E. 1852 Monograph of the Echinodermata of the British Tertiaries. Bartholomew, UK: C and J Adlard, Printers.

Ghiold J. 1982 Observations on the clypeasteroid *Echinocyamus pusillus* (O.F. Müller). J. Exp. Mar. Biol. Ecol. 61, 57 – 74.

Greven E, Magin W. 2004 Werkstoffkunde und Werkstoffprüfung für technische Berufe. Hamburg, Germany: Handwerk und Technik.

Grossmann JN, Nebelsick JH. 2013a Comparative morphological and structural analysis of selected cidaroid and camarodont sea urchin spines. Zoomorphology 132, 301 – 315.

Grossmann JN, Nebelsick JH. 2013b Stereom differentiation in spines of *Plococidaris verticillata*, *Heterocentrotus mammilatus* and other regular sea urchins. In Echinoderms in a Changing World: Proceedings of the 13th International Echinoderm Conference, January 5-9 2009, University of Tasmania, Hobart Tasmania, Australia (ed C Johnson), pp. 97 – 104. Boca Raton, FL: CRC Press.

Grun TB, Nebelsick JH. 2016 Taphonomy of a clypeasteroid echinoid using a quasimetric approach. Acta Palaeont. Pol. 61, 689 – 699.

Grun TB, Nebelsick JH. 2018 Data from: structural design analysis of the minute clypeasteroid echinoid *Echinocyamus pusillus*. Dryad Digital Repository. (doi: 10.5061/dryad.rg54h)

Grun TB, Nebelsick JH. 2018 Structural design analysis of the minute clypeasteroid echinoid *Echinocyamus pusillus*. J. R. Soc.Open Science. In press.

Grun T, Sievers D, Nebelsick JH. 2014 Drilling predation on the clypeasteroid echinoid *Echinocyamus pusillus* from the Mediterranean Sea (Giglio, Italy). Hist. Biol. 26, 745 – 757.

Grun TB, Kroh A, Nebelsick JH. 2017 Comparative drilling predation on time-averaged phosphatized and non-phosphatized assemblages of the minute clypeasteroid echinoid *Echinocyamus stellatus* from Miocene offshore sediments (Globigerina Limestone Fm., Malta). J. Paleont. 91, 633 – 462.

Grun TB, Koohi L, Schwinn T, Sonntag D, von Scheven M, Bischoff M, Knippers J, Menges A, Nebelsick JH. 2016 The skeleton of the sand dollar as a biological role model for segmented shells in building construction: a research review. In Biologically-inspired design and integrative structures: analysis, simulation and implementation in architecture (eds J Knippers, KG Nickel, T Speck), pp. 217 – 242. Cham, Switzerland: Springer.

Grun TB, Mancosu A, Belaústegui Z, Nebelsick JH. 2018 The taphonomy of *Clypeaster*: a paleontological tool to identify stable structures in natural shell systems. Neues Jahrb. Geol. Palaontol. Abh. In press.

Keyak JH, Meagher JM, Skinner HB and Mote CD. 1990 Automated three-dimensional finite element modelling of bone: a new method. Biomed. Eng. 12, 389 – 397.

Klang K, Bauer G, Toader N, Lauer c, Termin K, Schmier S, Kovaleva D, Haase W, Berthold C, Nickel KG, Speck T, Sobek W. 2016 Plants and animals as source of inspiration for energy dissipation in load bearing systems and facades. In Biologically-inspired design and integrative structures: analysis, simulation and implementation in architecture (eds J Knippers, KG Nickel, T Speck), pp. 109 – 133. Cham, Switzerland: Springer.

Kroh A, Nebelsick JH. 2010 Echinoderms and Oligo-Miocene carbonate systems: potential applications in sedimentology and environmental reconstruction. Int. Assoc. Sediment. Spec. Pub. 42: 201 – 228.

Lauer C, Grun TB, Zutterkirch I, Jemmali R, Nebelsick JH, Nickel KG. 2017 Morphology and porosity of the spines of the sea urchin *Heterocentrotus mamillatus* and their implications on the mechanical performance. Zoomorphology 137, 139 – 154.

Lawrence J. 1987 A functional biology of echinoderms. Baltimore, MA: John Hopkins University Press.

Lengsfeld M, Schmitt J, Alter P, Kaminsky J, Leppek R. 1998 Comparison of geometry-based and CT voxel-based finite element modelling and experimental validation. Med. Eng. Phys. 20, 515 – 522.

Mancosu A, Nebelsick JH. 2013 Multiple routes to mass accumulations of clypeasteroid echinoids: a comparative analysis of Miocene echinoid beds of Sardinia. Palaeogeogr. Palaeoclim. Palaeoecol. 374, 173 – 186.

Mancosu A, Nebelsick JH. 2015 The origin and paleoecology of clypeasteroid assemblages from different shelf setting of the Miocene of Sardinia, Italy. Palaios 30, 273 – 387.

Mancosu A, Nebelsick JH. 2017a. Ecomorphological and taphonomic gradients in clypeasteroid-dominated echinoid assemblages along a mixed siliciclastic-carbonate shelf from the early Miocene of northern Sardinia, Italy. In press.

Mancosu A, Nebelsick JH. 2017b Palaeoecology and taphonomy of spatangoid-dominated echinoid assemblages: A case study from the Early-Middle Miocene of Sardinia, Italy. Palaeogeogr. Palaeoclim. Palaeoecol. 466, 334 – 352.

Märkel K. 1990 Biomineralization in echinoderms. In Echinoderm Research (eds C de Ridder, P Dubois, MC Lahaye, M Jangoux), pp. 276 – 282. Rotterdam, Netherlands: Balkema.

Mortensen TH. 1907 The Danish Ingolf-Expedition IV.2 Echinoidea (II). Copenhagen, Denmark: Bianco Luno.

Mortensen TH. 1927. Handbook of the echinoderms of the British Isles. London, UK: Humpherey Milford Oxford University Press.

Müller M. 1854 Über die Gattungen der Seeigellarven. Siebente Abhandlung über die Metamorphose der Echinodermen. Abhandlungen der Königlichen Akademie der Wissenschaften zu Berlin. Berlin, Germany: Druckerei der Königlichen Akademie der Wissenschaften.

Nebelsick JH, Kowalewski M. 1999 Drilling predation on recent clypeasteroid echinoids from the Red Sea. Palaios 14, 127 – 144.

Nebelsick JH, Dynowski JF, Grossmann JN, Tötzke C. 2015 Echinoderms: hierarchically organized light weight skeletons. In Evolution of Lightweight Structures: Analyses and Technical Applications (ed C Hamm), pp. 141 – 156. Dodrecht, Netherlands: Springer.

Nichols D. 1959 The histology and activities of the tube-feet of *Echinocyamus pusillus*. J. Cell Sci. 100, 539 – 555.

Nichols D. 1962 Echinoderms. Tiptree, UK: Anchor Press.

Nickel KG, Klang K, Lauer C, Buck G. 2018 Sea urchin spines as role models for biologic design and integrative structures. In Highlights of Applied Mineralogy (eds S Heuss-Aßbichler, G Amthauer, M John-Stadler), pp. 1 – 14. Berlin, Germany: de Gruyter.

Nguyen LH, Schillinger D. 2018 A multiscale predictor/corrector scheme for efficient elastoplastic voxel finite element analysis, with application to CT-based bone strength prediction. Comp. Meth. Appl. Mech. Eng. 330, 598 – 628.

Pabst W, Gregorová E, Tichá G. 2006. Elasticity of porous ceramics – a critical study of modulus-porosity relations. J. Eur. Ceram. Soc. 26, 1085 – 1097.

Philippi U. 2001 Finite Element-Analyse von Seeigelschalen. In Prozeß und Form Natürlicher Konstruktionen (eds HW Reinhardt, R Reiner), pp. 185 – 189. Berlin, Germany: Ernst und Sohn.

Philippi U, Nachtigall W. 1996 Functional morphology of regular echinoid tests (Echinodermata, Echinoida): a finite element study. Zoomorphology 116, 35 – 50.

R Core Team. 2016 R: a language and environment for statistical computing. R Foundation for Statistical Computing, Vienna, Austria.

Rayfield EJ. 2007 Finite element analysis and understanding the biomechanics and evolution of living and fossil organisms. Annu. Rev. Earth Planet. Sci. 35, 541 – 576.

Richmond BG, Wright BW, Grosse I, Dechow PC, Ross CF, et al. 2005 Finite element analysis in functional morphology. Anat. Rec. 283, 259 – 74.

van Rietbergen B, Weinans H, Huiskes R, Odgaard A. 1995 A new method to determine trabecular-bone elastic properties and loading using micromechanical finite element models. J. Biomech. 28, 69 – 81.

Schaffer H. 1962 Die Scutelliden des Miozäns von Österreich und Ungarn. Paläont. Z. 36, 135 – 170.

Schmier S, Lauer C, Schäfer S, Klang K, Bauer G, Thielen M, Termin K, Berthold C, Schmauder S, Speck T, Nickel KG. 2016 Developing the experimental basis for an evaluation of scaling properties of brittle and 'quasi brittle' biological materials. In Biologically-inspired design and integrative structures: analysis, simulation and implementation in architecture (eds J Knippers, KG Nickel, T Speck), pp. 277 – 294. Cham, Switzerland: Springer.

Seilacher A. 1979 Constructional morphology of sand dollars. Paleobiology 5, 191 – 221. (doi: 10.1017/S0094837300006527)

Smith AB. 1980 Stereom microstructure of the echinoid test. Spec. Papers Palaeont. 25, 1 – 81.

Smith AB. 2005 Growth and form in echinoids: the evolutionary interplay of plate accretion and plate addition. In Evoloving form and function: fossils and development (ed DEG Briggs), pp. 181 – 193. New Haven, CT: Yale University Press.

Stratham RR. 1981 The role of spines in preventing structural damage to echinoid tests. Paleobiology 7, 400 – 406.

Telford M, Harold AS, Mooi R. 1983 Feeding structures, behavior and microhabitat of *Echinocyamus pusillus* (Echinoidea: Clypeasteroida). Biol. Bull. 165, 745 – 757.

Telford M. 1985a. Domes, arches and urchins: the skeletal architecture of echinoids (Echinodermata). Zoomorphology 105, 114 – 124.

Telford M. 1985b Structural analysis of the test of *Echinocyamus pusillus* (O. F. Müller). In Proceedings of the Fifth International Echinoderm Conference, Ireland 1985 (eds BF Keegan, BDS O'Conner), pp. 353 – 360. Rotterdam, Netherlands: Balkema.

Toader N, Sobek W, Nickel KG. 2017 Energy absorption in functionally graded concrete bioinspired by sea urchin spines. J. Bionic. Eng. 14, 369 – 378. (doi:10.1016/s1672-6529(16)60405-5)

Walther J. 1910 Die Sedimente der Taubenbank im Golf von Neapel. In Abhandlungen Der Königlich Preussischen Akademie Der Wissenschaften (ed G Reimer), pp. 1 – 49. Berlin, Germany: Reichsdruckerei.

Yang Z, Ruess M, Kollmannsberger S, Düster A, Rank E. 2012 An efficient integration technique for the voxel-based finite cell method. Int. J. Numer. Meth. Eng. 91, 457 – 471.

Zienkiewicz OC, Taylor RL, Zhu JZ. 2005 The finite element method: its basis and fundamentals. Amsterdam, Netherlands: Elsevier Butterworth-Heinemann.

Złotnik M, Ceranka T. 2005 Patterns of drilling predation of cassid gastropods preying on echinoids from the middle Miocene of Poland. Acta Palaeontol. Pol. 50, 409 – 428.

Manuscript 5

Structural design of the echinoid's trabecular system

Structural design of the echinoid's trabecular system

Tobias B. Grun*, James H. Nebelsick

Department of Geosciences, University of Tübingen, Germany
*Corresponding author: tobias.grun@uni-tuebingen.de [TBG]

Abstract

The multi-plated skeletons of echinoids are made of the stereom, a light-weight construction which resembles a micro-beam framework. Although the two-dimensional design of the stereom has been studied in the past, its spatial architecture is only little known. It is, however, essential to understand the spatial architecture of the trabecular system in order to interpret the structural principles of this load-bearing construction. The echinoid's trabecular system is thus analyzed in-depth with respect to eight topological descriptors. The echinoid's plates are divided into two regions, the center of which consists of an unordered stereom, and the margin which consists of an ordered stereom. The eight trabecular descriptors indicate that the underlying topology of the two plate regions are similar. The trabecular system predominantly consists of short and stocky trabeculae showing little tortuosity. The majority of trabeculae intersect in a 3N configuration, where three trabeculae intersect in one common node. When trabeculae in 3N configuration intersect in an angle of 120°, the resulting element possesses a planar and triangular motif. These planar elements, when arranged in an angular off-set, can resist multi-dimensional loads. Results also show that the trabecular orientation perpendicular to the plate's surface is at an angle of 60°. The trabecular orientation in the plate's horizontal plane is directional. Both trabecular orientations reflect a construction which is capable of resisting downward loads and can distribute these loads over the entire skeleton. The spatial architecture of the echinoid's trabecular system is thus considered to be a structurally performative light-weight and load-bearing system.

Introduction

The echinoid's skeleton is a multi-element construction, consisting of numerous individual skeletal parts, including the plates from which the test (shell) is formed, spines, skeletal discs of the tube-feet, and skeletal elements of the pedicellariae [1, 2]. These minute skeletal elements are constructed of the stereom, which resembles a micro-beam system (Fig 1). The stereom of the echinoid spines has been investigated for its structural design [3-6] and mechanical performance [6-8] using both 2-dimensional (2d) images and 3-dimensional (3d) models. The stereom of the plates was likewise examined by 2d imageries [3, 9, 10], but 3d analyses are still lacking. The 3d analyses of the echinoid's trabecular system are, however, of highest interest, as they allow for a detailed understanding and interpretation of the structural context and mechanical behavior, which can hardly be obtained from 2d analytics.

Echinoids of the order Clypeasteroida have become the focus of structural research as their often flattened tests demonstrate a high strength and robustness [11, 12-16]. The stable nature of these tests is not only reflected in the abundances of complete test or their stable fragments in recent environments [15, 17-19], but also in the rich fossil record [14, 15, 20-24]. The structural integrity of the clypeasteroid tests is a result of the plate

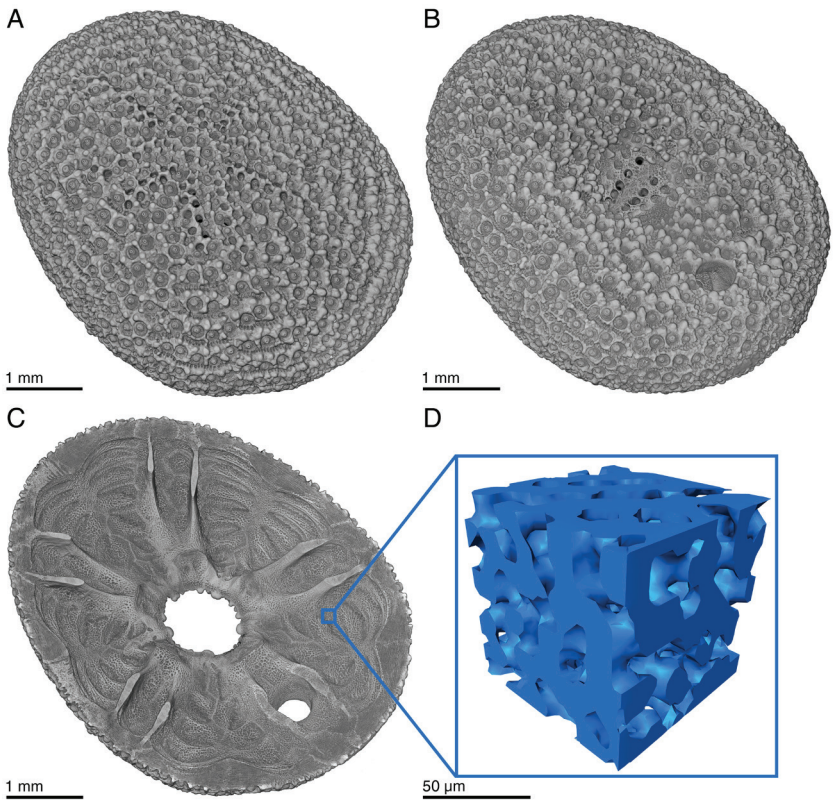

Figure 1. Orthographic rendering of *Echinocyamus pusillus*. (A) Aboral view showing the upper surface of the flattened echinoid. Anterior is upper left. (B) Oral view with the peristome in the center and the periproct posterior. (C) Horizontal section with view on the inner oral face of the echinoid. Blue square indicates the plate's marginal area. (D) Stereographic rendering of the lattice-like stereom.

arrangement [16], plate interlocking, and internal support systems [13, 15, 16, 18, 25]. The tests of clypeasteroid echinoids are thus of interest of biomimetic research, which aims to identify structurally performative constructions that potentially can be transferred into architectural and engineering disciplines. The mechanisms and principles of such structures are used to improve technical multi-element constructions [14]. The structural design of the echinoid's trabecular system is here analyzed for the first time in-depth using x-ray micro-computed tomography and is interpreted in the context of engineering concepts.

Trabecular descriptors

Trabecular descriptors are morphological parameters describing the spatial architecture of a structure [26]. These parameters can thereby yield information on the structural mechanics of the trabecular system. Eight trabecular descriptors are described that possess the potential for structural mechanic interpretations of the echinoid's trabecular system: (1) trabecular length, including the curved length and the chord length, (2) trabecular tortuosity, (3) trabecular radius, (4) trabecular slenderness ratio, (5) inter-trabecular angle, (6) node configuration, (7) theta orientation, and (8) phi orientation.

Trabecular length, tortuosity, radius and slenderness ratio

The four descriptors are closely associated to one another. Following structural mechanic principles, a slender trabecula is more subject to buckling than a stocky trabecula at a given length demonstrated by equation (1), where the radius r is to the power of four and hence can significantly influence flexural stiffness EI, which is the product of the material depended Young's modulus E and the second moment of area I.

$$I = \frac{\pi r^4}{4} \qquad (1)$$

I = second moment of area, r = trabecular radius.

Any increase in r will increase *I*, and hence the flexural stiffness *EI*, which prevents the trabeculae from buckling, as expressed in equation (2).

$$F_E = \frac{\eta \pi^2 EI}{L^2} \qquad (2)$$

F_E = critical Euler buckling force, η = coefficient for beams with two fixed ends = 4 [27-29], *E* = Young's Modulus, *I* = second moment of area, *L* = trabecular length.

A related parameter is the slenderness ratio, which is defined as the ratio between the trabecular length and the trabecular radius

$$R_S = \frac{L}{r} \qquad (3)$$

RS = slenderness ratio, *L* = trabecular length, *r* = trabecular radius. Any increase in trabecular length *L* at a given trabecular radius *r* decreases the critical Euler buckling force *FE*, which is the force at which structural failure is expected [28]: loadings on an ideal beam in longitudinal axis exclusively induces compressive stress resultants. Any deviation from an ideal beam results in bending moments along the longitudinal axis of a beam, which can be countered as long as the inner bending force is equal or larger than the outer bending force. The beam can return to its initial position after the load is removed. Structural failure occurs when the outer bending force exceeds the inner bending force [28]. This is the case when the critical Euler buckling value is reached.

Inter-trabecular angle and node configuration

The terminology of the inter-trabecular angle (ITA) was used by Reznikov et al. [26] for the cancellous bones of vertebrates. This topological parameter describes the trabecular architecture irrespective of trabecular length and thickness. The ITA was initially developed to correlate the angle between collagenous fibers on the micrometer level, and the angle between trabeculae at the millimeter scale [26]. The number of trabeculae intersecting in one common node (node configuration) has been interpreted with respect to its structural relevance and its conservation potential within vertebrates. In cases where three trabeculae intersect in a common node (3N), the ideal value for identical angles is 120 degrees. This configuration eventually results in a planar triangle. In cases where four trabecular intersect in a common node (4N), the ideal angle is 109.5 degrees resulting in a tetrahedron. In nodes where more than 4 trabeculae intersect in a single node, the angular configuration and spatial appearance is more complex [26]. In vertebrate bone, it was shown that the calculated ITAs followed the *a priori* determined ideal angles [26].

Trabecular orientations

The trabecular orientation describes the direction of a trabecula within the plate, which provides direct information of how the trabeculae are distributed. The orientation of the trabeculae has been attributed to the structural functionality [10], where a uniformly distributed orientation enables the mesh-work to absorb multi-directional stress, where unbalanced distributions are indicative for directional stress regimes.

Theta orientation is the orientation of a trabecula perpendicular to the plate's surface (Fig. 2). This descriptor indicates the ability of the stereom to deal with downward loads. Phi orientation describes the orientation of a trabecula in the plate's horizontal plane. These descriptors indicates the direction of trabeculae within a plate. The loads are undirected within a plate when the phi orientation is approximately uniform, or the loads can be directional when the distribution of phi is unbalanced.

Material and methods

Material

Denuded skeletons of *Echinocyamus pusillus* were collected in summer 2010 around Giglio, Tuscany, Italy by SCUBA. From 1080 samples, one pristinely preserved skeleton [GPIT/EC/00740:gg-al-1.73] [30] was chosen for x-ray micro-computed tomography scanning. Samples are stored under repository GPIT/EC/00740 at the University of Tübingen, Germany.

Computed tomography

The x-ray micro-computed tomography (μCT) scan was performed using a Phoenix Nanotom 180nF (General Electric Company Corporation, Boston, MA, USA) with an isotropic voxel size of 3 μm. The specimen was fixated on the sample-tray using a wax-base with the sample aligned with its longitudinal axis parallel to the detector plane. The scan was conducted with the parameters: voltage = 80 kV, power = 180 μA, exposure time = 800 ms, projections = 2000. Prior to scanning, the sample was cleaned for 30 min in a Bandelin DT106 (Bandelin Electronic, Berlin, Germany) ultrasonic bath and was then air-dried. Data are accessible via the dryad online repository [30].

Computed tomography data processing

Data are rendered and analyzed using Avizo in version 9.4 (Thermo Fisher Scientific, Waltham, MA, USA). Two subvolumes with an edge length of 90 µm were extracted from five plates, one at the plate's center and one at the plate's margin. A de-noising filter was applied to the subvolumes enhancing the contrast between material (stereom) and the surrounding non-material matrix (air) (filter: delineate, interpretation = 3d, neighborhood = 26, size = 3 px). Subvolumes were binarized using the interactive thresholding algorithm (intensity range = 76-172). Areas that are not connected to the stereom were removed using the remove small spots (interpretation = 3d, size = 1000 px) function.

The subvolumes are skeletonized using the auto skeleton command (smooth = 0, attach to data = 0.5, number of iteration = 1000). Euclidean point coordinates that describe the segments (trabeculae) and nodes (intersection of trabeculae) of the stereom, as well as the trabecular mean radius and the tortuosity (curvature) of the segments were exported from Avizo using the spatial graph statistics function. The coordinates are analyzed in the R software environment in version 3.2.2 [31]. Duplicated segments and nodes, that where generated in Avizo during the automatized skeletonization process were identified and removed for the analyses.

Length and tortuosity

The trabecular length is measured for two parameters. The chord length l_c is described by a straight line between two nodes. The curved length l_t represents the true length of a segment. The tortuosity is the ratio between curved length and the chord length, defined by equation (4) and describes the extent of curvature of a segment.

$$\tau = \frac{l_t}{l_c} \qquad (4)$$

A tortuosity of $\tau = 1$ indicates that the chord length of a segment is of equal length to the curved length, $\tau > 1$ indicates that a trabecula is longer than the direct connection between nodes, and thus curved.

Radius and slenderness ratio

Trabecular radii are obtained from the Avizo spatial graphs statistics. The radius of a trabecula is defined as the mean value of all point radii that describe a segment. The node radius is respectively the radius of a single point in which trabeculae intersect. Segment and node radii are compared by a non-parametric Wilcoxon rank-sum test. Additionally, node radii and segment radii are compared between the plate's center and margin areas. Results are reported as the median ± median absolute deviation (mad). Results are discussed with respect to their mechanical effects. Wilcoxon rank sum tests were applied to sub-sampled data so that differences in sample size and large sample sizes do not bias the statistical test. Data are sub-sampled to N = 300 for each compared group, the statistical analyses ran for 10000 iterations. The mean p-value is reported for evaluation. The slenderness ratios are determined for both the center and margin regions of the plates and are compared to one another using a Wilcoxon rank sum test where data are sub-sampled to N = 300 per group and ran for 10000 iterations.

Inter-trabecular angle and node configuration

The inter-trabecular angle ITA [26, 32] is the angle between two intersecting segments in a common node. Angle calculation is performed in two-step process, where in a first step, the position vectors of a segment are used to describe the direction vector of a segment, and in a second step, the angle between two direction vectors segments is calculated using equation (5).

$$\mathrm{ITA} = cos\theta = \frac{\vec{a} \cdot \vec{b}}{||\vec{a}|| \cdot ||\vec{b}||} \quad (5)$$

$\vec{a}$ = direction vector of one of the intersecting segments, $\vec{b}$ = direction vector of the other intersecting segment. The obtained ITA are averaged (mean ± standard deviation) for each node and correlated to the number of segments per node. The number of segments that intersect in one node is calculated to determine the most abundant intersections-per-node combination. The number of intersections per node follow equation (6).

$$\sum_{i=1}^{n-1} n_i = \frac{n(n-1)}{2} \quad (6)$$

n = number of segments per node, i = index. ITA of the plate's center and the plate's margin are compared by a Wilcoxon rank sum test.

Trabeculae orientation

The segment orientation perpendicular to the plate's surface is described by the angle theta (θ), which is formed by the trabecula and the z-axis (Fig 2). Theta can range between 0 and 90 degrees, where θ = 0 degree is a trabecula perpendicular to the plate's surface and θ = 90 degree is a trabecula in x-y direction (horizontal to the plate's surface). The segment orientation in x-y plane is described by phi (φ), which lies in the plate's horizontal plane (Fig 2) and can revolve from 0 to 360 degrees around the z-axis. The angles theta and phi are obtained from Avizo using the spatial graph statistics function. Their distribution provides information about the load-transfer direction. The distribution of theta is analyzed for normality using Shapiro-Wilk test in R [31]. The skewness and kurtosis of the distributions is calculated by the moments-package [33] in R. The distribution of phi is analyzed for uniformity using a $\chi 2$ test. Visualization of the phi distribution is performed by rose diagrams using the spatstat package [34] in R. The trabecular orientation is compared between the plate's center and the plate's margin using a Wilcoxon rank sum test.

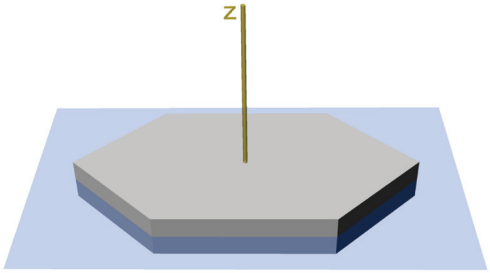

Figure 2. Definition of the theta and phi. Horizontal plane (blue) and the z-axis (yellow) of a plate model.

Rendering

Surface models of the stereom from the plate's center and the plate's margin are visualized in Avizo (options: compactify = unchecked, edge length = 0.2; settings: adjust coordinates = checked; smoothening: smoothening = constrained smoothening, smoothening extend = 1) with the surface parameters (draw style = transparent; more options = specular, fancy alpha, sorting, both faces, direct normal; base trans = 0 (for non-transparent stereom view) base trans = 0.6). Skeletonization results are visualized as tube networks, which include thickness parameters (node scale = constant, node scale factor = 1.24905, node coloring = constant, segment styles = tubes, segment coloring = thickness, segment colormap = physics, colormap range = -1.36986-3.9, tube scale factor = 0.152058).

Figure processing

Figure 2 and figure 7 were rendered in the 3d design software Rhinoceros 5 (McNeel, Seattle, WA, USA). Images were adjusted for brightness, contrast and color in Adobe Photoshop CC 2018 (Adobe Systems, San José, CA, USA). Final figure layout was processed in Adobe InDesign CC 2018 (Adobe Systems, San José, CA, USA).

Results

Length, tortuosity, radius and slenderness ratio

Plate center. — The chord length (shortest distance between nodes) is on average 16.43 ± 5.8 µm (N = 1419), the curved length (true length of a trabecula) 17.56 ± 6.1 µm (N = 1419) (Fig 3A-B, Table 1). A Wilcoxon rank-sum test of chord length and curved length shows that the two length parameters are statistically not different at a significance level of $\alpha = 5\%$ ($p = 0.131$, N = 600, iterations: 10000). The tortuosity of the segments is $\tau = 1.03 \pm 0.0$ (N = 1419) and is close to $\tau = 1$. The segments show an average radius of 2.33 ± 1.2 µm (N = 1418), nodes show an average radius of 1.50 ± 0.0 µm (N = 712), (Table 1).

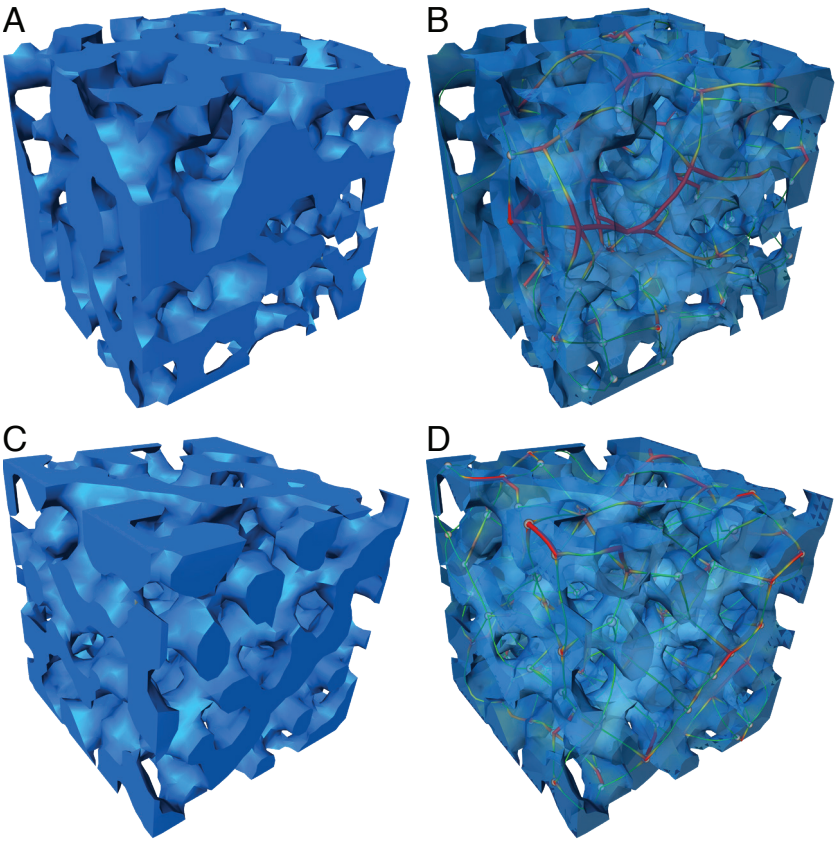

Figure 3. Rendering of the stereom of *Echinocyamus pusillus*. Trabeculae are tracked and color coded. (A) Trabecular system at the plate's center. (B) Trabeculae tracked (C) Trabeculae at the plate's margin, and (D) trabeculae tracked. Red = sturdy trabecula, green = slender trabecula.

Table 1. Trabecular measurements and orientation in plates of *Echinocyamus pusillus*.

		median	mad	min	max	N
center	segment chord length	16.43	5.80	0.0	42.1	1418
	segment curved length	17.55	6.13	6.0	51.3	1418
	segment tortuosity	1.03	0.03	1.0	3.0	1415
	segment radius	2.33	1.21	1.5	7.6	1418
	slenderness ratio	7.62	4.22	1.4	26.0	1418
	node radius	1.50	0.00	1.5	9.0	711
	orientation theta	59.09	22.82	0.0	90.0	1418
	orientation phi	180.00	133.51	0.0	360.0	1418
margin	segment chord length	16.43	5.48	0.0	34.2	1559
	segment curved length	17.43	5.39	6.0	49.6	1559
	segment tortuosity	1.03	0.03	1.0	2.4	1559
	segment radius	2.22	0.79	1.5	5.3	1559
	slenderness ratio	8.07	3.88	1.4	26.3	1559
	node radius	1.50	0.00	1.5	5.0	775
	orientation theta	59.67	27.14	0.0	90.0	1559
	orientation phi	180.10	133.62	0.0	360.0	1559

A Wilcoxon rank-sum test indicates that segment are on average thicker than the nodes based on a significance level of $\alpha = 5\%$ ($p < 0.001$, $N = 600$, iterations: 10000). The average slenderness ratio is 7.62 ± 4.2 ($N = 1418$).

Plate margin. — The chord length (shortest distance between nodes) is on average 16.43 ± 5.5 µm ($N = 1560$), the curved length (true length of a trabecula) 17.43 ± 5.4 µm ($N = 1560$) (Fig 3B-C, Table 1). A Wilcoxon rank-sum test of chord length and curved length shows that the two length parameters are statistically not different at a significance level of $\alpha = 5\%$ ($p = 0.150$, $N = 600$, iterations: 10000). The resulting tortuosity of the segments is $\tau = 1.03 \pm 0.0$ ($N = 1560$) and is close to $\tau = 1$. The segments show an average radius of 1.50 ± 0.0 µm ($N = 6543$), nodes show an average radius of 1.50 ± 0.0 µm ($N = 775$). A Wilcoxon rank-sum test indicates that segment are on average thicker than the nodes based on a significance level of $\alpha = 5\%$ ($p < 0.001$, $N = 600$, iterations: 10000). The average slenderness ratio is 8.07 ± 3.9 ($N = 1559$).

Comparison of the plate's center and margin. — The statistical analysis indicates that segments from both the plate's center and the plate's margin are similar in their curved length

(p = 0.403, N=600, iterations: 10000). The segment radii are similar between the two plate regions based on an significance level of α = 5% (p = 0.054, N = 600, iterations: 10000). The tortuosity of both plate regions are statistically not different (p = 0.287, N = 600, iterations: 10000). The radii of the two plate areas are statistically not different from one another (p = 0.375, N = 600, iterations: 10000). The slenderness ratios of the plate's center and the plate's margin are statistically not different (p = 0.307, N = 600, iterations: 10000).

Inter-trabecular angle (ITA) and node configuration

Plate center. — The analysis of the plates' centers (Fig 3A-B) involved 1419 segments, which intersected in 538 nodes. In 1.3 % of the 538 nodes, two segments intersected in one common node (Table 2), in 66.4%, three segments intersected in one common node, in 21.4%, four segments intersected in one node, in 6.5% five segments intersected in one node, in 3.9% six segments intersected in one node, and in 0.6% seven or more segments intersected in one node. The average inter-trabecular angle is ITA = 104.35 ± 13.1° (N = 538) with a mode of 120° (Fig 4A). The majority of intersection nodes involve three segments. In the cases where three segments share one common node, the ITA is 105.76 ± 13.4° (N = 357) with a mode of 120° (Fig 4B). In the cases where more than three segments intersect in one common node, the ITA decreases compared to 2N – 4N (Table 2).

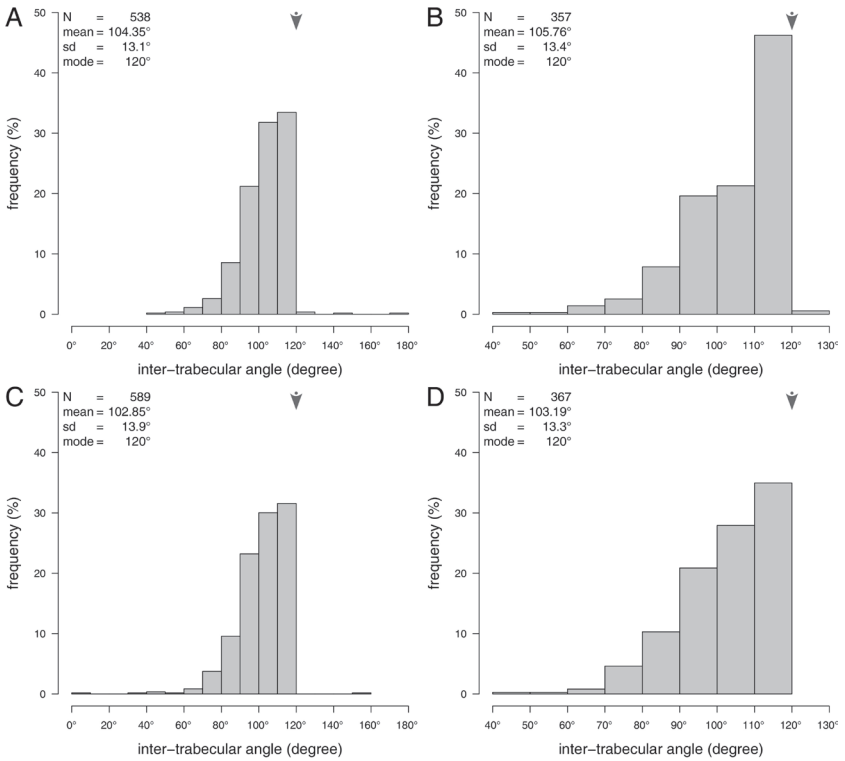

Figure 4. Histograms of the inter-trabecular angles. (A) All inter-trabecular angles of the plate centers. (B) Inter trabecular angles of the plate centers, where 3 segments intersect in a single common node. (C) All inter-trabecular angles of the plate margins. (D) Inter-trabecular angles of the plate margins, where 3 segments intersect in a common node. N = sample size, med. = median, mad. = median absolute deviation, mode is indicated by arrows.

Table 2. Inter-trabecular angles and node-configuration. ITA = inter-trabecular angle, N = sample size, deg = degree, sd = standard deviation.

	ITA	total	2N	3N	4N	5N	6N	7N	8N	9N
center	N	538	7	357	115	35	21	2	n/a	1
	fraction (%)	100.00	1.30	66.40	21.38	6.51	3.90	0.37	n/a	0.19
	mean (deg)	104.35	117.19	105.76	102.40	99.68	95.88	95.27	n/a	99.68
	sd (deg)	13.1	30.2	13.4	10.2	10.7	9.6	4.7	n/a	n/a
	mode (deg)	120.00	146.87	120.00	98.91	94.96	85.03	91.96	n/a	n/a
margin	N	589	5	369	149	38	20	4	1	n/a
	fraction (%)	100.00	0.93	68.59	27.70	7.06	3.72	0.74	0.19	n/a
	mean (deg)	102.85	117.04	103.19	102.19	102.89	99.38	92.91	113.76	n/a
	sd (deg)	13.9	20.1	13.3	15.2	12.4	15.3	5.7	n/a	n/a
	mode (deg)	120.00	150.17	120.00	100.12	99.78	100.11	100.53	n/a	n/a

Plate margin. — The analysis of the plates' margins (Fig 3B-C) involved 1559 segments, these segments intersected in 589 intersection nodes. In 0.9% of the 589 nodes, two segments intersected in one common node, in 68.6%, three segments intersected in one node, in 27.7%, four segments intersected in one node, in 7.0% five segments intersected in one node, in 3.7% six segments intersected in one node, and in 0.9% seven or more segments intersected in one node (Table 2). The average inter-trabecular angle is ITA = 102.85 ± 13.9° (N = 589) with a mode of 120° (Fig 4C). The majority of intersection nodes involve three segments. In the cases where three segments share one common node, the ITA is 103.19 ± 13.3° (N = 369) with a mode of 120° (Fig 4D). In the cases where more than three segments intersect in one common node, the ITA decreases compared to 2N – 4N (Table 2).

Comparison of the plate's center and margin. — The inter-trabecular angles of the plate's center and those of the plates margin are statistically not different as shown by the Wilcoxon rank sum comparison (p = 0.313, N = 600, iterations: 10000). The inter-trabecular angles between segments, where three segments intersect in one common node are likewise statistically not different (p = 0.060, N = 600, iterations: 10000).

Trabecular theta orientation

Plate center. — The angle theta between the segments and the z-axis (axis perpendicular to the plate's surface) is on average θ = 59.09 ± 22.8° (N = 1418, Fig 5A). A Shapiro-Wilk test for normality reveals that the distribution of theta is statistically different from a Gaussian distribution at a significance level of α = 5% (W = 0.972, p < 0.001, N = 1418). The distribution of theta is left skewed and flattened compared to a Gaussian distribution (skewness = -0.369, kurtosis = 2.480, N = 1419) (Fig 5A).

Plate margin. — The angle theta between the segments and the z-axis (axis perpendicular to the plate's surface) is on average θ = 59.67 ± 27.1° (N = 1560, Fig 5B). A Shapiro-Wilk test for normality reveals that the distribution of theta is statistically different from a Gaussian distribution at a significance level of α = 5% (W = 0.954, p < 0.001, N = 1560). (Fig 5B). The distribution of theta is left skewed and flattened compared to a Gaussian distribution (skewness = -0.351, kurtosis = 2.105, N = 1560).

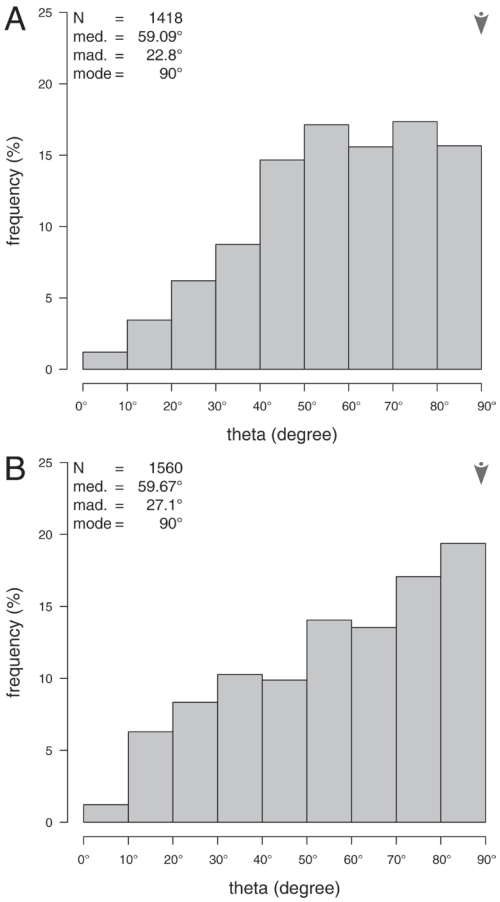

Figure 5. Histograms of the trabecular orientation compared to the plate's horizontal plane. (A) Trabecular distribution at the plate's center. (B) Trabecular distribution at the plate's margin. N = sample size, med. = median, mad. = median absolute deviation, mode is indicated by arrows.

Comparison of the plate's center and margin. — The trabecular orientation in relation to the z-axis (axis perpendicular to the plate's horizontal plane) is similar at the plate's center and the plate's margin (p = 0.502, N = 600, iterations: 10000).

Trabecular phi orientation

Plate center. — The trabecular orientation within the plate's horizontal plane does not follow a uniform distribution ($\chi2(36) = 152.91$, $p < 0.001$, $N = 1418$). The respective rose diagram indicates that trabeculae are directional orientated within the plate's horizontal plane (Fig 6).

Plate margin. — The trabecular orientation within the plate's horizontal plane does not follow an uniform distribution ($\chi2(36) = 303.13$, $p < 0.001$, $N = 1559$). The respective rose diagram indicates that trabeculae are directional orientated within the plate's horizontal plane (Fig 6).

Comparison of the center and margin. — The trabecular orientation within the plate's horizontal plane is similar in both plate areas ($p = 0.478$, $N = 600$, iterations: 10000).

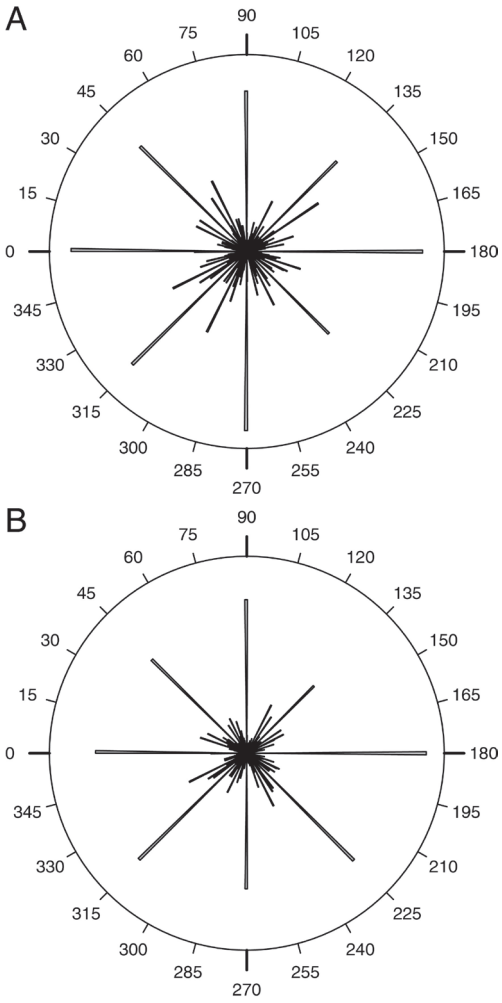

Figure 6. Rose diagrams of the trabecular orientation within the plate's horizontal plane. (A) Phi distribution at the plate's center. (B) Phi distribution at the plate's margin. Both diagrams indicate that trabeculae are directional aligned within the plate's horizontal plane.

Discussion

Length and radius

The trabeculae follow a direct course between two nodes, demonstrated by tortuosity values close to $\tau = 1$. The chord length and curved length are additionally statistically not different in and between both the plate's center and margin (Table 1). The trabecular length at the plate's center and at the plate's margin, as well as the average segment radius are similar. The slenderness ratios of the two plate regions also indicate that the critical Euler buckling force and thus the ability of absorbing energy is comparable. Both plate areas can thus resist similar magnitudes of loads. This result is not surprising, as loads occur along the entire skeleton and are not restricted to specific areas.

Inter-trabecular angle (ITA) and node configuration

Reznikov et al. [26] demonstrated that the ideal ITA of a 3N configuration is 120°, as this angular motif spans the longest space. This 3N and 120° motif results in a planar and triangular geometric element [26]. In nodes where four segments share a common node (4N), the geometric motive is tetrahedral with a maximum segment offset of 109.5° [26]. Results show that the planar 120° triangular motifs account for around two thirds of the node configuration. In terms of its structural performance, the planar triangular geometry can be used to counter multi-dimensional loadings when arranged in an angular off-set (Fig 7).

The inter-trabecular angles of the plate's center and the plate's margin are similar, with the overall ITA slightly lower than the ITA for three segments per node (3N). Although the average ITA at the plate's center is 105.76° and 103.19° at the plate's margin, the majority of ITA are in both regions at 120° (Fig 4B, D) indicating that the triangular and planar geometrical configuration is a preferred trabecular arrangement, which can be interpreted to be advantageous for multi-directional stress handling. In the 3N configuration, more 120° angles are present on the plate's center than in the plate's margin (Fig 4B, D) indicating that the center is more likely adapted to multi-directional stress. This result can be explained by the load-distribution in the echinoid skeleton [16], where loads applied to a plate are distributed via the galleried stereom to adjoining plates.

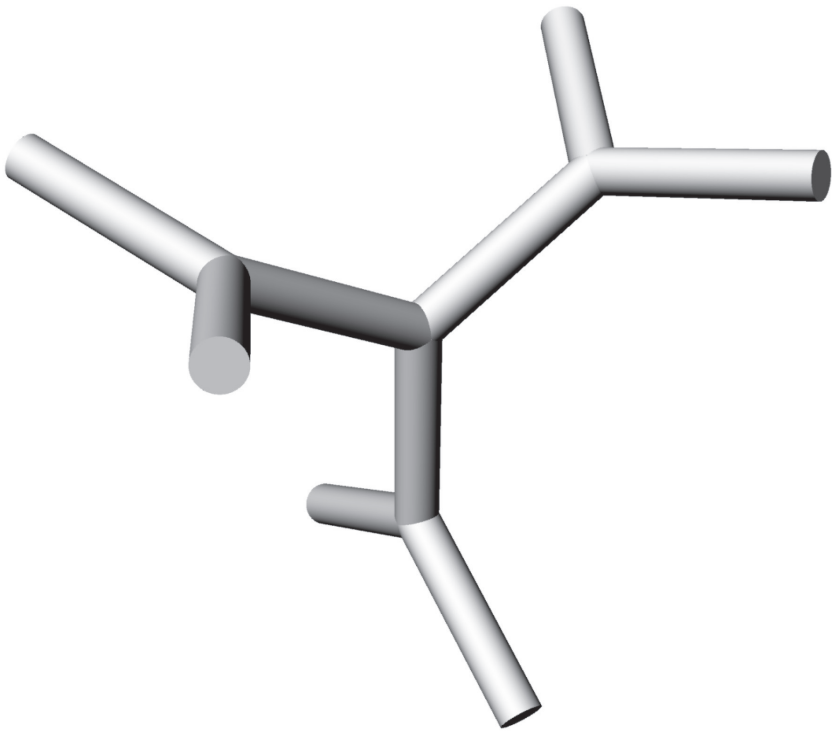

Figure 7. Lattice-system built-up from multiple 3N members. All inter-trabecular angles possess an offset of 120 degrees to one another.

Trabecular theta orientation

Trabeculae of both the plate's center and the plate's margin show a similar distribution pattern of theta, which ranges between 0 and 90 degrees with the z-axis (Fig 2). In both plate areas, the mean angle formed by the trabeculae and the z-axis is around 60 degrees with a mode of 90 degrees (Fig 5). The distribution indicates that trabeculae are orientated in all spatial directions, capable to meet multi-directional stress [3, 26]. The most frequent theta for both the plate's center and the plate's margin is found at 90 degrees, which is parallel to the plates surface. The distribution of theta in the plate's margin is slightly more left skewed than the distribution of theta in the plate's center, which indicates a slightly, yet statistically insignificant higher frequency of 90 degree trabeculae (Fig 5). The orientation of the trabeculae within the plate is in contrast to general descriptions of trabecular orientations within echinoid plates, where the center is usually described as unordered labyrinthic stereom, whereas the marginal areas consist of the highly ordered galleried stereom [3].

The differentiation between labyrinthic and galleried stereom has been discussed with respect to their function: the labyrinthic stereom with its unordered trabeculae is considered to absorb loads from multiple directions, whereas the ordered galleried stereom can distribute loads from its point of origin along the echinoid's skeleton [3, 10]. Micro-CT sections [35] also indicate that there is a visual separation between the center and the margin of a plate in *Echinocyamus pusillus*. The spatial architecture in both areas is interpreted to be based on two parameters: first, trabeculae at the plate's center are assumed to counter loads from multiple directions. These loads need to be deflected from vertical loads to horizontal loads in order to be distributed by the marginal areas to other plates. Second, loads are applied to the entire surface of the echinoid, including both the plate's center and the plate's margin. Therefore, the margins also have to counter loads from above. Although the main direction of the primary trabeculae at the plate's margins show a distinctive direction, other trabeculae vary in orientation to counter loads from multiple directions respectively to the plate's center. The trabecular system in *Echinocyamus pusillus* can thus be considered to be a multi-directional load bearing system, which is capable to counter stress over the entire plate area.

Trabecular phi orientation

The trabecular orientation within the plate's horizontal plane in both the plate's center and the plate's margin are highly directed indicated by the angular distribution (Fig 6) and supported by statistical tests. The directional alignment of the trabecular system is indicative for a directional load transfer system. Applied loads are here interpreted to imping on the echinoid's shell surface, where the loads can be retained by the trabeculae in theta direction. The loads are then transferred into lateral thrust [36]. The directional trabeculae in phi direction can distribute this stresses laterally onto neighboring plates. The resulting stress is thereby dispensed which leads to a lower chance of structural failure.

Conclusions

The echinoid's trabecular system is characterized by the eight descriptors of (1) trabecular length, (2) trabecular tortuosity, (3) trabecular radius, (4) trabecular slenderness ratio, (5) inter-trabecular angle, (6) node configuration, (7) theta orientation, and (8) phi orientation. Single trabeculae are short, stocky and possess very little tortuosity. The minor slenderness ratio in echinoids indicate that their trabecular system is able to resist high loads before the critical Euler buckling is reached. The majority of trabecular intersections follow the 3N configuration, where three trabeculae intersect in one common node. The most abundant ITA is thereby at 120°. The resulting triangular and planar geometry can, when combined, form a three-dimensional meshwork able to counter multi-dimensional stress. The trabecular orientation in z-direction indicates that the plate is capable of handling loads along the entire surface. The trabecular orientation within the plate's horizontal plane is directional, enabling the plate to distribute loads to neighboring plates.

Acknowledgments

We thank Raouf Jemmali for computer tomographic scanning.

References

[1]Durham JW. Clypeasteroids. In: Moore RC, editor. Treatise on invertebrate paleontology. Lawrence: University of Kansas Press; 1966. pp. 450–491.

[2]Nebelsick JH, Dynowski JF, Grossmann JN, Tötzke C. Echinoderms: hierarchically organized light weight skeletons. In: Hamm C, editor. Evolution of lightweight structures: analyses and technical applications, biologically-inspired systems, Vol. 6. Cham: Springer; 2015. pp. 141–156. doi: 10.1007/978-94-017-9398-8_8

[3]Smith A. Stereom microstructure of the echinoid test. Spec Pap Palaeontol. 1980; 25: 1–81.

[4]Grossmann N, Nebelsick JH. Stereom differentiation in spines of Plococidaris verticillata, Heterocentrotus mammillatus and other regular sea urchins. In: Johnson CR, editor. Echinoderms in a changing world: proceedings of the 13th International Echinoderm Conference. Boca Raton: CRC Press; 2013. pp. 97–104.

[5]Grossmann JN, Nebelsick JH. Comparative morphology and structural analysis of selected cidaroid and camarodont sea urchin spines. Zoomorphology; 2013; 132: 301–315.

[6]Lauer C, Grun TB, Zutterkirch I, Jemmali R, Nebelsick JH, Nickel KG. Morphology and porosity of the spines of the sea urchin Heterocentrotus mamillatus and their implications on the mechanical performance. Zoomorphology. 2017; 137: 139–154. doi: 10.1007/s00435-017-0385-4

[7]Presser V, Gerlach K, Vohrer A, Nickel KG, Dreher WF. Determination of the elastic modulus of high porous samples by nanoindentation: a case study on sea urchin spines. J Mater Sci. 2010; 45: 2408–2418. doi: 10.1007/s10853-010-4208-y

[8]Tsafnat N, Fitz Gerald JD, Le HN, Stachurski ZH. Micromechanics of sea urchin spines. PLoS One. 2012; 7: e44140. doi: 10.1371/journal.pone.0044140

[9]Smith A. Biomineralization in echinoderms. In: Carter JG, editor. Skeletal biomineralization: patterns, processes and evolutionary trends. New York: Van Nostrand Reinhold; 1990. pp. 413–443.

[10]Lawrence J. A functional biology of echinoderms. Baltimore: John Hopkins University Press; 1987. doi: 10.1002/iroh.19890740316

[11]Donovan SK. The taphonomy of echinoderms: calcareous multi-element skeletons in the marine environment. In: Donovan SK, editor. The process of fossilization: London: Belhaven Press; 1991. pp. 241–269.

[12]Telford M. Domes, arches and urchins: the skeletal architecture of echinoids (Echinodermata). Zoomorphology. 1985; 105: 114–124. doi: 10.1007/BF00312146

[13]Telford M. Structural analysis of the test of *Echinocyamus pusillus* (O. F. Müller). In: Keegan BF, O'Connor BDS, editors. Echinodermata: proceedings of the fifth International Echinoderm Conference. Rotterdam: Balkema; 1995. pp. 353–360.

[14]Grun TB, Koohi L, Schwinn T, Sonntag D, von Scheven M, Bischoff M, et al. The skeleton of the sand dollar as a biological role model for segmented shells in building construction: a research review. In: Knippers J, Nickel KG, Speck T, editors. Biologically-inspired design and integrative structures: analysis, simulation and implementation in architecture. Cham: Springer: 2016. pp. 217-242. doi: 10.1007/978-3-319-46374-2_11

[15]Grun TB, Mancosu A, Belaústegui Z, Nebelsick JH. The taphonomy of Clypeaster: a paleontological tool to identify stable structures in natural shell systems. Neues Jahrb Geol Palaont Abh. 2018; 288: 000-000 in press. http://doi.org/10.1127/njgpa/2018/0737

[16]Grun TB, Nebelsick JH. Structural design of the minute clypeasteroid echinoid *Echinocyamus pusillus*. R Soc Open Sci. 2018; 000: 000–000 in press.

[17]Nebelsick JH, Kowalewski M. Drilling predation on recent clypeasteroid echinoids from the Red Sea. Palaios. 1999; 14: 127–144. doi: 10.2307/3515369

[18]Grun T, Sievers D, Nebelsick JH. Drilling predation on the clypeasteroid echinoid *Echinocyamus pusillus* from the Mediterranean Sea (Giglio, Italy). Hist Biol. 2014; 26: 745–757. doi: 10.1080/08912963.2013.841683

[19]Grun TB. Recognizing traces of snail predation on the Caribbean sand dollar Leodia sexiesperforata. Palaios. 2017; 32: 448–461. doi: 10.2110/palo.2017.001

[20]Belaústegui Z, Nebelsick JH, Gibert de JM, Domènech R and Martinell J. A taphonomic approach to the genetic interpretation of clypeasteroid accumulations from Tarragona (Miocene, NE Spain). Lethaia. 2012; 45: 548–565. doi: 10.1111/j.1502-3931.2012.00314.x

[21]Belaústegui Z, Gibert de JM, Nebelsick JH, Domènech R and Martinell J. Clypeasteroid echinoid tests as benthic islands for gastrochaenid bivalve colonization: evidence from the middle Miocene of Tarragona (North–East Spain). Palaeontology. 2012; 56: 783–796. doi: 10.1111/pala.12015

[22]Mancosu A, Nebelsick JH. Multiple routes to mass accumulations of clypeasteroid echinoids: a comparative analysis of Miocene echinoid beds of Sardinia. Palaeogeogr, Palaeoclimatol, Palaeoecol. 2013; 374: 173–186. doi: 10.1016/j.palaeo.2013.01.015

[23]Mancosu A, Nebelsick JH. The origin and paleoecology of clypeasteroid assemblages from different shelf setting of the Miocene of Sardinia, Italy. Palaios. 2015; 30: 273–387. doi: 10.2110/palo.2014.087

[24]Mancosu A, Nebelsick JH. Ecomorphological and taphonomic gradients in clypeasteroid-dominated echinoid assemblages along a mixed siliciclastic-carbonate shelf from the early Miocene of northern Sardinia, Italy. Acta Palaeontol Pol. 2017; 62: 627–646. doi: 10.4202/app.00357.2017

[25]Seilacher A. Constructional morphology of sand dollars. Paleobiology. 1979; 5: 191– 221. doi: 10.1017/S0094837300006527

[26]Reznikov N, Chase H, Ben-Zvi Y, Tarle V, Singer M, Brumfeld V, et al. Inter-trabecular angle: a parameter of trabecular bone architecture in the human proximal femur that reveals underlying topological motifs. Acta Biomater. 2016; 44: 65–72. doi: 10.1016/j.actbio.2016.08.040

[27]Wainwright SA, Biggs WD, Currey JD, Gosline JM. Mechanical design in organisms. London: Edward Arnold; 1973.

[28]Mann W. Vorlesung über Statik und Festigkeitslehre: Einführung in die Tragwerkslehre. Stuttgart: BG Teubner; 1986.

[29]Gross D, Hauger W, Schröder J, Wall AW. Technische Mechanik 2: Elastostatik. Berlin: Springer; 2007.

[30]T.B. Grun, J.H. Nebelsick. Data from: Micro-morphological and structural design analysis of the minute clypeasteroid echinoid *Echinocyamus pusillus*. Dryad Digital Repository, 2018. doi: 10.5061/dryad.rg54h.

[31]R Core Team. R: a language and environment for statistical computing. Vienna, Austria, R Foundation for Statistical Computing, 2017. www.r-project.org

[32]Ben-Zvi Y, Reznikov N, Shahar R, Weiner S. 3D architecture of trabecular bone in the pig mandible and femur: inter-trabecular angle distribution. Front Mat Sci. 2017; 4: 1–15. doi: 10.3389/fmats.2017.00029

[33]Komsta L, Novomestky F. Moments: moments, cumulants, skewness, kurtosis and related tests. R package version 0.14., 2015. www.cran.r-project.org/package=moments.

[34]Baddeley A, Rubak E, Turner F. Spatial point patterns: methodology and applications with R. London: Chapman and Hall CRC Press; 2015.

[35]Grun TB, von Scheven M, Bischoff M, Nebelsick JH. Structural design of the minute clypeasteroid echinoid *Echinocyamus pusillus*. J R Soc Interface. under review.

[36]Gordon JE. Structures: or why things don't fall down. New York: Da Capo Press; 1978.

Appendix III:

Further Manuscripts

Further Manuscript 1

Morphology and porosity of the spines of the sea urchin *Heterocentrotus mamillatus* and their implications on the mechanical performance

Zoomorphology
DOI 10.1007/s00435-017-0385-4

ORIGINAL PAPER

Morphology and porosity of the spines of the sea urchin *Heterocentrotus mamillatus* and their implications on the mechanical performance

Christoph Lauer[1] · Tobias B. Grun[2] · Isabel Zutterkirch[1] · Raouf Jemmali[3] · James H. Nebelsick[2] · Klaus G. Nickel[1]

Received: 22 July 2017 / Revised: 16 October 2017 / Accepted: 19 October 2017

Abstract Spines of the slate pencil sea urchin *Heterocentrotus mamillatus* Linnaeus, 1758, are in focus of biomimetic research as they feature a "graceful" failure behaviour under uniaxial compression dissipating energy and resisting high loads even after high strain. This study elucidates and quantifies the organization of calcitic trabeculae and pores in large primary spines of the slate pencil urchin *H. mamillatus* by image analysis from scanning electron microscopy, X-ray micro-computed tomography (µCT) and gravimetry. This study delivers a detailed distribution of porosities within the whole spine and shows that parts of the spines have a much higher porosity then hitherto thought. The central part (medulla) of the high-magnesium calcitic stereom of *H. mamillatus* spines has a porosity range of 75% to nearly 90%. From this innermost structure, more than 200 radially aligned, but often sinuous trabeculae extend to the spine rim. The structure of this complicated meshwork (radiating layer) is best seen in basal cross sections and was confirmed by µCT scans. The radiating layer has a porosity range from 40–70% and is irregularly separated by the dense growth layers (15–35% porosity). Growth layers were classified in proximal and distal growth layers with numbers ranging within a single animal between 3–14 and 2–7, respectively. These growth layers are characteristic for *H. mamillatus* spines and play a major role in their remarkable mechanical properties. The porosity of the spine increases from base to tip. Biological and mechanical implications of the variations are discussed.

Keywords Morphology · Echinoids · Sea urchin spines · Porosity · µCT scans

✉ Christoph Lauer
christoph.lauer@uni-tuebingen.de

[1] Division of Applied Mineralogy, Department of Geosciences, University of Tübingen, Wilhelmstraße 56, 72074 Tübingen, Germany

[2] Division of Invertebrate Paleontology and Paleoclimatology, Department of Geosciences, University of Tübingen, Hölderlinstraße 12, 72074 Tübingen, Germany

[3] German Aerospace Institute (DLR), Institute for Structure and Design, Pfaffenwaldring 38, 70569 Stuttgart, Germany

Introduction

Sea urchin spines consist of magnesium calcite ($(Mg_{(1-x)}Ca_x)CO_3$) (Clarke and Wheeler 1915; Weber 1969a) forming a lattice-like 3d meshwork, called stereom (e.g. Smith 1980). Spines of sea urchins show a wide variety of shapes with respect to size, internal morphology and surface sculpturing (e.g. Durham 1955; Kroh and Smith 2010). Hesse (1900) distinguished six spine types by the architecture of the radial septa and showed that the different spine types can be common in a specific echinoid group, though are not necessarily restricted to these groups. Spines of various taxa have been investigated focusing on the microstructure and functional morphology alike (Nichols 1962; Dotan and Fishelson 1985; Lawrence 1987; Moureaux et al. 2010; Tsafnat et al. 2012; Grossmann and Nebelsick 2013a, b; Nebelsick et al. 2015). The various forms of the spines have been correlated to environmental interactions such as predator defence, sediment penetration or feeding (e.g. Telford 1982; Mooi 1986; Lawrence 1987). The lightweight architecture of the stereom reflects an economic way of constructing skeletons which has been discussed as an important factor for the evolutionary success of the echinoderms in general (e.g. Emson 1985;

Published online: 04 November 2017

Simkiss and Wilbur 1989). Smith (1980) distinguished ten stereom types within the echinoids and described their occurrence in the skeleton along with functional interpretations.

More recently, the spines of *H. mamillatus* have come into the focus of biomimetic research as they exhibit an outstanding crushing behaviour under uniaxial compression recognized as "graceful" failure (Presser et al. 2009a, b; Klang et al. 2016; Toader et al. 2017). The failure is based on a brittle foam type behaviour, which allows a layer-by-layer breakdown and the porosity changes within the stereom where cracks become deflected at the densest parts (growth layers) resulting in a successive crushing. Due to this construction, the spine can resist high loads even after a considerable strain (> 0.2) and a "graceful" failure has been observed (Presser et al. 2009a; Klang et al. 2016).

It should be emphasized, that in this context, strength is always structural strength caused by structural behaviour. Strength in brittle materials is never a material property as such. The strength of the building material calcite depends on its orientation towards stress, the distribution of inner defects and therefore, the stressed volume (e.g. Danzer et al. 2007; Danzer 2014). The structural features making the construction of a spine a strong component are exactly those, which can potentially improve constructions in civil engineering with respect to exceptional high impacts (Weber et al. 1969; Presser et al. 2011; Klang et al. 2016; Toader et al. 2017).

Morphology

The *H. mamillatus* spines belong to the thickest, largest and heaviest among sea urchins. The primary spines of this species vary in shape and size from the oral side, where they are flat and blade-shaped and comparatively small, to the aboral side, where they are large and almost round in cross section (Dotan and Fishelson 1985). The large and robust aboral spines (Fig. 1) can protect the echinoid against predators and serve as mechanical fixation structure in reef cavities and fissures where the nocturnal *H. mamillatus* is found during the day (Grossmann and Nebelsick 2013b). Besides the large primary spines, the test is also covered by blunt secondary spines (Deutler 1926; Dotan and Fishelson 1985), which are only a few millimetres in length.

In sections, the most prominent features of the primary spines of *H. mamillatus* are the conspicuously brownish-red coloured growth layers (Fig. 1a). They resemble smaller versions of the spine and separate growth cycles from one other with the oldest part of the spine in the centre (e.g. Weber 1969b; Dotan 1990). The colouration is caused by naphthaquinones (Vevers 1966), embedded in the fairly thin (usually < 50 µm) structure. The structures termed as growth layers have been synonymously named "growth rings" (Grossmann and Nebelsick 2013b), "growth bands" (Weber 1969b) or "growth lines" (Ebert 1986, 1988). In the present paper, the term "growth layer" is preferred in order to reflect the three-dimensional character of this structural entity.

On the microscale, the growth layers are composed of a relatively dense microperforate stereom (Fig. 1b, c) (Grossmann and Nebelsick 2013b) following Smith's classification (1980). A single growth layer is composed out of numerous radial septa giving the growth layers a radiating appearance (Hesse 1900). The radial septa are separated by channels, seen as large pores in cross sections (Fig. 1c). Growth layers belong to the densest parts of the spine (Presser et al. 2010). As the spine surface is equivalent to the youngest growth layer of the spine, the radial septa give the spine a corrugated surface seen as ribs in SEM micrographs (Fig. 1d) (e.g. Hasenpusch 2000; Grossmann and Nebelsick 2013a). Furthermore, the surface is covered by an epithelium.

Besides the conspicuous growth layers, the spine's architecture consists of the central medulla (Fig. 1a) with a laminar stereom type (Grossmann and Nebelsick 2013b). The stereom in between the medulla and the growth layers, the radiating layer, was reported to consist of labyrinthic stereom (Grossmann and Nebelsick 2013b). The seemingly random stereom distribution in the radiating layer was already noted by Hesse (1900). He described the radiating nature of *H. mamillatus* spines being restricted to the growth layers only and is lost in foam-like meshwork in between. In contrast, spines of other species exhibit a radiating microstructure resembling wedges (Kroh and Nebelsick 2010) with the number and shape of radiating units even being used as a species diagnostic feature (e.g. Coppard and Campbell 2004). The present study investigates the stereom distribution in *H. mamillatus* spines in detail adding to the description of Hesse (1900) and Grossmann and Nebelsick (2013b). The occurrence, shape and distribution of growth layers is discussed also with respect to mechanical performance of the spines as investigated by Presser et al. (2009a).

Porosity

Porosity is one of the most important factors influencing mechanical properties of porous materials, such as sea urchin spines, where the elastic properties as for example the Young's modulus are directly dependent on porosity (e.g. Coble and Kingery 1956; Gibson and Ashby 1982; Lu et al. 1999; Pabst et al. 2006; Ji et al. 2006). Despite being mechanically tested extensively (Su et al. 2000; Presser

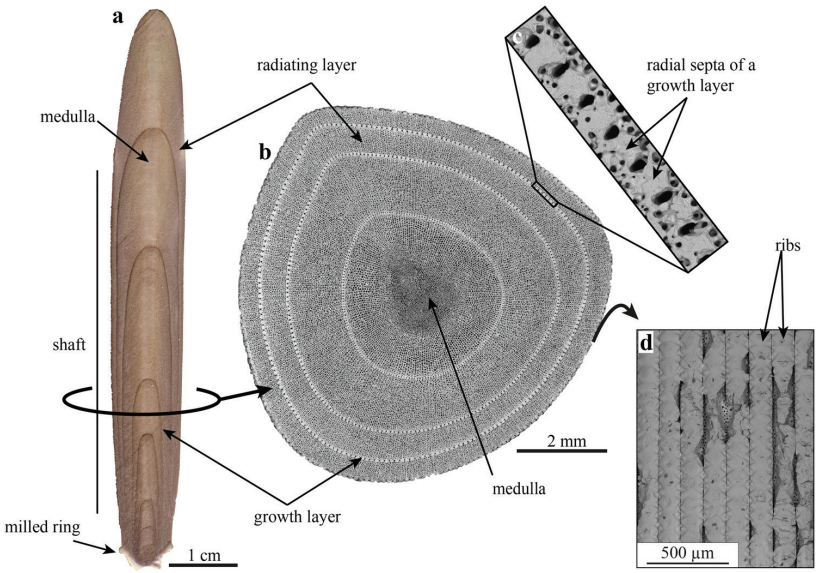

Fig. 1 Morphology and terminology of spines of *H. mamillatus*. In longitudinal sections (**a**) the growth layers are highlighted by their brownish-red colour. In SEM pictures of cross sections, the three different stereom types (medulla, radiating layer and growth layers) are best seen (**b**). Growth layers are composed out of numerous radial septa (**c**) that are ribs (**d**) giving the spine a corrugated surface. The surface of the spine is usually equivalent with the youngest growth layer

et al. 2009a; Grossmann and Nebelsick 2013a; Klang et al. 2016; Schmier et al. 2016), the porosity of sea urchin spines in general, and of *H. mamillatus* in particular, has not attracted much attention to date. Most studies state that the stereom structure is highly porous, without providing exact measures of the porosity (Burkhardt et al. 1983; Su et al. 2000; Presser et al. 2009a; Tsafnat et al. 2012; Grossmann and Nebelsick 2013b). Presser et al. (2010) determined porosity highly locally around nanoindentations in the stereom structure of *H. mamillatus* and reported values of 16 ± 1.9–19 ± 2.4% for the growth layers, 38 ± 3.8% for the radiating layer and 61 ± 4.8% for the medulla. The present study aims to provide a more global porosity distribution across the spine length and from the interior to the exterior of the spine. Implications for mechanical properties are discussed with respect to biological implications and mechanical tests performed by Presser et al. (2009a), Grossmann and Nebelsick (2013b) and Schmier et al. (2016). The data presented in these studies are characterized by a considerable scatter that is usually referred to "biological heterogeneity".

Materials and methods

Material

Eight adult individuals of *H. mamillatus* (HMf1-HMf8) were obtained from a material supplier (Mineralien- und Fossilienhandlung Peter Gensel, Weimar, Germany). In addition, an assortment of disarticulated *H. mamillatus* primary spines was obtained (Fischhaus Zepkow, Zepkow, Germany).

Methods

Growth layers and primary spine morphology

The specimen with the largest spines (HMf1) was selected for studying the shape and variation of growth layers within the spines. All primary spines larger than 15 mm (n = 69) were removed and sectioned longitudinally along the *z*-axis (crystallographic *c*-axis) with a Buehler med 1000 diamond saw (blade thickness: 500 µm). To assure that all growth layers were encountered, the section was not cut exactly along the middle of the spine, as the smallest layers can be somewhat off-centred after growth of the following layers. The spines were subsequently ground using carborundum abrasive paper with a grain size of 10 µm to the point where the growth layers close to the base were best visible. Spines smaller than 3 cm were polished only, as they were too thin for sectioning. Despite this careful procedure, not all growth layers at the base were exposed in some spines, thus their numbers are reported as "minimum values".

Spines were scanned by an Epson V370 high-resolution scanner to a resolution of 1200 dpi. Growth layers were then identified and counted from the scanned images. The growth layers were statistically analysed for a potential relationship between different growth layer types using a major axis regression in R (R Core Team 2016) with the

smatr extension (Warton et al. 2012). The length and mass variation along the oral spines and aboral spines was analysed by non-parametric Kruskal–Wallis *H* tests followed by pairwise Benjamini, Hochberg and Yekutieli *p*-adjusted Wilcoxon post hoc analyses to determine possible length and mass differences between groups.

Complete specimens of *H. mamillatus* were used to determine the shape of the primary spines with respect to their position on the test. Length (maximum distance from base to tip), diameter (maximum thickness perpendicular to the spine's longitudinal axis) and mass of the spines were measured on the same primary spines that were used for growth layer description prior to sectioning. Length was determined by a calliper with an accuracy of ± 0.05 mm. The spines were weighed on a Sartorius BP 211D scale with a precision of ± 0.0001 g.

Microstructural description

Microstructural analyses are based on micrographs obtained from a Hitachi TM 3030 Tabletop scanning electron microscope (SEM). SEM samples were prepared as cross sections and longitudinal sections of numerous spines from both complete individuals and spines from the spine assortment. After dissection, the samples were cleansed for 15 min in an ultrasonic bath with deionized water. The samples were then dried for at least 30 min at 110 °C in a drying cabinet. Dried and cleaned samples were analysed uncoated in the SEM.

The number of radial septa per growth layer was determined from SEM micrographs at six aboral spines. Therefore, cross sections at 10, 25, 50, 75 and 90% of the spine length measured from the base were used. The consistency of the number of radiating septa in cross section of a single spine and along different spines was analysed.

2d porosity determination and gravimetry

The porosity was determined based on SEM micrographs of five specimens in cross sections used for counting the radial septa. The samples were prepared for SEM analyses by infiltrating the stereom with epoxy resin Araldite 2020/A for 15 min at 0.05–0.15 bar. The samples were then polished. A full infiltration and a smooth surface is necessary for 2d porosity determination, otherwise struts or pores not lying in the analysed plane are mistakenly included in the analysis and would result in false porosities.

The porosity was calculated using the ImageJ software environment Fiji 2.0.0. The images were binarized using the iterative "default" threshold based on Ridler and Calvard (1978) which is accurate as the stereom is pale grey to white and can be distinguished by binarization from the dark grey or black epoxy resin that fills the pores. Pixel-clusters larger than 8 connected pixels were counted in the "analyse particles" function for porosity determination. Pixel-clusters smaller than 8 connected pixels can result from impurities in the Araldite 2020/A epoxy resin and were thus not analysed. The spine segment porosity was also determined gravimetrically prior to infiltration by assuming a density of 2.711 g/cm^3 for calcite (DeFoe and Compton 1925). Therefore, the volume of the spines was calculated by measuring the area of the cross section (A) on the SEM picture and by multiplying it with the mean thickness (d) of ten measurements of the segment that were carried out prior to infiltration. Together with the mass (m) that was also measured before the infiltration the porosity (ϕ) could be estimated with Eq. 1. Error bars were calculated with the standard deviation of the thickness.

$$\phi[\%] = \left(1 - \left(\frac{m[\mathrm{g}]}{A[\mathrm{cm}^2] \times h[\mathrm{cm}] \times 2.711[\mathrm{g} \times \mathrm{cm}^{-3}]}\right)\right) \times 100. \quad (1)$$

In 2d analysis, the porosity was analysed for the whole cross section, the growth layer(s), the radiating layer(s) and the medulla. Growth layers were numbered in an ascending order from old to young (interior to exterior). The radiating layer is separated by the growth layers in as many ring-shaped sections of radiating layer as there are growth layers. These radiating layers were numbered in the same ascending order from old to young.

3d porosity determination

For 3d porosity determination, two X-ray micro-computed tomography (µCT) scans were performed, one in the medulla and one in the radiating layer. In both cases, the scanned volume was a cube with an edge length of 1.278 mm within a thin bar extracted at 50% of the spine length of a large aboral spine from the articulated spine collection. The spine was prepared in the same way as described above for the microstructural analysis. The µCT scans were conducted using a Nanotom (GE Sensing & Inspection Technologies GmbH, Wunstorf) equipped with a microfocus X-ray tube. The samples were scanned at 80 kV/180 µA with an exposure time of 800 ms to a resolution of 1.27 µm per voxel. The acquired 2d X-ray images were reconstructed with a Filtered Back Projection reconstruction algorithm (datos|x). The µCT data were visualized and analysed with the commercially available software packages VGStudioMax 3.0 (Volume Graphics GmbH, Heidelberg), Avizo 9.3 (FEI SAS, Mérignac) and MAVI 1.5.2 (Fraunhofer IWTM, Kaiserslautern).

An anisotropic diffusion filter was applied to the µCT scans reducing the noise while preserving edges of the structures. The reconstructed objects were than binarized

by Otsu's threshold method (Otsu 1979) as it is suitable for data sets with bimodal grey value distributions and is user independent. In the µCT scans, porosity was determined in x_1, x_2 and z-direction (crystallographic c-axis) meaning the porosity in the z-direction is the porosity measured on the plane perpendicular to the z-axis (x_1, x_2 plane), etc. The mean porosity is composed out of the porosity in x_1, x_2, and z-direction. The porosities of the medulla and the radiating layers are compared to the porosities obtained by gravimetric porosity determination, 2d SEM analysis and to porosities reported in the literature.

Results

Growth layer description

Growth layers in primary and secondary *H. mamillatus* spines in both, cross- and longitudinal section, are recognized as thin, often brownish-red lines (Figs. 1, 2). Two different types of growth layers were found: Proximal growth layers (1) are present as densely packed loops near the base (Fig. 2b, c). They merge into each other and rarely exceed a few millimetres in size. These layers resemble growth layers found on secondary spines (Fig. 2d). Secondary spines possess proximal growth layers only. Distal growth layers (2) are more widely spaced and the regular distal type extends from the milled ring to the tip of the spine where they form the typical blunt tip (Fig. 2a). A succession of these regular distal growth layers provide the spine a matryoshka-doll-like appearance (Fig. 2a). Two sub-types of distal growth layers beside the regular ones were encountered: capping growth layers (1) are characterized by an isolated growth cap (Fig. 2a) separated from its disjunct basal layer emanating from the milled ring towards the cap (Fig. 2e). Incomplete distal growth layers (2) lack the characteristic cap (Fig. 2g). Whether or not such an incomplete distal growth layer can be present at the surface of the spine or occurs due to later resorption is unclear.

A sequence of all distal growth layer types can develop in a single spine and may form a complex growth pattern as present in the spine shown in Fig. 2a. Here, the incomplete distal growth layer is the oldest distal growth layer followed by three regular distal growth layers. This construction is topped by two capping growth layers. The disjunct basal layer of growth cap 1 is already overgrown by the younger disjunct basal layer of growth cap 2 (Fig. 2f). Distal growth layers are usually not evenly spaced (Fig. 2a).

Primary spines

Primary spines show a wide variety of sizes and shapes within a single individual. In cross section, oral primary spines are flat and blade-shaped, where aboral primary spines are triangular to round. A graded transition of the spine morphology can be found from the oral to the aboral side of the test (Fig. 3). Nearly perfect circular spine cross sections are not found on every individual. Oral spines are the smallest (median: 26.1 mm) and lightest (median: 0.340 g) spines (Fig. 4a, b, Table 1). The aboral primary spines are the largest spines of this echinoid. Two groups of aboral primary spines were distinguished: aboral spines without capping growth layer and with capping growth layer. Capping growth layers were only found on aboral spines longer than 44 mm and are always present on spines longer than 73 mm (Fig. 4a, c, Table 1). Aboral spines lacking these capping growth layers are lighter and shorter than aboral spines with capping growth layers, but still heavier and longer than the oral spines (Table 1, Fig. 4a–c). All three groups show a considerable scatter in their masses, maximal diameters and lengths. Only for oral spines and aboral spines with capping growth layer the group distinction is statistically significant with $p < 0.05$ (Fig. 4a, b, Table 2). An increasing spine length is correlated by an increase of the spine mass (Fig. 4c). These correlations are statistically significant for all three spine groups (Table 2).

There are slight differences in the distribution of growth layers in oral and aboral spines. Oral spines appear to have an approximately equal distribution of proximal and distal growth layers, as they scatter around the bisecting line (Fig. 4d). There is only weak correlation between the number of proximal and distal growth layers for oral spines, although it is significant (Table 2). Aboral spines without capping growth layers tend to have a higher number of proximal than distal growth layers (Fig. 4e) with again a weak, though significant correlation (Table 2). The highest number of proximal and least number of distal growth layers are found in the aboral spines closest to the apical disc (Fig. 4e). Aboral spines with capping growth layers show no correlation in number of distal and proximal growth layers (Fig. 4f, Table 2). They usually have less proximal growth layers than distal growth layers (Fig. 4f).

Microstructure description

On the microscale and best seen in cross sections, growth layers are composed of numerous radial septa as pointed out by previous authors (Hesse 1900; Grossmann and Nebelsick 2013a) and is confirmed by this study (Fig. 1b–

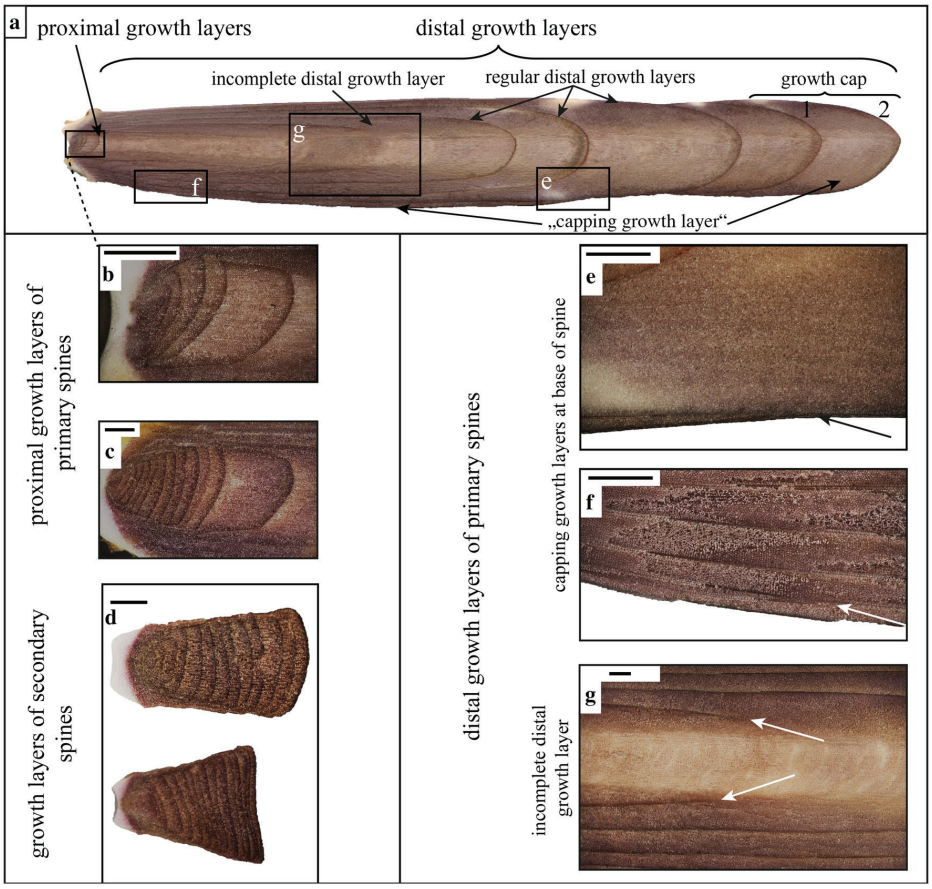

Fig. 2 The different types of growth layers in longitudinal sections in a primary spine (**a**) with magnifications (**b**, **e**, **f**, **g**). **b**, **c** show the closely packed proximal growth layers in the base of primary spines which resemble the growth layers found in secondary spines (**d**). Regular distal growth layers usually extend from the base to the tip of the spine (**a**), but two variations were found: (1) capping growth layers (**a**), that top the regular distal growth layers with caps, but also have a corresponding succession at base (**d**, **e**) and (2) incomplete distal growth layers lacking the dome shaped cap (**a**, **g**). Scale bars = 1 mm

Fig. 3 Cross section series of spines from the oral towards the aboral side. All spines taken from HMf3. The brownish-red lines within the cross sections represent growth layers, which appear as bands or lines in 2d sections. The largest spine on the right shows healed wounds indicated by arrows. Possible reasons for this damage is a predator attack or exposure to high-energy marine environment

d). The number of radial septa was counted in all growth layers of six aboral spines (Table 3).

The number of radial septa per growth layers is remarkably constant (Table 3), considering the shape and variations and increasing circumference of the spines with age. The fewest radial septa per spine were observed in HMf4 (196-214), the most in HMf2 (260-272). The largest increase of radial septa within a single growth layer is 15, the largest decrease found is 27 (Table 3). Nevertheless, for the majority of growth layers, the number of radial septa is nearly constant throughout the spine and all growth layers.

In cross sections close to the milled ring, the radial septa of the growth layers are interconnected by radiating trabeculae which extend from the middle of one radial septa to the next (Fig. 5a–c). These radiating trabeculae start

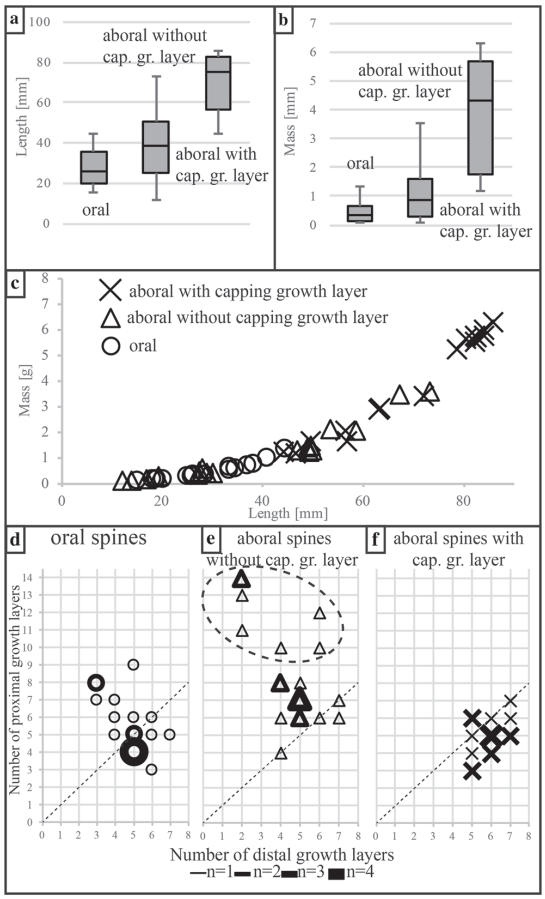

Fig. 4 Correlations of different spine types of HMf1 to mass (**a**, **b**), length (**a**, **c**) and number of growth layer type (**d**–**f**). All correlations are listed in Table 2. Dashed lines in d–f represent an equal distribution of proximal and distal growth layers. "cap. gr. layer" refers to capping growth layer

right after the medulla (Fig. 5b) and connect the growth layer's radial septa until the spines rim. The radiating trabeculae are not always straight, but can be slightly sinuous (Fig. 5c). In longitudinal sections, the interconnecting radiating trabeculae appear as a perforated wall with a more regular structure and a smaller pore size than the stereom filling the interspace between the radiating trabeculae (Fig. 5d). In cross section, this stereom interspace has the width of a single pore right after the radiating trabeculae emanate from the medulla (Fig. 5b). In later stages, two pores are situated between the radiating trabeculae (Fig. 5c). The transition from one to two pores is highlighted by the line in Fig. 5a and occurs in a similar distance to the medulla between all radiating trabeculae. This overall radiating structure is best seen close to the milled ring and generally in smaller aboral spines (Fig. 5) of *H. mamillatus*.

The radiating structure is also traceable in large spines (Fig. 6). A radiating trabecula is highlighted by the white line in Fig. 6a–d and a schematic representation of the whole radiating structure with a shaded background for the basic radiating unit is given (Fig. 6e). Numerous repetitions of this radiating unit consisting of radiating trabeculae, radial septa and stereom interspace are present. The radiating trabeculae arise from the medulla, where laminar stereom meets the ordered radiating trabeculae (Fig. 6b). By placing the radiating trabeculae in the centre of the basic radiating unit (Fig. 6a, e), it is then framed by the width of half a pore of the stereom interspace on each side (Fig. 6b, e). At a critical pore diameter, the single pore between two radiating trabeculae splits up into two smaller pores with a thin strut in between, such that the radiating trabeculae is now framed by the width of a full pore on each side (Fig. 6c, e). Close to the spine edge, at least two pores to each side of the radiating trabeculae make the overall stereom appear more chaotically arranged (Fig. 6d, e). Nevertheless, the radiating trabeculae are still visible, as they are thicker than the ordinary struts of the stereom interspace (Fig. 6a, d). Although the whole stereom seems to merge into a chaotic structure at some parts, the radiating trabeculae can still be recognized (white box, Fig. 6a).

Porosity distributions

Gravimetric porosities and the porosity determined by 2d image analysis of the 15 segments show good accordance. The 2d porosity coincides within the error range of the gravimetric porosity (Fig. 7a). In the 15 segments, the overall porosity ranges from 54.3 to 71.6%. The medulla has the highest porosity (average of 75.4–88.3%) and the growth layers the lowest porosity (14.9–36.2%) with the radiating layer ranging in between. This means the densest part of the spine is close to the spine surface, the lightest stereom is in the centre (medulla) and the radiating layer is filled with stereom of intermediate porosity. The resulting porosity gradient is occasionally interrupted by older growth layers. This porosity gradient is, on the one hand, stepwise between the morphological distinct stereom types of medulla, radiating layers and growth layers, but on the other hand gradual in the radiating layer as seen in Fig. 7b, c. The radiating layer (RL1) between medulla and the oldest growth layer (GL1) has a porosity of 67.4% while the radiating layer (RL3) between the youngest growth layer (GL3) and the second growth layer (GL2) has a porosity of 56.3% which is a reduction of 11.1% points. Porosities of the radiating layer in cross sections at 50 and 90% of the spine length are generally higher, but still

Table 1 Measurements of oral and aboral *H. mamillatus* spines from HMf1

Position on test	*n*	Length (mm)			Mass (g)			Max. diameter (mm)		
		Range	Median	Mad	Range	Mean	Mad	Range	Median	Mad
Aboral (without capping growth layer)	18	11.7–73.1	38.4	11.5	0.090–3.546	0.892	0.565	2.5–10.6	8.0	2.0
Aboral (with capping growth layer)	16	44.2–85.8	75.2	9.7	1.173–6.295	4.298	1.458	7.9–12.3	11.0	0.8
Oral	17	15.0–44.4	26.1	7.3	0.080–1.325	0.340	0.213	4.3–10.5	6.5	1.4

Only spines where the number of proximal growth layers could be determined are listed. *n* sample size, *mad* median absolute deviation

Table 2 Pairwise Benjamini, Hochberg and Yekutieli *p*-adjusted Wilcoxon post hoc analyses to determine possible length and mass differences between groups (Fig. 3a, b)

		n	*p*	R^2
Figure 3a	Oral spines with capping growth layers vs. aboral spines without capping growth layers	17	0.0513	
	Oral vs. aboral with capping growth layers	18	< 0.001	
	Aboral without vs. with capping growth layers	16	< 0.001	
Figure 3b	Oral vs. aboral without capping growth layers	17	0.07	
	Oral vs. aboral with capping growth layers	18	< 0.001	
	Aboral without vs. with capping growth layers	16	0.029	
Figure 3c	Oral	17	< 0.001	0.992
	Aboral without capping growth layers	18	< 0.001	0.975
	Aboral with capping growth layers	16	< 0.001	0.981
Figure 3d	Oral	17	0.015	0.315
Figure 3e	Aboral without capping growth layers	18	< 0.001	0.362
Figure 3f	Aboral with capping growth layers	16	0.094	0.18

Major axis regressions of proximal and distal growth layers (see Fig. 3c–f). *n* sample size, *p* *p* value, R^2 regression coefficient

decreasing from interior to exterior (Fig. 7c, Table 4). Porosity changes within the radiating layer alongside with the values for growth layers and medulla are listed for all analysed segments in Table 4.

Over the spine length from the bottom cross section at 10% to the cross section close to the tip at 90%, the porosity consistently increases for all five analysed spines (Fig. 7d). The porosity of the medulla remains constant at around 80% and the porosity of the growth layers decreases from around 30% to below 20% along the spine length. The radiating layer exhibits the same increasing porosity trend at similar values as the whole cross sections showing that it contributes most to the overall porosity (Fig. 7d). The number of growth layers present in the cross section influences the overall porosity of the cross section as well (Fig. 7e). It correlates linearly with the porosity ($R^2 = 0.7878$). The higher the porosity, the fewer growth layers were encountered. No significant correlation was found between the number of basic radiating units that constitute the spine and the overall porosity of the cross section ($R^2 = 0.0025$, Fig. 7f).

The porosity obtained by µCT scans (Fig. 8) reflects the 2d porosity determination in the cross sections. The radiating layer has an average porosity of 63.2% and the medulla of 79.7% (straight lines in Fig. 8). The porosities in *x*1, *x*2 and *z*-direction coincide closely with the average porosity, however, there are two exceptions. (1) In the *z*-direction (crystallographic *c*-axis) the porosity of the medulla is first higher than 79.7% peaking at 84.7% and after 0.6 mm it is lower than the average. (2) In the x_1-direction of the radiating layer, periodic oscillations with a wavelength of 30–70 µm are present with decreasing amplitude.

Discussion

Basic radiating units as building principle of spines of *H. mamillatus*

On a micrometre scale the stereom of the radiating layer might appear chaotic (Fig. 6) as described in Grossmann

Table 3 Number of radial septa counted per growth layer (GL) in cross sections taken at 10, 25, 50, 75 and 90% of the spine length measured from the base, respectively

Sample	Length [mm]	Mass [g]	Number of radial septa per GL at length of spine measured from base				
			At 10%	At 25%	At 50%	At 75%	At 90%
HMf2	65	3.83					
GL 1			266	274	273		
GL 2			265	268	272	271	
GL 3			262	266	270	272	272
GL 4			260	263	268		272
HMf4	69	3.67					
GL 1			202				
GL 2			202	202			
GL 3			202	202			
GL 4			202	202	202		
GL 5			202	202	202		
GL 6			202	202	204	204	
GL 7			202	202	204	203	196
GL 8			202	202	204	203	214
HMf5	70	4.04					
GL 1			208				
GL 2			218	213			
GL 3			218	218	218		
GL 4			218	218	218	204	
GL 5			218	218	218	218	221
HMf7	67	2.97					
GL 1			231	225			
GL 2			232	230	225	215	
GL 3			232	232	230	226	225
HMf8	72	3.9					
GL 1			213				
GL 2			237	210			
GL 3			240	235	225		
GL 4			240	238	232	224	
GL 5			240	240	236	231	230
HMrs1	93	7.04					
GL1			231	–	–	–	–
GL2			249	–	–	–	–
GL3			249	249	–	–	–
GL4			249	249	257	–	–
GL5			249	249	256	263	265
GL6			249	–	–	–	–
GL7			249	249	–	–	264

Spines were sampled form six different animals

and Nebelsick (2013a, b); however, when zooming out to the mm scale, it becomes obvious that the stereom is ordered in a radiating manner. This order has been reported for spines of *Heterocentrotus trigonarius* (Hesse 1900; Weber 1969b), the closest relative of *H. mamillatus*, where it is much more obvious due to an overall lower porosity of the spines and more growth layers with their radial septa present in cross sections. Both facilitates tracking the radiating unit. This is probably the reason why the radiating structure is more clearly seen in *H. mamillatus* basal cross sections where the porosity is lower and more growth layers are present than in distal cross sections close to the

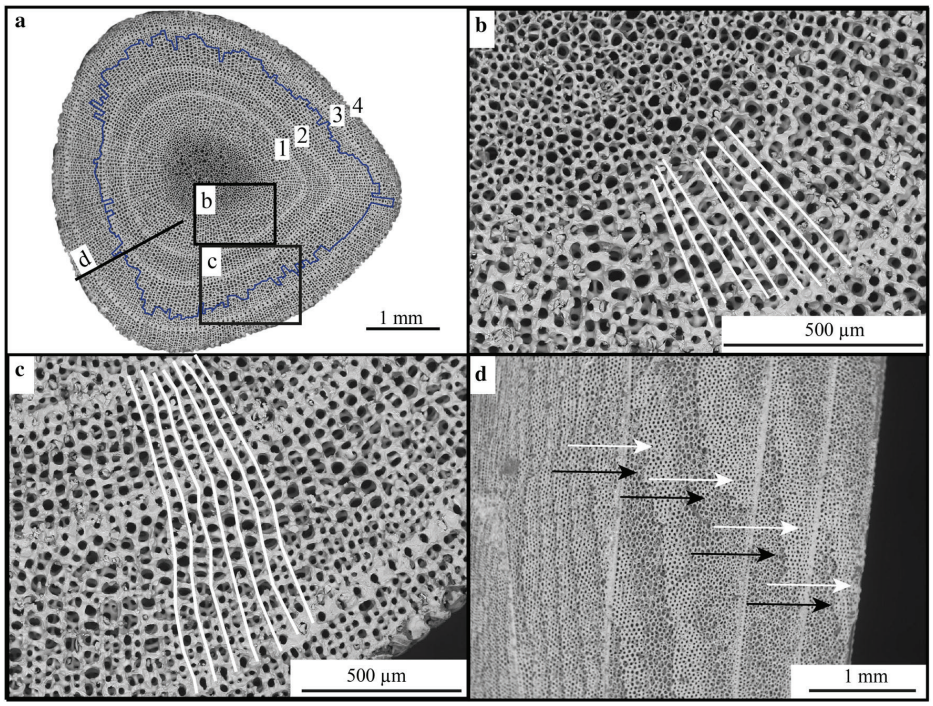

Fig. 5 A small aboral spine with 4 growth layers (1–4) displays radiating trabeculae well traceable from the medulla to the outside of the spine (**a**). The line marks the transition from 1 to 2 pores between the radiating trabeculae (**a**). The detail pictures **b** and **c** are enlargements of the frames in **a**, showing the radiating structure in higher detail. In longitudinal sections (**d**) the radiating trabeculae (in 3d a wall-like structure) stand out with smaller pore sizes and visually higher pore order (white arrows) compared to the stereom interspace filling the space in between the radiating trabeculae (black arrows)

tip. Hesse (1900) described the radiating nature of *H. mamillatus* spines being restricted to the growth layers only and is lost in foam-like meshwork in between. The SEM micrographs presented here show that radiating trabeculae connecting the radiating septa of the growth layers, although sometimes sinuous, and give the spine an overall radiating arrangement as typical for many sea urchin spines (e.g. Hesse 1900; Coppard and Campbell 2004; Kroh and Nebelsick 2010). Strong evidence for the presence of this radiating structure comes also from the µCT analysis, where perpendicular to the direction of the radiating structure porosity oscillations with the wavelength typical for the width of a radiating unit ranging between 30 and 70 µm (Fig. 8). Lower porosities reflect denser radiating trabeculae and higher porosities reflect the stereom interspace.

The basic radiating unit occurs in numerous repetitions and at least 200 per spine were found. In contrast to *H. trigonarius*, where new radiating units are frequently added in new growth cycles in order to keep geometry with the increasing spine diameter (Weber 1969b), their number is nearly constant in aboral spines of *H. mamillatus*. This implicates a growth mechanism by a subsequently widening of the radiating unit. Furthermore, the number of radiating units is not diagnostic for *H. mamillatus* as has been found for other species (e.g. Coppard and Campbell 2004) since their number differs largely among spines. In contrast to other species, where few but dense and thick wedges make up the basic radiating unit (e.g. *Paracentrotus lividus*, see i.e. Kroh and Nebelsick 2010), *H. mamillatus* has a delicate radiating structure which serves the overall lightweight construction. In this manner, the advantages of a lightweight construction as a compromise between functional aspects and energetic costs are achieved.

Porosity distributions

Presser et al. (2010) determined gravimetrically the porosity of a cuboid segment of a *H. mamillatus* spine for 4-point bending tests. In this sample, medulla and radiating layer were present and they detected a porosity of 59%,

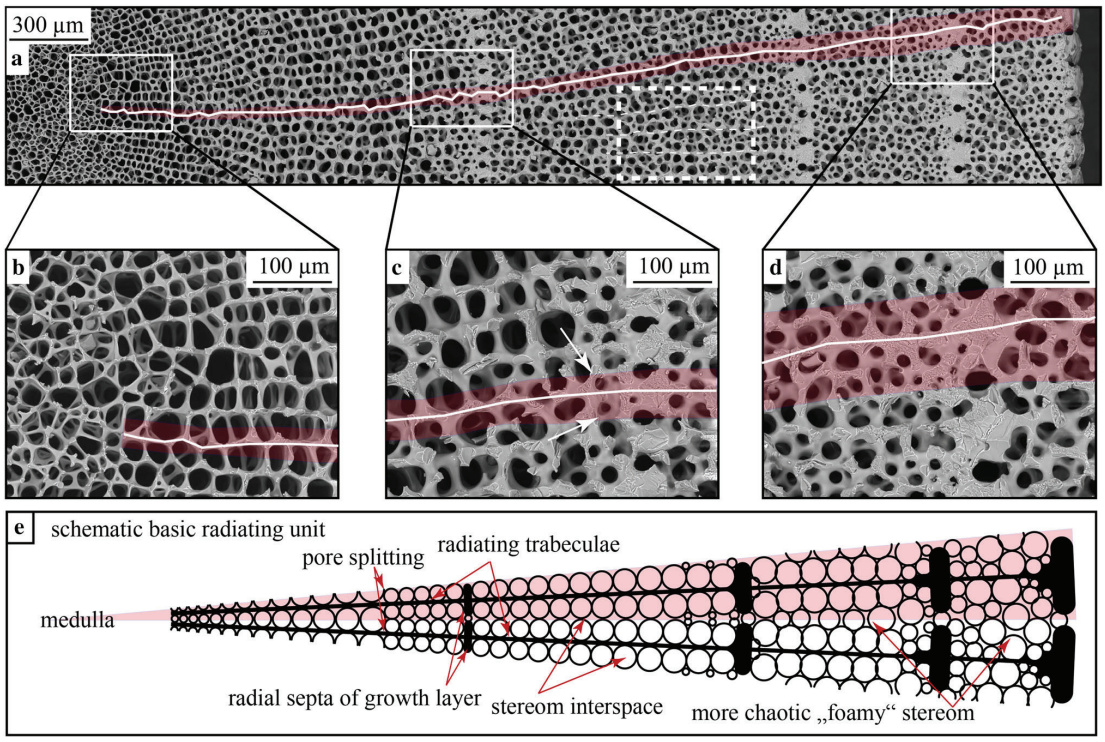

Fig. 6 Tracking a shaded basic radiating unit in a large aboral spine (**a**). The radiating trabeculae initiates right after the medulla (**b**), the first "pore-splitting" occurs right before the oldest growth layer (**c**). Close to the surface of the spine, the basic radiating unit reaches a width of four pores (**d**). The white dashed box in **a** shows an example region, were the radiating structure is difficult to discern. A schematic representation of a radiating unit is given in **e** to highlight the main observations and facilitate orientation

which is slightly lower than the porosity reported here. In the same study, porosity around nanoindentations was determined and gave systematically lower porosities ($61 \pm 4.8\%$ for the medulla and $38 \pm 3.1\%$ for the radiating layer) than in this study. These differences in porosity determination may be due to sample size and location of the measurements within the stereom.

The two major porosity trends found in this study have an important implication for the mechanical performance of *H. mamillatus* spines. A spine with the most porous part (medulla) in the centre and the densest part (growth layers) at or closely beneath the surface may be abstracted as a cylinder with a porous, hence more compliant filling, a structure, which is quite common in nature (Dawson and Gibson 2007). From simple beam theory, it is clear that the change in geometrical moment of inertia results in an increase in stiffness for a given weight and, for the same reason, an increase in bending strength. This is a straight forward case of how to maintain the strength of an enlarged spine structure without becoming a burden by weight.

The further here identified porosity increase from spine base to its tip has other consequences. Because of the simple inverse relation of porosity and strength (e.g. Ji et al. 2006) the spine will be weaker in compression at the distal region, i.e. it will start to fracture at the tip. If this would be true in a bending case depends on the geometrical boundary conditions of the bearing. One may assume, however, that on average the failure of the spine is more likely to occur in the distal tip region. This effect might be beneficial for the regeneration of truncated spines, which is a slow process (Dotan and Fishelson 1985; Ebert 1988). The extent of extra costs incurred by regeneration for the living animal would be reduced by more distally located failure sites.

Distal growth layers and their implications on mechanical performance

The growth layers in *H. mamillatus* are crucial structural elements for a cascading manner within a graceful failure behaviour by deflecting cracks along the interface of the

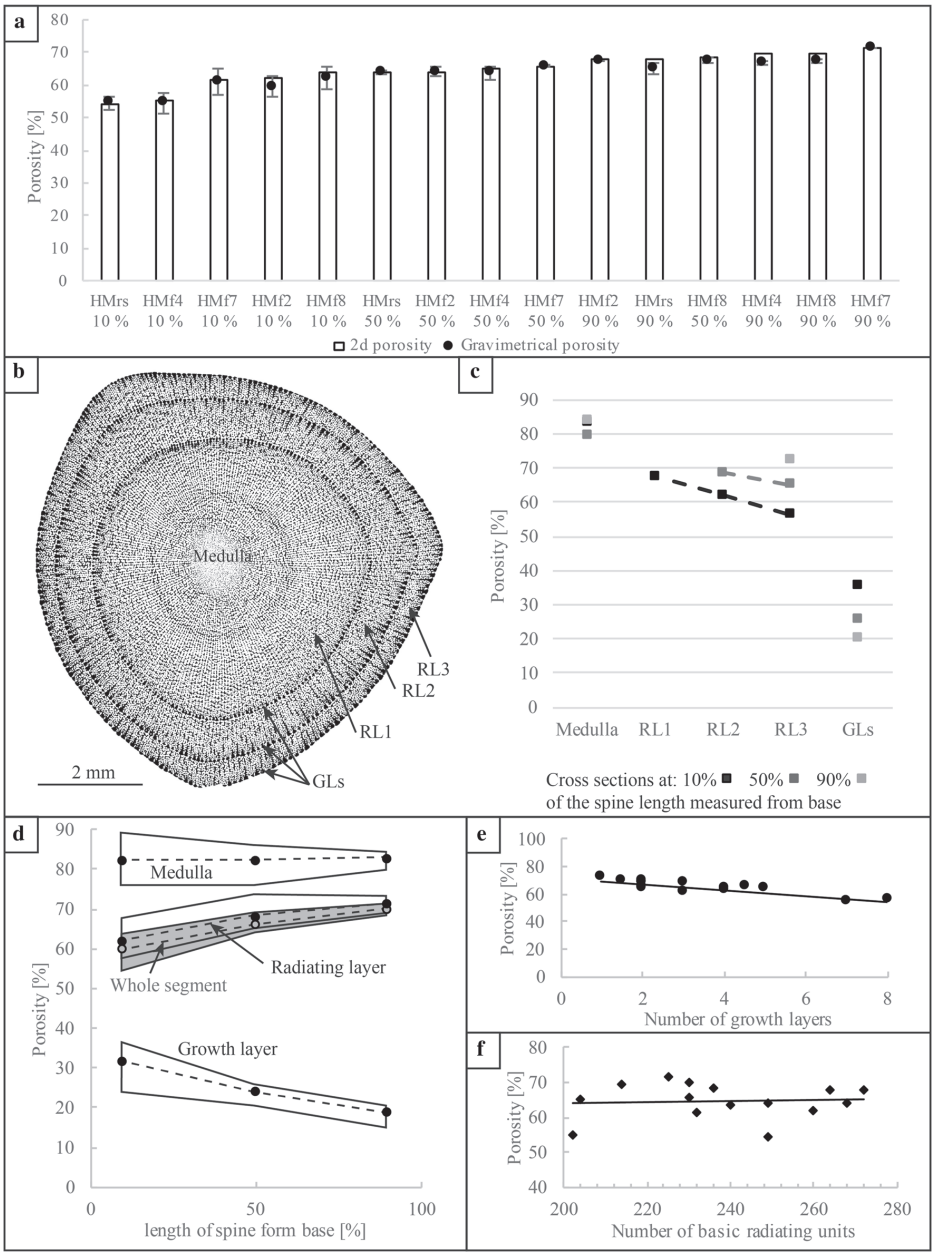

Fig. 7 Porosity of *H. mamillatus* spines. There is a good accordance between gravimetrically determined porosity and by 2d analysis (**a**). Porosity generally decreases within a cross section (**b**) from interior to exterior with a gradient also present in the radiating layer (**c**). Over the spine length the bulk porosity (grey shaded area) increases considerably (**d**). Interpolated areas correspond to all 5 measured spines and data dots represent the mean of all 5 porosities. The porosity of the growth layer shows an opposing trend to the overall porosity, while the porosity of the medulla remains constant over the whole spine length. Radiating layer and overall porosity show the same trend and similar values (**d**). The porosity of the cross sections correlates linearly with the number of growth layers (**e**, $R^2 = 0.7878$). There was no correlation found between the number of basic radiating units overall porosity of the cross section (**f**, $R^2 = 0.0025$)

Table 4 Porosities of all cross sections analysed for medulla, radiating layer and growth layers

Specimen	Segment at (%)	Porosities [%] of:				
		Medulla	Radiating layer (range)	Radiating layer (mean)	Growth layers	Whole cross section
HMf2	10	88.3	46.9–64.1	60.1	28.7	62.0
	50	85.2	51.3–71.6	66.8	23.5	64.1
	90	80.8	66.1–73.2	69.7	14.9	67.7
HMf4	10	76.7	42.3–65.5	58.5	32.1	55.0
	50	84.3	42.4–72.4	66.6	23.6	65.0
	90	84.1	62.8–73.1	69.5	20.4	69.6
HMf7	10	83.3	56.3–67.4	63.5	35.5	61.4
	50	79.5	65.0–68.5	67.2	25.7	65.6
	90	83.8	61.0–78.0[a]	72.5	20.3	71.6
HMf8	10	84.0	61.1–70.9	67.1	36.2	63.6
	50	84.3	60.4–70.8	68.6	24.6	68.4
	90	–[b]	–[b]	72.0	18.7	69.8
HMrs1	10	75.6	39.9–64.6	57.3	23.9	54.3
	50	75.4	61.9–65.2	64.4	20.4	63.8
	90	79.4	66.3–71.4	69.1	18.2	67.9

For radiating layer a range of porosities is given. The highest value corresponds to the radiating layer between medulla and oldest growth layer, the lowest value to the radiating layer situated between youngest and 2nd youngest growth layer

[a]As there was only one growth layer present the radiating layer and the radiating layer was not separated naturally, max value was obtained in a 0.4-mm band around the medulla and min value in a 0.4-mm band adjacent to the growth layer

[b]The stereom structure was overall unclear because of the termination of a growth layer exactly in this cross section. The medulla was replaced by the terminating growth layer and could not be measured

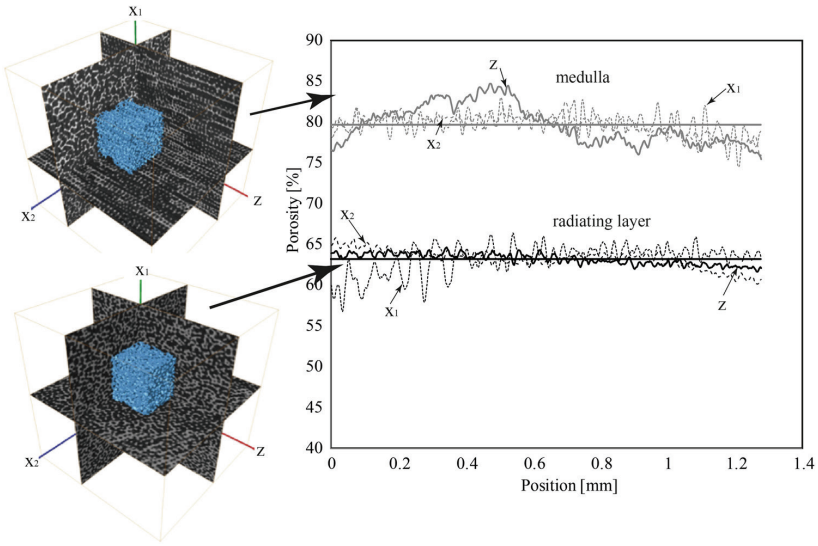

Fig. 8 Porosity determined by µCT. Areas of analysis are shown on the left (upper: medulla, lower: radiating layer). The *z*-direction corresponds to the crystallographic *c*-axis, *x*1 and *x*2-directions are in the plane perpendicular to the *z*-direction. Porosities are given in *x*1-direction (thin dotted line), *x*2-direction (dashed line) and *z*-direction (full line). The straight lines correspond to the overall porosity in the analysed cube obtained from the porosities in *x*1, *x*2 and *z*-direction

denser growth layers and the more porous radiating layer (Presser et al. 2009a). The present study found that the number of growth layers is highly variable (2–7) in aboral primary spines of a single individual, that they are unevenly spaced over the spine length and that there are 3 different types of distal growth layers. All these observations in addition to the porosity gradient help to explain the large variations found for mechanical properties of the

spines of this species (Presser et al. 2009a; Grossmann and Nebelsick 2013b; Schmier et al. 2016). More growth layers within the tested segment will lead to a pronounced cascaded graceful failure under uniaxial compression. In contrast to regular distal growth layers, the growth caps of capping growth layers can deflect the crack directly to the surface of the spine, which will lead to a direct spallation of parts of the stereom reducing the compressive strength. Incomplete distal growth layers have no growth cap and hence do not have the ability to deflect cracks in the same way as regular distal and capping growth layers.

Depending on whether the tested segment has been extracted from the base or the tip, the overall porosity can differ by more than 10% (Fig. 8d, Table 4). This has a significant influence on the Young's modulus of the segment and thus the mechanical properties such as compressive and bending strength or stiffness. Modelling the porosity–Young's modulus relationship according to Pabst et al. (2006), a porosity of 58% for the basal segment and of 70% for the tip segment yields Young's moduli of 12.8 and 6.5 GPa, respectively.

Brittle materials do show a natural scatter of data in terms of strengths, because of the statistical nature of defect distribution (e.g. Danzer 2014). By adding the structural variations like the amounts of growth layers and growth layer types, the structural mechanical performance of two segments out of the same spine can be entirely different. Both effects will contribute to the large scatter of data in compression tests of Presser et al. (2009a), 3-point bending tests of Grossmann and Nebelsick (2013b) and indentation experiments of Schmier et al. (2016). Quantifying the porosity and the number and type of growth layers prior to mechanical experiments is thus paramount to distinguish the differing influences and to help to understand the mechanical data in light of their material, their basic construction and the heterogeneity of biological individuals.

Conclusions

1. In the large primary spines of the sea urchin *H. mamillatus*, proximal and distal growth layers have been identified. The latter can be subdivided in (1) the regular distal growth layers spanning from the shaft to the base, (2) incomplete distal growth layers, and (3) capping growth layers. The number of proximal and distal growth layers is variable in primary spines and may be diagnostic for oral, aboral spines without capping growth layer and aboral spines with capping growth layer.
2. Besides the striking growth layers, a basic radiating structure is recognized. The number of radiating units is not diagnostic for this species, but is approximately constant throughout a single large aboral primary spine and can be obtained by counting the ribs of the corrugated surface.
3. The porosity of the spines found here is higher than previously reported. Values obtained by 2d image analysis and 3d analysis with μCT range from more than 80% in the central medulla to 20–30% in the comparably dense growth layers and the radiating layer laying somewhere in between. The overall porosity of a whole spine is around 60% as confirmed by gravimetry and 2d analysis.
4. Two major porosity trends have been recognized: (1) an increase in porosity from milled ring to the tip of up to 15% and (2) a decrease from interior to exterior, which can exceed 60%.
5. The variations in porosity and structural units all contribute to the structural strength of the spines in compression and bending. This opens the possibility to learn which feature has a positive effect for which property under which stressing mode, which in turn can potentially inspire new building construction materials. The advantage for the animal from those features remains somewhat speculative, but can certainly inspire further structural and behavioural research.

Acknowledgements The authors gratefully thank the German Research Foundation (DFG—Deutsche Forschungsgemeinschaft) for funding this work within the framework of the Collaborative Research Centre (SFB/Transregio) 141 "Biological Design and Integrative Structures" project B01. We also thank Barbara Maier and Simone Schafflick in the workshop for their support. The work of an anonymous reviewer is kindly appreciated.

Compliance with ethical standards

Conflict of interest The authors declare that they have no conflict of interest.

Statements on the welfare of animals The sea urchins were purchased dead from a fossils collector, were not killed for the purpose of this study and are not listed as endangered species.

Informed consent This article does not contain any studies with human participants performed by any of the authors.

References

Burkhardt A, Hansmann W, Märkel K, Nieman HJ (1983) Mechanical design in spines of diadematoid echinoids (Echinodermata, Echinoidea). Zoomorphology 102:189–203

Clarke FW, Wheeler WC (1915) The inorganic constituents of echinoderms. US Geol Surv Prof Pap 90:191–196

Coble R, Kingery W (1956) Effect of porosity on physical properties of sintered alumina. J Am Ceram Soc 39:377–385

Coppard SE, Campbell AC (2004) Taxonomic significance of spine morphology in the echinoid genera diadema and echinothrix. Invertebr Biol 123:357–371

Danzer R (2014) On the relationship between ceramic strength and the requirements for mechanical design. J Eur Ceram Soc 34:3435–3460

Danzer R, Supancic J, Pascual T, Lube T (2007) Fracture statistics of ceramics—Weibull statistics and deviations from Weibull statistics. Eng Fract Mech 74:2912–2932

Dawson MA, Gibson LJ (2007) Optimization of cylindrical shells with compliant cores. Int J Solids Struct 44:1145–1160

DeFoe OK, Compton AH (1925) The density of rock salt and calcite. Phys Rev 25:618–620. https://doi.org/10.1103/PhysRev.25.618

Deutler F (1926) Das Wachstum des Seeigelskeletts. In: Hartmann M, Hesse R (eds) Zoologische Jahrbücher Abteilung für Anatomie und Ontogenie der Tiere. Verlag von Gustav Fischer, Jena, pp 119–200

Dotan A (1990) Population structure of the echinoid *Heterocentrotus mammillatus* (L.) along the littoral zone of the south-eastern Sinai. Coral Reefs 9:75–80

Dotan A, Fishelson L (1985) Morphology of spines of *Heterocentrotus mammillatus* (Echinodermata: Echinoidae) and its ecological significance. In: Keegan BF, O'Connor BDS (eds) Echinodermata: Proceedings of the international echinoderm conference, Galway 24–29 Sept 1984. A.A. Balkema, Rotterdam, pp 253–260

Durham JW (1955) Classification of clypeasteroid echinoids. Univ Calif Press Geol Sci 31:73–198

Ebert TA (1986) A new theory to explain the origin of growth lines in sea urchin spines. Mar Ecol 34:197–199

Ebert TA (1988) Growth, regeneration, and damage repair of spines of the slate-pencil sea urchin *Heterocentrotus mammillatus*. Pac Sci 42:160–172

Emson RH (1985) Bone idle—a recipe for success? In: Keegan BF, O'Connor BDS (eds) Echinodermata. Balkema, Rotterdam, pp 25–30

Gibson LJ, Ashby MF (1982) The mechanics of three-dimensional cellular materials. Proc R Soc Lon 382:43–59

Grossmann JN, Nebelsick J (2013a) Stereom Differentiation in spines of Plococidaris verticillata, *Heterocentrotus mammillatus* and other regular sea urchins. In: Johnson C (ed) Echinoderms in a changing world. Taylor & Francis, London, pp 97–104

Grossmann JN, Nebelsick JH (2013b) Comparative morphological and structural analysis of selected cidaroid and camarodont sea urchin spines. Zoomorphology 132:301–315. https://doi.org/10.1007/s00435-013-0192-5

Hasenpusch W (2000) Die Stachel der Griffelseeigel. Mikrokosmos 89:23–27

Hesse E (1900) Die Mikrostruktur der fossilen Echinoidenstacheln und deren systematische Bedeutung. In: Bauer M, Koken E, Liebisch T (eds) Neues Jahrbuch für Mineralogie, Geologie und Paläontologie, E. Schweizertbart'sche Verlagshandlung, Stuttgart, pp 185–264

Ji S, Gu Q, Xia B (2006) Porosity dependence of mechanical properties of solid materials. J Mater Sci 41:1757–1768

Klang K, Bauer G, Toader N, Lauer C, Termin K, Schmier S, Kovaleva D, Haase W, Berthold C, Nickel KG, Speck T, Sobek W (2016) Plants and animals as source of inspiration for energy dissipation in load bearing systems and facades. In: Knippers J, Nickel KG, Speck T (eds) Biomimetic research for architecture and building construction. Springer, Switzerland, pp 109–133. https://doi.org/10.1007/978-3-319-46374-2_7

Kroh A, Nebelsick JH (2010) Echinoderms and Oligo-Miocene Carbonate Systems: potential applications in sedimentology and environmental reconstruction. Int Assoc Sedimentol Spec Publ 42:201–228

Kroh A, Smith AB (2010) The phylogeny and classification of post-Palaeozoic echinoids. J Syst Palaeontol 8:147–212

Lawrence JM (1987) A functional biology of echinoderms. The Johns Hopkins University Press, Baltimore

Lu G, Lu GQ, Xiao ZM (1999) Mechanical properties of porous materials. J Porous Mater 6:359–368

Mooi R (1986) Structure and function of clypeasteroid miliary spines (Echinodermata, Echinoides). Zoomorphology 106:212–223. https://doi.org/10.1007/bf00312042

Moureaux C, Perez-Huerta A, Compere P, Zhu W, Leloup T, Cusack M, Dubois P (2010) Structure, composition and mechanical relations to function in sea urchin spine. J Struct Biol 170:41–49. https://doi.org/10.1016/j.jsb.2010.01.003

Nebelsick JH, Dynowski JF, Grossmann JN, Tötzke C (2015) Echinoderms: hierarchically organized light weight skeletons. In: Hamm C (ed) Evolution of light weight structures. Analyses and technical applications. Springer, Dordrecht, pp 141–154

Nichols D (1962) Echinoderms. Anchor Press, Essex, p 200

Otsu N (1979) A threshold selection method from grey-level histograms. IEEE Trans Syst Man Cybern SMC 9:62–66

Pabst W, Gregorová E, Tichá G (2006) Elasticity of porous ceramics—a critical study of modulus-porosity relations. J Eur Ceram Soc 26:1085–1097

Presser V, Schultheiß S, Berthold C, Nickel KG (2009a) Sea urchin spines as a model-system for permeable, light-weight ceramics with graceful failure behavior. Part I. Mechanical behavior of sea urchin spines under compression. J Bionic Eng 6:203–213

Presser V, Kohler C, Zivcová Z, Berthold C, Nickel KG, Schultheiß S, Gregorová E, Pabst W (2009b) Sea urchin spines as a model-system for permeable, light-weight ceramics with graceful failure behavior. Part II. Mechanical behavior of sea urchin spine inspired porous aluminum oxide ceramics under compression. J Bionic Eng 6:357–364

Presser V, Gerlach K, Vohrer A, Nickel KG, Dreher W (2010) Determination of the elastic modulus of highly porous samples by nanoindentation: a case study on sea urchin spines. J Mater Sci 45:2408–2418

Presser V, Schultheiß S, Kohler C, Berthold C, Nickel KG, Vohrer A, Finckh H, Stegmaier T (2011) Lessons from nature for the construction of ceramic cellular materials for superior energy absorption. Adv Eng Mater 13:1043–1049. https://doi.org/10.1002/adem.201100066

R Core Team (2016) R: A language and environment for statistical computing. R Foundation for Statistical Computing, Vienna, Austria

Ridler TW, Calvard S (1978) Picture thresholding using an iterative selection method. IEEE Trans Syst Man Cybern 8:630–632

Schmier S, Lauer C, Schäfer I, Klang K, Bauer G, Thielen M, Termin K, Berthold C, Schmauder S, Speck T, Nickel KG (2016) Developing the experimental basis for an evaluation of scaling properties of brittle and 'Quasi-Brittle' biological materials. In: Knippers J, Nickel KG, Speck T (eds) Biomimetic research for architecture and building construction. Springer, Switzerland, pp 277–294. https://doi.org/10.1007/978-3-319-46374-2_14

Simkiss K, Wilbur KM (1989) Echinoderms - cells and syncytia. Biomineralization: cell biology and mineral deposition. Harcourt Brace Jovanovich, San Diego, pp 146–149

Smith A (1980) Stereom microstructures of the echinoid test. Spec Pap Palaeontol 25:1–81

Su X, Kamat S, Heuer AH (2000) The structure of sea urchin spines, large biogenic single crystals of calcite. J Mater Sci 35:5545–5551

Telford M (1982) Echinoderm spine structure, feeding and host relationships of four species of dissodactylus (Brachyura: Pinnotheridae). Bull Mar Sci 32:584–594

Toader N, Sobek W, Nickel KG (2017) Energy absorption in functionally graded concrete bioinspired by sea urchin spines. J Bionic Eng 14:369–378. https://doi.org/10.1016/s1672-6529(16)60405-5

Tsafnat N, Fitz Gerald JD, Le HN, Stachurski ZH (2012) Micromechanics of sea urchin spines. PLoS One 7(9):e44140. https://doi.org/10.1371/journal.pone.0044140

Vevers HG (1966) Pigmentation. In: Boolootian RA (ed) Physiology of Echinodermata. Interscience Publishers, New York, pp 265–267

Warton DI, Duursma RA, Falster DS, Taskinen S (2012) smatr 3- an R package for estimation and inference about allometric lines. Methods Ecol Evol 3:257–259. https://doi.org/10.1111/j.2041-210X.2011.00153.x

Weber JN (1969a) The incorporation of magnesium into the skeletal calcites of echinoderms. Am J Sci 267:537–566

Weber JN (1969b) Origin of concentric banding in the spines of the tropical Echinoid *Heterocentrotus*. Pac Sci 23:452–466

Weber J, Greer R, Voight B, White E, Roy R (1969) Unusual strength properties of echinoderm calcite related to structure. J Ultrastruct Res 26:355–366

Bauprinzipien und Strukturdesign von Seeigeln

Further Manuscript 2

Bauprinzipien und Strukturdesign von Seeigeln
– Vorbilder für bioinspirierte Konstruktionen

Bauprinzipien und Strukturdesign von Seeigeln – Vorbilder für bioinspirierte Konstruktionen

Tobias B. Grun / Malte von Scheven / Florian Geiger / Tobias Schwinn / Daniel Sonntag / Manfred Bischoff / Jan Knippers / Achim Menges / James H. Nebelsick

Im Laufe der Evolution haben sich Seeigel an unterschiedlichste Lebensräume im Meer angepasst. Besonders auffällig sind Entwicklungen im Bau ihrer Skelette, die zum Teil sehr spezifisch an die Umweltbedingungen gekoppelt sind. Die Schalen müssen vielen Anforderungen gerecht werden, um zum Beispiel Strömungen, Sturmereignissen und Räuberangriffen zu widerstehen. Dabei lassen sich durchaus auch grundlegende Bauprinzipien in den Schalen erkennen, welche als Inspiration für die Entwicklung innovativer Mechanismen für technische Konstruktionen dienen können. Hierbei steht vor allem die Entwicklung leistungsfähigerer Schalentragwerke unter dem Aspekt einer ressourceneffizienten Nutzung und architektonischer Ästhetik im Vordergrund.

Hart und elegant – Formenvielfalt der Skelette

Stachelige Meeresbewohner

Seeigel erhielten ihren Namen nicht von ungefähr ⌜70. Durch ihre meist kugelige und von Stacheln überdeckte Gestalt gleichen diese rein marinen Vertreter der Stachelhäuter ihrem an Land lebenden Namensvetter auf den ersten Blick. Seeigel kommen in allen Meeren und Tiefen vor. In marinen Ökosystemen sind sie eine wichtige Schlüsselgruppe, da sie eine rasche Algenausbreitung und eine für das Ökosystem schadhaft hohe Besiedelung von anderen Tieren im Riff und auf dem Meeresboden eindämmen und dabei selbst auch ein wichtiges Element in der Nahrungskette darstellen. Das Erscheinungsbild verschiedener Seeigelarten kann, abhängig von ihrem Lebensraum, sehr unterschiedlich sein. Grob kann man Seeigel in die regulären und die irregulären Formen unterteilen. Die meist kugelförmigen regulären Seeigel ⌜70, 72 sind häufig vom Strandurlaub bekannt, in dem sie durch ihre schmerzhaften Stacheln in Erinnerung bleiben können. Die irregulären Vertreter ⌜71, 73 sind oft abgeflacht und leben vor allem verborgen und unauffällig im Sand eingegraben. Eine besondere Gruppe irregulärer Seeigel bilden die Clypeasteroiden[1] Diese Seeigelgruppe zeichnet sich durch ihre sehr stabile modulare Leichtbauweise, ihre leistungsfähigen Plattenverbindungen und eine beeindruckende Formvielfalt aus.

[1] *Zu den Clypeasteroida zählen die Sanddollars (im engeren Sinn), die Sea Biscuits und die Zwergseeigel. Einen allgemein akzeptierten deutschen Namen für die Gruppe gibt es leider nicht. Der Einfachheit sprechen wir hier von Sanddollars (im weiteren Sinn), wenn wir die Clypeasteroiden meinen.*

70 *Der reguläre Seeigel Diadema antillarum wird seinem Namen auf faszinierende Weise gerecht: Er besitzt bis zu 30 cm lange Stacheln, die er zur Verteidigung gegen Fressfeinde einsetzt. Die Stacheln schrecken Räuber so effektiv ab, dass der Raum zwischen ihnen von Fischen sogar als Kinderstube genutzt wird.*

Seeigel technisch gesehen

Seeigel besitzen ein streng hierarchisch organisiertes Skelett aus Kalk (Calciumcarbonat, Calcit, $CaCO_3$), welches aus vielen, teilweise mehreren hundert individuellen und oft effektiv miteinander verbundenen Platten besteht. Ähnlich wie ein Außenskelett umgibt und schützt das Skelett der Seeigel die inneren Organe. Es ist aber von Gewebe bedeckt und damit ein Innenskelett. Die Platten selbst sind aus dem Stereom, einem hochporösen, netzgitterartigen System von ineinandergreifenden Stäbchen, den Trabekeln, aufgebaut **77**.
Das Skelettsystem bietet aus technischer Sicht zwei beeindruckende Eigenschaften: Durch seine hohe Porosität wird das Gewicht der Seeigelschale stark reduziert, gleichzeitig aber ist die Leichtbaukonstruktion so stabil, dass das Seeigelskelett sogar heftigen Beanspruchungen während eines Sturmes standhalten kann. Eine weitere Errungenschaft der Seeigel ist ihr modular und aus vielen Einzelelementen aufgebautes Skelett, welches eine faszinierende Bandbreite an Formen hervorbringen kann. Vorgefertigte, modulare Konstruktionen spielen auch in der Bautechnik eine wichtige Rolle, da sie meist günstig herzustellen sind und sich ihr Aufbau recht schnell verwirklichen lässt. Seeigel aus der Gruppe der Sanddollars bestehen aus Platten, die meist fest über Skelettfortsätze und Bindegewebe miteinander verbunden sind **77**. Eine weitere Besonderheit liegt in ihrem Inneren verborgen: Durch ihre teils starke Abflachung haben diese Arten innere Stützapparate ausgebildet, welche die Ober- und Unterseite des Skeletts miteinander verbinden und so eine tragfähige

Brücke innerhalb des Skelettes bilden. Es lassen sich im Allgemeinen drei Typen solcher internen Stützstrukturen unterscheiden ⌜73. (1) Der auch als Sea Biscuit bekannte *Clypeaster rosaceus* weist ausgeprägte und wandartig aufgebaute, freistehende Pfeiler auf. Diese im Vergleich wenig abgeflachte Art ist mit etwa 20 cm Länge einer der wohl größte Vertreter der Clypeasteroiden. Der Sea Biscuit lebt meist auf dem Sediment, wo er sich gelegentlich unter Felsen versteckt und mit Algen, Muschelschalen und dergleichen maskiert, um sich vor Fressfeinden zu schützen ⌜71. (2) Der im Gegensatz dazu winzige, meist nur wenige Millimeter messende Zwergseeigel *Echinocyamus* besitzt Stützen, welche über ihre gesamte Länge mit der äußeren Schale in Verbindung stehen. Das Skelett dieses ausschließlich im Boden lebenden Winzlings ist so widerstandsfähig, dass es massenweise fossil gefunden wird und dabei kaum Beschädigungen aufweist. (3) Sanddollars, hierzu zählen die mitunter stark abgeflachten Gattungen von *Leodia*, *Mellita* und *Dendraster*, leben vollkommen oder zumindest teilweise eingegraben im Sand. Diese oft scheibenähnlichen Seeigel besitzen ein netzartig verzweigtes Stützsystem aus dünnen Wänden, welches vor allem an den Rändern der Skelette stärker ausgebildet ist.

Formvielfalt und ihr (r)evolutionärer Hintergrund

Die segmentierten Schalenskelette der Sanddollars weisen eine große Formenvielfalt auf, die von hochgewölbt bis stark abgeflacht, von im Längsschnitt kreisrund bis elliptisch und von klein bis groß reichen. Die Skelette können dabei als sehr kräftige Schalen ausgebildet und ihre Platten durch interne Stützapparate zusätzlich verstärkt sein. Diese Vielfalt der Seeigelskelette spiegelt die Anpassungen der Tiere an ihre spezifischen Lebensräume wider. Trotz der immensen Variation innerhalb der Seeigel lassen sich gemeinsame Grundelemente des Seeigelskelettes erkennen. So besitzen zum Beispiel heute lebende (rezente) Seeigel trotz der großen Formunterschiede genau

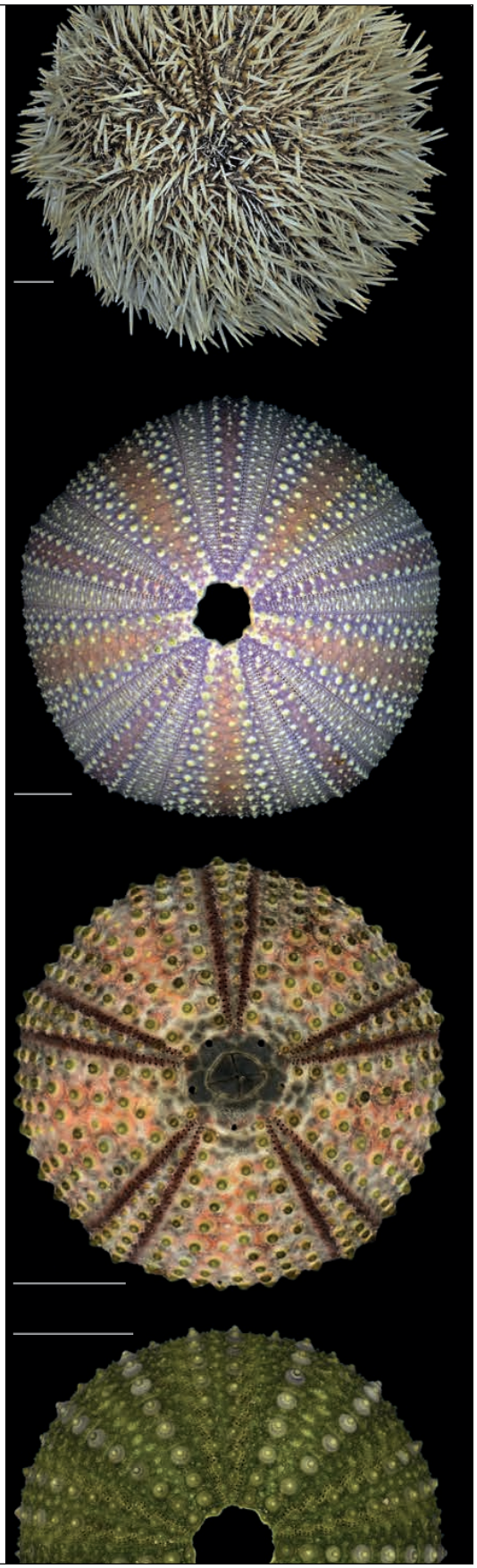

71 *Der Sea Biscuit Clypeaster rosaceus hat sich mit Algen, Schalenbruchstücken und Sediment maskiert, um sich zu tarnen und damit vor Fressfeinden zu schützen.*

72 *Reguläre Seeigel sind meist kugelig rund und zeigen eine ausgeprägte Fünffachsymmetrie. Die Formvariation innerhalb der regulären Seeigel ist bereits verblüffend, aber nicht zu vergleichen mit der der irregulären Seeigel. Von oben nach unten sind Vertreter der Gattung Tripneustes (mit Stacheln), Tripneustes (Skelett ohne Stacheln), Arbacia und Paracentrotus (Skelette ohne Stacheln) abgebildet. Maßlinie 1 cm.*

20 Plattenreihen. Auch die Anordnung der Segmente, bei der sich jeweils drei Platten in einem Punkt treffen, lässt sich bei den Seeigeln wiederfinden. Aus technischer Sicht lässt sich hinter der enormen Formvariation der Seeigel ein theoretisches Strukturmodell erkennen, welches sich im Laufe der Evolution nicht grundlegend verändert hat. In der Architektur und im Bauwesen sind sowohl die Aspekte der Formenvielfalt durch Anpassung als auch die Idee eines abstrakten Modells von großer Bedeutung, da Gebäude in der Regel so geplant werden, dass sie den Anforderungen der Nutzer, den spezifischen Gegebenheiten des Ortes und anderen Anforderungen gerecht werden müssen – allein daraus ergibt sich eine große Vielfalt der Gebäude. In der Architekturplanung werden zunehmend computerbasierte Methoden verwendet, mit deren Hilfe auf Grundlage von Bauprinzipien digitale Modelle entwickelt werden, welche geometrische Variation durch die Veränderung von bestimmten Parametern erzeugen. Kombiniert mit entsprechenden Methoden der Tragwerksanalyse lässt sich dadurch am Computer sogar eine Evolution von Tragwerken simulieren, die zu leistungsfähigeren Ergebnissen führt, als traditionell geplante Konstruktionen es könnten.

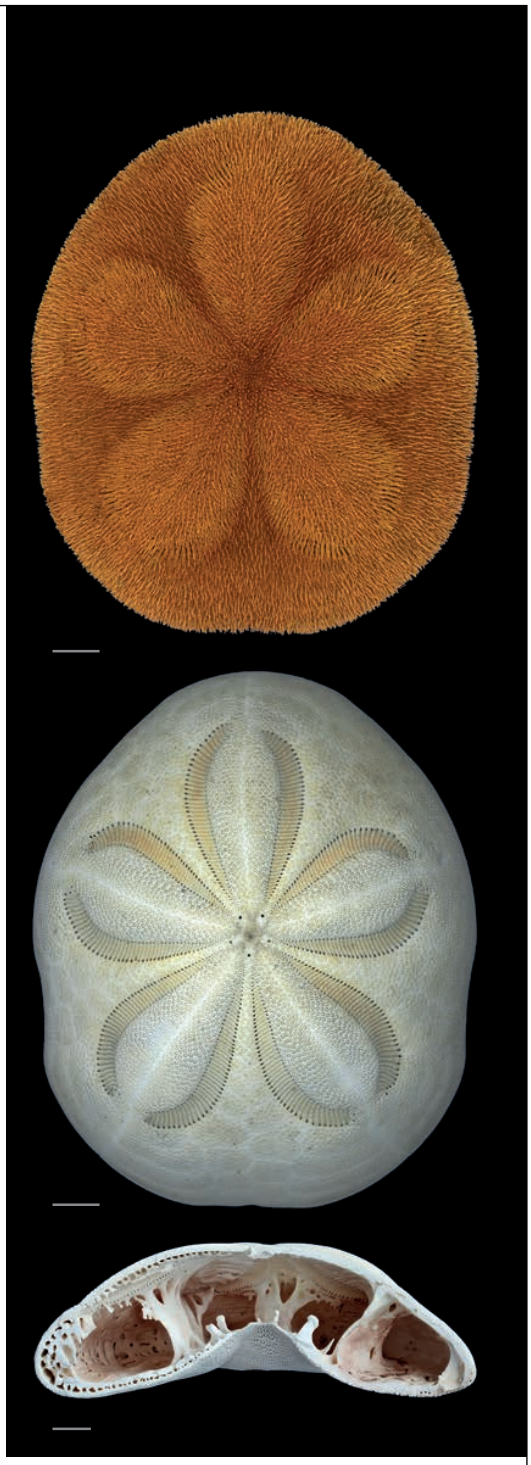

73 *Irreguläre Seeigel aus der Gruppe der Sanddollars (Clypeasteroiden) sind bitaleral symmetrisch, haben also eine linke und eine rechte Körperhälfte. Die Form und Krümmung der Schalen sind sehr variabel und die internen Stützapparate verstärken das Kalkskelett maßgeblich. Links: Clypeaster rosaceus;*

86

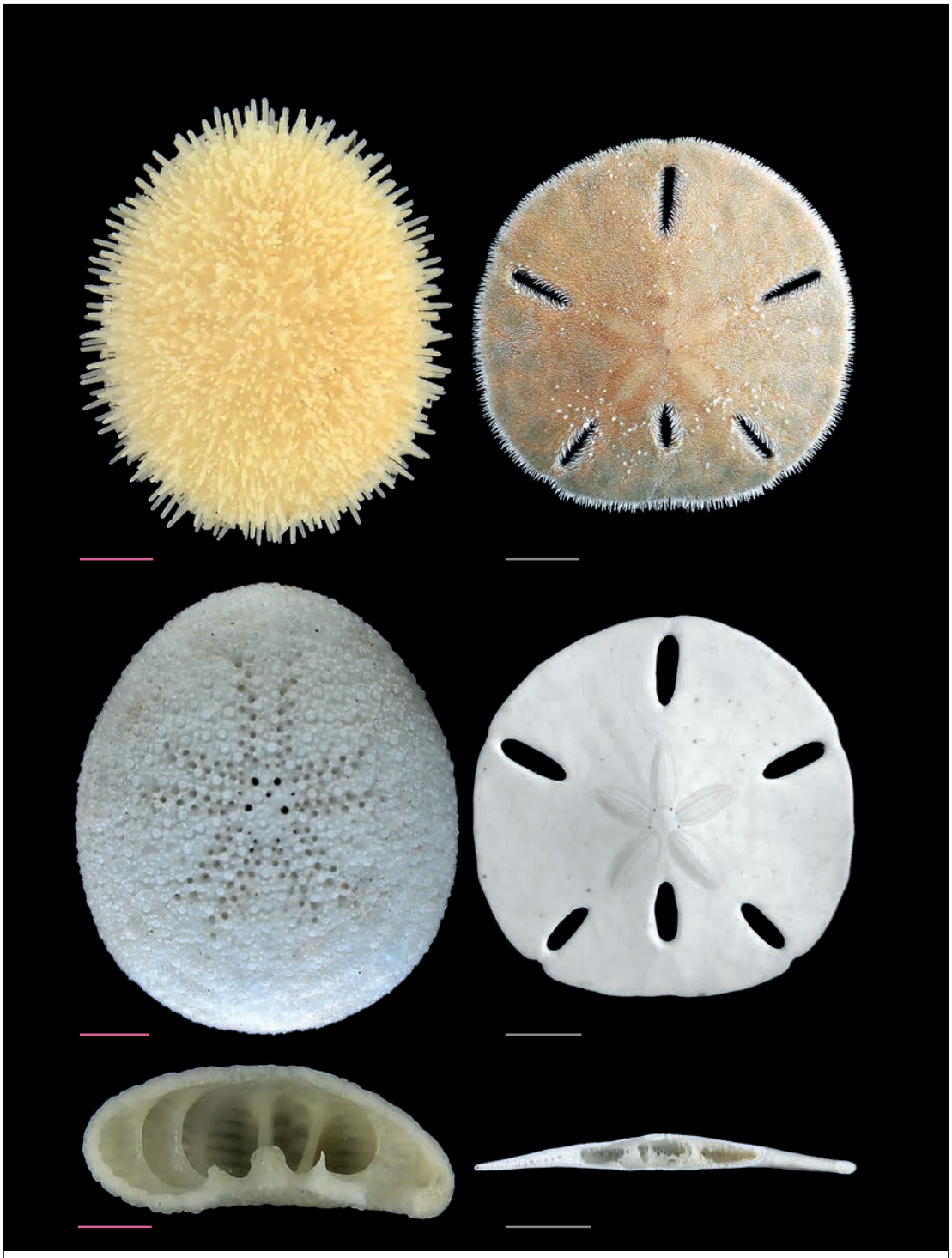

Mitte: Echinocyamus pusillus; rechts: Leodia sexiesperforata; oben: mit Stacheln; Mitte: Skelett ohne Stacheln, unten: Längsschnitt.

Maßlinie (grau) 1 cm, Maßlinie (rot) 1 mm.

87

Schalentragwerke und deren Vorbilder in der Natur

Unter Schalentragwerken versteht man in der Architektur flächige, doppelt gekrümmte Konstruktionen, welche aufgrund ihrer Form besonders leistungsfähig sein können und daher oft bei Bauten mit großen Spannweiten Verwendung finden. Historische Beispiele hierfür sind Kuppeln, wie beispielsweise im Pantheon in Rom (fertiggestellt um 128 n.Chr), welche es ermöglichten, mit den damaligen technischen Verfahren große Flächen zu überspannen. Auch gibt es viele Beispiele aus der modernen Architektur, in denen freigeformte, doppelt gekrümmte Schalen einen hohen ästhetischen Wert besitzen, wie beispielsweise das von Félix Candela entworfene L'Oceanogràfic in Valencia (eröffnet 2003) ⌜74. Durch die doppelte Krümmung werden Kräfte ausschließlich in der Schalenebene übertragen. Das führt zu einem vorteilhaften Tragverhalten und einer optimalen Ausnutzung des Materials und lässt daher relativ schlanke und leichte Konstruktionen zu. Die Herstellung solcher Tragwerke ist infolge ihrer Größe, ihrer unregelmäßigen Geometrie und ihrer doppelten Krümmung oft mit großem Aufwand verbunden. Aus diesem Grund gehen aktuelle Bestrebungen dahin, Schalen aus vorgefertigten Elementen herzustellen, welche vor Ort nur noch zusammengefügt werden müssen. Dies wurde bereits im Forstpavillon der Landesgartenschau in Schwäbisch Gmünd (2014) in Form eines Prototyps realisiert ⌜75. Die Schalen der Sanddollars sind in vielerlei Hinsicht den Schalen in der Architektur nicht unähnlich. So entsprechen die Platten der Seeigel auf niedrigerer hierarchischer Ebene den Segmenten der Schalentragwerke. Die relativ dünnen Seeigelschalen haben ein ähnliches Tragverhalten wie Schalenkonstruktionen in der Architektur und können daher als wichtiger Ideengeber für die Modulanordnung in segmentierten Schalentragwerken dienen.

88

74 *Das von Félix Candela entworfene L'Oceanogràfic in Valencia ist ein Beispiel für eine monolithische (aus einem Stück bestehende) Schale aus Stahlbeton.*

75 *Der Forstpavillon der Landesgartenschau in Schwäbisch Gmünd ist ein Prototyp für eine Segmentschale aus Furnierstreifenholzelementen.*

Außerdem können sie Vorbild für die Entwicklung besonders leistungsfähiger Modulverbindungen sein. Während Module in traditionellen technischen Konstruktionen oft einheitliche Formen aufweisen, zeigen die Platten der Seeigelschale beträchtliche Unterschiede in ihrer Geometrie und Krümmung. Die Anordnung der Platten folgt dabei aber einem strikten Grundbauplan, in dem sich immer drei Platten in einem Punkt treffen 76. Durch die Variation der Plattenform sowie der Verzahnung kann allein schon die Anordnung der Platten eine leistungsfähige Schalenkonstruktion erzeugen und ist damit eine wichtige Grundlage für bioinspirierte Schalentragwerke.

Die Verbindungen zwischen den Modulen stellen meist Schwachstellen segmentierter Schalenkonstruktion dar, da an diesen Übergängen die materielle und geometrische Kontinuität unterbrochen ist. Infolgedessen muss entweder die Kraftübertragung in der Fuge oder die Anordnung der Fugen selbst optimiert werden, um leistungsfähigere segmentierte Schalen bauen zu können. Seeigel aus der Gruppe der Sanddollars geben dabei wichtige Hinweise, wie diese Optimierung aussehen kann: Sie besitzen nämlich eine Kombination aus mechanischer Verzahnung 77 und Einlagerung von weicherem und elastischerem Gewebe innerhalb des Skelettes, wodurch eine leistungsfähige Fuge entsteht.

Durch interne Stützsysteme sind die obere und untere Schalenhälfte des Seeigelskeletts miteinander fest verbunden 73, 78. Kräfte können zwischen den beiden Schalenhälften übertragen werden und sorgen

76 *Im Skelett des Seeigels Leodia sexiesperforata treffen sich jeweils drei Platten in einem Punkt.*

dadurch für eine gleichmäßige Verteilung der Kräfte innerhalb der Schale. Hierdurch wird das Skelett insgesamt mechanisch weniger beansprucht. Schalentragwerke sind aus technischer Sicht Konstruktionen, die bei geringer Wandstärke große Flächen überspannen und dabei gänzlich ohne Stützen auskommen. Dem Verzicht auf Stützsystemen sind allerdings auch statische Grenzen gesetzt, insbesondere dann, wenn es sich um flache und wenig gekrümmte Schalenbereiche handelt. Speziell hier sind Anordnung und Geometrie der internen Stützapparate der clypeasteroiden Seeigel von Interesse, da sie Wege zur statischen Optimierung bei gleichzeitiger Einsparung von Baumaterial aufzeigen.

Zwar gibt es heute bereits weitgespannte und freitragende Schalentragwerke, doch ist ihre Herstellung oft mit einem vergleichsweise hohen Material- und Kostenaufwand verbunden. Von dem Verständnis der Struktur und des Tragverhaltens des Seeigelskelettes sowie der Übertragung ausgewählter Bauprinzipien in die Technik erhoffen sich Ingenieure und Architekten einen besseren Einblick in die Optimierung von Schalentragwerken. Ziel ist, Schalenkonstruktionen zu entwickeln, welche aus einzelnen vorgefertigten Bausegmenten bestehen. Das soll nicht nur den Material- und Ressourcenverbrauch senken, sondern auch vollkommen neue und leistungsfähige Leichtbaukonstruktionen ermöglichen. Die clypeasteroiden Seeigel weisen viele – für die Architektur wichtige – Eigenschaften auf, wie beispielsweise leistungsfähige Plattenverbindungen und interne Stützmechanismen. Daher stehen sie aktuell im Fokus biomimetischer Untersuchungen, von denen sich Paläontologen, Biologen, Ingenieure und Architekten neue Konzepte erhoffen, die einerseits revolutionär in Form und Funktion sind und andererseits das Verständnis über den Bau, die Funktion und die Entwicklungsgeschichte der Seeigel erweitern.

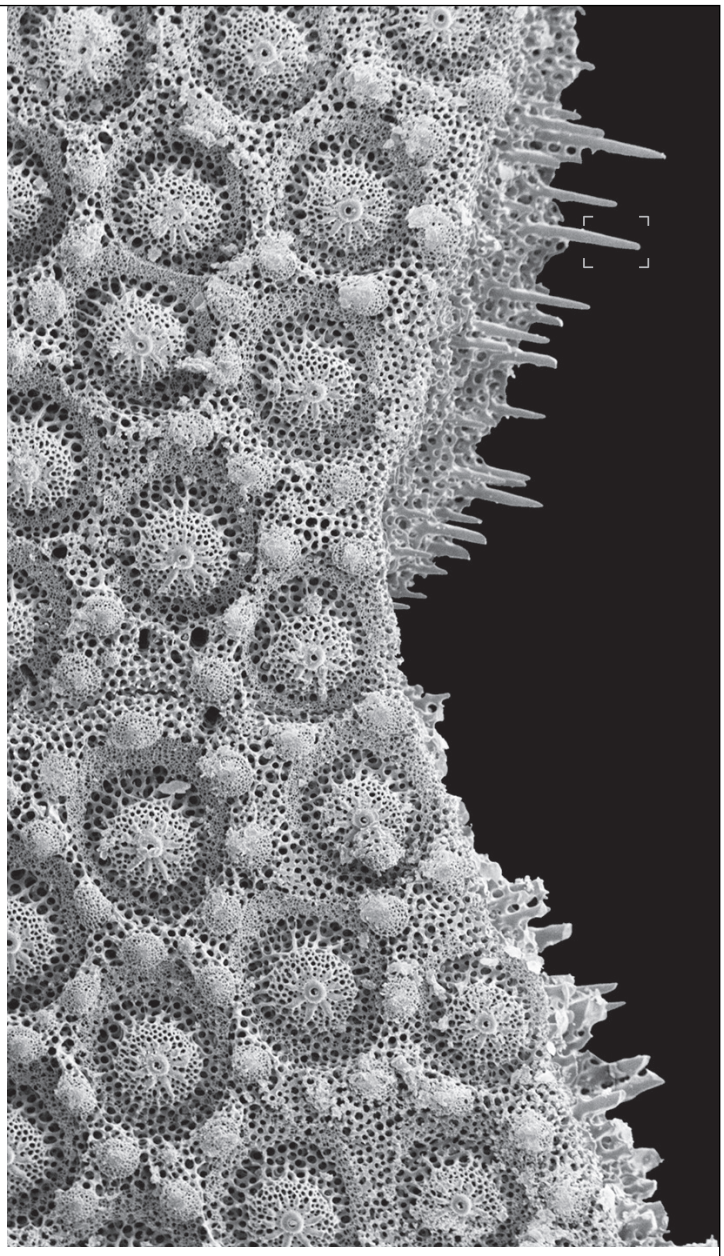

77 *Rasterelektronenmikroskopische Aufnahme der Stereomfortsätze an einer einzelnen Platte, welche eine leistungsfähige Verbindung der Platten erzeugen.*

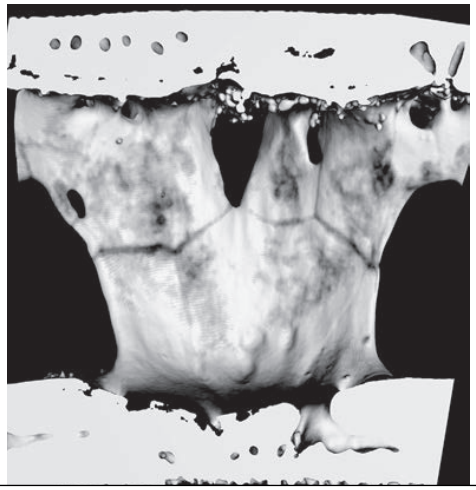

78 *Computertomographische Aufnahme eines internen Stützpfeilers des Seeigels Clypeaster rosaceus.*

91

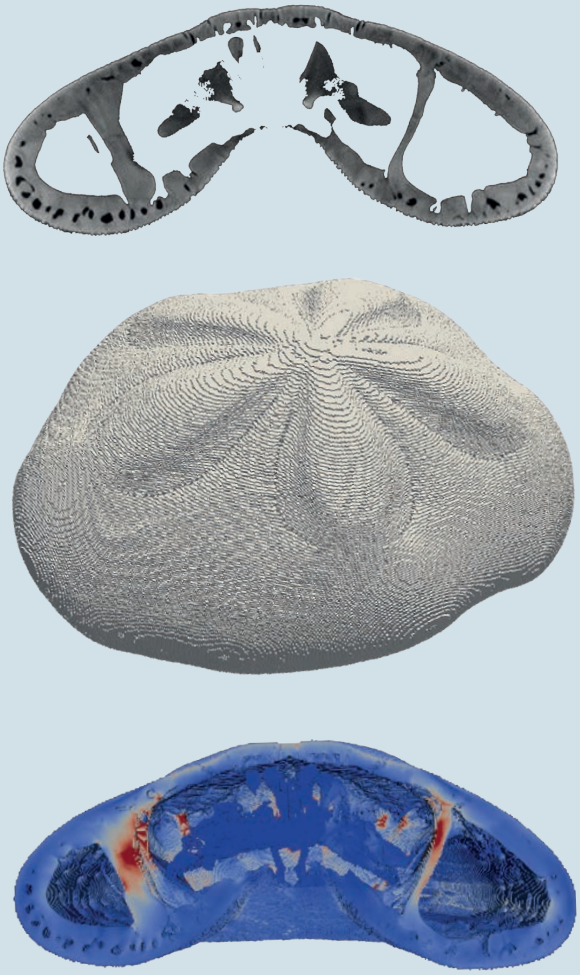

79 *Computertomographie-Scan (CT-Scan) und Voxelmodell des Skelettes des Seeigels Clypeaster roseaceus.*

Oben: Eine Scheibe des CT-Scans des Seeigelskeletts (je heller der Voxel, desto dichter ist das Material).

Mitte: Außenansicht des Voxelmodells.

Unten: Schnitt durch das Voxelmodell mit farblicher Darstellung der Materialbeanspruchung (rot = hohe Beanspruchung).

Seeigel in 3D

Um den inneren Aufbau und das mechanische Tragverhalten der Seeigelschalen zu untersuchen, wurden computertomographische Aufnahmen verschiedener Seeigel erstellt. Dabei erhält man Bilddateien, welche die Materialverteilung in einer sehr dünnen Scheibe des Seeigels zeigen 79. Die Helligkeit jedes Bildpunkts repräsentiert dabei die Dichte des Materials, wobei sich an schwarzen Punkten kein Material befindet und mit steigender Dichte die Punkte heller werden.

Auf Basis dieser scheibchenweisen Darstellung der Geometrie und Dichteverteilung der Seeigelschale wird ein dreidimensionales Voxelmodell (Würfelmodell) erzeugt. (Ein „Voxel" ist ein Bildpunkt im dreidimensionalen Raum, entsprechend dem „Pixel" in zweidimensionalen Darstellungen.) Dabei werden teilweise Voxel aus mehreren Bildpunkten von hintereinanderliegenden Bildern zu einem größeren Voxel zusammengefasst, um die Auflösung und damit den späteren Rechenaufwand zu reduzieren. Es werden nur Voxel erzeugt, deren Helligkeit über einer vorgegebenen Schwelle liegt. Im Anschluss wer-

92

den Voxel entfernt, die nicht mit der eigentlichen Seeigelschale verbunden sind und abschließend die für die statische Berechnung notwendigen mechanischen Lasten und Randbedingungen definiert.

Die dreidimensionalen Voxelmodelle der Seeigel ermöglichen die Untersuchung des mechanischen Verhaltens der Seeigelschalen in Simulationen. Das mechanische Verhalten lässt sich hierbei durch ein mathematisches Modell beschreiben. Die Gleichungen ähneln denen des Hookeschen Gesetzes zur elastischen Verformung von Festkörpern, mit dem sich Federdehnungen berechnen lassen. Sie beschreiben jedoch nicht das Verhalten einer einzelnen Feder unter Krafteinwirkung, sondern das eines dreidimensionalen, kontinuierlichen Körpers.

Die entsprechende wissenschaftliche Disziplin wird als Kontinuumsmechanik bezeichnet. Sie ist die Grundlage für Computersimulationen, die heute in vielen industriellen Bereichen durchgeführt werden, und beispielsweise eine Simulation des Crashverhaltens von Fahrzeugen erlaubt oder die Vorhersage des Tragverhaltens von geplanten Brücken. Die Lösung dieser Gleichungen erfolgt mit einem numerischen Modell, in diesem Fall der Finite-Elemente-Methode (FEM). Dabei kann durch die Aufteilung des Berechnungsgebietes in eine begrenzte Anzahl an Elementen eine Näherungslösung bestimmt werden. Als Lösung erhält man die Kräfteverteilung in der Seeigelschale, die sich für eine angenommene Belastung ergibt. Die Qualität der Näherungslösung wird mit kleiner werdenden Elementen und deren damit steigender Anzahl besser. Allerdings erhöhen sich dadurch auch der Berechnungsaufwand und insbesondere die Rechenzeit.

Durch die Untersuchung der Seeigelschale mit ingenieurwissenschaftlichen Methoden kann man ein vertieftes Verständnis ihrer Funktionen gewinnen.

Mit den oben beschriebenen mathematischen und numerischen Modellen können so unter anderem virtuelle Experimente am Computer durchgeführt werden, die mit einem realen Präparat nicht möglich wären. Außerdem lassen sich Ergebnisse wie z. B. Kräfteverteilungen oder Deformationen visualisieren und quantifizieren, die man in realen Experimenten nicht beobachten kann. Die Simulationen helfen so nicht nur bei der Umsetzung von Ideen aus der Biologie in die Technik, sondern tragen auch zu einem besseren Verständnis der biologischen Strukturen bei – ein Ansatz, der auch als „technische Biologie“ bezeichnet wird.